Experimental investigations relevant to the development of a laser interferometric gravitational wave detector

by

Euan Morrison

Department of Physics and Astronomy
University of Glasgow.

Presented as a thesis for the degree of

Ph.D. in the University of Glasgow.

January 1993.

ProQuest LLC.
789 East Eisenhower Parkway
P.O. Box 1346
Ann Arbor, MI 48106 – 1346

Contents

List of Figures

Acknowledgements

I would like to thank Harry Ward for his help, advice and good humour during the past three years at Glasgow. Dave Robertson deserves a special mention for his help in much of the experimental work which is described, especially in running the 10 m prototype. Thanks also go to Gavin Newton and Brian Meers for inspiration and interesting discussions, to Jim Hough for his support and to the rest of my colleagues in the gravitational waves group; Norna Robertson, Ken Strain, Norman McKenzie, Peter Veitch, Caroline Cantley, Allan Carmichael, Anne Campbell, Jennifer Logan, Ken Skeldon, Sheila Rowan and Alison McLaren. I would also like to acknowledge the stimulating discussions I have had with many of the people in the gravitational wave field throughout the world whom I've had the pleasure of meeting at various conferences and seminars during the course of my PhD studies.

I am grateful to the technicians in the group – Jim Pittillo, Angus McKellar, Allan Latta and Dave Edwards, and also to the staff in the workshop for their help and assistance.

Thanks also go to my Mum and Dad for supporting me throughout my time at University, and to Rachel – for providing a necessary distraction.

During my PhD studies I was in receipt of an SERC research grant and acknowledge the support of Prof. R. P. Ferrier and the University of Glasgow.

This thesis was written using the LaTeXdocument preparation system.

Preface

Ultra high sensitivity laser interferometers for detecting gravitational waves have been under development now for several years. With the advances which have been made in the understanding of the operation and limitations of the various prototype detectors around the world (including the 10 m detector in Glasgow), the possibility of detecting gravitational radiation using a full scale ground-based laser interferometer in the near future now looks very promising.

This thesis describes the work carried out by the author, in conjunction with colleagues in the gravitational waves research group in Glasgow, on the development of a 10 m protoype interferometeric detector and also on some theoretical and experimental investigations of relevance to the design of full scale detectors.

Chapter 1 gives a brief introduction to gravitational radiation as predicted by Einstein's general theory of relativity, including a discussion of some of the most likely sources which may be detectable using a ground-based detector. Possible methods of detecting gravitational waves using resonant bar detectors and laser interferometric detectors are outlined, along with a description of the potential noise limitations of these devices.

In Chapter 2 a general description of the analysis of control systems is given, with particular reference to laser interferometric detectors. The problem of noise in the various control systems associated with laser interferometers is discussed and some general conclusions drawn. Evaluation of the performance of a test mass damping control system for use in a full scale detector is given, along with an experimental investigation into a novel inertial damping control system. Most of the theoretical work was initiated by the author with help from Dr H. Ward. The experimental investigation of the inertial damping system was carried out with the help of Dr D.I. Robertson and Dr H. Ward. Some of the calculations relating to

the performance of the inertial damping system were independently verified by Dr P. J. Veitch.

Chapter 3 discusses in detail the theoretical and experimental investigation of an automatic alignment technique for use in high precision optical interferometers. The technique was initially tested on a simple benchtop Michelson interferometer and subsequently implemented on one of the suspended cavities in the 10 m prototype. This work was carried out with the help and advice of Dr H. Ward, Dr B.J. Meers and Dr D.I. Robertson.

A discussion of the operation and performance of the 10 m prototype detector is given in Chapter 4. Extensive checks on the calibration of the detector made by the author are described, followed by the investigations and improvements made to the performance of the detector in the period from early 1991 to the end of 1992. Much of this was prompted by the analysis of control systems discussed in Chapter 2. The majority of the experimental work carried out on the prototype in this period was by the author with help from Dr D.I. Robertson and also Dr H. Ward, Dr G.P. Newton and Dr K.A. Strain.

A discussion of the experimental development and evaluation of double pendulum local damping control systems constructed and tested by the author are given in Chapter 5. These systems were succesfully installed in the prototype detector and were responsible for much of the low frequency improvements in the detector sensitivity discussed in Chapter 4.

Chapter 6 gives a brief summary of the work of this thesis in relation to future detectors and the prospects for detecting gravitational waves.

Summary

The direct detection of gravitational radiation is one of the greatest challenges facing modern experimental physics. Successful detection of the minute changes in the curvature of spacetime caused by violent astrophysical phenomena could open up an entirely new branch of astronomy, furthering our understanding of the nature of the surrounding Universe.

Over the past few years much progress has been made in finding possible methods of detecting these gravitational waves. In particular, current investigations into the use of laser interferometric sensing techniques are showing great promise, indicating that ground-based laser interferometric detectors could potentially reach the sensitivities required.

In this thesis some of the aspects of the development of a 10 m prototype interferometeric gravitational wave detector are discussed. In addition, some aspects of the techniques necessary for the successful operation of a full scale detector are investigated.

A general discussion of feedback control systems used in laser interferometeric detectors is given, and some of the implications of the various noise sources and their effects on the potential sensitivity of the detector are pointed out. With these considerations in mind, a description of an electronic damping system for controlling the high Q pendulum resonances of the suspended test masses in a full scale laser interferometric gravitational wave detector is detailed and its noise performance analysed. In addition to this an experimental demonstration of a novel inertial damping control system for the suspended interferometer test masses is described and the performance of the system evaluated.

An ultra high precision automatic alignment technique for use in optical interferometers is presented, followed by a detailed mathematical description of its

operation and performance. It is expected that such a scheme, which can detect angular and lateral offsets of two interfering laser beams, along with mismatches in the beam size and phase front curvature, will be of particular importance in accurate alignment of a full scale detector. A description of the experimental testing of this alignment technique on one of the 10 m long suspended optical cavities forming part of the prototype detector in Glasgow is given.

The current status of the 10 m prototype laser interferometric gravitational wave detector is described, outlining the present configuration of the detector and its method of operation. A detailed description of the method of calibrating the detector is given. Some of the optical and mechanical problems which previously set severe limits to the performance of the detector are examined and the steps taken to reduce these effects are discussed. In particular, the development of two double pendulum suspension systems, designed to reduce the noise imposed on the detector output signal due to electronic noise in the pendulum control system is described. Much of this work is based on the earlier theoretical discussions on control systems and noise.

Finally, a summary of the work carried out is given and the prospects for detecting gravitational waves are discussed.

Chapter 1

Gravitational radiation - its production and possible methods of detection.

1.1 Introduction

In 1916 Einstein showed that the existence of gravitational waves was a direct consequence of his general theory of relativity [1]. These waves can be thought of as being wave-like disturbances on the curvature of spacetime, the effect of the waves being to change the relative separation of free test masses.

Gravitational radiation is quadrupole in nature, monopole and dipole radiation being forbidden due to the single sign of mass and the conservation of momentum. The weak nature of the gravitational interaction implies that fast coherent motion of large quantities of matter are required in order to produce a significant amount of gravitational radiation. As a result of this, the only sources of gravitational radiation which might be detectable experimentally are violent astrophysical events such as supernovae, pulsars or coalescing binary star systems. Detection of the gravitational radiation from such sources would provide new astrophysical information from the very heart of these events since the gravitational waves, unlike electromagnetic radiation, are able to pass almost unattenuated through the large quantities of surrounding matter.

This chapter gives a brief introduction to gravitational waves and reviews some of the more likely sources which may be detectable on earth based on current theoretical estimates. This is followed by a discussion of the techniques for detecting

gravitational waves which are currently being investigated.

1.2 Gravitational waves

In general relativity, the Einstein field equation is given by (see *e.g.* [2], [3])

$$G_{\alpha\beta} = \frac{8\pi G}{c^4} T_{\alpha\beta} \ , \tag{1.1}$$

where $G_{\alpha\beta}$ is the Einstein tensor representing the curvature of spacetime and $T_{\alpha\beta}$ the stress energy tensor representing the distribution of matter which gives rise to the spacetime curvature. If we consider a region of spacetime where the curvature is almost flat, the metric, $g_{\alpha\beta}$, can be approximated to

$$g_{\alpha\beta} = \eta_{\alpha\beta} + h_{\alpha\beta} \ , \tag{1.2}$$

where $\eta_{\alpha\beta}$ represents the flat Minkowski metric,

$$\eta_{\alpha\beta} = \begin{bmatrix} -1 & 0 & 0 & 0 \\ 0 & 1 & 0 & 0 \\ 0 & 0 & 1 & 0 \\ 0 & 0 & 0 & 1 \end{bmatrix} \ , \tag{1.3}$$

and $h_{\alpha\beta}$ a small perturbation term where $|h_{\alpha\beta}| << 1$. It can be shown that in this weak field approximation, in vacuum, the field equation 1.1 can be written as [3]

$$\left(\frac{1}{c^2} \frac{\partial^2}{\partial t^2} + \nabla^2 \right) h_{\alpha\beta} = 0 \ . \tag{1.4}$$

This is the simple three dimensional wave equation, showing the existence of gravitational waves propagating at the speed of light, c. If we consider a wave propagating along the z-axis, the solution to equation 1.4 is given by

$$h_{\alpha\beta} = A_{\alpha\beta} e^{i(\omega t - kz)} \ , \tag{1.5}$$

where ω is the angular frequency of the wave and k the wavenumber. The particular choice of coordinates which gives rise to this solution is referred to as the transverse, traceless (TT) coordinate system. The amplitude of the gravitational wave field, $A_{\alpha\beta}$, can be written as

$$A_{\alpha\beta} = \begin{bmatrix} 0 & 0 & 0 & 0 \\ 0 & A_{xx} & A_{xy} & 0 \\ 0 & A_{xy} & -A_{xx} & 0 \\ 0 & 0 & 0 & 0 \end{bmatrix} , \tag{1.6}$$

where A_{xx} and A_{xy} represent the amplitudes of the two independent polarisation states, normally denoted by h_+ ($A_{xy} = 0$ and $A_{xx} \neq 0$) and $h_\times$ ($A_{xx} = 0$ and $A_{xy} \neq 0$).

1.2.1 Effect of gravitational waves on free particles

Let us consider a gravitational wave of amplitude h in a single polarisation state such that $A_{xx} = h$ and $A_{xy} = 0$. Consider now the effect of this wave on the separation of two free particles in the plane $z = 0$, one of which is at the origin of the coordinate system and the other a distance l away in the x direction. The proper separation of the two particles is given by

$$\begin{aligned} l(t) &= \int_0^l \left| g_{\alpha\beta}\, dx^\alpha dx^\beta \right|^{\frac{1}{2}} \\ &= \int_0^l (1 + h_{xx})^{\frac{1}{2}}\, dx \, . \end{aligned} \tag{1.7}$$

Substituting in equation 1.5 gives

$$\begin{aligned} l(t) &\simeq l + \frac{h}{2} \int_0^l e^{i(\omega t - kx)}\, dx \\ &= l + \frac{h}{k} \sin\left(\frac{kl}{2}\right) e^{i\left(\omega t - \frac{kl}{2}\right)} \, . \end{aligned} \tag{1.8}$$

If we assume that the separation of the two particles is much smaller than the wavelength of the gravitational wave (*i.e.* $kl << 1$), then the magnitude of the change

in separation of the two free particles with respect to their original separation, $\frac{\delta l}{l}$, is given by

$$\frac{\delta l}{l} = \frac{h}{2} \,. \tag{1.9}$$

It is easy to show that the effect of the same wave on two particles separated by a distance l along the y axis is

$$\frac{\delta l}{l} = -\frac{h}{2} \,. \tag{1.10}$$

A similar analysis can be carried out to evaluate the effect on separated test particles of a gravitational wave of the orthogonal polarisation. These results are summarised in figure 1.1 where the change in separation of a ring of test particles due to a gravitational wave in both orthogonal polarisations is shown over one full cycle of the wave.

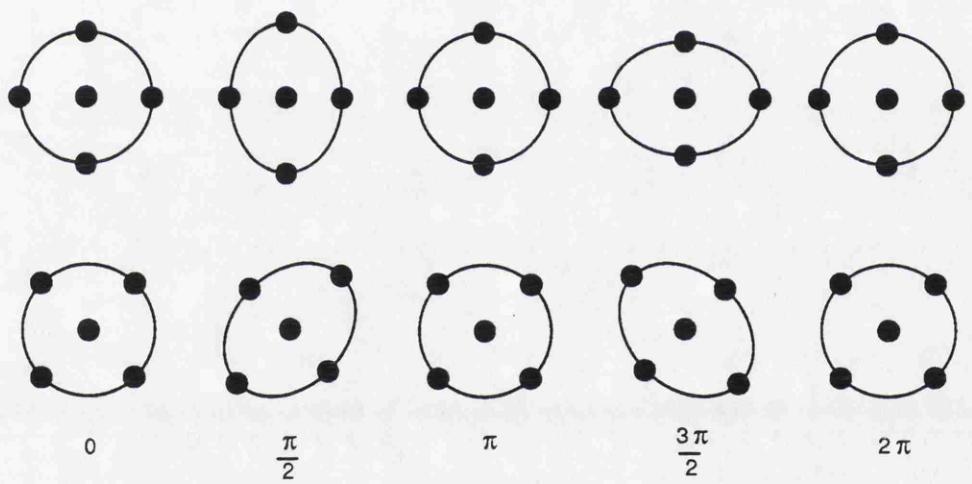

Figure 1.1: *A ring of free test particles showing the change in separation of the particles as a gravitational wave passes. The upper sequence shows the effect of a gravitational wave in the h_+ polarisation state, the lower trace the $h_\times$ state.*

1.3 Possible sources of gravitational radiation

Any system of masses whose quadrupole moment changes with time will produce gravitational radiation. However, theoretical estimates of the amount of energy

radiated from laboratory sources reveal that such sources are simply too weak to enable detection of the emitted radiation. For example, it has been estimated [4] that a 1 metre dumbbell weighing 1 tonne and spinning at 10,000 rpm (conditions which incidently no known material can withstand) would only radiate $\sim 5 \times 10^{-33}$ watts. The only possible detectable sources appear to be due to extremely violent astrophysical phenomena, where large quantities of matter, travelling close to the speed of light are capable of producing a significant amount of gravitational radiation.

Observations of the orbital parameters of the binary pulsar PSR1913+16 have given indirect evidence that gravitational waves are being emitted by this system [5]. However the detection of gravitational radiation would provide a direct verification of general relativity. By comparing the arrival times of the first bursts of light and gravitational radiation from a supernova it should be possible to confirm with high accuracy the prediction of general relativity that gravitational radiation propagates at the speed of light. Similarly the prediction of general relativity that gravitational waves are transverse and traceless could be confirmed by measuring the polarisation of the waves using two or more detectors. However, probably the most exciting aspect of detecting astrophysical gravitational waves is the information which could be gathered from the detectors relating to the source of the waves themselves. Such information would give new insight into the nature of the events producing the radiation, effectively opening up an entirely new branch of astronomy.

The gravitational radiation emitted from the most likely of sources is usually separated into three main categories: bursts, where the gravitational radiation only lasts for a few cycles; periodic waves, where the radiation is roughly constant over many cycles; and stochastic waves where the radiation fluctuates stochastically. These sources are discussed in the following pages, however, a more comprehensive review can be found in [6].

1.3.1 Burst sources

Supernovae

Supernovae are classified into two classes, Type I and Type II. Type I supernovae are thought to result from the nuclear explosion of a white dwarf which accretes matter from a close companion star. This may or may not result in the collapse of the stellar core to a neutron star; if not then it is unlikely that significant amounts of gravitational radiation will be emitted. Type II supernovae are believed to be due to the gravitational collapse of the core of a massive, highly evolved star into a neutron star.

The amount of energy radiated by a collapsing star will depend on the change in the quadrupole moment of the system (a perfectly symmetric collapse producing no gravitational waves) and also the rate at which the stellar core collapses. It is thought that there may be two different types of collapse, a fast collapse where the amount of energy emitted as gravitational radiation may be as much as $10^{-2}\,M_{\odot}c^2$, where $M_{\odot}$ is one solar mass, and a slow hot collapse, where the collapse of the system is slowed down by the effect of radiation pressure. In this last case the energy emitted in the form of gravitational radiation may be as little as $10^{-5}\,M_{\odot}c^2$. An estimate of the gravitational wave amplitude due to a burst with a centre frequency of 1 kHz is given by [7]

$$h = 10^{-21}\left[\frac{E}{10^{-2}\,M_{\odot}c^2}\right]^{\frac{1}{2}}\left[\frac{r}{15\,\mathrm{Mpc}}\right]^{-1}, \tag{1.11}$$

where r represents the distance to the source and E the amount of energy emitted as gravitational radiation. Typically several Type I and II supernovae are observed a year out to 15 Mpc, the distance to the Virgo cluster of galaxies.

Coalescence of compact binary systems

Most stars are thought to begin as members of binary systems. There is a good chance, therefore, that a reasonably large fraction will remain binary after the individual stars have completed their evolution. This would mean that there could

be a significant number of binary systems consisting of highly compact objects, such as neutron stars or black holes, which are close enough to coalesce, emitting significant amounts of gravitational radiation. As the two bodies in such a compact binary system spiral together they will emit periodic gravitational waves that sweep upwards in frequency. The expected signal from such an event has been estimated [8] as

$$h \sim 10^{-23}\left[\frac{r}{100\,\mathrm{Mpc}}\right]^{-1}\left[\frac{M}{M_\odot}\right]^{\frac{2}{3}}\left[\frac{\mu}{M_\odot}\right]\left[\frac{f}{100\,\mathrm{Hz}}\right]^{\frac{2}{3}}, \tag{1.12}$$

where M is the total mass of the source, μ the reduced mass and f the instantaneous frequency of the emitted radiation. The frequency of the emitted waves will change on a timescale τ given by

$$\tau = \frac{f}{\dot{f}} = 7.8\left[\frac{M}{M_\odot}\right]^{-\frac{2}{3}}\left[\frac{\mu}{M_\odot}\right]^{-1}\left[\frac{f}{100\,\mathrm{Hz}}\right]^{-\frac{8}{3}}. \tag{1.13}$$

By observing such a gravitational wave it is possible to solve equations 1.12 and 1.13 to obtain a value for r representing the distance to the source. If, in addition, the galaxy in which the event took place could be optically identified and a redshift obtained, then the observation of a few such events should allow an accurate calculation of Hubble's constant [8].

The event rate for such coalescences is very uncertain. It has been estimated that there may be between several to several thousand events which may be observable with a detector capable of reaching sensitivities of $h \sim 10^{-22}$ every year, out to $\sim 500\,\mathrm{Mpc}$.

1.3.2 Periodic sources

Pulsars and other rotating neutron stars are thought to produce a significant amount of periodic gravitational radiation due to deviations from symmetry of the star about its rotation axis. Possible non-axisymetric distortions of the star may be due to the crust or core of the star supporting deformations or lumps that exist from the star's past history. For example, the presence of glitches in the

measured rotational period of some pulsars is thought to be due to the release of crustal distortions.

It is also possible that unstable pulsars, spinning down after having been formed with too large an angular velocity, could produce reasonable amounts of gravitational radiation.

Another class of stars which could potentially radiate large quantities of gravitational waves are unstable accreting neutron stars, known as Wagoner stars. In such systems, a non-axisymmetric instability in the star is driven by the accretion of angular momentum causing it to radiate gravitational waves.

Very little is known about the possible abundance of such sources in our galaxy, or indeed the strength of the radiation which they emit (which depends critically on the degree of asymmetry of the system). Consider a pulsar, whose ellipticity is given by δ (where δ is given by one minus the ratio of the minor and major equitorial axes of the star). The gravitational wave amplitude a distance r away from the star is given by [9]

$$h \sim 10^{-21}\,\delta \left[\frac{f}{100\,\mathrm{Hz}}\right]^2 \left[\frac{r}{10\,\mathrm{kpc}}\right]^{-1}, \tag{1.14}$$

at a frequency f which is twice the frequency of rotation. It has been estimated that this gives $h \sim 10^{-26}$ for the Crab pulsar and $h \sim 5 \times 10^{-27}$ for the Vela pulsar, assuming ellipticities of $\delta \sim 10^{-5}$. Although these appear to be rather small signals, it should be possible to 'tune' a detector to the frequency of the gravitational wave and integrate the output of the detector over long timescales, leading to an increase in the signal/noise ratio for a continuous source proportional to $\sqrt{\tau_{obs}}$ (where τ_{obs} is the observation time over which the output is integrated). For example, it should be possible to reach $h \sim$ a few $\times 10^{-28}$ for continuous waves with an observation time of 10^7 seconds with a full scale interferometric detector such as proposed by Hough *et al.* [7].

Binary star systems are also promising sources of continuous periodic gravitational waves. However, in order to emit continuous radiation it is necessary for the two stars to be sufficiently well separated so that they do not coalesce (as described

in section 1.3.1). This means that the frequency of the radiation emitted will probably be below 10 Hz and extremely hard to detect using ground based detector, because of the severe sensitivity limit set by seismic noise. However, such sources may be detectable using space borne detectors.

1.3.3 Stochastic sources

It is possible that there may be a stochastic background of gravitational waves due to many different sources, including perhaps gravitational waves produced very early in the history of the universe.

It is likely that there will be a strong background of gravitational waves emitted by binary star systems at frequencies below 0.03 Hz [6]. It has also been suggested that if there was a pre-galactic population of massive population III stars that these could have rapidly evolved and perhaps terminated in violent events such as supernovae or collapse to black holes. Such events would result in an isotropic and stochastic background of gravitational waves.

Another source of background gravitational radiation may be due to cosmic strings. These are thought to have acted as the 'seeds' for the condensation of galaxies and it is possible that their decay has led to a background of stochastic gravitational waves.

Because of the stochastic nature of these waves it is necessary to use two or more independent gravitational wave detectors and cross-correlate the outputs in order to detect such radiation.

1.4 Gravitational wave detectors

Over the past 30 years, since the development of the first bar detectors, many different possible methods and techniques for detecting gravitational waves have been suggested (for a review see *e.g.* [6]). Current experimental efforts are focussed on two main types of detector: resonant bar detectors and laser interferometer based detectors, both of which are discussed in the following two sections.

1.5 Resonant bar detectors

The first resonant bar detectors were built by Joseph Weber at the University of Maryland in the early 1960's [10], [11]. Since then, many groups around the world have developed resonant bar gravitational wave detectors with continually improving performance and sensitivity.

The early bar detectors consisted of large cylinders of aluminium, typically 1→2 tonnes and 1→2 m in length, suspended inside a vacuum system in order to isolate the bar as much as possible from external seismic and acoustic excitation. The effect of a passing gravitational wave is to strain the bar, driving the mechanical oscillations of the bar. For short bursts of gravitational radiation the strain induced in the bar, $\frac{\delta l}{l}$, is roughly equal to the gravitational wave amplitude, h. The motion of the bar can be measured using a suitable sensor; the early Weber bars had small piezoelectric crystals glued around the middle of the bar measuring the induced strain.

The signal obtained from the sensor is usually amplified and filtered so that only the fundamental mode of the bar is monitored, *i.e.* the mode involving the motion of the ends of the bar with a single node at the bar's centre. The frequency of oscillation of this mode is given by

$$f_0 = \frac{v_s}{2l} , \tag{1.15}$$

where v_s is the speed of sound in the bar and l the length of the bar. The resonant frequency of the fundamental mode of a 2 m long cylindrical aluminium bar is therefore $\sim$ 1 kHz. Any signal which may be due to a passing gravitational wave has to compete with the various noise sources present in the detection system. The main sources of noise in a resonant bar detector are due to thermal noise in the bar and noise inherent in the sensing system. The thermal noise is due to the weak coupling of the fundamental mode of the bar to its environment. For a bar at a temperature T, the amplitude of a single mode of vibration is random, with an amplitude corresponding to an energy kT. If the fundamental mode of the bar has a high enough Q, such that the time interval between successive measurements,

τ is less than the damping time of the bar, τ_d (where $\tau_d = \frac{Q}{\pi f_0}$), then the mean change in energy of the mode between measurement is given by

$$kT\frac{\tau}{\tau_d} . \tag{1.16}$$

Treating the bar as a simple harmonic oscillator, the root mean square motion of the ends of the bar in the fundamental mode due to thermal excitation is then given by

$$|\Delta x| = \left(\frac{kT\,\tau}{2\pi f_0 M Q}\right)^{\frac{1}{2}} , \tag{1.17}$$

where Δx is measured over the period τ. When trying to optimise the sensitivity of the bar to short, broad band, bursts of gravitational radiation, the effect of thermal noise fluctuations can be reduced by suitably reducing the sampling time τ. Unfortunately, this has the disadvantage that it increases the sensor noise, leading to an 'optimal' sampling time for operation of the bar. For present bar detectors this is typically $\tau \sim 0.1$s. If we consider a 1 tonne cylindrical aluminium bar at room temperature, with a Q of $\sim 10^5$, $f_0 \sim 1$ kHz and a measurement sampling time of 0.1 s, equation 1.17 gives a limit to the detectable gravitational wave amplitude for a short broad band pulse of $h \sim 10^{-17}$.

In order to improve the sensitivity, most current bar detectors are cryogenically cooled to a temperature of ~ 4 K. In addition, some highly sophisticated sensing systems have been developed – piezoelectric crystals having been abandoned because of their high intrinsic losses. Current sensing systems include passive, inductively coupled, superconducting transducers using ultra low noise SQUID amplifiers and also superconducting parametric upconverters (see [12], [13]). The bars currently operated by the Stanford and Rome (at CERN) groups have sensitivities corresponding to $h \sim 5 \rightarrow 8 \times 10^{-19}$ for millisecond bursts around 1 kHz and are very close to the thermal noise limit (see [14], [15]).

Despite having overcome some tough experimental challenges to reach these sensitivities, it will be very difficult to improve the performance of these detectors significantly beyond these levels. A fundamental limit to the sensitivity which can be achieved is set by the Heisenberg uncertainty principle. For a bar this is given

by

$$|\Delta x|^2 = \frac{\hbar}{M\omega_0} , \tag{1.18}$$

which limits the sensitivity of a $1 \rightarrow 2$ tonne bar to $h \sim 10^{-21}$. There are however some proposed methods for circumventing this quantum limit, known as 'quantum non-demolition' or 'back-action evasion' techniques. Nevertheless, the experimental difficulties associated with further improving the sensitivities of existing detectors are considerable and it appears unlikely that bar detectors will be able to reach sensitivities much better than $h \sim 10^{-20}$ in the near future.

1.6 Laser interferometric gravitational wave detectors

The first laser interferometer to be developed as a prototype gravitational wave detector was built in 1972 by Robert Forward at Hughes Research Laboratories [16]. The detector, although relatively simple in design, reached a sensitivity of $h \sim 2 \times 10^{-16}/\sqrt{\text{Hz}}$ between 2.5 and 25 kHz, illustrating the great potential of laser interferometers for detecting gravitational waves. Following on from this, several research groups around the world have developed significantly more advanced and sensitive interferometric detectors. The groups at the Max-Planck-Institut für Quantenoptik at Garching (near Munich) and the Massachusetts Institute of Technology (MIT) developed detectors based on multiple bounce optical delay lines, whereas the groups at the California Institute of Technology (Caltech) and Glasgow have concentrated on Fabry-Perot based interferometers.

After more than 10 years of development, these detectors are now beginning to reach the same sensitivities as the cryogenically cooled bar detectors. Several groups are now proposing to build long kilometre scale interferometric detectors (see [7], [17] and [18]) in an effort to improve sensitivities to $h \sim 10^{-22}$ (for millisecond bursts), sensitivities at which gravitational waves should be detectable.

The following section gives a brief introduction to laser interferometric gravitational wave detectors, discussing their potential sensitivity and some of the factors which may limit their performance.

1.6.1 Laser interferometers – principle of operation

As discussed in section 1.2.1, the effect of a gravitational wave is to induce a strain in space, causing a change in separation of two free test masses. Laser interferometers can be used to measure this relative change in separation by comparing the separation of the masses with respect to the wavelength of light. In such a detector, the masses are suspended as pendulums (with resonant frequency of the order of 1 Hz), isolating them from external seismic disturbances and allowing them to act as essentially free test masses at frequencies above the pendulum resonance. However, it is not practical to simply measure the relative change in separation of two free test masses, since the extremely small change in separation which must be detected places unreasonable demands on the wavelength stability of the source laser. Instead it is much easier to monitor the relative lengths of two orthogonal arms. This is essentially what is measured using a simple Michelson interferometer, as shown in figure 1.2. Here, the light from a laser is directed towards a

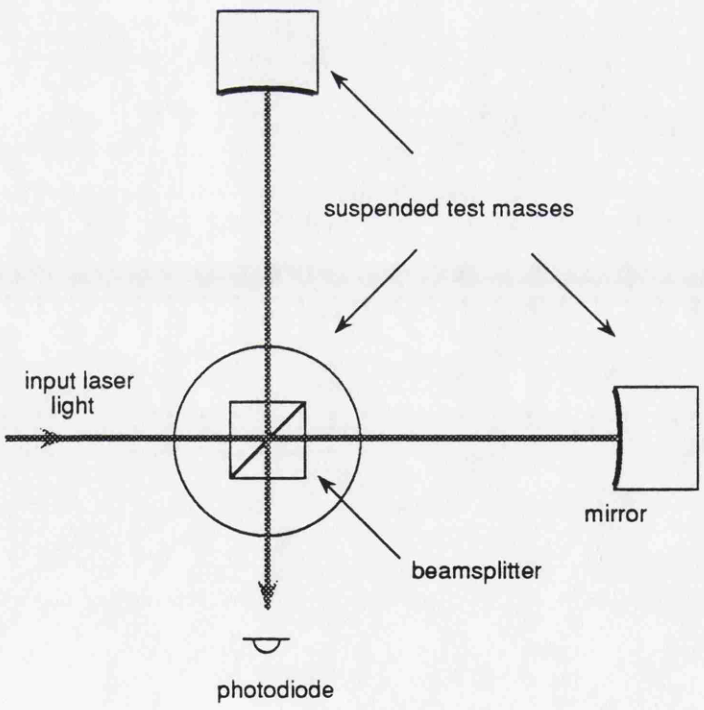

Figure 1.2: *A simple Michelson interferometer.*

beamsplitter from which the light travels along the two arms of the interferometer. Mirrors at the end of each arm reflect the light back towards the beamsplitter and the interference of the two beams is viewed at the output of the interferometer using a photodetector. Any change in the length of one arm with respect to the other, Δx, causes a phase shift $\phi = \frac{2\pi}{\lambda}\Delta x$ between the two interfering beams at the output, resulting in a change in the intensity of the light detected using the photodiode. The intensity of light at the output is given by

$$I = \frac{I_0}{2}(1 - \cos\phi) \ , \tag{1.19}$$

where I_0 is the input light power. Therefore by monitoring the intensity of the interfering beams at the output of the interferometer, we can measure the differential arm length change.

This detector configuration is particularly appropriate because of the quadrupole nature of gravitational radiation (as discussed in section 1.2.1). If we consider a gravitational wave which is vertically incident on such a detector in the h_+ polarisation state, a change in length of one arm of the interferometer due to the incident wave will be accompanied by a change in length of the other arm with the opposite sign. Since the change in separation of two test masses due to a gravitational wave of amplitude h is given by $hl/2$, the fractional differential arm length change between two arms of a Michelson interferometer, $\Delta l/l$ is equal to h.

The sensitivity of such an interferometer can be enhanced by multiply reflecting the light up and down each arm using either an optical delay-line or a Fabry-Perot cavity as shown in figure 1.3. In the delay line the light enters through a hole in the near mirror and traverses the arm length many times before exiting the delay line (either through the same hole in the near mirror as the light enters or through a different one). The storage time of the light in the delay line is given by $\tau_{dl} = 2Nl/c$, where N is the number of complete traverses of the light up and down one arm (the lower diagram in figure 1.3 showing $N = 3$).

In the Fabry-Perot, light enters through a partially transmitting input mirror and resonates in the cavity. There is no separation of the beams as in the delay line, instead the beams overlap on each traverse. The phase change induced on

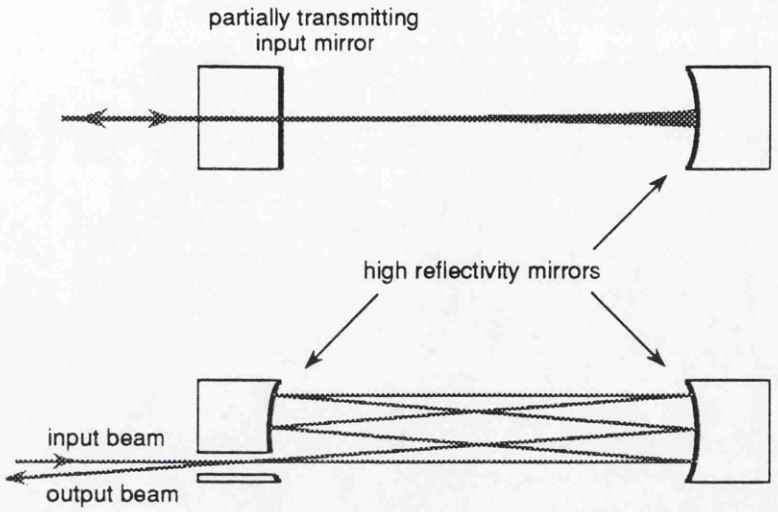

Figure 1.3: *A Fabry-Perot cavity (above) and a multiple beam delay line (below).*

the reflected light from the Fabry-Perot is slightly more complicated (for a full description of its operation see *e.g.* [19]). It is possible however to calculate a value for the effective number of traverses of the light inside the cavity, $N_{eff} = \frac{F}{\pi}$, where F is the finesse of the cavity given by $F = \frac{\pi R_1 R_2}{(1-R_1 R_2)^2}$ where R_1 and R_2 are the amplitude reflectivities of the cavity mirrors. The effective storage time is therefore given by $\tau_{fp} = \frac{2Fl}{c\pi}$.

The phase shift $\delta\phi$ between the two beams at the output of an interferometer with multiple reflection delay lines in the arms due to a gravitational wave of amplitude h is [7]

$$\delta\phi = 2h\frac{\nu}{f_g}\sin(\pi f_g \tau_{dl}) \ , \tag{1.20}$$

where ν is the frequency of the light and f_g the frequency of the gravitational wave. This is clearly a maximum when $f_g\tau_{dl} = \frac{1}{2}$, *i.e.* when the storage time is half the gravitational wave period. This is commonly referred to as the storage time limit. The equivalent expression for an interferometer with Fabry-Perot cavities in the arms is [20]

$$\delta\phi = h\,\alpha_c\frac{\nu}{f_g}\frac{2\pi f_g \tau_{fp}}{[1+(2\pi f_g \tau_{fp})^2]^{\frac{1}{2}}} \ , \tag{1.21}$$

where α_c is the amplitude of the light leaking out of the cavity on resonance

and is a function of the losses inside the cavity and also the cavity input mirror transmission.

1.6.2 Fundamental limits to the sensitivity of an interferometric gravitational wave detector

Photon shot noise

A fundamental limit to the sensitivity of a laser interferometer is set by photon shot noise, due to the discrete nature of photons. The signal detected at the output of the interferometer due to n photons will have a $\sqrt{n}$ uncertainty associated with it due to photon counting statistics.

In order to estimate this limit consider the simple Michelson interferometer described in section 1.6.1 with delay lines in the arms. The intensity at the output of the interferometer varies as the phase of the two interfering beams at the output changes (due to a differential change in the interferometer arm length). The signal, δI, detected at the output due to a change in ϕ, from equation 1.19, is just

$$\delta I = \frac{I_0}{2} \sin\phi \, \delta\phi \ , \tag{1.22}$$

where $\delta\phi$ is as given in equation 1.20 for an interferometer in which the light is reflected many times up and down each arm. The detected photocurrent, for a gravitational wave of amplitude h is given by

$$\delta I_p = \left(\frac{q\,\epsilon}{2\pi\,\hbar\,\nu}\right) \frac{I_0}{2} \sin\phi \left(2h\frac{\nu}{f}\sin(\pi f_g \tau_{dl})\right) \ , \tag{1.23}$$

where ϵ is the quantum efficiency of the detection photodiode.

The shot noise in the detected photocurrent, I, is given by [21]

$$\begin{aligned} \delta I_n &= \sqrt{2\,q\,\bar{I}\,\Delta f} \\ &= \sqrt{2\,q\left(\frac{q\,\epsilon}{2\pi\,\hbar\,\nu}\right)\frac{I_0}{2}(1-\cos\phi)\,\Delta f} \ . \end{aligned} \tag{1.24}$$

The detected signal must be greater than the noise, *i.e.* $\delta I_p > \delta I_n$, giving a limit to the detectable gravitational wave amplitude of

$$h > \left(\frac{\pi \hbar \lambda \Delta f}{\epsilon I_0 c}\right) \frac{1}{\cos^2 \frac{\phi}{2}} \frac{f_g}{\sin(\pi f_g \tau_{dl})} . \tag{1.25}$$

Clearly this is a minimum if $\phi = 0$ *i.e.* if the output of the interferometer is held on a dark fringe. In the storage time limit (*i.e.* $f_g \tau_{dl} = \frac{1}{2}$) equation 1.25 can be re-written as

$$h > 2.4 \times 10^{-21} \left[\frac{\epsilon I_0}{50\,\mathrm{W}}\right]^{-\frac{1}{2}} \left[\frac{f}{1\,\mathrm{kHz}}\right]^{\frac{3}{2}} , \tag{1.26}$$

where a bandwidth of $\Delta f = \frac{f}{2}$ has been chosen and $\lambda = 514\,\mathrm{nm}$. A similar expression can be derived for an interferometer which has Fabry-Perot cavities in the two arms. This equation indicates the great potential which laser interferometers have as possible detectors of gravitational waves.

In practice it is extremely difficult to reach the limit set by equation 1.26 with this particular interferometer configuration – the sensitivity being limited by a number of different factors including losses in the interferometer optics and the effect of the various modulation techniques used to extract the detector signal in a real interferometer. The calculation of the shot noise limit for a realistic interferometer, with Fabry-Perot cavities in the arms is discussed in Appendix A.

It should however be possible to reach higher sensitivities (*i.e.* $h \sim 10^{-22}$) using one or more of the advanced interferometric techniques (power and dual recycling) which are discussed later in section 1.6.4.

Radiation pressure and the Heisenberg uncertainty principle

From equation 1.26 it can be seen that by increasing the light power in an interferometer, the shot noise limited sensitivity can be improved. It is not possible, however, to improve the sensitivity of such an interferometer indefinitely, since increasing the light power results in an increase in the radiation pressure which acts on the test masses in the interferometer.

A fundamental limit to the accuracy of a test mass position measuring system is set by the Heisenberg uncertainty principle. This occurs in an interferometer when

the shot noise is balanced by the effect of fluctuations in radiation pressure. The limit to the detectable gravitational wave amplitude h using a laser interferometer with arms of length l and freely suspended test masses of mass m is given by (see [6])

$$h > \left(\frac{8\hbar}{m(2\pi f)^2 l^2}\right)^{\frac{1}{2}} , \tag{1.27}$$

where the measurement frequency f is well above the test mass suspension resonant frequencies ($\sim 1\,\mathrm{Hz}$). In practice extremely high levels of light power are required before this limit can be reached.

1.6.3 Technical noise sources

In a real interferometer there are many possible sources of noise which can seriously limit the sensitivity, preventing the detector reaching the shot noise limit discussed in section 1.6.2. The most important of these are discussed in the following pages.

Seismic noise

The level of seismic noise present at the detector site will vary depending on the exact location of the site and possibly also on the time of day (if some of the noise is man-made). Several measurements of seismic noise have been made [22], but in general, for a reasonably quiet site, the amplitude of seismic noise can be approximated by

$$\delta x \sim \frac{10^{-7}}{f^2}\,\mathrm{m}/\sqrt{\mathrm{Hz}} . \tag{1.28}$$

This represents a displacement noise of $\sim 10^{-11}\,\mathrm{m}/\sqrt{\mathrm{Hz}}$ at 100 Hz illustrating the need for good seismic isolation of the interferometer test masses. Suspension of the test masses using single or multi stage pendulums provides some isolation from this seismic noise, the motion of the test masses being reduced by $\sim \frac{1}{f^2}$ above the resonant frequency of the suspension system (and below the resonances of the suspension wires) for each stage of isolation.

In addition to these pendulum suspension systems, lead and rubber isolation stacks can be used to further reduce the effects of seismic noise. Essentially these

stacks, which are designed to have low Q, attenuate the seismic noise by $\sim \frac{1}{f}$ above the stack resonances which are typically below 10 Hz [23].

The combined use of stacks and two or more stage test mass suspension system should allow seismic noise to be suitably reduced at detection frequencies of 100 Hz→ a few kHz. However it is likely that seismic noise will severely limit measurements made at lower frequencies. Investigations into the effectiveness of a 7-stage 'super attenuator' as a possible method of providing good isolation at frequencies between 10 and 100 Hz are being carried out at Pisa ([24]).

Thermal noise

Thermal noise in the internal modes of the interferometer test masses and also in the suspension systems used to isolate the test masses from seismic noise could provide a serious limit to the sensitivity of a laser interferometer.

The frequencies of the internal modes of the test mass are usually arranged to be well outside the gravitational wave detection bandwidth (in the 10 m prototype for example, the first resonance is at $\sim$ 17 kHz). The limit to the detectable gravitational wave amplitude h at frequencies well below the first resonance is given by [7]

$$h \sim \left(\alpha \frac{32\, k\, T\, \Delta f}{\pi^3\, \rho\, {\nu_s}^3\, Q\, l^2} \right)^{\frac{1}{2}} , \tag{1.29}$$

where $\alpha \sim 2.5$ is a factor which takes into account the summation of the effects of several modes of the mass, ρ is the density of the test mass, ν_s is the speed of sound in the test mass material, Q is the internal quality factor and Δf is the measurement bandwidth. Clearly, by ensuring that the test mass has a sufficiently high Q, the effect of thermal noise can be minimised.

Although the current prototype detectors are at sensitivities well above the limit set by thermal noise, it is likely that future detectors could well be limited by thermal noise effects. Recently it has been suggested [25] that the thermal noise below the resonant frequency of the internal modes of the test mass may be larger than that given in equation 1.29, depending on the exact form of the

damping mechanisms present in the test mass material. This could seriously limit the performance of future detectors and further experimental investigations are under way to investigate the possible loss mechanisms associated with test mass materials.

The thermal noise associated with the test mass pendulum suspension system is given by [7]

$$h \sim \left(\frac{16\, k\, T\, \omega_0\, \Delta f}{m\, Q_s\, \omega^4\, l^2} \right)^{\frac{1}{2}}, \tag{1.30}$$

where ω_0 is the pendulum resonant frequency and Q_s the quality factor of the pendulum suspension system. Clearly then a high Q suspension system is required in order to minimise the effect of thermal noise in the test mass suspension system on the performance of the detector. It should be noted that equation 1.30 will also depend on the exact form of the damping mechanisms involved in the suspension system. However, since in this case, the frequency region of interest for detecting gravitational waves is above the resonance, it is likely that the thermal noise associated with the pendulum suspension could well be lower than that given by equation 1.30.

Laser frequency and intensity noise

Laser frequency noise can couple into the output signal of an interferometric detector in a number of different ways. For example, a detector which has Fabry-Perot cavities in the arms will be susceptible to frequency noise if the storage times of the two cavities are different. Similarly, in a delay line based interferometer, if the lengths of the two arms are slightly different, then frequency noise can couple into the detector output. Much work has been carried out into the frequency stabilisation of lasers for use in gravitational wave detectors [26]. The particular scheme which is currently used in Glasgow on the 10 m prototype consists of a two loop stabilisation system, where the laser is initially stabilised to a small rigid reference cavity and then to one of the 10 m long suspended cavities which forms one of the arms of the detector (described in greater detail in Chapter 4). This system

typically operates with a loop gain of $\sim 10^7$ at 1 kHz, reducing the frequency noise of the laser to a few $\times 10^{-5}\,\mathrm{Hz}/\sqrt{\mathrm{Hz}}$ at detection frequencies.

Intensity noise present in the laser light can also couple into the output signal of an interferometric detector. Normally, *rf* phase modulation techniques are used to extract the main interferometer signal. This ensures that the phase measurement which determines the arm length (or differential arm length) of the interferometer is made at frequencies where the laser intensity is shot noise limited. Provided the interferometer is sufficiently well locked on a dark fringe at its output, low frequency intensity noise should not couple into the detected signal. However, if the interferometer is slightly offset from the null fringe, perhaps due to a lack of gain in the servo which is used to lock the interferometer, intensity noise will couple into the detector output. This will limit the detector sensitivity to

$$h \sim \frac{\Delta l}{l}\frac{\Delta I}{I}\,, \tag{1.31}$$

where $\frac{\Delta I}{I}$ represents the level of intensity noise in the laser and Δl the offset of the interferometer from the locking point. Typically one might expect a maximum offset of the order of $\Delta l \sim 10^{-12}$ m (depending on the loop gain of the servos used to lock the interferometer) due to seismic noise at low frequencies, requiring an intensity stability of $\frac{\Delta I}{I} \sim 3\times 10^{-8}/\sqrt{\mathrm{Hz}}$ for a detector which can reach sensitivities of $h \sim 10^{-22}$ for millisecond bursts. Fortunately it is relatively easy to stabilise the laser intensity by detecting a small fraction of the intensity of the laser light and feeding back to an electro-optic variable attenuator positioned at the output of the laser [27].

Laser beam geometry and positional fluctuations

Any fluctuations in the position or geometry of the input laser beam of an interferometric detector can lead to spurious signals in the detector output if the interfering phase fronts are not correctly matched or aligned. These fluctuations can be passively suppressed with the use of modecleaning cavities [28] or single mode optical fibres. These essentially filter out the higher order spatial modes

present in the laser beam corresponding to positional or geometrical fluctuations. Active suppression of these fluctuations has also been investigated [29]. Here the positional fluctuations in the pointing of the beam were monitored using quadrant photodiodes and signals fed back to control the position of the beam.

In addition, an automatic alignment system, such as the one described in Chapter 3, can be used to minimise the mismatch of the interfering phasefronts at the output of the interferometer, so reducing any possible coupling of positional and geometrical fluctuations into the interferometer signal.

Refractive index fluctuations

The residual gas molecules present inside the interferometer vacuum system can potentially cause noise in the detector output. Fluctuations in the number of molecules moving through the light path cause a change in the refractive index in the interferometer arms and therefore an apparent change in the arm lengths. The magnitude of this effect depends very much on the type of molecules which are present in the vacuum system. The Glasgow prototype typically operates with vacuum of the order of 10^{-5} mbar, most of the residual gas probably being water vapour. It has been estimated that this would limit the sensitivity to $\sim 5 \times 10^{-20}\,\mathrm{m}/\sqrt{\mathrm{Hz}}$ at detection frequencies which is well below the current noise levels. It has been proposed that future long baseline detectors will need to have vacuum systems where the average pressure is $\sim 10^{-8}$ mbar for hydrogen and less than $\sim 10^{-9}$ mbar for heavier molecules such as water and nitrogen in order to reach the target sensitivities of $h \sim 10^{-22}$ for millisecond bursts [7].

Scattered light

Any light from the fundamental mode of the main beam in an interferometer which is scattered off one of the mirrors (due to dust or imperfections in the mirror) and subsequently reflected back into the main beam by reflection or scattering off either the vacuum pipes or the optical or suspension components in the system, will produce a slight phase shift in the main beam, modulated by any motion of

the reflecting component. Fortunately this effect can be reduced by using suitably designed optical baffles placed in the vacuum system, the effect of the baffles being to reduce the amount of stray scattered light that can return to the main interferometer output. A description of this and some suggestions on baffle design are discussed by Thorne [30].

Mirror losses and heating effects

In order to achieve good performance with a laser interferometer it is essential that high quality, low loss optical components are used. At present it is possible to obtain high quality 'supermirrors' which have losses of the order of a few tens of ppm [31] and it is probable that even lower loss mirrors will become available in the near future as mirror coating technology improves.

Thermal distortions of the mirrors and the beamsplitters may also become a limiting factor to the performance of systems incorporating high light levels or those which incorporate techniques such as power recycling (described later in section 1.6.4). Such distortions can occur because of thermal lensing in the mirror substrates with a temperature gradient in the region of the passing beam and it is also possible that surface deformation can occur due to thermal expansion of the optical components (see Winkler *et al.* [32]). It is therefore important when choosing the material for the interferometer mirror masses to ensure that it has a high thermal conductivity and a low coefficient of thermal expansion (in addition to having a high Q to reduce the effects of thermal noise).

1.6.4 Advanced interferometric techniques

Power recycling

As discussed in section 1.6.2 a laser interferometer is normally operated with its output locked on a dark fringe, in order to minimise the effect of shot noise. If the losses in the interferometer are low, this means that most of the input light is reflected back towards the laser. It is possible to 'recycle' this lost light power by

inserting a mirror in between the beamsplitter and the input laser beam as shown in figure 1.4. If the mirror is correctly positioned, the light reflected back from

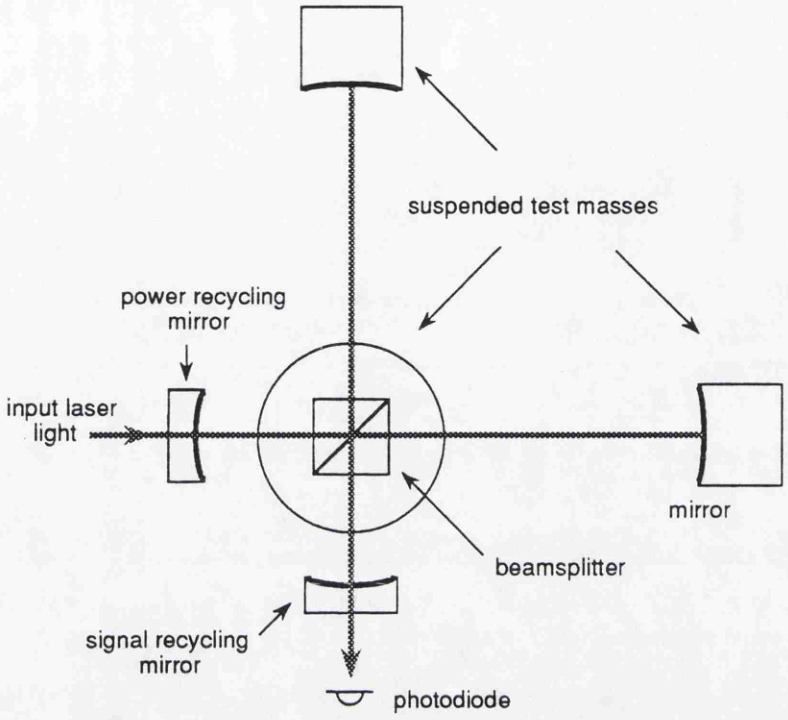

Figure 1.4: *A simple Michelson interferometer with power and signal recycling mirrors.*

the interferometer when it is locked on a null fringe at its output, can be added back in phase with the main input light. This technique, first published by Ron Drever [33], is called power recycling. It allows the circulating light power in an interferometer to be increased resulting in improved shot noise limited sensitivity. The increase in the shot noise limited sensitivity of an interferometer using power recycling compared to a non-recycled system is given by [20]

$$\sim \left(\frac{l \pi f_g}{2 c A^2} \right)^{\frac{1}{2}} , \tag{1.32}$$

where A represents the losses in the interferometer. Therefore for a kilometre scale detector one might expect an increase in the detector sensitivity at 1 kHz of ~ 10 (assuming $A^2 \sim 5 \times 10^{-5}$). The technique has been successfully demonstrated on number of benchtop experiments at MIT, Orsay and Glasgow (see [34], [35]).

Dual recycling

In addition to increasing the circulating light power in an interferometer by recycling the rejected light, it is also possible to enhance the signal size by placing a suitable mirror in front of the main detection photodiode, as shown in figure 1.4, and coherently reflecting the signal back towards the interferometer. This resonant enhancement of the signal size means that near storage time limited performance can be achieved with an interferometer at low frequencies without increasing the storage times in the arms of the interferometer. This technique is know as dual recycling and was first suggested by Brian Meers [20].

The position of the dual recycling mirror can be adjusted so that the main laser beam is resonant in the cavity formed between the interferometer and the dual recycling mirror. Provided the linewidth of this cavity is wider than the gravitational wave frequency, both the main laser light and the signal sideband frequency will be resonant. This technique is known as broadband dual recycling. Alternatively, the transmission of the dual recycling mirror can be decreased, effectively narrowing the linewidth of the dual recycling cavity. Resonant enhancement of the detector signal at a specific frequency can be achieved by tuning the dual recycling cavity so that it is resonant at the signal sideband frequency. As the sensitivity of such a detector is increased, the bandwidth will decrease. This particular form of dual recycling is commonly referred to as tuned or narrowband dual recycling. Such a system may be particularly attractive when searching for continuous gravitational waves from pulsars, where the frequency of the gravitational waves may be well know, allowing a narrowband high sensitivity detector to be used. This technique has also been experimentally tested on a small benchtop experiment at Glasgow [34], [36].

Recently a new configuration, resonant sideband extraction, has been proposed by Jun Mizuno [37]. The idea behind this technique relies on using very high finesse Fabry-Perot cavities in the arms of the interferometer, increasing the storage time of the arms past the storage time limit. A single signal extraction mirror is placed at the output of the interferometer, much in the same way as a dual recycling mirror, ensuring that any signal sidebands produced by a gravitational wave can

be coupled out of the system. It is therefore possible to optimise the effective signal storage time whilst maximising the storage time for the main circulating laser light in the interferometer. The advantage of this technique is that high light power can be achieved in each arm of the interferometer without having high light powers circulating around the beamsplitter (as is the case in normal power and dual recycling methods). Losses in the beamsplitter and effects such as thermal distortion are likely to be the major limiting factors in achieving high light powers with power and dual recycling schemes.

1.6.5 Summary

Figure 1.5 shows a summary of the extent to which the various noise sources discussed in the previous sections may limit the sensitivity of a large scale ($\sim 3\,\mathrm{km}$) interferometric gravitational wave detector, such as proposed by Hough *et al.* [7], to burst sources. As can be seen the estimated detection 'window' should allow the observation of gravitational radiation from sources such as coalescing binary star systems and supernovae events, based on current theoretical estimates of the strengths of gravitational wave emission from these sources. In the figure it has been assumed that an optimised recycling detector is used.

Despite the significant experimental difficulties associated with the construction, development and operation of such large scale detectors, progress on the various prototype interferometers in recent years has been extremely encouraging. The prospects for detecting gravitational waves in the near future with full scale laser interferometric detectors therefore look very promising.

The following chapters of this thesis describe some experimental investigations carried out on the 10 m prototype laser interferometric gravitational wave detector at Glasgow University and also address some problems which are of relevance to the design of a full scale detector.

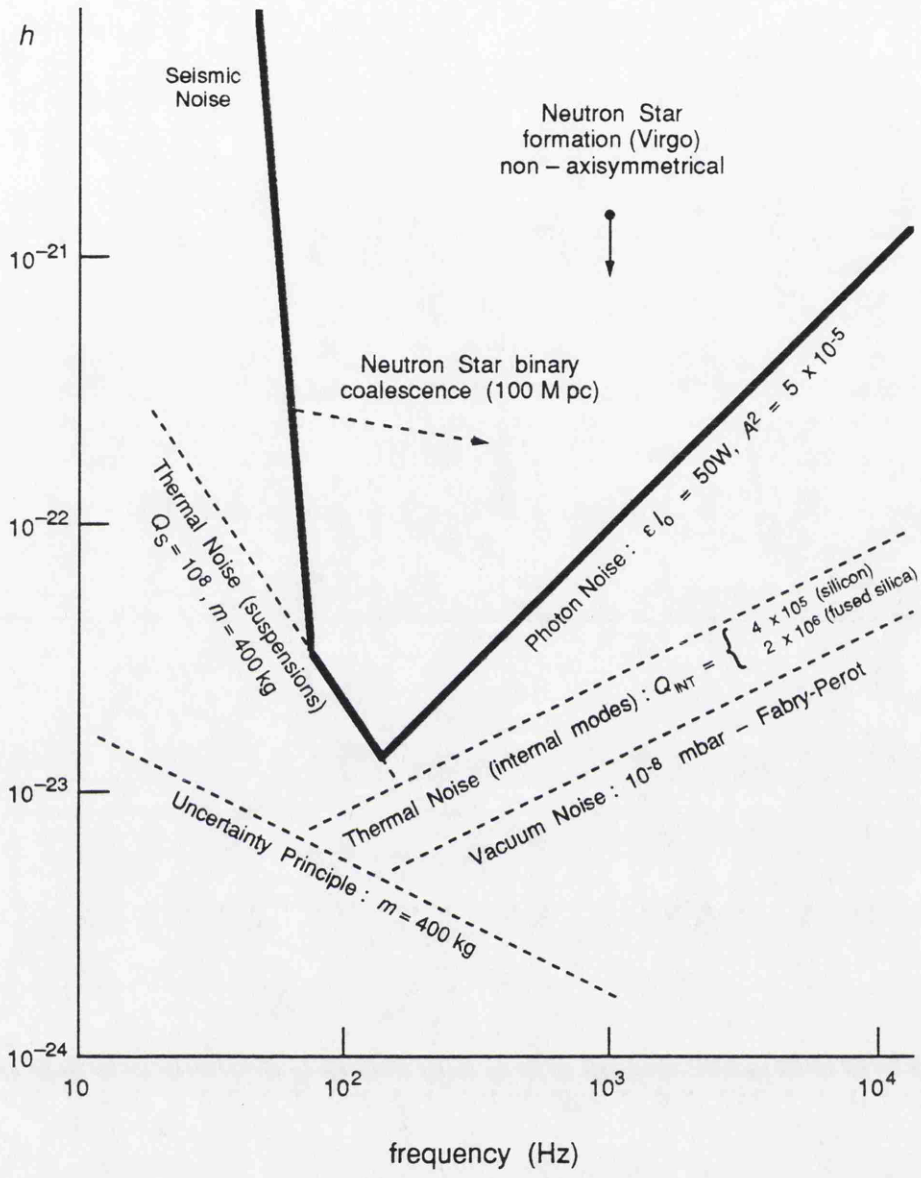

Figure 1.5: *Estimated limits to the detectable gravitational wave amplitude, h, of a large scale ($\sim$ 3 km) interferometric gravitational wave detector for burst sources, where a bandwidth of $\Delta f = \frac{f}{2}$ has been assumed. The photon shot noise limit is that of an optimised interferometer incorporating the recycling techniques discussed in the text. The limit due to thermal noise is that which is given in the text. This graph has been taken directly from the GEO proposal [7].*

Chapter 2

Control systems for laser interferometric gravitational wave detectors

2.1 Introduction

Laser interferometric gravitational wave detectors rely heavily on many different forms of control systems for their correct functioning and operation.

In order to make high precision measurements necessary to be able to detect gravitational waves it is essential that these systems are designed to meet the specifications required in terms of noise performance, dynamic range, bandwidth and reliability.

In particular, such control systems are required to stabilise the laser frequency, intensity and beam geometry to ensure that these effects do not place serious limits on the performance of the detector. Mechanical control of the suspended mirrors is also of vital importance. Various control systems are required from the relatively simple narrowbandwidth local damping and orientation controls for the high Q mirror suspension systems, to the wider bandwidth feedback necessary to keep the interferometer stably locked (usually) to a dark fringe. This locking servo ultimately provides the main output signal from the interferometer.

The aim of this chapter is to give a general description of control systems and some of the noise considerations in the context of laser interferometric gravitational wave detectors, concentrating in particular on some of the problems associated with the mechanical control of the suspended interferometer components.

A brief introduction to control systems and their analysis based on block diagram representation and transfer functions in the Laplace domain is given. Following this, a simple model is constructed of a typical control system used in laser interferometric gravitational wave detectors. By including various noise sources in the model it is possible to make some general comments regarding the effects of noise on the performance and potential sensitivity of the system. The conclusions drawn from this analysis form the basis of the design of local control damping systems which are subsequently discussed. Finally some general comments are made with respect to the implications of the model in influencing the design of the interferometer locking control systems used to produce the main detector output signal.

2.2 Simple feedback control systems

2.2.1 Block diagram representation of control systems and the Laplace transform

In most control problems, a simple mathematical model is usually formulated and its solution used to predict the performance of the system. In the majority of cases, the simple mathematical models used to describe the various mechanical, optical and electronic components in the system can be expressed in terms of ordinary linear differential equations. The solution of these equations will give both the dynamic and steady state characteristics of the system. However, when building up even relatively simple systems, the general solutions of the resulting differential equations are not always easy to obtain. Therefore it is convenient to use the Laplace transform in order to help solve these equations.

Basically, the Laplace transform can be used to transform the linear differential equation model of the system from the time domain into the complex frequency or Laplace domain. Once in the Laplace domain, the solutions required can be derived by simple algebraic manipulation of the transformed equations. The solutions can then be expressed in the time domain by performing the inverse Laplace transform.

Normally it is the forced response of a system which is of interest, *i.e.* the

output of a system given a well defined set of sinusoidal inputs, rather than the transients due to the initial conditions. All of the initial conditions are therefore assumed to be zero. It is therefore possible to represent the model of the system as a ratio of the Laplace transforms of the output and the input. This is called the transfer function of the system. The transfer function of a system is just the Laplace transform of the system's impulse response.

These transfer functions can be incorporated into a block diagram representation of the entire control system under study. Each block contains a transfer function representing some part of the system which has a well defined input and output. By building up such a block diagram, the task of analysing and understanding the control system is greatly simplified. A comprehensive discussion of feedback control analysis can be found in *e.g.* [38], [39].

2.2.2 Negative feedback

Consider the system shown in figure 2.1. In this example, negative feedback is

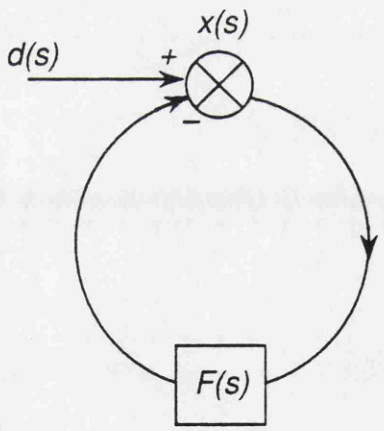

Figure 2.1: *Block diagram of a simple negative feedback control system.*

used to control the effect of some unwanted disturbance, $d(s)$, on some parameter of the system, $x(s)$. For example, $d(s)$ could represent the effect of seismic noise disturbing the position of a test mass in an interferometer represented by $x(s)$.

In order to reduce the effect of $d(s)$ on $x(s)$, negative feedback can be applied. Some of $x(s)$ is fed back through a system whose open loop transfer function is given by $F(s)$. With the feedback loop closed, $x(s)$ is given by

$$x(s) = \frac{d(s)}{1 + F(s)} , \tag{2.1}$$

where $\frac{1}{1+F(s)}$ is the closed loop transfer function of the system. Now for $F(s) \gg 1$, $x(s)$ can be written as

$$x(s) = \frac{d(s)}{F(s)} . \tag{2.2}$$

So from this simple picture it can see that for large values of $F(s)$ (*i.e.* strong negative feedback) the effect of $d(s)$ on $x(s)$ is reduced by the feedback.

2.2.3 Stability

In general a linear system is said to be stable if its impulse response is well defined, bounded and eventually results in the system returning to a steady state condition. By examining the closed loop transfer function of a system (*i.e.* the transform of the system's impulse response) it is possible to determine whether or not the system is stable.

Consider a general closed loop system whose Laplace transform is of the form

$$\frac{1}{1 + F(s)} = \frac{N(s)}{D(s)} , \tag{2.3}$$

where $N(s)$ and $D(s)$ are polynomials in s and have no common factors. A partial fraction expansion of $\frac{N(s)}{D(s)}$ can be performed so that terms are obtained whose denominators are of the form $(s - r_i)$ where r_i represent the roots of the denominator of the closed loop transfer function. If the expression for the closed loop transfer function is then transformed back into the time domain, the impulse response of the system will contain terms of the form $e^{r_i t}$. The closed loop system is therefore unstable if any of the roots of the denominator of the closed loop transfer function have positive real parts.

Given any closed loop transfer function then, it is possible to determine whether or not the system is stable. Unfortunately this particular method of analysis of the

loop gives no real indication of how to design feedback servo systems. In order to this it is convenient to employ other techniques such as a Bode or Nyquist analysis of the system.

2.2.4 Bode diagrams

Bode diagrams are complementary gain and phase plots of the open loop system ($|F(s)|$ and $arg\,[F(s)]$) as a function of frequency.

By examining the phase of the open loop transfer function at points where the gain of the system is unity, it is possible to judge whether or not the system will be stable when the loop is closed.

As a general rule, for simple single path feedback systems, the closed loop response will be stable if the phase of the open loop system at the unity gain points lies between $+180°$ and $-180°$.

The phase margin, a term often used when describing the stability of control systems, is defined as the difference in the phase of the open loop system from $\pm 180°$ at the unity gain point. The gain margin is the reciprocal of the gain of the open loop system at the frequency where the phase is $\pm 180°$.

In general then, Bode diagrams give a clear picture of how the gain and phase of the open loop system varies with frequency, which is of prime importance when designing feedback control systems. Furthermore, the stability of the system can be assessed by examining both the gain and the phase plots.

However this general rule only holds if the open loop system is itself stable. A feedback system in which the open loop response is unstable (*e.g.* a non-minimum phase system) can lead to Bode diagrams in which the stability of the closed loop system cannot be readily judged.

Although many different techniques exist for assessing and designing control systems (such as Nyquist plots, which are basically polar diagrams representing the phase and gain of the open loop system), in the following sections and chapters only Bode plots will be dealt with. For simple control systems, a Bode analysis gives a good indication of the stability of the system and is extremely useful in

the design stages. A combination of this with an examination of the roots of the denominator of the closed loop system has proved to be an effective method of designing and evaluating the particular control systems described.

2.3 Noise in control systems

Consider the feedback system shown in figure 2.2. In the diagram, the position

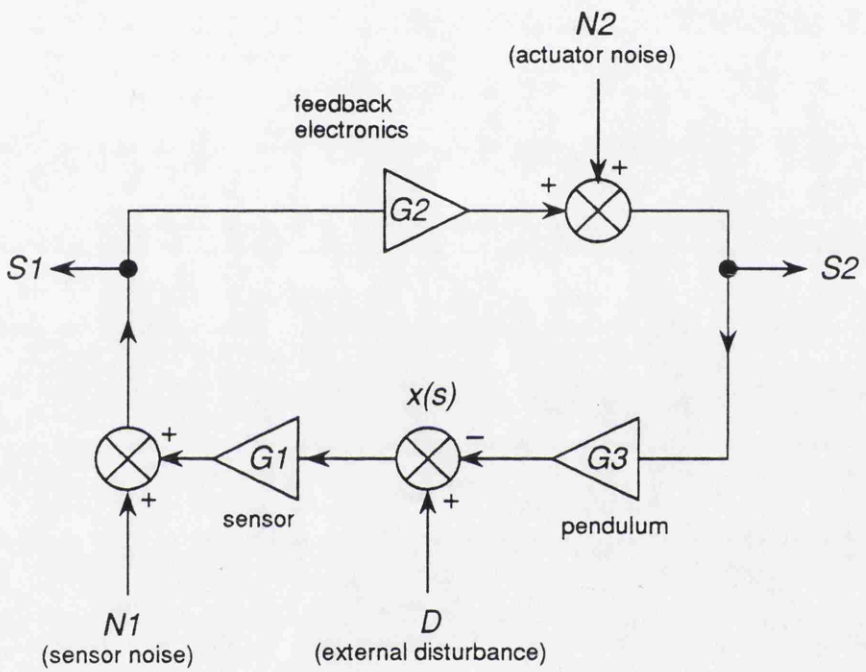

Figure 2.2: *Block diagram of a typical feedback system used to control the test masses in a suspended interferometer.*

of a test mass in the interferometer is to be controlled using the feedback system shown. The position of the test mass, x, is determined by some sensing system whose characteristics are given by $G1$. This signal is then amplified, filtered and fed back to the test mass *via* some actuator which acts on the pendulum suspension of the test mass. The transfer function of the electronic filtering is represented by $G2$ and the response of the pendulum suspension system in terms of metres/volt

is given by $G3$. In order to study the effect of noise in the system, $N1$ and $N2$ are added into the feedback loop. $N1$ can be though of as representing some noise source inherent in the sensing technique (*e.g.* shot noise in an optical sensor) and $N2$ represents the noise associated with the actuator used to feedback signals to the test mass. The quantity D is also included to represent some external signal disturbing the motion of the test mass (*e.g.* at low frequencies this will be due to seismic noise and at frequencies $> 100\,\mathrm{Hz}$, hopefully, gravitational radiation).

In order to generalise the feedback system so that the servo used to lock the interferometer can be studied, it is necessary to include the points $S1$ and $S2$ on the diagram. $S1$ is often referred to as the 'error point signal' of the servo and $S2$ the 'feedback signal'. The main locking servo is used to produce the output signal from the interferometer by looking at the signals in the loop at points $S1$ and $S2$.

The analysis of the system can therefore be split into two sections, one which deals with the main interferometer locking servo and one which deals with other servo systems in the detector which are used to control the test masses (*e.g.* local damping control systems).

2.3.1 Main interferometer locking servos

These systems are normally used to lock the interferometer to (usually) a dark fringe at the output. In doing so, this servo also provides a method of extracting the main detector signal. It is possible to look at the signals in the feedback loop at points $S1$ and $S2$ in order to deduce the motion of the test mass (or as is usually the case, the differential motion of two test masses) in the interferometer. It is essential that any signal which may be due to a gravitational wave can be seen above these noise sources in the feedback loop.

Carrying out some simple loop algebra, the signals, $S1$ and $S2$, can be expressed in terms of the various parameters of the system.

$$S1 = \frac{D\,G1}{1 + G1\,G2\,G3} + \frac{N1}{1 + G1\,G2\,G3} + \frac{N2\,G1\,G3}{1 + G1\,G2\,G3} \tag{2.4}$$

and

$$S2 = \frac{D\,G1\,G2}{1 + G1\,G2\,G3} + \frac{N1\,G2}{1 + G1\,G2\,G3} + \frac{N2}{1 + G1\,G2\,G3}\,. \tag{2.5}$$

As can be seen, each term in the expression is modified by $\frac{1}{1+G1\,G2\,G3}$, the closed loop response of the system.

The error point signal

Concentrating on the expression for $S1$, in order to see a signal of size D above the various noise sources in the system the following conditions must be satisfied

$$D\,G1 > N1 \tag{2.6}$$

and

$$D > N2\,G3\ . \tag{2.7}$$

It will be assumed that in the frequency range of interest for detecting gravitational waves (100 Hz up to a few kHz) the detection system is limited by shot noise. The shot noise limited sensitivity is therefore given by $D = \frac{N1}{G1}$. Equation 2.6 simply states that the detection system can only sense signals above the shot noise limit set by $N1$.

The second limit is due to the actuator noise. In principle this can always be reduced by decreasing the effective gain of the actuator whilst keeping the overall loop gain constant (by increasing $G2$ for example), although there may be practical difficulties associated with this. Reducing the gain of the actuator however also reduces the maximum signal which can be fed back to correct the position of the test mass, since the dynamic range of the actuator will also be reduced. Therefore the maximum size of signals which can be fed back to the test mass will be restricted in order to ensure that the actuator noise does not compromise the shot noise limited sensitivity of the detector.

The feedback signal

Looking now at $S2$ in order to see a signal above the various noise sources in the system

$$D\,G1\,G2 > N1\,G2 \tag{2.8}$$

and

$$D\,G1\,G2 > N2\ . \tag{2.9}$$

The first of these two expressions is just equivalent to equation 2.6. The second condition can be re-expressed as

$$D(G1\,G2\,G3) > N2\,G3\ . \tag{2.10}$$

This condition is always satisfied below the unity gain point of the servo (*i.e.* at frequencies where $G1\,G2\,G3 > 1$) when $D > N2\,G3$ (which is just the condition set by equation 2.7). However, when the loop gain is high, it may be possible to allow $N2\,G3 > D$. This effectively allows a noisier actuator to be used to provide the main feedback signal.

In any case, equation 2.10 is always satisfied when shot noise can be seen above the actuator noise at $S2$ (*i.e.* $N1\,G2 > N2$).

Since these noise sources can potentially limit the sensitivity of a detector which relies on such a servo in order to derive its main output signal, it is essential that the design of the main feedback system is such that the conditions mentioned above are satisfied. The implications of these conclusions and how they influence the design of the main interferometer feedback system are discussed later in section 2.6.

2.3.2 Test mass local control servos

Typically in these servos (discussed in greater detail in section 2.4) the position of the test masses in the interferometer is controlled using a narrowband servo (where the bandwidth is much less than the lowest frequencies of interest for searching for gravitational waves) and a sensing system external to the main interferometer signal (*e.g.* shadow sensors, optical levers *etc.*). It is essential that these systems do not impose excess noise onto the motion of the test mass in the frequency range of interest for detecting gravitational waves. These control systems are not used to produce a high quality output signal such as in the previous case, they are simply trying to control the position of the test mass x, without compromising the performance of the detector

Carrying out some simple loop algebra, the position of the test mass, x, can be expressed in terms of the various parameters of the system.

$$x = \frac{D}{1 + G1\,G2\,G3} + \frac{N1\,G2\,G3}{1 + G1\,G2\,G3} + \frac{N2\,G3}{1 + G1\,G2\,G3} \; . \tag{2.11}$$

The implications of this expression for interferometric gravitational wave detectors can be summarised as follows:

The signal due to an incoming gravitational wave must dominate this expression at frequencies of $> 100\,\mathrm{Hz}$. Therefore at these frequencies

$$D > N2\,G3 \; , \tag{2.12}$$

and

$$D > N1\,G2\,G3 \; . \tag{2.13}$$

The first condition here is the same as equation 2.7, *i.e.* that the 'back-end noise' from the actuator must not limit the sensitivity of the detector. The second condition places strict limitations on the design of the servo used to perform the local control. As can be seen, the level of noise inherent in the sensor must be sufficiently attenuated at the frequencies of interest for detecting gravitational radiation so that this noise does not limit the sensitivity of the detector. When using relatively poor sensors, such as the standard shadow sensors, this last condition is far from trivial to satisfy.

This last point forms the basis of the next section which deals with the question of sensor noise and servo design of the local control systems required for a full scale interferometric gravitational wave detector.

2.4 Local damping control systems

The test masses in a laser interferometric gravitational wave detector are suspended as pendulums in order to isolate them from seismic noise in the frequency range of interest for detecting gravitational waves (100 Hz up to a few kHz).

The undamped resonances of a high Q pendulum cause the test mass to move considerably at the pendulum resonant frequencies when excited by seismic noise.

The successful operation of a suspended laser interferometer will depend on being able to damp the pendulum resonances and control the position of the interfering laser beams to a high accuracy – at least until the interferometer is stably locked. It is possible that once the interferometer is in this locked state, some of the signals used to damp the suspended test masses and control their orientation can be derived from the main interferometer locking signal; these signals can then be used instead of the local damping system. However, in a complex interferometer with many suspended components, it may not always be possible to derive enough signals from the main interferometer light to control all the components.

Dissipative damping is undesirable since it degrades the natural Q of the pendulum which increases the level of thermal noise and could therefore limit the sensitivity of the detector. Some form of active electronic local damping must therefore be used. Extreme care however must be taken to ensure that the conditions set by equation 2.12 and 2.13 are satisfied *i.e.* that these local damping systems do not impose noise onto the test masses at detection frequencies which would swamp any signal present due to a gravitational wave.

The following discussion focuses specifically on damping of the longitudinal motion of the mass. This degree of freedom of the mass is the most critical as far as the detector signal is concerned since any longitudinal motion of the mass will couple directly into the interferometer output signal. In general it is necessary to damp and control all degrees of freedom of a suspended test mass (*e.g.* tilt, rotation *etc.*). With careful design of the pendulum it should be possible to apply the same techniques discussed here for longitudinal damping to damping of the other degrees of freedom without introducing excess noise onto the motion of the test mass.

2.4.1 Sensors and noise

In order to damp a pendulum a suitable sensor is required to detect its motion. Any sensor will have some limit to its sensitivity – this is usually some noise source inherent in the sensor. It is essential that this noise is not imposed onto the motion

of the test mass at the frequencies relevant for the detection of gravitational waves (*i.e.* 100 Hz and above). Shadow sensors are one obvious method of obtaining a signal corresponding to the motion of the test mass. These sensors consist of a simple LED/photodiode arrangement, where a flag which is attached to the object whose motion is to be measured, partially obscures the path between the LED and photodiode. Motion of the flag modulates the intensity of the light from the LED which is detected by the photodiode and so a signal can be derived which is proportional to the displacement of the flag relative to the LED and photodiode. The typical noise floor of such a sensor is $\sim 10^{-10}\,\mathrm{m}/\sqrt{\mathrm{Hz}}$, determined by the shot noise in the detected photocurrent of the sensor. Standard LED/photodiode shadow sensors such as this have the advantage that they are robust, have a reasonably large working range (can detect displacements of up to 1 mm) and are relatively easy to use.

Other sensors which could possibly be used are capacitive sensors, interferometric sensors, inertial sensors, velocity sensors *etc.* Some of these have considerably better noise performance than the shadow sensors but in general they are less easy to use – precision alignment is required in the set up of the capacitive and interferometric systems and their working ranges are relatively small. Standard piezo-electric (*pzt*) based inertial sensors suffer from drifting at very low frequencies and are also quite poor at detecting motions in the region of a few Hz. A local damping system based on this type of sensor was investigated experimentally and is discussed later in section 2.5.

Assuming then that shadow sensors are to be used to sense the motion of the pendulum in the local damping control servo, consider first a system which feeds back forces directly to the test mass (suspended as a simple one stage pendulum). The pendulum will, typically, have a resonant frequency of ~ 1 Hz. In order to control and adequately damp this resonance it is necessary to have a servo system which has a unity gain point is above this frequency. Also, for stability of the servo, the phase lag in the feedback loop must be less than 180° at the unity gain frequency. Since the feedback forces are being applied directly to the suspended test mass, above the resonant frequency of the pendulum the phase of the response

of the mechanical system is $-180°$ and the magnitude of the response (*i.e.* motion of the pendulum with respect to the feedback forces applied to it) falls as $\frac{1}{f^2}$. A small amount of phase advance must therefore be provided by the electronics in the feedback loop if the system is to be stable and have sufficient gain when the loop is closed. By steeply filtering the feedback signal above the unity gain frequency, it is possible to achieve a loop gain of $\sim 10^{-8}$ at 100 Hz (including the mechanical attenuation which is provided by the pendulum). The amount of attenuation is limited by the phase lag which can be tolerated at the unity gain frequency whilst still keeping the servo stable. Using a shadow sensor in such a feedback system would lead to a noise level of $\sim 10^{-18}\,\mathrm{m}/\sqrt{\mathrm{Hz}}$ being imposed onto the motion of the test mass at 100 Hz.

A large scale interferometer, such as that proposed by Hough *et al.* [7], capable of reaching a strain sensitivity of $\mathrm{h} \sim 10^{-24}/\sqrt{\mathrm{Hz}}$ at 100 Hz (see figure 1.5) can tolerate a maximum mirror displacement noise of $\sim 10^{-22}\,\mathrm{m}/\sqrt{\mathrm{Hz}}$ at 100 Hz on its most sensitive components. Therefore, it would appear that a test mass suspended using a single stage pendulum could not be damped and controlled quietly enough using a shadow sensor.

It is therefore necessary to consider suspending the most sensitive interferometer components using a two stage pendulum. This is also highly desirable in order to reduce the level of seismic noise propagating through to the test mass.

A two stage pendulum has two resonant modes which can be damped by sensing and feeding back signals only to the intermediate mass. The noise which is imposed on the main test mass by feeding back only to the intermediate mass is passively attenuated by an extra factor of $\sim 10^4$ at 100 Hz. It seems plausible then, that such a damping system could be used to control the resonant modes of a test mass pendulum suspension system for use in a large scale interferometric gravitational wave detector.

The particular details of this are discussed in the following sections.

2.4.2 Two stage pendulum – equations of motion

In order to model the two stage pendulum and the effect of electronically damping the pendulum resonances, it is necessary to know the response of the pendulum to a force applied to the intermediate mass.

Consider then the two stage pendulum shown in figure 2.3. For simplicity,

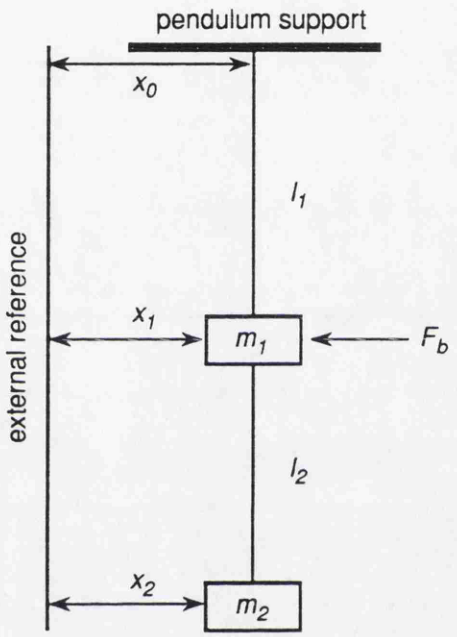

Figure 2.3: *Schematic diagram of a double pendulum suspension system with a local control system feeding back signals only to the intermediate mass.*

it will be assumed that the suspension wires are massless, m_1 and m_2 are point masses and there are no external damping forces applied to the pendulum other than our feedback force F_b (*i.e.* the suspension has an infinitely high Q).

The equations of motion of the pendulum are derived by considering the various forces acting on the two masses. The forces acting on m_2 give

$$\ddot{x}_2 + {\omega_2}^2(x_2 - x_1) = 0 \ , \tag{2.14}$$

and the forces on m_1 give

$$\ddot{x}_1 = (1+\alpha){\omega_1}^2 x_0 - [(1+\alpha){\omega_1}^2 + \alpha{\omega_2}^2]x_1 + \alpha{\omega_2}^2 x_2 + \frac{F_b}{m_1} , \tag{2.15}$$

where $\alpha = \frac{m_2}{m_1}$, ${\omega_1}^2 = \frac{g}{l_1}$, and ${\omega_2}^2 = \frac{g}{l_2}$.

By taking the Laplace transforms of the above equations, the transfer functions of the two pendulum system in the s domain can be derived. If $\mathcal{F}(s) = \mathcal{L}\{F(t)\}$ represents the Laplace transform of $F(t)$, then the Laplace transforms of x_0, x_1, x_2 and F_b are given by $\mathcal{X}_0$, $\mathcal{X}_1$, $\mathcal{X}_2$ and $\mathcal{F}_b$ respectively. Also, for convenience, it will be assumed that the pendulum is stationary at $t = 0$.

The transfer function which gives the response of the intermediate mass, m_1, to a force applied to it is given by

$$\frac{\mathcal{X}_1}{\mathcal{F}_b/m_1} = \frac{s^2 + {\omega_2}^2}{s^4 + s^2(1+\alpha)({\omega_1}^2 + {\omega_2}^2) + (1+\alpha){\omega_1}^2{\omega_2}^2} . \tag{2.16}$$

As can be seen by looking at the roots of the denominator of this equation, the pendulum has two resonant frequencies. In the absence of any external damping forces, the pendulum resonances are given by

$$\omega^2 = \frac{(1+\alpha)({\omega_1}^2 + {\omega_2}^2)}{2} \pm \frac{1}{2}\sqrt{[(1+\alpha)({\omega_1}^2 + {\omega_2}^2)]^2 - 4(1+\alpha){\omega_1}^2{\omega_2}^2} . \tag{2.17}$$

The response of the intermediate mass as given by equation 2.16 is flat at frequencies below the two resonances and behaves like $\frac{1}{s^2}$ above the resonances (*i.e.* the response falls as $\frac{1}{f^2}$ and has a phase lag of $-180°$).

Consider now a feedback system which senses signals only at m_1, the intermediate mass. If the electronics used to derive the feedback force have a transfer function whose Laplace transform is given by $\mathcal{E}$, then the Laplace transform of the feedback term is just

$$\frac{\mathcal{F}_b}{m_1} = \mathcal{E}\mathcal{X}_1 . \tag{2.18}$$

The open loop gain of the intermediate damping system is then given by

$$G = \frac{\mathcal{E}(s^2 + {\omega_2}^2)}{s^4 + s^2(1+\alpha)({\omega_1}^2 + {\omega_2}^2) + (1+\alpha){\omega_1}^2{\omega_2}^2} , \tag{2.19}$$

and the closed loop transfer function is just

$$\frac{1}{1+G} \, . \tag{2.20}$$

Another transfer function which is of interest is that which expresses how much disturbances at the top of the pendulum propagate through to the main test mass. This is given by

$$\frac{\mathcal{X}_2}{\mathcal{X}_0} = \frac{(1+\alpha){\omega_1}^2{\omega_2}^2}{s^4 + s^2(1+\alpha)({\omega_1}^2+{\omega_2}^2) + (1+\alpha){\omega_1}^2{\omega_2}^2 - \mathcal{E}(s^2+{\omega_2}^2)} \, . \tag{2.21}$$

As can be seen, this transfer function is flat below the two pendulum resonances but falls off as $\frac{1}{f^4}$ above the resonances with a phase lag of $-360°$.

The amount by which basic sensor noise in the intermediate mass damping system is attenuated by the the time it propagates through to the test mass can be calculated using

$$\left(\frac{G}{1+G}\right)\left(\frac{{\omega_2}^2}{s^2+{\omega_2}^2}\right) \, , \tag{2.22}$$

and, since in this particular type of feedback system $|G| \ll 1$, at 100 Hz the attenuation of the front end noise is just

$$\frac{\mathcal{E}{\omega_2}^2}{s^4 + s^2(1+\alpha)({\omega_1}^2+{\omega_2}^2) + (1+\alpha){\omega_1}^2{\omega_2}^2} \, . \tag{2.23}$$

2.4.3 Control of the pendulum using electronic feedback

As can be seen from equation 2.19 (the open loop gain of the feedback system which senses and feeds back signals only to the intermediate mass), without any electronic filtering the phase of the feedback signal above the two pendulum resonances is $-180°$. In order to create a stable feedback system, and have a loop gain of > 1 up to frequencies slightly beyond the upper pendulum resonance, the electronic filtering must be capable of advancing the phase in this frequency region.

Consider then a servo which is designed to have a phase of $-135°$ at the upper pendulum resonance, f_u, say (*i.e.* a phase margin of 45° if f_u is chosen as the unity gain point). This can be expressed as

$$arg(\mathcal{E})|_{\omega=2\pi f_u} = +45° \, . \tag{2.24}$$

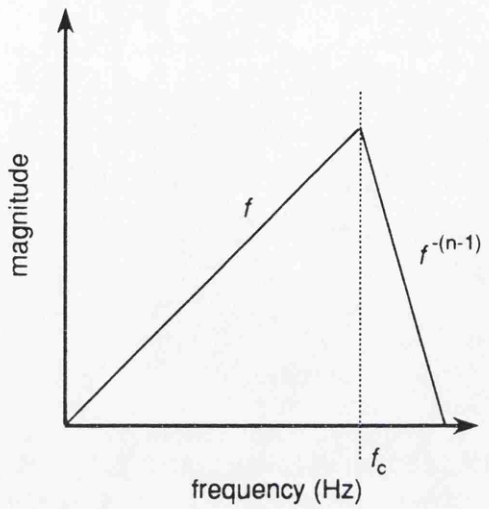

Figure 2.4: *Simplified Bode magnitude plot showing one possible form of the transfer function of the electronics in the feedback loop.*

Also, assume that the simple electronic filtering system shown as a Bode plot indicated schematically in figure 2.4 is used. In the Laplace domain this can be expressed as

$$\mathcal{E} = \frac{K \frac{s}{(2\pi f_c)}}{(1 + \frac{s}{(2\pi f_c)})^n} , \tag{2.25}$$

where K is a constant representing the overall gain of the electronics.

Equation 2.25 represents a single differentiation stage which acts up to a corner frequency f_c, at which there are n simple RC low pass filters rolling off the gain.

For any value of f_u it is possible to calculate at what frequency the low pass filters should be placed (*i.e.* f_c) and how many are needed to optimise the attenuation of the sensor noise at 100 Hz. This is by no means the only form which the electronic feedback system can take. It is possible that more sophisticated filtering (*e.g.* Chebyshev or Butterworth filters) could be used to achieve more attenuation of the sensor noise at 100 Hz. However, as shall see, a simple system such as the one described by equation 2.25 would appear to be adequate.

2.4.4 Pendulum response and noise performance

The ideas discussed in the previous sections can now be applied to the case of a realistic pendulum suspension system for use in an interferometric gravitational wave detector. In order to attenuate the local control noise as much as possible at 100 Hz, it is desirable to to keep the pendulum resonances as close together and at as low a frequency as possible, without making the pendulum too long. For these reasons consider $l_1 = l_2 = 0.5\,\mathrm{m}$ and $m_1 = m_2$. From equation 2.17 the resonant frequencies of the pendulum can be calculated. These occur at 0.54 Hz and 1.30 Hz. If the servo system, which feeds back to the intermediate mass, is designed to have 45° phase margin at 1.30 Hz, then for $n = 6$, it is possible to calculate from equations 2.24 and 2.25 that $f_c = 9.9\,\mathrm{Hz}$. With such a system, it can be calculated from equation 2.23 that the front end sensor noise which is imposed on the test mass is attenuated by $\sim 1.4 \times 10^{12}$ at 100 Hz.

This filtering used with a shadow sensor would have a noise performance, at least as far as longitudinal damping of the mass is concerned, which is good enough for use in a large scale interferometric gravitational wave detector.

Using the transfer functions derived in sections 2.4.2 and 2.4.3, the above system was modelled. Figure 2.5 shows $\frac{x_2}{x_0}$, the transfer function of the complete double pendulum (as given in equation 2.21) with and without the electronic damping to the intermediate mass. The effect of the damping system on the two pendulum resonances can be clearly seen.

The open loop gain and phase Bode plots of the intermediate damping system are shown in figure 2.6. From these Bode plots it can be seen that in regions where the gain approaches unity, the magnitude of the phase of the system is always less than 180° indicating that the system is stable for this particular gain setting.

Figure 2.7 shows the step response of the complete closed loop double pendulum system (*i.e.* the motion of the main test mass if an impulse is applied to the top of the double pendulum). As can be seen, with the damping turned on, the system calms down to a steady state in the matter of a few seconds. More formally, by examining the roots of the denominator of the closed loop transfer function (equation 2.20) the stability of the system can be confirmed and also the new

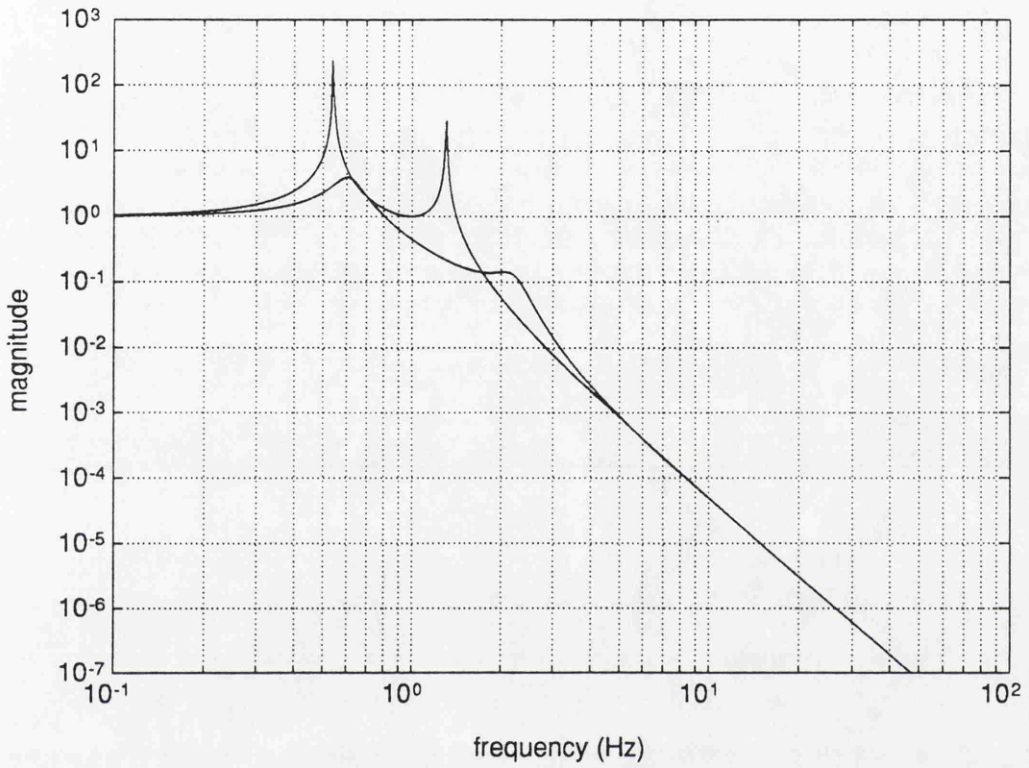

Figure 2.5: *Computed transfer function of a double pendulum system with and without electronic damping.*

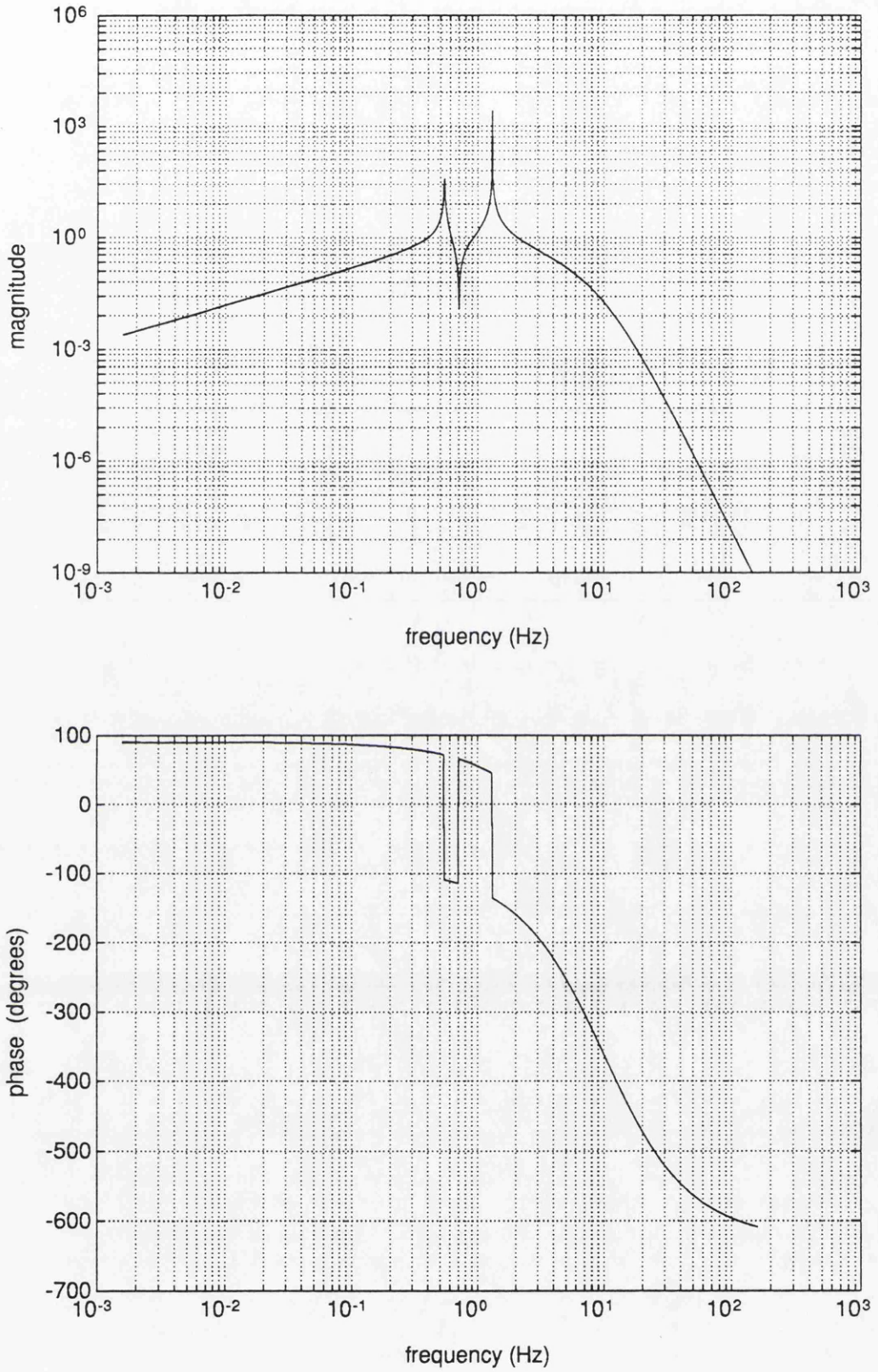

Figure 2.6: *Open loop Gain and phase Bode plots for the complete intermediate damping system.*

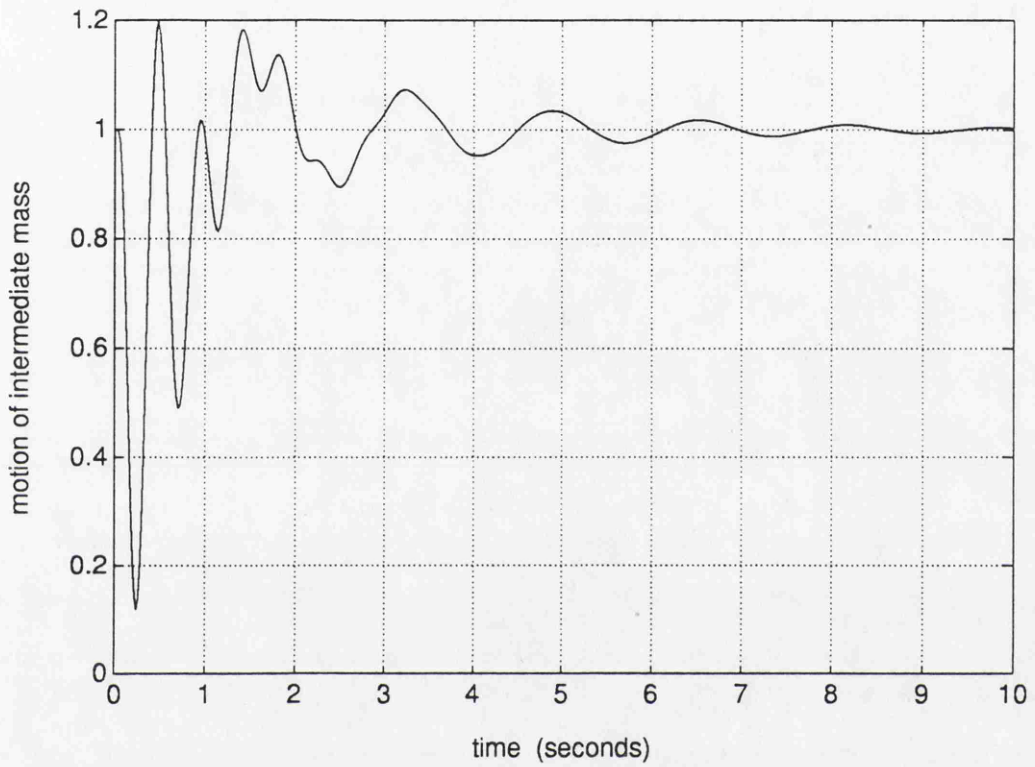

Figure 2.7: *Computed step response of the intermediate mass system with the electronic damping switched on.*

resonant frequencies of the system and the Q of each resonance can be calculated. In this particular case, the resonances are at 0.61 and 2.20 Hz and their Qs are 4.62 and 4.26 respectively.

2.4.5 Summary and concluding remarks

A local control system for damping the high Q pendulum resonances of a suspended test mass, based on sensing and feeding back signals to the intermediate stage of a double pendulum, has been studied.

Theoretical calculations show that it should be possible to design a system such that even if a relatively noisy sensor is used (*e.g.* a shadow sensor) the noise from the sensor is attenuated sufficiently by 100 Hz so that it does not limit the performance of even an advanced receiver.

The actual displacement noise imposed onto the motion of the test mass by the particular damping system here corresponds to a level of around $7 \times 10^{-23}\,\mathrm{m}/\sqrt{\mathrm{Hz}}$ at 100 Hz (the sensor considered here was a shadow sensor whose noise corresponds to a displacement level of around $10^{-10}\,\mathrm{m}/\sqrt{\mathrm{Hz}}$).

As explained in section 2.3.2 it is also important to ensure that the noise in the actuator ('back end' noise) does not limit the noise performance of the system any more than the 'front end' noise (this is just the condition set by equation 2.12). This is taken care of if the servo is designed to be 'front end' limited – *i.e.* it is possible to see the front end noise above any other noise sources in the servo system. In order to ensure that this condition is satisfied for this particular type of servo, it is necessary to limit the maximum size of correction signals which can be applied to the intermediate mass. For example, consider the standard coil/magnet actuators driven through suitably low noise current drivers (such as those described later in section 5.2.4). The maximum output of these devices is $\sim 10\,\mathrm{V}$ with a corresponding noise floor of $\sim 1\,\mathrm{nV}/\sqrt{\mathrm{Hz}}$ at 100 Hz. Assuming that no low pass filtering is used after the output of the current driver (in practice it is difficult to achieve any significant filtering of the driver output at 100 Hz since the impedance of the coils is typically a few ohms), then the maximum signal which

can be applied to the intermediate mass using such an actuator is $\sim 100\,\mu$m. This ensures that the noise imposed onto the main test mass due to the driver noise is less than $10^{-22}\,\mathrm{m}/\sqrt{\mathrm{Hz}}$ at 100 Hz.

Typically, the maximum size of signal which might have to be fed back to the intermediate mass will be of the order of a few μm around the pendulum resonances (due to seismic disturbance of the pendulum) and so an actuator which has a maximum output range of $100\,\mu$m should be sufficient to cope with these signals.

However it should be noted that even if an extremely good low noise sensor could be found to use in such a local damping servo, a feedback system which fed signals back directly to the main test mass could not be designed with the required performance. The noise from the feedback actuator would limit the maximum size of signal which could be applied to the main test mass to around 10 nm. Such an actuator could not cope with the large amount of seismic disturbance present at low frequencies. Note that these considerations are also of importance to the design of main interferometer feedback system as discussed later in section 2.6.1.

The control system described can be applied to locally damp all degrees of freedom of the suspended test mass. In order to achieve the required noise performance it is necessary to ensure that both resonances in all degrees of freedom are at or below 1.3 Hz. This can be achieved through careful design of the double pendulum.

The basic design features described here have been applied to the construction of a double pendulum suspension system for the test masses in the 10 m prototype. This is described later in Chapter 5.

2.5 An inertial damping system

As mentioned in section 2.4.1 one possible method of locally damping a suspended test mass is to feed back signals derived from an inertial sensor mounted directly on the test mass, or on the intermediate stage of a double pendulum suspension system. Noise estimates (evaluated later in section 2.5.4) for such a sensor give an effective displacement sensing noise at 100 Hz of a few $10^{-14}\mathrm{m}/\sqrt{\mathrm{Hz}}$ using a standard *pzt*, a 1 kg 'moving mass' and a simple charge sensitive amplifier (the noise being due to the input voltage noise in the charge sensitive amplifier). Not only is the displacement noise of this system much less than that of the standard shadow sensor systems, but no external DC reference is required.

It was decided therefore to investigate the feasibility of such a system for providing the signals required to locally damp the test masses in an interferometer.

2.5.1 Experimental test of inertial damping system

In order to test out an inertial damping system a single stage pendulum was initially constructed. The experimental setup of the apparatus is shown in figure 2.8. The pendulum was ~43 cm long with the test mass consisting of a 3 kg disk of aluminium, 14 cm diameter and 5 cm long. The pendulum was damped in the tilt, rotation and sideways degrees of freedom using shadow sensors and coil/magnet actuators. Three shadow sensors mounted on a supporting backplate sensed the motion of the mass. By suitably combining the signals from these sensors it was possible to derive signals corresponding to the tilt and rotation motions of the test mass as well as the longitudinal motion. The signals were then suitably filtered and fed back to coils mounted on the backplate. By driving current through the coils, forces could be applied to small permanent magnets attached to the back of the test mass to damp down the motion of the mass. Control of the sideways motion of the mass was done *via* a shadow sensor and coil mounted on the side of the support structure.

The mass was therefore effectively free to move longitudinally. In order to damp this motion, a small accelerometer was attached to the front of the mass

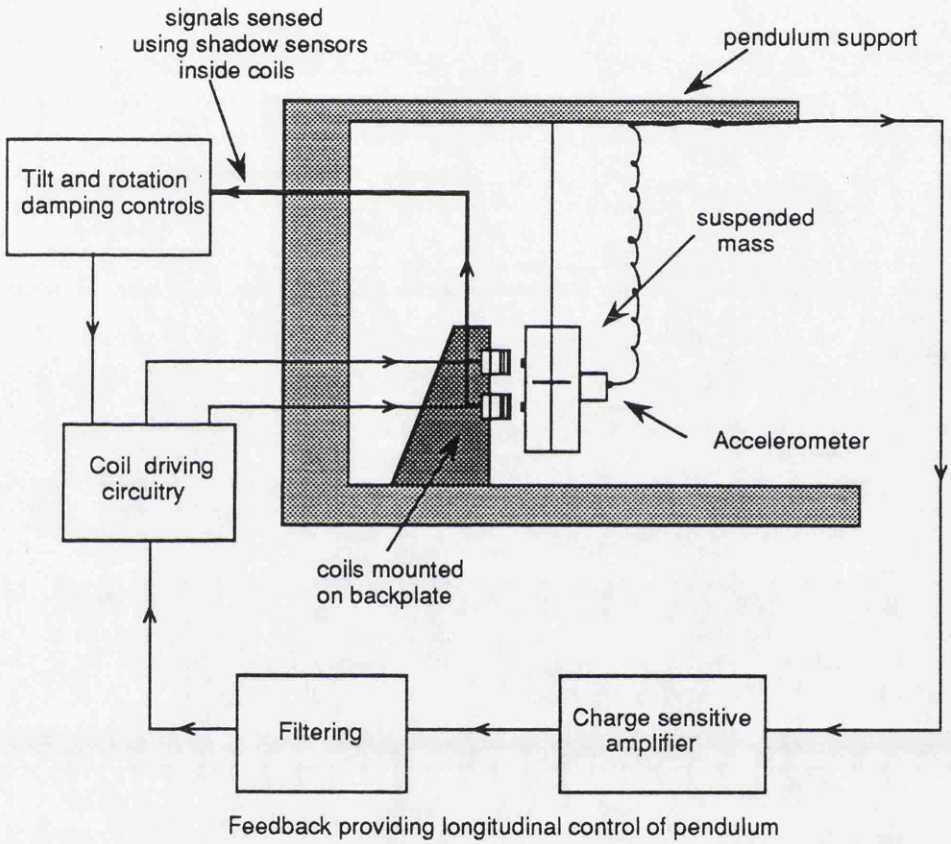

Figure 2.8: *Experimental arrangement of the system used to test inertial damping of a pendulum.*

(Brüel&Kjær accelerometer type 4378). The signal derived from the accelerometer could then be fed back to the coils mounted on the backplate to damp down the longitudinal motion of the test mass.

2.5.2 Feedback system

A block diagram representation of the feedback system is shown in figure 2.9. The particular form of the electronic filtering is designed to keep the feedback system stable for a loop gain of a few at around 0.7 Hz (near the pendulum resonance).

A Bode plot of the complete open loop transfer function of the damping system is shown in figure 2.10. From the Bode plots it can be seen that the system will become unstable if the overall loop gain is >1 at around 0.1 Hz, where the phase approaches 180°.

2.5.3 Operation

Great care was required in setting up the system. It was essential that all degrees of freedom (tilt, rotation and sideways) were sufficiently well damped using the shadow sensor systems before the longitudinal feedback system derived from the accelerometer could be switched on. The reason for this appeared to be due to a tendency for motion in other degrees of freedom (particularly tilting of the mass) to couple in quite strongly to the signal sensed by the accelerometer.

However, with a little care, the mass could be well damped in all degrees of freedom and left to move freely in the longitudinal direction. Switching on the inertial damping system resulted in the damping of the motion of the pendulum as shown in the upper two plots in figure 2.11. Here the longitudinal pendulum motion, as sensed by the shadow sensors, settles down to a steady state in only a few seconds after a DC voltage is applied to the coil/magnet actuators acting on the mass. It was expected that turning up the gain would result in the system becoming unstable at around 0.1 Hz. However, as shown in the lower two plots in figure 2.11, an increase in the gain of the system resulted in better damping of

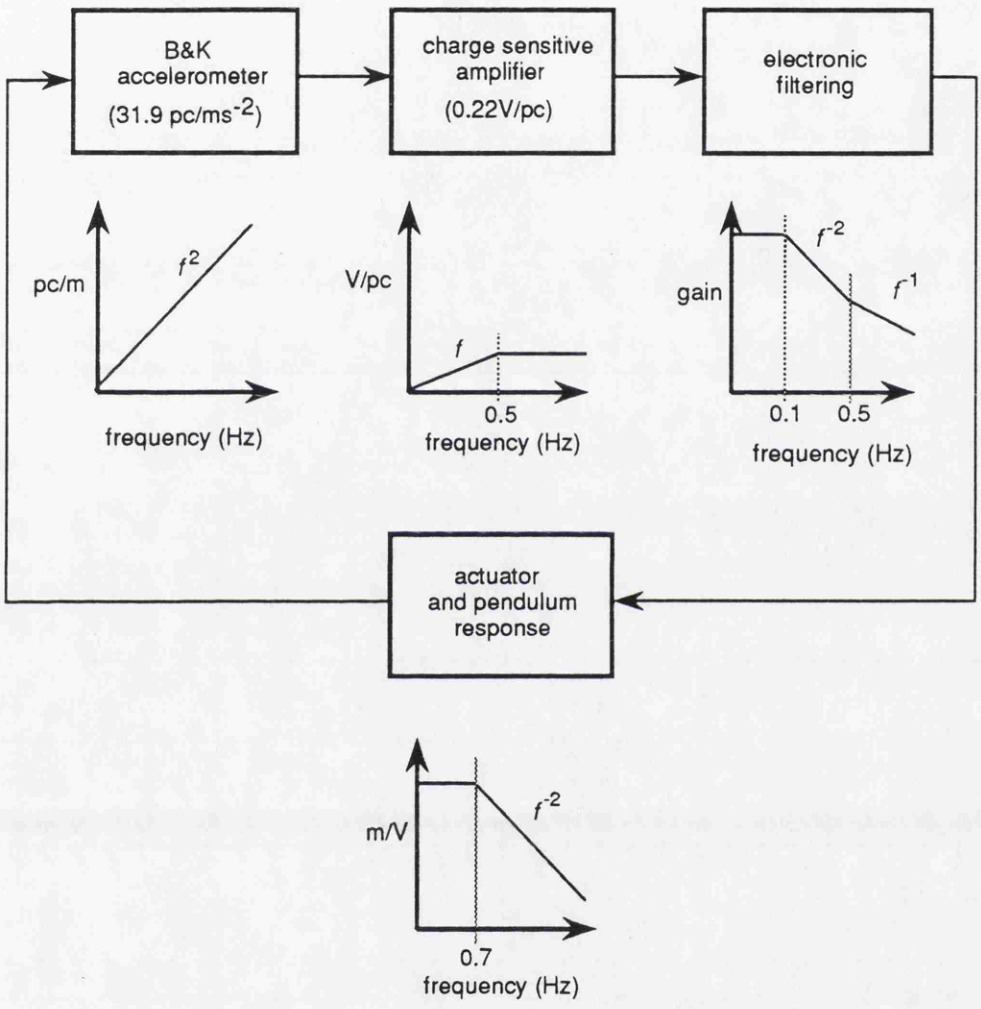

Figure 2.9: *Block diagram representation of the inertial damping system with transfer functions of the various components shown as simplified Bode diagrams.*

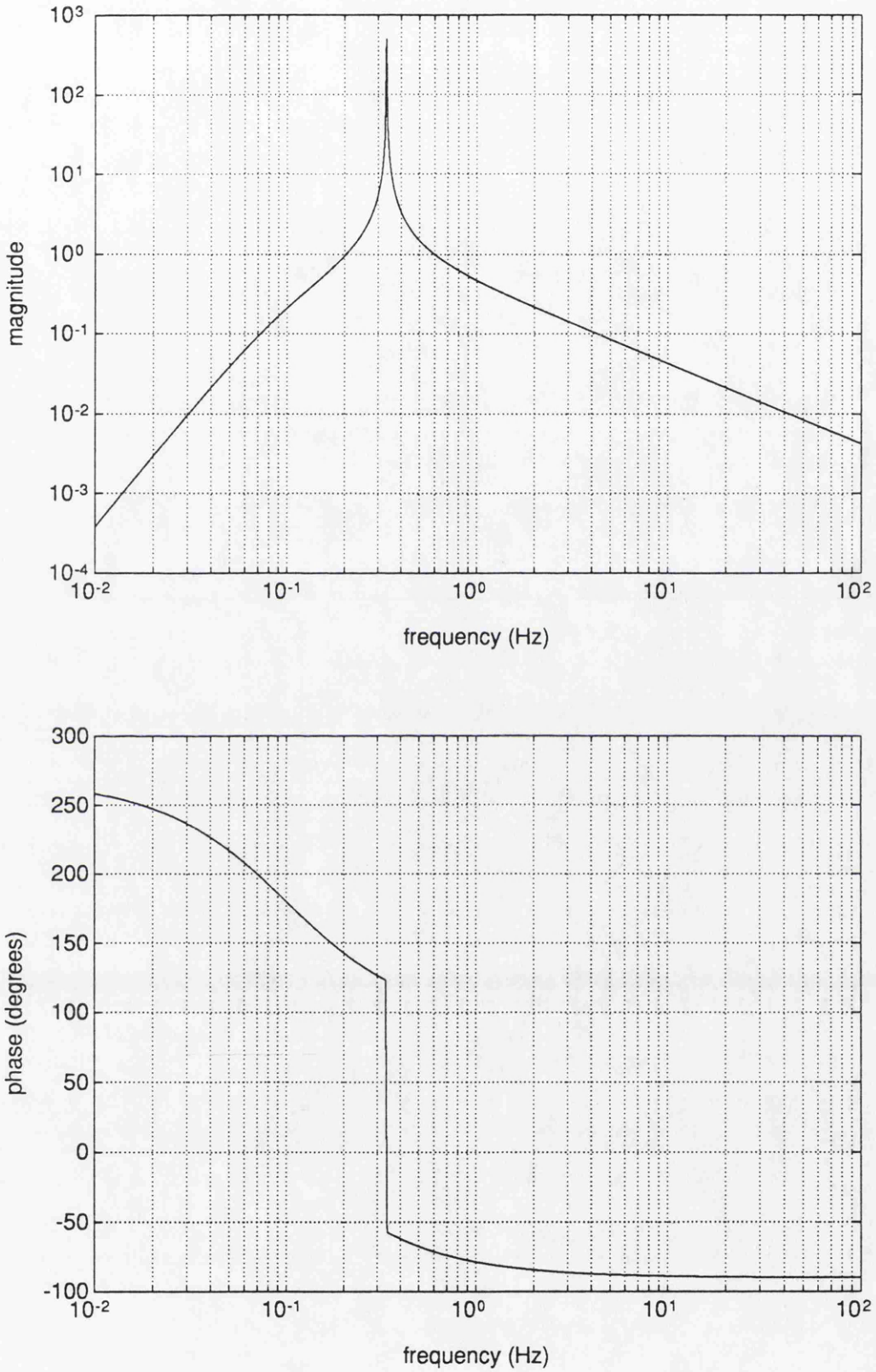

Figure 2.10: *Magnitude and phase plots of the open loop transfer function of the inertial damping system.*

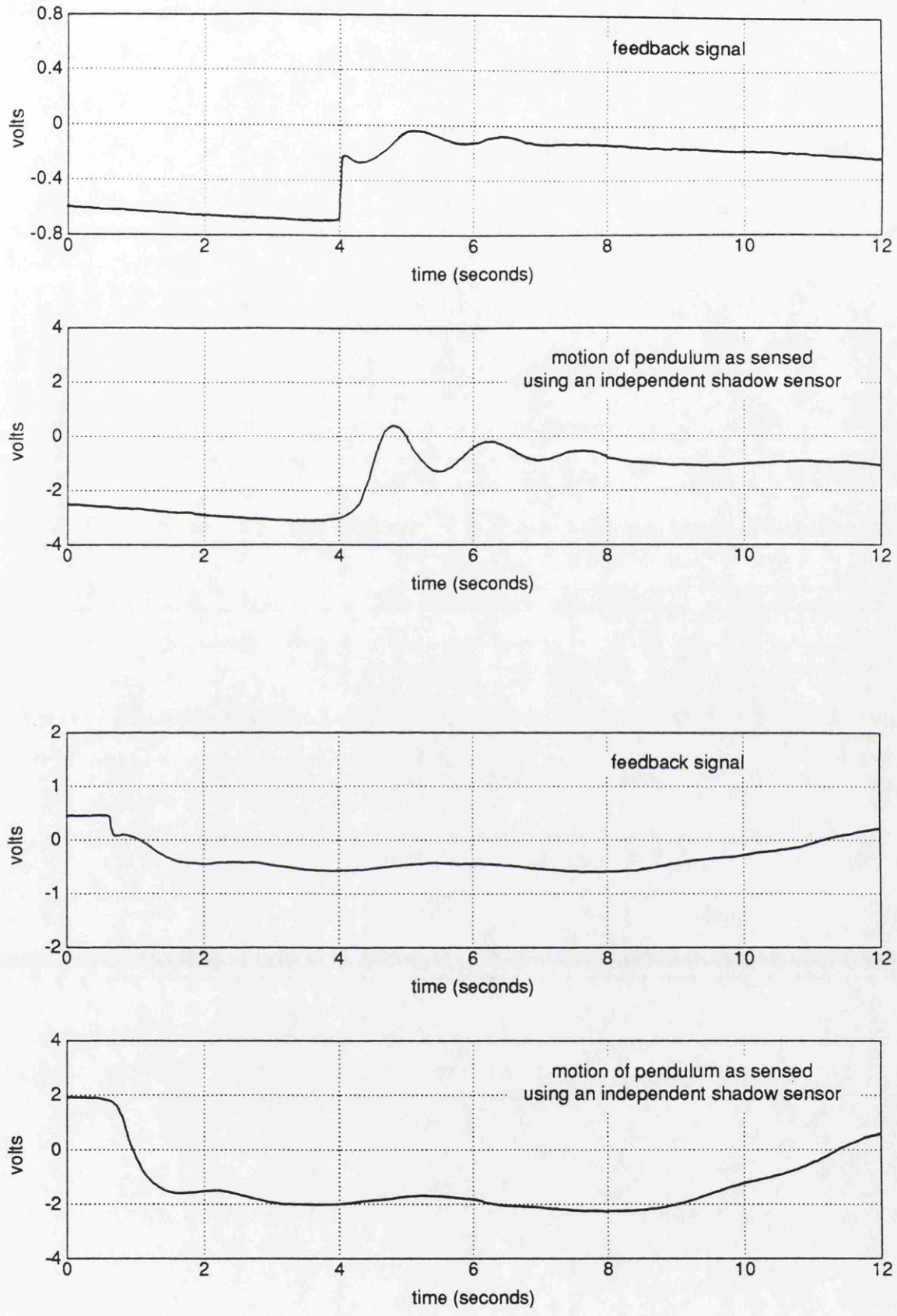

Figure 2.11: *Damping of the pendulum using a signal derived from an inertial sensor. The upper two plots show the response of the feedback system with the gain set for light damping, the lower two plots show the behaviour of the system with higher gain (~ a factor of 4 higher)*

the pendulum, but noticeably increased the level of low frequency drifting of the position of the test mass.

The amount of drifting can be estimated by looking at the trace which shows the position of the test mass as measured by an independent shadow sensor. The sensitivity of the sensor was measured to be $\sim 10\,\mathrm{V/mm}$. In the case of light damping of the pendulum, the low frequency drifting was $\sim 50\,\mu\mathrm{m}$ rms whereas with the gain turned up, the low frequency drifting corresponded to $\sim 200\,\mu\mathrm{m}$ rms.

Subsequent measurements on the system revealed that this was not due to the system becoming unstable because of a lack of phase margin at low frequencies; it was the result of low frequency noise in the charge sensitive amplifier being imposed onto the motion of the pendulum. In order to fully understand the reason for this and to estimate the extent of the problem it is necessary to study the characteristics and noise performance of the charge sensitive amplifier.

2.5.4 Charge sensitive amplifier – characteristics and noise performance

Figure 2.12 shows a simple model of a charge sensitive amplifier with a *pzt* based accelerometer (modelled here as a capacitor, C_p, and resistor, R_p, connected in parallel) attached to its input. The amplifier is designed so that charge produced by the accelerometer is converted into a voltage signal at the output. C_f and R_f represent the capacitor and resistor providing the feedback path around the op-amp. Also indicated in the diagram are the various noise sources inherent in the device; e_n represents the input noise voltage of the op-amp, i_n the input noise current and e_{fth}, e_{pth} the thermal noise associated with the feedback resistor and the internal resistance of the accelerometer respectively.

The sensitivity of the device is given by

$$\left(\frac{j\omega C_f R_f}{1+j\omega C_f R_f}\right)\left(\frac{\omega^2 S}{C_f}\right)\ \mathrm{V/m}\,, \tag{2.26}$$

where S represents the charge sensitivity of the accelerometer in $\mathrm{Q/ms^{-2}}$.

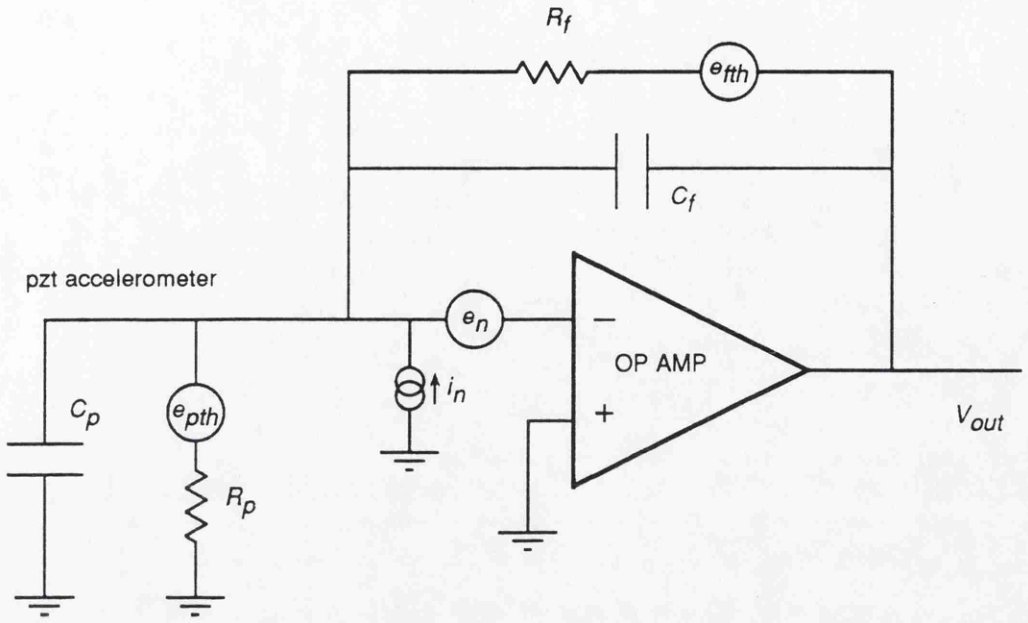

Figure 2.12: *Simplified model of a charge sensitive amplifier.*

The output noise voltage can be written in terms of all the various noise sources in the system.

$$|V_{n,out}|^2 = \left|1 + \left(\frac{R_f}{1 + j\omega C_f R_f}\right)\left(\frac{1 + j\omega C_p R_p}{R_p}\right)\right|^2 e_n^2 + \left|\frac{R_f}{1 + j\omega C_f R_f}\right|^2 \left(\frac{4kT}{R_f} + \frac{4kT}{R_p} + i_n^2\right) . \quad (2.27)$$

The particular op-amp used in the experiments was a low noise precision FET amplifier (OPA111, Burr-Brown). The noise characteristics of this device are quoted by the manufacturer as [40]

$$i_n = 0.5\,\mathrm{fA}/\sqrt{\mathrm{Hz}} \text{ up to } \sim 10\,\mathrm{kHz}$$

and

$$e_n \sim \left(12 \times \left(\frac{30}{f}\right)^{0.56} + 6\right) \mathrm{nV}/\sqrt{\mathrm{Hz}} .$$

The values of the various components used were as follows; $R_f = 2 \times 10^{10}\,\Omega$, $R_p = 1 \times 10^{11}\,\Omega$, $C_f = 15\,\mathrm{pF}$ and $C_p = 1000\,\mathrm{pF}$.

These figures allow an estimate to be made of the noise at the output of the charge sensitive amplifier, $V_{n,out}$, given by equation 2.27. This is plotted in figure 2.13. At low frequencies ($< 1\,\mathrm{Hz}$) the noise is $\sim 2.2 \times 10^{-5}\,\mathrm{V}/\sqrt{\mathrm{Hz}}$ and is dominated by the input current noise and the thermal noise due to R_f and R_p. Above 100 Hz the noise is due to the input voltage noise of the op-amp and is $\sim 1.2 \times 10^{-6}\,\mathrm{V}/\sqrt{\mathrm{Hz}}$.

From these figures it is possible to calculate the noise floor of such a sensing device at 100 Hz. The B&K accelerometer used in the experiment had a 'moving mass' of 70 g and its charge sensitivity was given as $31.9\,\mathrm{pC/ms^{-2}}$. Assuming that a similar accelerometer can be constructed with a 1 kg moving mass and the feedback capacitor can be reduced to 3 pF, then the sensitivity at 100 Hz (as given by equation 2.26) is $\sim 6 \times 10^7\,\mathrm{V/m}$. The output noise level of $\sim 1.2 \times 10^{-6}\,\mathrm{V}/\sqrt{\mathrm{Hz}}$ at the output of the charge sensitive amplifier corresponds to a sensing limit of $\sim 2 \times 10^{-14}\,\mathrm{m}/\sqrt{\mathrm{Hz}}$ at 100 Hz. The noise performance of this device at 100 Hz is clearly far superior to that of a standard shadow sensor arrangement.

Consider now the low frequency performance of such a device. As was discovered during the experimental test of the inertial damping system, there was a tendency for low frequency noise in the front end to get amplified up by the servo imposing large low frequency drifts on the position of the test mass.

Examining the open loop gain characteristics of the particular servo used (shown in figure 2.10) it can be seen that the servo has been designed so that it has a gain of > 1 only over a very small frequency band around the resonance. Therefore at low frequencies the noise at the output of the charge sensitive amplifier is imposed directly through the feedback loop onto the motion of the mass without any reduction due to the action of the servo.

The resulting displacement of the test mass due to this noise can be calculated from the gain of the electronic filtering and pendulum stages. This is shown in figure 2.14 where the gain of the feedback loop between the output of the charge sensitive amplifier and the position of the test mass is plotted as a function of frequency. The overall open loop gain is the same as in figure 2.10. From the graph it can be seen that this part of the servo has a gain of ~ 2 from DC up to

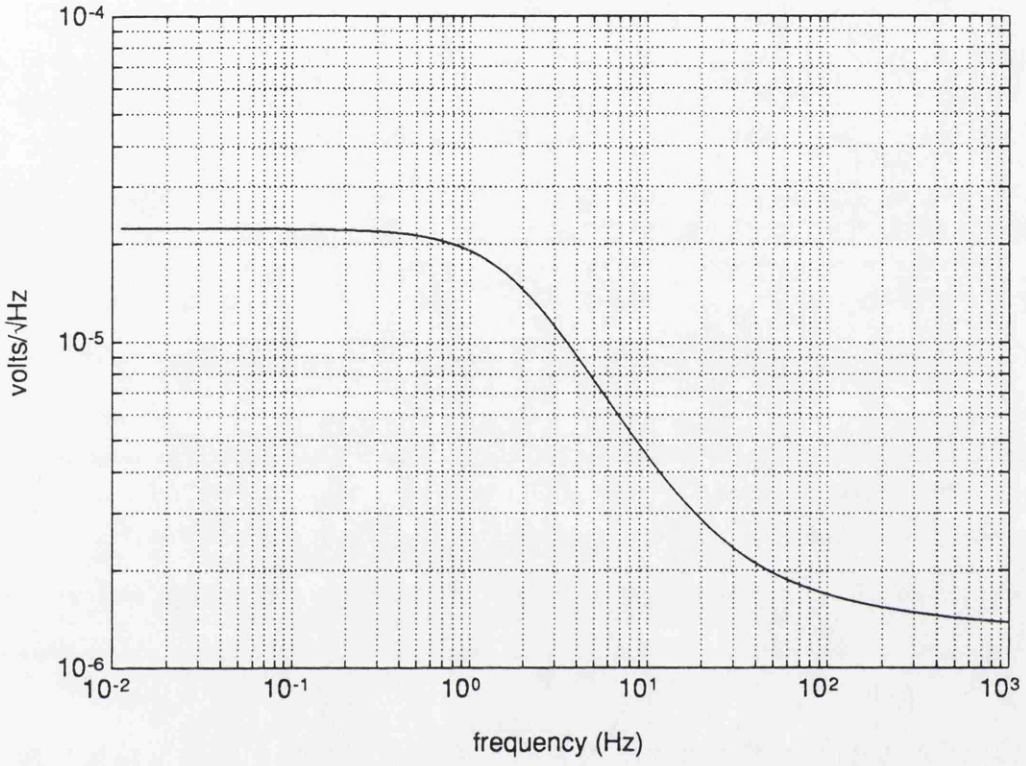

Figure 2.13: *Electronic noise at the output of the charge sensitive amplifier.*

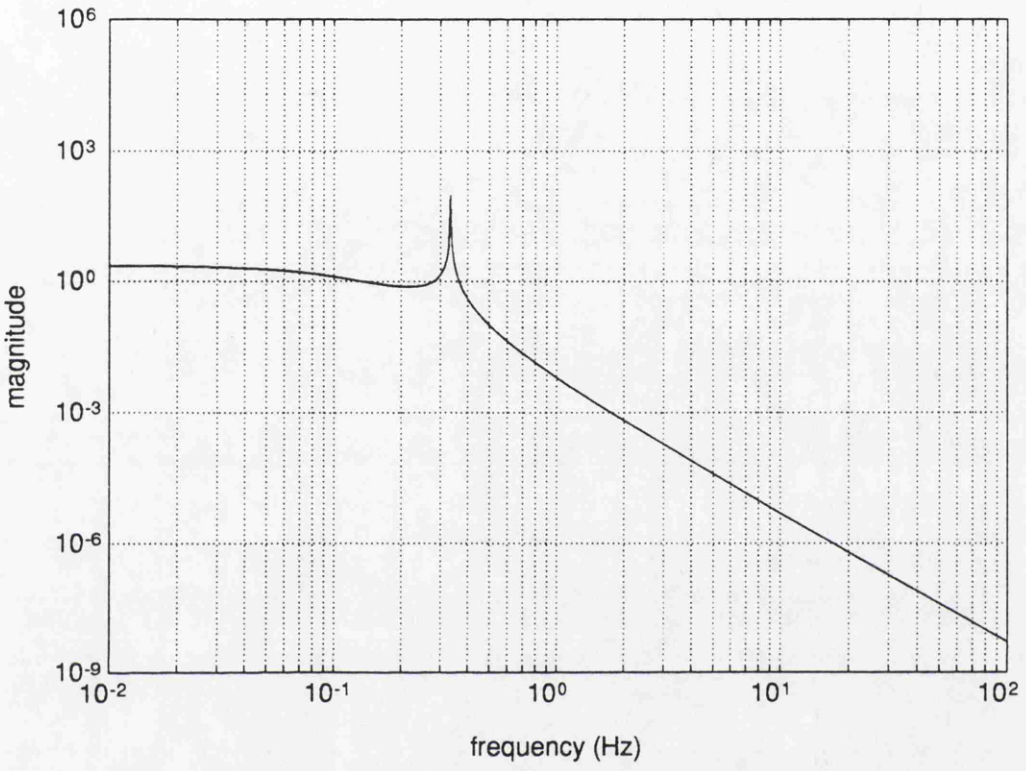

Figure 2.14: *Open loop servo gain between output of charge sensitive amplifier and test mass.*

around the pendulum resonant frequency at 0.7 Hz. The noise at the output of the charge sensitive amplifier of $\sim 2.2 \times 10^{-5}\,\mathrm{V}/\sqrt{\mathrm{Hz}}$ will result in $\sim 50\mu$m rms motion of the test mass. This figure agrees roughly with what was observed during the experimental trials of the damping system and in fact can be made much worse by turning up the gain of the feedback.

The large amount of low frequency drifting of the test mass damped using an inertial sensing system is obviously a serious problem if the system is to be used in an interferometer to control the position of the suspended mirrors.

Some extra high pass filtering could perhaps be introduced into the servo loop after the charge sensitive amplifier. However, although it is no doubt possible to improve on the filtering which has been used here, it is unlikely that much extra filtering at low frequencies can be achieved without seriously compromising the phase margin of the servo. Another possibility would be to reduce the gain of the electronics by increasing the sensitivity of the accelerometer, whilst keeping the overall open loop gain constant. It is possible to do this by increasing the 'moving mass' of the accelerometer. If an accelerometer is constructed with a 1 kg 'moving mass' it should be possible to reduce the low frequency drifting due to the noise in the charge sensitive amplifier to less than 1 μm rms which is typically less than the low frequency motion of the mass due to seismic noise.

2.5.5 Conclusion and summary

A local damping system for control of a suspended test mass based on an inertial sensing system has been experimentally demonstrated. Using such a system it was possible to damp down the pendulum resonance to a Q of a few. However the system tended to drift considerably at low frequencies. This problem was due to front end noise in the charge sensitive amplifier/*pzt* accelerometer arrangement and the particular design of the servo required to ensure a stable feedback system using an inertial sensor. Although the extent of the low frequency motion of the suspended test mass in the system demonstrated here (the drifts were of the order of 50 μm rms) would make this particular set up unattractive for use in a

sensitive interferometer, it should be possible, at least in theory, to devise a similar system with a modified accelerometer whose low frequency noise performance was adequate.

Because of the superior noise performance of the inertial sensing system at higher frequencies (>100 Hz) it should be relatively easy to design a local damping system using such a sensor which meets the stringent requirements set in order for the system to be useful in a full scale interferometric gravitational wave detector. This would probably involve the sensor being used to sense and feedback signals to the intermediate mass of a double pendulum suspension system similar to that described in section 2.4.4.

There are however some disadvantages associated with the use of inertial sensors. The sensor itself must be mounted on the test mass to be damped, and if the mass is to be damped in more than one degree of freedom using this system, a rather complicated compound mass would have to be constructed. The Q of such a mass is likely to be quite low so it is very unlikely that such a system could be mounted on the main test mass. Also, it is important to ensure that all degrees of freedom which require damping are adequately sensed and that the cross coupling between sensing different degrees of freedom does not cause problems. This last point caused great difficulties during the experimental test of the inertial damping system described in section 2.5.1 due to the sensitivity of the accelerometer, used to sense the longitudinal motion of the mass, to tilting of the mass. The wires attached to the accelerometer need to be carefully suspended so that excess noise (due to *e.g.* seismic noise) does not bypass the mechanical filtering of the pendulum suspension system. Further, it is possible that any movement of these wires can cause charge to flow through the charge sensitive amplifier, causing spurious motion of the test mass requiring perhaps some small pre-amplifier to be built into the accelerometer front end.

2.6 Main interferometer locking system – some general comments

In high precision interferometers the signal obtained from the interfered output is usually used to hold the system locked to a dark fringe. The servo which does this also produces the main output signal from the interferometer.

To hold the system stable on the null fringe, it is desirable to have reasonably high loop gain at low frequencies. This prevents large excursions of the locking point from the bottom of the fringe due to seismic (or other) disturbances perturbing the interferometer, which could couple in intensity noise (and possibly other noise sources) into the detector output signal. Although the exact amount of loop gain will depend to a large extent on the level of the external disturbances, such as seismic noise at the detector site, a servo with a bandwidth of a few kHz will probably be required. This is typically the bandwidth of the servo used on the 10 m prototype here in Glasgow, discussed in Chapter 4.

The feedback signals can be applied to control the longitudinal position of one or more of the suspended mirrors using, for example, coil/magnet force actuators. Small permanent magnets attached to the test mass are acted upon using the magnetic field produced by driving a current through a wirewound coil (the coils being being mounted on a suitable suspended or fixed reaction mass).

The noise model for such a servo system, discussed in section 2.3.1, places some strict limits on the design and feedback strategies required.

The prototypes currently operating in Caltech and Glasgow feed back signals directly to move one of the suspended mirrors in one arm of the interferometer. The Garching prototype on the other hand relies on feeding back signals to Pockels cell phase modulators, situated in the two arms of the interferometer, in order to maintain lock of the interferometer. It is unlikely however that this technique could be used with the high powers required for more sensitive interferometers.

For the second generation of high precision laser interferometers to be built on 3 km baselines, it is likely that either a mechanical feedback system where signals are fed back directly to the main test mass is used, or, that a split feedback system

is employed, where some of the main feedback signal is applied at low frequencies to the intermediate mass of a double pendulum system, whilst the high frequency signals are applied directly to the main test mass. A preliminary experimental test of such a system has been carried out in Glasgow [23] and has also been recently investigated in Munich [41].

The implications of the noise model for these two different feedback systems are discussed in the following sections.

2.6.1 Feedback directly to the main test mass

From the noise model considered in section 2.3.1 it is clear that if the main interferometer output signal from the error point is used, the condition set by equation 2.7 must be satisfied, *i.e.* that 'back-end' noise in the actuator must not impose excess noise on the detected signal.

This condition effectively sets the maximum signal size which can be applied to the test mass *via* the actuator and has previously been discussed in the context of local damping control systems in section 2.4.5. In order to understand the implications of this, consider the standard coil/magnet actuators driven through suitably low noise current drivers (such as those discussed later in Chapter 5). The amplifiers used for the current drivers typically have a maximum output of order 10 V with a corresponding noise floor of $\sim 1\,\mathrm{nV}/\sqrt{\mathrm{Hz}}$ at 100 Hz. Since the coils which are used to feedback forces to the suspended masses are of fairly low impedance (typically a few tens of ohms), it is extremely hard to achieve any significant filtering of the noise from the output of the current drivers at frequencies as low as 100 Hz. For a 1 Hz pendulum then, in order to reach a sensitivity of $10^{-22}\,\mathrm{m}/\sqrt{\mathrm{Hz}}$ at 100 Hz (the design goal for a 3 km interferometer discussed in section 2.4.1) the maximum signal which can be applied using such a transducer corresponds to $\sim 10^{-8}$ m.

This is insufficient to deal with the large low frequency motions present in the interferometer due to seismic noise, which propagates through to the test mass almost unattenuated at frequencies below 1 Hz. The level of seismic noise will be

very dependent on the actual site chosen for the interferometer, but typically it may be expected that the test masses will move by a few μm rms at low frequencies.

It may be possible to achieve a slightly better performance using higher voltage amplifiers to drive the coils, provided the ratio of the maximum output voltage to the noise floor of the amplifier is better than the factor of 10^{10} which is considered above.

In order to overcome this dynamic range problem, a split feedback system, such as discussed in section 2.6.2 is required.

However, it is also possible, and perhaps more sensible, to use the feedback signal as the source of the main detector output signal. Examining the condition set by equation 2.9 in section 2.3.1, it can be seen that at this point in the feedback loop the actuator noise is effectively reduced by the loop gain of the feedback system. Clearly then, a loop gain of $\sim 10^3$ at 100 Hz would reduce the noise in the actuator to a level corresponding to $10^{-22}\,\mathrm{m}/\sqrt{\mathrm{Hz}}$ at 100 Hz, and allow signals as large as $\sim 10\,\mu$m to be fed back to the main test mass.

In this case, as far as the noise considerations in section 2.3.1 are concerned, it is not essential to have a split feedback system in order to reach the design goals mentioned earlier.

It should however be pointed out that there may be some practical problems associated with achieving high loop gain using such a system. In particular, in the prototype system in Glasgow, the bandwidth of the main interferometer feedback locking servo (which acts on the end mirror in the secondary cavity, as described in Chapter 4) is restricted in order to prevent exciting up the internal resonances of the test mass, which in this case occur above 17 kHz. This may make it reasonably difficult to achieve loop gains of the order of 10^3 at 100 Hz.

2.6.2 Split feedback control systems

If the main interferometer system has insufficient loop gain at 100 Hz, or if the detector output signal is derived from the error point of the main interferometer locking servo, then a split feedback system may be desirable. By feeding back

the large low frequency signals to the intermediate stage, it should be possible to use suitable actuators to ensure that 'back-end' noise does not compromise the performance of the system at the frequencies of interest for detecting gravitational waves. The extra passive isolation ($\sim 10^4$) of the actuator noise resulting from acting on the intermediate mass means that a noisier actuator can be used – *i.e.* one which is capable of driving signals corresponding to $\sim 100\,\mu$m.

It is important when designing such a system to correctly choose the cross-over frequency of the two feedback paths. The magnitude of the relative phase difference of the two paths must be less than 180° at the cross-over frequency to ensure stability. Further, the gain of the feedback to the main test mass must be attenuated below the cross over frequency (in order to ensure that the large low frequency signals are not fed back to the main test mass actuator which has limited dynamic range) and similarly the gain of the system feeding back to the intermediate stage must be attenuated at frequencies above the cross-over (primarily to avoid exciting up the wire resonances in the double pendulum suspension system).

2.6.3 Conclusion and comments

The design of the main interferometer feedback system will depend on many factors, such as the seismic noise at the detector site, required bandwidth of the locking servo *etc.*

There are however some other important factors which could influence the design of such a system and determine whether a split or single feedback system is used. One such concern is the problem of non-linearities occurring either in the actuator, or earlier on in the servo system. Non-linearities can cause large amounts of low frequency noise to be up-converted, causing excess levels of noise at higher frequencies, in particular at 100 Hz and above, *i.e.* frequencies which are of interest for detecting gravitational waves. It is commonly assumed that a split feedback system would improve matters in such a situation since the high frequency noise would be passively attenuated by the extra stage of isolation. However, depending on the frequencies at which the up-conversion was taking place, it is possible that

a split feedback system could enhance the level of high frequency noise.

For example, consider a split feedback system with a cross-over frequency around 10 Hz. Below this frequency the feedback path to the intermediate mass dominates, whereas above the cross-over the feedback to the main test mass dominates. In order to ensure that the system is stable, the magnitude of the phase difference between the two feedback paths must be less than 180° at 10 Hz. As a result of this, the difference in gain between the two feedback paths at 100 Hz may be as little as a factor of 10. However, the feedback signal which is applied to the actuator acting on the intermediate mass at 10 Hz could be as much as 100 times larger than the signal which is applied to the main test mass at that frequency. If the amount of noise produced at 100 Hz due to non-linear up-conversion increases linearly with the size of the signal applied to the actuator, then the split feedback system considered here will be no better in terms on noise performance at 100 Hz. However, more worrying is the possibility that if the amount of noise produced at 100 Hz due to non-linear up-conversion increases non-linearly with the size of the signal applied to the actuator, then the level of noise at 100 Hz could be greater if such a split feedback system is used (compared to the level of noise which would have been produced if the feedback had been applied directly to the main test mass).

It is also important when designing such a system to ensure that the isolation provided by the pendulum suspension of the test mass is not bypassed at any stage. For example, any actuator used to feedback signals to the main test mass must not couple in excess amounts of seismic noise. This can be ensured by using suitable zero-gradient force coils [42],[43] and/or by suspending the reaction mass to which the coils are attached.

Chapter 3

Automatic alignment systems

3.1 Introduction

In order to obtain maximum sensitivity from an interferometric gravitational wave detector, it is necessary to have the main interfering beams optimally aligned. Where the arm lengths in the interferometer are of the order of 3km, and the optical components are not rigidly mounted, this alignment must be maintained during the operation of the interferometer by an automatic control system.

Ideally the signals for any such system should be derived directly from the interference of the two beams; suitable control signals may then be applied to move components in the interferometer causing the beams to overlap optimally.

The main purpose of this chapter is to describe the theoretical and experimental development of such a system.

3.2 Beam misalignments and mismatches in optical interferometers

In general, the two beams at the output of an interferometer can be angularly or laterally misaligned and also mismatched in beam size and curvature. To illustrate how these beams can be angularly or laterally misaligned (mismatches in beam size and curvature will be neglected for the moment, but discussed later), consider the following examples.

Figure 3.1 shows an equal path length Michelson interferometer. Misaligning either of the mirrors, M1 or M2, or the beamsplitter, B1, by an angle α, results

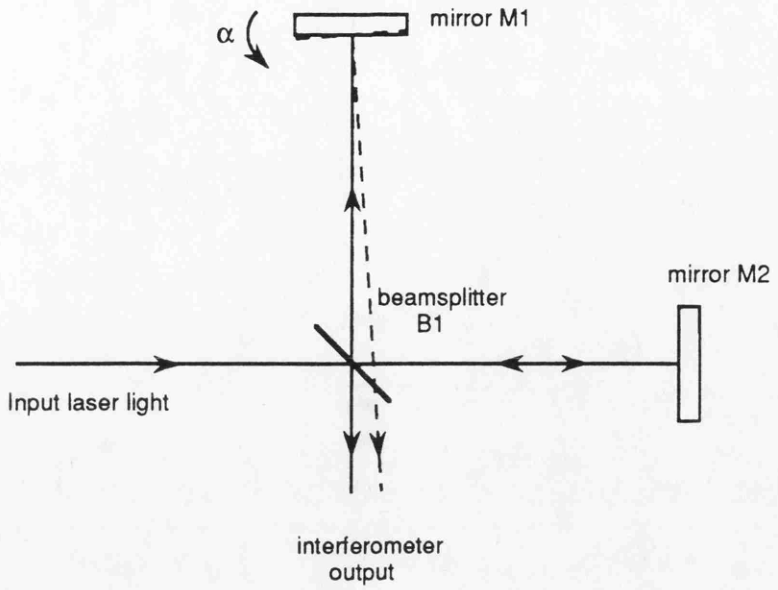

Figure 3.1: *A simple Michelson interferometer showing the effect of a misalignment of one of the end mirrors on the two interfering beams at the output.*

in an angular misalignment of the two interfering beams at the output of the interferometer. Note that the misalignment appears to originate at one of the mirrors M1 or M2 as viewed at the output.

Consider now the Mach-Zehnder interferometer shown in figure 3.2. As can be seen in the diagram, misalignment of beamsplitter B1 along with a misalignment of mirror M1 results in a pure translational misalignment of the two beams at the output of the interferometer. Angular misalignments are also possible, due to misalignment of any of the mirrors or beamsplitters in the system.

Such angular and lateral misalignments are also possible in a resonant optical cavity. If the cavity is viewed in reflection, then the two interfering beams of interest are the beam which is directly reflected off the front surface of the input mirror and the light which leaks out of the cavity on resonance. Figure 3.3 shows the effect of misalignment of the two mirrors in a plane/curved cavity. As can be seen, the misalignment of the rear curved mirror results in a lateral displacement of the light leaking out of the cavity with respect to the directly reflected light. Misalignment of the front mirror in this particular configuration results in an angular misalignment between the directly reflected beam and the light leaking out of the cavity.

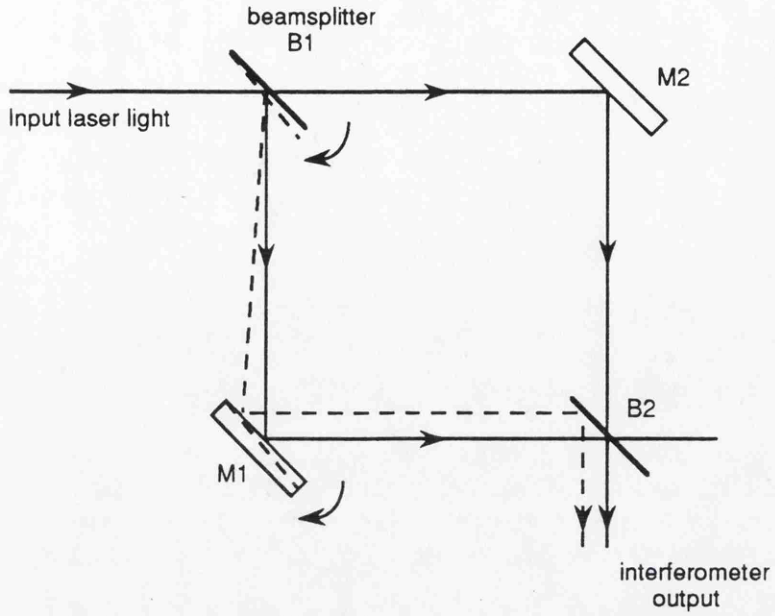

Figure 3.2: *A Mach-Zehnder interferometer showing the combined effect of a misalignment of a beamsplitter and a mirror on the two interfering beams at the output.*

In addition to angular and lateral offsets, it is also possible for the two interfering beams to have mismatches in beam size and curvature. This occurs for example in an optical cavity where the input light is incorrectly modematched into the cavity *i.e.* the input beam waist position and size does not correspond to those of the cavity.

In general then, the two interfering beams at the output of any interferometer may be angularly or laterally misaligned and may be mismatched in size and curvature.

3.2.1 Alignment techniques

In order to correct for beam misalignments and mismatches in optical systems it is necessary to have some method of detecting these offsets. In most interferometers the relative path length difference in the interferometer is detected by observing the change in intensity of the interference pattern at the output. One way of detecting the misalignment of the two interfering beams would be to modulate the relative alignment of the two interfering beams and coherently detect the change in intensity at the output. The modulation can be achieved by modulating the position

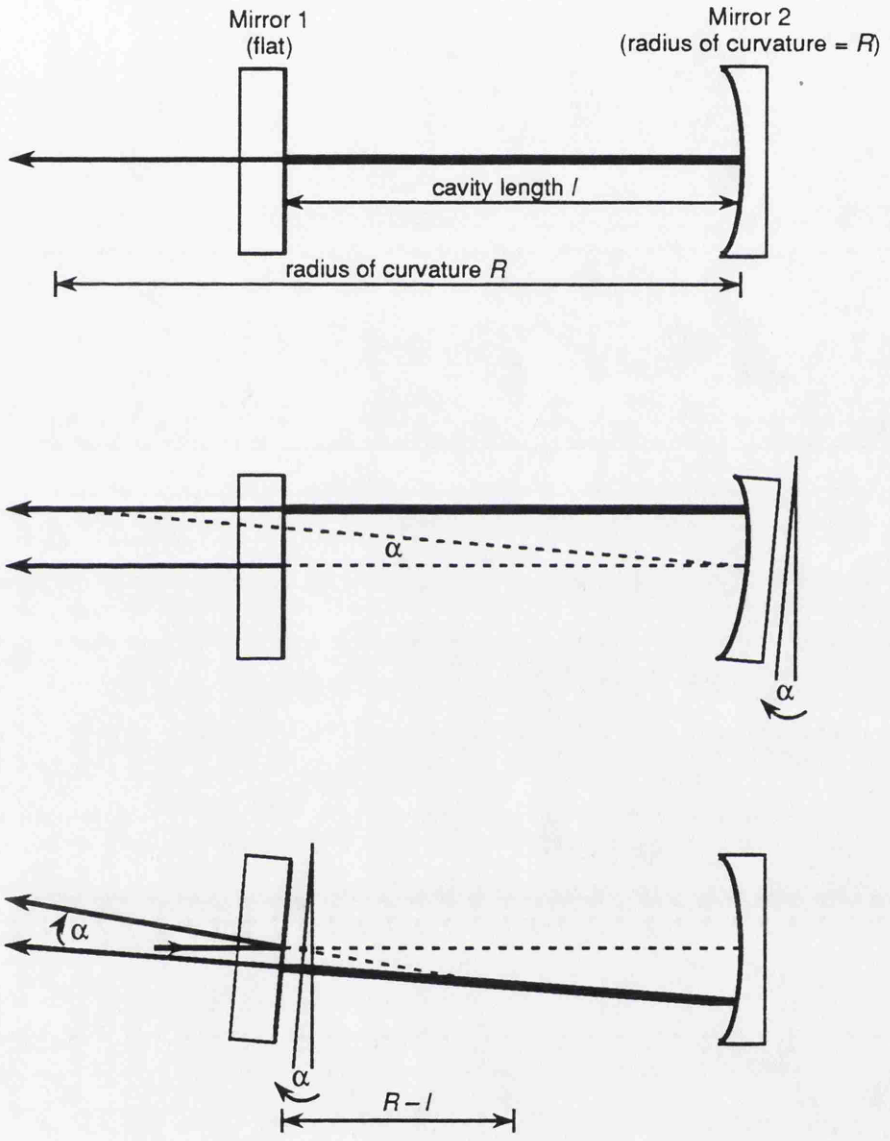

Figure 3.3: *A resonant optical cavity showing the effect of misalignment of the mirrors on the two interfering beams viewed in reflection.*

and angle of the input laser beam with respect to the interferometer components or by modulating the position of a suitable number of mirrors in the interferometer. Feedback signals can then be applied to components in the interferometer to correct for the misalignment. This scheme, referred to as alignment modulation, has been successfully tested here in Glasgow, both on the 10 m optical cavities in the prototype gravitational wave detector [44], and on a small benchtop Michelson interferometer.

A method for sensing the misalignment of a resonant optical cavity has also been described by Anderson [45] and demonstrated experimentally on a small ring cavity [46]. This technique involves using an auxiliary phase modulation system to monitor the amplitude of higher order modes in the cavity, present due to misalignment. The laser frequency is stabilised to the fundamental cavity mode resonance and phase modulation applied to produce sidebands on the laser light at frequencies corresponding to the first order off-axis modes. Misalignment of the cavity allows the first order modes to be resonant in the cavity, and so some of the sidebands will be transmitted along with the main laser light. The light transmitted in the first order mode is directly proportional to the misalignment, and can be detected by sensing the amplitude modulation of the transmitted light at the modulation frequency.

Although both of these techniques have been successfully demonstrated, they do have some disadvantages. The auxiliary phase modulation technique is only applicable to optical cavities and cannot be applied to an arbitrary interferometric system. It also involves the use of modulation frequencies other than those used to lock the cavity and stabilise the laser to the fundamental cavity mode resonance. Alignment modulation has the advantage that it is applicable to all types of interferometer. However in a more complex arrangement of interferometric systems, such as those currently being proposed for advanced interferometric gravitational wave detectors (incorporating techniques such as dual recycling), it may not always be possible or desirable to modulate the position of the input laser beam to obtain full information about the misalignment of the interferometer. It would therefore be necessary to modulate the position of some of the mirrors in the interferome-

ter. The mirrors in a gravitational wave detector, because they are suspended as pendulums, can only move appreciably at low frequencies and the imposition of four modulation frequencies required to obtain full alignment information could severely limit the attainable bandwidth of alignment control.

3.3 Sensing a differential phase gradient

3.3.1 Basic idea

In order to lock an interferometer and obtain a signal which is proportional to the phase difference between the two interfering beams at the output, it is normal in high precision interferometry to apply differential phase modulation. This can be achieved in practice by inserting a Pockels cell in one arm of the interferometer, or alternatively, by modulating the longitudinal position of one of the interferometer mirrors. The interferometer locking signal is obtained by detecting the change in the interference pattern at the modulation frequency. It is possible to use this to detect the angular and lateral misalignment and size and curvature mismatch of the two beams as well as the phase difference between them (this idea was first suggested by Ron Drever at Caltech). Such a scheme has the advantage that no further modulation need be applied to the interferometer. In fact any interferometer which is locked using differential phase sensing can be aligned using this technique.

Consider now a simple angular misalignment between two interfering beams, one of which has phase modulation applied to it. This is shown in figure 3.4 where the two beams are misaligned by an angle α at the waist where the phase fronts are plane. Examining the phase fronts, it can be seen that the overall phase difference between the two beams is 180° *i.e.* the interferometer is locked onto a dark fringe at its output. Now consider looking at the two beams using a split photodiode with the split centered on the middle of the interference pattern. The phase difference detected using one half of the photodiode is $\pi + \phi$, whereas the phase difference detected using the other half of the photodiode is $\pi - \phi$, where ϕ is proportional to the misalignment α. In other words, angularly misaligning the two

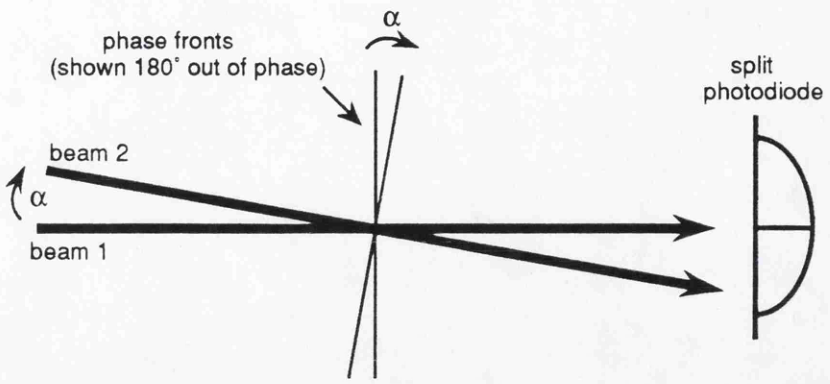

Figure 3.4: *Two beams misaligned in angle.*

beams introduces a differential phase gradient between the two beams which can be detected using a split photodiode. If the phase differences detected using each half of the photodiode are subtracted then a signal is obtained which is directly proportional to the angular misalignment of the two beams.

The technique can be extended to allow detection of lateral offsets of the two beams. By placing a lens in front of the split photodiode it is possible to convert a purely lateral offset of the two interfering beams into a purely angular misalignment. This angular misalignment can then be sensed using the differential phase sensing method described above. This is shown schematically in figure 3.5.

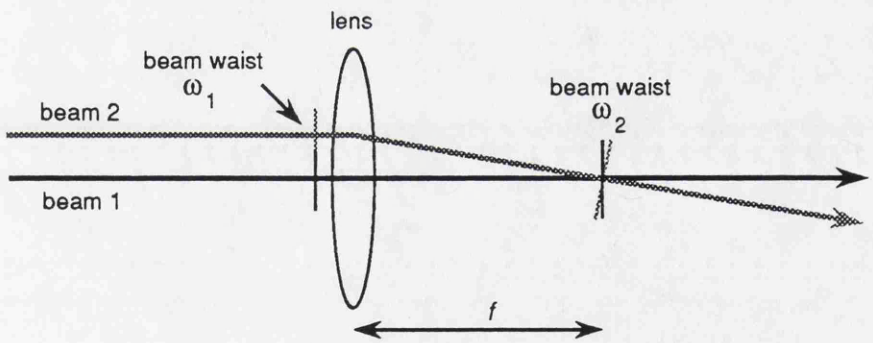

Figure 3.5: *Conversion of a lateral offset of two beams into an angular misalignment using a single lens.*

The differential phase sensing technique can also be applied to detect any mismatch in beam size or curvature of the two interfering beams. This can be done by using an annularly split photodiode – the signal being deduced by subtracting the signals detected from the centre and outer annulus of the diode. Figure 3.6 shows

the effect of offsetting the relative waist positions of the two interfering beams. Detection of the phase difference between the two sections of an annularly split

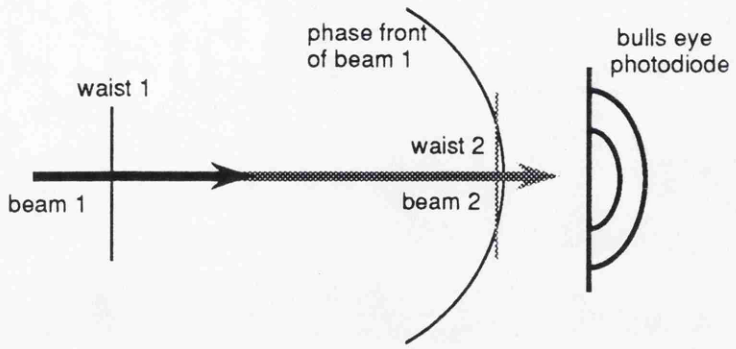

Figure 3.6: *Sensing a mismatch in the phase fronts of the two interfering beams due to a displacement of the beam waists.*

photodiode positioned near the second waist results in a signal proportional to the offset.

A mismatch in the relative beam waist size of the two interfering beams is shown in figure 3.7. As can be seen, no signal can be detected at the beam waists

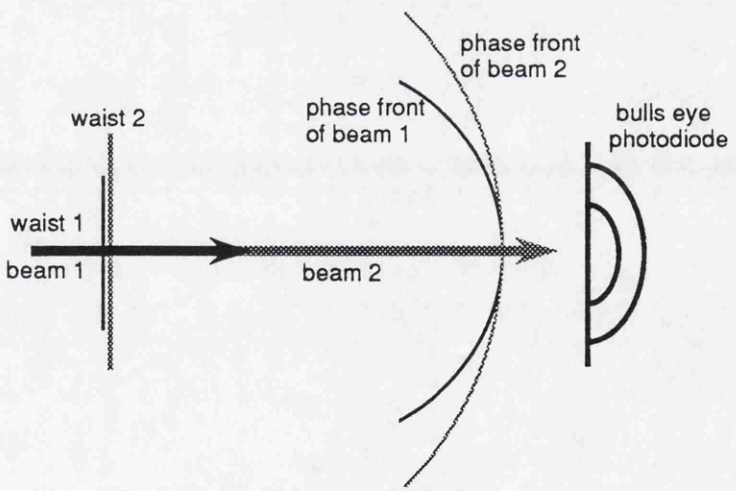

Figure 3.7: *Sensing a mismatch in the phase fronts of two interfering beams due to a difference in waist size.*

– since there is no phase difference across the waists – but a signal can be detected if the annularly split photodiode is placed a sufficient distance away from the waists.

However, in order to gain a proper understanding of this particular alignment technique it is necessary to develop a simple mathematical description of what is actually happening. In particular, it is useful to describe the laser beams in terms of their normal spatial modes as discussed in the following few sections.

3.3.2 Misalignments - a mode picture

When considering the interference of two laser beams and the effects of relative misalignments of the beams, it is convenient, and helpful, to express the electric field of the beams in terms of their normal spatial modes (see *e.g.* [47], [48]). If a Cartesian coordinate system is used, then the electric field distribution can be expressed as

$$E(x,y) = \sum_{n=0}^{\infty} \sum_{m=0}^{\infty} A_n \, h_n(x) \, A_m \, h_m(y) \; , \tag{3.1}$$

where A_n is the amplitude coefficient for the nth mode. The normal modes $h_n(x)$ are Hermite-Gaussian functions for spherical mirrors given by

$$h_n(X) = \frac{\Gamma(\frac{n}{2}+1)}{\Gamma(n+1)} H_n(X) \, e^{-X^2/2} \; , \tag{3.2}$$

where $X = \sqrt{2}x/\omega$, ω is the beam size and $H_n(X)$ a Hermite polynomial. The gamma functions represent a normalisation function included so that $h_n(0) = \pm 1$ for n even.

Of particular importance will be the lower order modes. The first 3 of these, referred to as the fundamental, first and second order modes are given, in one dimension, by

$$h_0(x) = e^{-x^2/\omega^2} \tag{3.3}$$

$$h_1(x) = \sqrt{2\pi}\frac{x}{\omega} e^{-x^2/\omega^2} \tag{3.4}$$

$$h_2(x) = \left(4\frac{x^2}{\omega^2} - 1\right) e^{-x^2/\omega^2} \; . \tag{3.5}$$

However, these expressions only describe the relative amplitudes of the various normal modes. In order to describe fully the propagation of the nth order mode

along the direction of the positive z axis the following expression is used [47]

$$U_n(x,z) = \frac{\omega_0}{\omega(z)} h_n(x) exp\left[-j\left(kz - \phi_n(z) + \frac{kx^2}{2R}\right)\right] . \tag{3.6}$$

The beam size, $\omega(z)$, and the radius of curvature of the phase front of the beams, $R(z)$, are the same for all modes and are given by

$$\omega^2(z) = {\omega_0}^2\left[1 + \left(\frac{\lambda z}{\pi {\omega_0}^2}\right)^2\right] \tag{3.7}$$

and

$$R(z) = z\left[1 + \left(\frac{\pi {\omega_0}^2}{\lambda z}\right)^2\right] . \tag{3.8}$$

The difference in phase, $\phi_n(z)$, between the nth order mode and an ideal plane wave is however a function of the mode number and is given by

$$\phi_n(z) = (n+1)\arctan\left(\frac{\lambda z}{\pi {\omega_0}^2}\right) . \tag{3.9}$$

Beam misalignments

Consider now the effect of misalignment of two beams in terms of their normal spatial modes. In order to simplify the argument, the following discussion will concentrate on the effect of misalignments of the two beams at the beam waist, *i.e.* $z = 0$, where the phase fronts of the two beams are plane. From equation 3.6 it can be seen that at the beam waist $U_n(x) = h_n(x)$. Also, since misalignments in only one dimension will be considered, the dependence on x in the expression for $U_n(x)$ will be omitted.

Beam 1 will be defined to be the beam which has the phase modulation applied to it. This beam, which is in the fundamental mode, will define our reference frame. The electric field of this beam can be expressed as $E_1 = A_1 U_0$

Consider now the second beam, which will initially be in the fundamental mode, *i.e.* $E_2 = A_2 U_0$, but will subsequently be misaligned by a small amount with respect to the first beam. The second beam can therefore be expressed in

terms of the normal spatial modes in the frame of reference of the first beam and hence the couplings into the various different modes due to the misalignment can be calculated.

Lateral offsets

Consider first the effect of laterally offsetting beam 2. A purely lateral offset results from the coordinate transformation $x \rightarrow x - d$, where d represents the size of the lateral offset. This is given by

$$E_2 = A_2\, e^{-(x-d)^2/{\omega_0}^2} \; . \tag{3.10}$$

Expanding the exponential term and assuming that d is small compared to ω gives

$$\begin{aligned} E_2 &\simeq A_2 \left(1 + \frac{2dx}{{\omega_0}^2}\right) e^{-x^2/{\omega_0}^2} \\ &= A_2 \left[U_0 + \sqrt{\frac{2}{\pi}}\frac{d}{\omega_0} U_1\right] \; . \end{aligned} \tag{3.11}$$

In other words, a beam which is originally in the fundamental mode and is then laterally offset looks like the original fundamental mode with some first order mode added in-phase with the fundamental. The amount of coupling into the first order mode is directly proportional to the lateral offset, d.

Angular offsets

Consider now the effect of an angular misalignment between the two beams. This can be thought of as introducing a phase dependent term into the expression for E_2, which is proportional to x. A beam which is originally in the fundamental and is angularly offset by an angle α can be expressed as

$$E_2 = A_2\, e^{-x^2/{\omega_0}^2}\, e^{j\left(\frac{2\pi}{\lambda}\right)\alpha x} \; . \tag{3.12}$$

Again the exponential term can be expanded, and for small angles the beam can be written as

$$\begin{aligned} E_2 &\simeq A_2 \left(1 + j\left(\frac{2\pi}{\lambda}\right)\alpha x\right) e^{-x^2/{\omega_0}^2} \\ &= A_2 \left[U_0 + j\alpha\left(\frac{\sqrt{2\pi}\omega_0}{\lambda}\right) U_1\right] . \end{aligned} \tag{3.13}$$

As can be seen, an angular offset also couples proportionately into the first order mode, but this time the coupling is 90° out of phase with the fundamental.

Waist position mismatches

A mismatch in beam curvature can arise if the waist position of beam 2 is displaced by a small amount b in the positive direction along the z axis from the waist position of beam 1. Assuming that the waist sizes in the x-direction are both ω_0, the radius of curvature of beam 2 at the position of the waist of beam 1 (*i.e.* at $z = 0$) will differ slightly from zero and is given by

$$R_2 = b\left[1 + \left(\frac{\pi{\omega_0}^2}{\lambda b}\right)^2\right] . \tag{3.14}$$

The electric field of beam 2 can be written as

$$E_2 = A_2 \exp\left[-\frac{x^2}{{\omega_0}^2} - j\frac{\pi x^2}{\lambda R_2}\right] . \tag{3.15}$$

Expanding the exponential and simplifying the expression gives

$$E_2 \simeq A_2 \left[U_0 - j\frac{\pi{\omega_0}^2}{4\lambda R_2}\{U_2 + U_0\}\right] , \tag{3.16}$$

which, provided $b \ll \frac{\pi{\omega_0}^2}{\lambda}$, can be expressed as

$$E_2 \simeq A_2 \left[U_0 - j\frac{\lambda b}{4\pi{\omega_0}^2}\{U_2 + U_0\}\right] . \tag{3.17}$$

A curvature mismatch is therefore represented by a coupling into the second order mode which is 90° out of phase with the fundamental. A full description of a curvature mismatch would, of course, have an equivalent term in the expansion in the y direction.

Waist size mismatches

The final form of mismatch to be considered is that of a difference in the beam size. Consider the case where beam 2 has a waist size in the x-direction differing by a small amount $\Delta\omega$ from that of beam 1. The electric field of beam 2 can be written as

$$E_2 = A_2 e^{-x^2/(\omega_0+\Delta\omega)^2} , \tag{3.18}$$

which can be expanded and simplified to give

$$\begin{aligned} E_2 &\simeq A_2 \left[U_0 + \frac{\Delta\omega}{2\omega_0}\{U_2 + U_0\} \right] \\ &\simeq A_2 \left[U_0 + \frac{\Delta\omega}{2\omega_0} U_2 \right] . \end{aligned} \tag{3.19}$$

Clearly then, a mismatch in the waist size gives a coupling into the second order mode which is in-phase with the fundamental. Once again a full description of a size mismatch would have an equivalent term in the expansion in the y direction.

Summary

The various errors considered are all simply described as in-phase or quadrature couplings into the first or second order spatial modes (provided that the errors are sufficiently small). The following discussion focuses on how signals proportional to these mismatches can be deduced from observations of the interference between the two electric fields E_1 and E_2.

3.3.3 Signal Detection

Beam 1 can be expressed as $E_1 = A_1 a_0 U_0$ where the complex number a_0 includes the time dependence of the field, the effect of the differential phase modulation, and any static phase difference with respect to the fundamental mode component of beam 2. If the phase modulation is given by $m(t)$ then a_0 can then be written as

$$a_0 = e^{j(\omega t + m(t) + \Phi)} , \tag{3.20}$$

where ω is the angular frequency of the light, and Φ is the relative phase difference between the fundamental mode components of the two beams.

Similarly beam 2, the unmodulated but mismatched beam, can be expressed as

$$E_2 = A_2 \left[b_0 U_0 + b_1 U_1 + b_2 U_2 \right] \ , \tag{3.21}$$

where the coefficients b_n are complex and depend on the type and magnitude of the mismatch between the two beams, and also on the distance z from the waist position of beam 1. The coefficients b_n can be written in a general way as

$$b_n = r_n e^{j\theta_n} e^{j[\omega t + \phi_n(z)]} \ , \tag{3.22}$$

where the r_n and θ_n are determined by the mismatches and $\phi_n(z)$ is the phase differences that evolves between the fundamental and the nth mode as the beams propagate along the z axis. From equation 3.9 it can be seen that

$$\phi_n(z) = n \arctan\left(\frac{\lambda z}{\pi {\omega_0}^2}\right) \ . \tag{3.23}$$

For the four mismatches considered earlier $r_0 \sim 1$ and $\theta_0 = 0$. It has also been shown that for misalignments in tilt $\theta_1 = \frac{\pi}{2}$ and in translation $\theta_1 = 0$; in both these cases $r_1 \ll 1$ and $r_2 = 0$. For mismatches in waist position $\theta_2 = \frac{\pi}{2}$ and in waist size $\theta_2 = 0$, with $r_1 = 0$ and $r_2 \ll 1$ in both cases.

It is now straightforward to compute the resulting interference pattern. The resultant field E is given by

$$E = E_1 + E_2 = (a_0 A_1 + b_0 A_2) U_0 + b_1 A_2 U_1 + b_2 A_2 U_2 \tag{3.24}$$

and the intensity is just proportional to EE^*. Coherent detection at the modulation frequency is used to process the signals from photodiodes looking at the interference pattern and therefore only terms in the expansion of EE^* that contain a_0 or ${a_0}^*$ can contribute. Extracting such terms gives

$$\begin{aligned} [EE^*]_{\text{mod}} &= {U_0}^2 A_1 A_2 \left[b_0 {a_0}^* + {b_0}^* a_0 \right] \\ &+ U_0 U_1 A_1 A_2 \left[b_1 {a_0}^* + {b_1}^* a_0 \right] \\ &+ U_0 U_2 A_1 A_2 \left[b_2 {a_0}^* + {b_2}^* a_0 \right] \ . \end{aligned} \tag{3.25}$$

The terms of the form $[b_n a_0^* + b_n^* a_0]$ can be written as

$$[b_n a_0^* + b_n^* a_0] = 2r_n \cos\left[m(t) + [\Phi - \theta_n - \phi_n(z)]\right] \ , \tag{3.26}$$

which can be expanded to the form

$$2r_n \left[\cos m(t) \cos \Psi_n + \sin m(t) \sin \Psi_n\right] \ , \tag{3.27}$$

where $\Psi_n = [\Phi - \theta_n - \phi_n(z)]$. Assuming that the modulation depth is small (*i.e.* ($|m(t)| \ll 1$)) then the component at the modulation frequency is simply proportional to $r_n m(t) \sin \Psi_n$.

We therefore have three different components of the resultant field that contain spatially dependent amplitude modulation. Detection of the intensity of the signal produced due to the interference pattern using single, rectangularly split or annularly split photodiodes will provide different sensitivities to combinations of these components.

Detection using a single photodiode

The modulated light intensity I_m that results when the combined beam is incident on a single photodetector is proportional to the integral of $[EE^*]$ over the photodiode area, and provided the detector area is large compared to the beam size the limits of integration are effectively $\pm\infty$. (In our one-dimensional treatment the integral is simply evaluated along the x-axis.) Orthogonality of the modes of propagation ensures that no net contribution to the integral results from terms involving U_0U_1 or U_0U_2. The modulated intensity can therefore be expressed as

$$I_m \ \propto \ m(t)\, A_1\, A_2 \sin \Phi \ . \tag{3.28}$$

For maximum sensitivity to small changes in Φ the interferometer path difference is normally adjusted so that the mean value of Φ is a multiple of π. Optimum signal-to-noise ratio is obtained when this condition is met and when the standing light power on the photodetector is at a minimum, so in practice an interferometer

is usually locked on a null fringe for which $\Phi = \pi$, a condition that will be assumed in the following discussions. This is simply the conventional differential phase modulation technique for obtaining an error signal proportional to small offsets from the null setting.

Detection using a rectangularly split photodiode

Consider now the result of using a split photodetector, divided along the y-axis, to view the interference pattern. (Again it will be assumed that the entire area of the beam is intercepted by one or other of the detectors.) If the combined beam is incident symmetrically on the split photodiode and if the outputs of the two detectors are differenced, the effective modulated light intensity I_m can be deduced from

$$I_m \propto \int_0^\infty [EE^*]dx - \int_{-\infty}^0 [EE^*]dx \ . \tag{3.29}$$

Only odd functions can provide a net contribution, so

$$\begin{aligned} I_m &\propto r_1\, m(t)\, A_1\, A_2 \sin \Psi_1 \\ &= r_1\, m(t)\, A_1\, A_2 \sin\left[\theta_1 + \phi_1(z)\right] \ . \end{aligned} \tag{3.30}$$

In general, therefore, the demodulated signal will be a measure of some combination of tilt and translational errors. It is straightforward to see that the signal resulting from a given tilt error ($\theta_1 = \frac{\pi}{2}$) will be proportional to $\cos[\phi_1(z)]$, giving a maximum response at the position of the waist ($z = 0$), while the signal produced by a translational error ($\theta_1 = 0$) will be proportional to $\sin[\phi_1(z)]$, yielding maximum sensitivity in the far-field $\left(z \gg \frac{\pi {\omega_0}^2}{\lambda}\right)$ where $\phi_1(z) = \frac{\pi}{2}$.

These results can also be derived from simple geometrical considerations.

For the case of an angular misalignment it is clear that a signal can be detected at the location of the beam waist where the phasefronts are plane. However, as the beams propagate to a large distance $d \gg \frac{\pi {\omega_0}^2}{\lambda}$ from the waist, the radius of curvature of the phasefronts will approximate d for both beams. There will thus be no phase gradient across the combined beam and hence no signal will result.

A lateral offset of one beam will cause no phase gradient at the position of the beam waists and hence no signal will result from a split photodiode measurement at that location. At large distances from the waist the phasefronts of the two beams will have the same curvature, but because of the lateral displacement the phasefronts of one beam will exhibit a net lead above the x-axis while below the axis they will lag. Detection using a split photodiode therefore does yield a signal. Once into the far-field region the signal size becomes approximately independent of distance along the z-axis; although the curvature $\left(\frac{1}{R}\right)$ of the phasefronts continues to decrease, the beam width increases at the same rate and so the detected phase difference will remain constant.

Detection using an annularly split photodiode

Consider now looking at the interference pattern with a split diode comprising a circular centre region of radius r and a separate surrounding annular region. If the combined beam is centred and if the signals from the two sections are differenced, then, in our one-dimensional example, the effective modulated light intensity will be given by

$$I_m \propto \int_{-\infty}^{-r} [EE^*]dx + \int_{r}^{\infty} [EE^*]dx - \int_{-r}^{r} [EE^*]dx \ , \tag{3.31}$$

provided the beam width is greater than r and the outer radius of the annular region is much greater than the beam width.

From symmetry considerations only even functions appearing in EE^* can provide a net contribution. It follows that

$$\begin{aligned} I_m &\propto r_2\, m(t)\, A_1\, A_2 \sin \Psi_2 \\ &= r_2\, m(t)\, A_1\, A_2 \sin\left[\theta_2 + \phi_2(z)\right] \ , \end{aligned} \tag{3.32}$$

where

$$\phi_2(z) = 2 \arctan\left(\frac{\lambda z}{\pi {\omega_0}^2}\right) \ . \tag{3.33}$$

Here it is clear that the demodulated signal will have a maximum response to a beam curvature mismatch ($\theta_2 = \frac{\pi}{2}$) at the position of the waist of the reference

beam and also when $z \gg \frac{\pi\omega_0^2}{\lambda}$. Sensitivity of the measurement to an error in relative waist size ($\theta_2 = 0$) will be at a maximum when $\phi_2(z) = \frac{\pi}{2}$ which occurs when $z = \frac{\pi\omega_0^2}{\lambda}$.

Once again these results may be understood from simple geometrical arguments.

A signal can only be detected when the curvatures of the phasefronts at the position of the split photodiode are different. When there is a small mismatch in curvature it is clear that the split diode will respond when placed at the waist of the reference beam. As the two beams propagate, however, there is always a value of z at which they will have the same curvature and hence a position at which the differential measurement will yield no signal. It is straightforward to show in general that if the relative waist displacement is b, then the curvatures are equal when $z = \left[\frac{\pi\omega_0^2}{\lambda} + \frac{b}{2}\right]$. As $z \rightarrow \infty$ the curvatures will always be different and a signal will once again become detectable. Looking at the phase difference between the two beams at, say, $x = \omega$ it is found that the phase difference tends to a constant value of $\frac{b\lambda}{\pi\omega_0^2}$ radians.

If the original mismatch is in beam size there is clearly no signal detectable if the split photodiode is placed at the (common) waist position. As the beams propagate, they expand at different characteristic rates, and hence their curvatures become different giving rise to a detectable signal. As $z \rightarrow \infty$ the two radii of curvature both tend to z, reducing the detection sensitivity for this kind of error to zero. The maximum response therefore occurs at an intermediate distance.

When using this type of split photodiode some care has to be taken to choose the dimensions of the diode segments to suit the size of the beam. The relevant integral that determines the signal coupling is

$$\int_r^\infty U_0 U_2 dx - \int_0^r U_0 U_2 dx \ . \tag{3.34}$$

Since $U_0 U_2 = (4\frac{x^2}{\omega^2} - 1)e^{-2x^2/\omega^2}$, the largest signal will result when $\int_r^\infty$ is maximally positive and $\int_0^r$ is maximally negative. This will occur when $4\frac{r^2}{\omega^2} = 1 \Rightarrow r = \frac{\omega}{2}$. It can be shown that greater than 70% of the maximum possible signal will be obtained provided $\frac{\omega}{4} \leq r \leq \frac{3\omega}{4}$.

3.3.4 Positional offsets of photodiodes

It is important to consider the effect on the various error signals of small movements of the interference pattern away from the symmetrical positions on the detection photodiodes. When using a single photodiode there is, of course, negligible dependence of the error signal provided the photodiode response is uniform and the beam remains within its active area. However one might expect some variation in the error signals derived using rectangularly and annularly split photodiodes.

Consider the signal sensed using a rectangularly split photodiode. If the photodiode is offset a small amount d from the centre of the interference pattern then the signal sensed

$$I_m \propto \int_d^{\infty} [EE^*]dx - \int_{-\infty}^{d} [EE^*]dx \ , \tag{3.35}$$

which can be rewritten as

$$I_m \propto m(t)\left[r_1 A_1 A_2 \left[\int_0^{\infty} U_0U_1dx - \int_0^{d} U_0U_1dx\right] - r_2 A_1 A_2 \int_0^{d} U_0U_2dx\right] \ , \tag{3.36}$$

where it has been assumed that the term involving $\int_0^d {U_0}^2 dx$ has been driven to zero by a servo system controlling the path difference between the interfering beams.

The introduction of an offset in the position of the photodiode is thus seen to cause a small reduction in the size of the signal detected due to an angular or lateral misalignment, together with the coupling in of a small amount of signal proportional to mismatches in beam curvature and size.

Similarly, when using an annularly split photodiode, the signal detected due to beam curvature and size mismatches will be slightly reduced by a positional offset of the photodiode, and a small amount of signal due to any angular or lateral misalignments will couple in.

However, provided in each case that the desired signal dominates over the contaminating one, optimum alignment will be achieved once servos for all degrees of freedom (angular and lateral misalignments and mismatches in the beam curvature and size) are simultaneously operative.

3.3.5 Information derived from the first harmonic of the modulation frequency

Another important point to note is that it is in principle possible to use the first harmonic of the modulation frequency to determine full alignment information from a single photodiode. As an example consider the use of a rectangularly split photodiode to determine the lateral and angular offsets of the interfering beams. In this case the effective modulated intensity in this case is given by

$$I_m \propto r_1\, m(t)\, A_1\, A_2\, (\cos m(t) \cos \Psi_1 + \sin m(t) \sin \Psi_1)\ . \tag{3.37}$$

If $\cos m(t)$ is expanded terms are obtained at twice the modulation frequency, since $\cos m(t) \simeq 1 - \frac{m^2(t)}{2}$ for small modulation depths, and hence information which is orthogonal to that derived from the signal detected at the modulation frequency can be obtained by looking at the component of the intensity at twice the modulation frequency. One could therefore in principle gain full alignment information about the angular and lateral offsets of the two beams using a single photodiode. In practice, however, small offsets of the photodiode with respect to the interference pattern would allow other signals to couple in at twice the modulation frequency, in particular a signal which is proportional to ${U_0}^2$. Since only small misalignments of the interfering beams are being considered this term is liable to dominate over those present at the first harmonic even for very small offsets of the split photodiode.

One possible solution to this problem would be to use some kind of multi-element detector such as a CCD array or a scanning camera to map the amplitudes of the fundamental and first harmonic intensity modulation over the beam profile. Computer analysis of the resulting data could then produce the required signals. However the size of the signal due to a lateral offset obtained from observations at the first harmonic will be intrinsically small since it is proportional to $|m^2(t)|$ where $|m(t)|$ is typically $\ll 1$. Together with its inherent complexity this relative insensitivity may limit the applicability of this approach.

3.3.6 The use of lenses

It has been shown that it is possible to detect relative lateral offsets and errors in beam size using the differential phase sensing technique, by placing split photodiodes at suitable distances away from the beam waist. The propagation from the beam waist introduces the required phase shift between the fundamental and the first and second order modes.

However, for relatively large beam waists this may require placing a photodiode several meters away from the waist. For example, for $\omega_0 = 10^{-3}$ m and $\lambda = 514$ nm, the photodiode must be placed ~ 5 m away from the waist in order to detect $\sim 50\%$ of the maximum signal possible due to a lateral offset.

It is possible to shorten this path length by placing a system of lenses very close to the original waist, and viewing the interference pattern after the lenses. To illustrate the technique consider a lens system that provides sensitivity to lateral offsets, *i.e.* one that causes a phase shift between the fundamental and first order modes of 90° to develop over a reasonably compact distance. A similar approach can be used to design a system suitable for sensing errors in relative beam size, where it is the phase difference between the fundamental and second order modes that must be made close to 90°.

One possible set up is that shown previously in figure 3.5. Here a lens is placed near to the position of the beam waist of two laterally offset beams. A new waist is formed very close to the focal point of the lens. At this point the phase fronts are plane and angularly misaligned. Therefore if the split photodiode is placed at this point a signal is detected which is directly proportional to the angular offset of the two beams. The lens has effectively introduced a phase shift of 90° between the first order and fundamental modes between the two waists.

Having said this, care must be taken to avoid making ω_2 too small. Not only does this make the detection of a signal difficult using a split photodiode (since the 'split' in the photodiode must be much smaller than ω_2), but also, if the photodiode is not placed exactly at the beam waist, then the signal sensed will decrease by $\cos[\phi(z)]$. For a small beam waist (*e.g.* $\omega_0 = 10^{-4}$m) most of the signal can be lost over a distance of only a few mm. In practice it is possible to

use a more complicated arrangement of lenses, such as the system discussed later in section 3.5.2, to avoid these difficulties (a more detailed discussion can be found in Morrison *et al.* [49]).

3.3.7 Signal mixing and feedback

It has been shown that in principle it is possible to detect angular and lateral offsets of two interfering beams using a differential phase sensing technique. Two split photodiodes (one of which has a lens, or series of lenses placed in front of it) can be used to detect these two types of misalignment which fully describe the alignment mismatch of two beams. In a practical situation however it is likely that the signal obtained from each sensing arrangement will be a linear combination of the angular and lateral offsets of the two beams. The two signals can be expressed as

$$S_1 = B_1\alpha + C_1 d \tag{3.38}$$

$$S_2 = B_2\alpha + C_2 d\,, \tag{3.39}$$

where B_1 and B_2 represent the proportion of each signal which is due to the angular offset, α, of the two beams, and C_1 and C_2 the proportion of each signal which is due to the lateral offset, d. The angular and lateral offset signals can be derived from signals S_1 and S_2 by correctly mixing these two signals together. In a matrix formalism this can be expressed as

$$\begin{bmatrix} S_1 \\ S_2 \end{bmatrix} = \begin{bmatrix} B_1 & C_1 \\ B_2 & C_2 \end{bmatrix} \begin{bmatrix} \alpha \\ d \end{bmatrix} . \tag{3.40}$$

It follows that $\begin{bmatrix} B_1 & C_1 \\ B_2 & C_2 \end{bmatrix}^{-1}$ represents the 'mixing matrix' required to deduce α and d from signals S_1 and S_2.

Consider now feeding back signals to control the alignment of two mirrors in the interferometer. A signal P_1 fed back to one of the mirrors will, in general, cause

the two beams at the output of the interferometer to be misaligned in angle by an amount D_1 and laterally by an amount E_1. Similarly a signal P_2 fed back to control the alignment of the other mirror will cause angular and lateral misalignments proportional to D_2 and E_2. In matrix terms

$$\begin{bmatrix} P_1 \\ P_2 \end{bmatrix} = \begin{bmatrix} D_1 & E_1 \\ D_2 & E_2 \end{bmatrix} \begin{bmatrix} \alpha \\ d \end{bmatrix} . \tag{3.41}$$

In order to correctly mix S_1 and S_2 so that they can be sensibly fed back to the mirrors in the interferometer, correct 'mixing algebra' needs to be performed. If $S_m = \begin{bmatrix} B_1 & C_1 \\ B_2 & C_2 \end{bmatrix}$ and $F_m = \begin{bmatrix} D_1 & E_1 \\ D_2 & E_2 \end{bmatrix}^{-1}$ then the overall feedback system can be expressed as

$$\begin{bmatrix} \alpha \\ d \end{bmatrix} \overset{S_m}{\longrightarrow} \begin{bmatrix} S_1 \\ S_2 \end{bmatrix} \overset{M_m}{\longrightarrow} \begin{bmatrix} P_1 \\ P_2 \end{bmatrix} \overset{F_m}{\longrightarrow} \begin{bmatrix} \alpha \\ d \end{bmatrix} . \tag{3.42}$$

The correct mixing of S_1 and S_2 to provide sensible signals which can be fed back to the two mirrors in the interferometer is given by

$$M_m = S_m^{-1} F_m^{-1} . \tag{3.43}$$

This mixing can be done electronically, or by suitably arranging the positions of the split photodiode and lens arrangements such that

$$S_m^{-1} F_m^{-1} = I , \tag{3.44}$$

where I is the multiplicative identity matrix.

A similar analysis can be carried out to deal with the signal mixing and feedback required to control any beam size and curvature mismatch.

3.3.8 Shot noise limited sensitivity of technique

The shot noise limit to the sensitivity of differential phase modulation as a technique for sensing the phase difference between two interfering beams has been discussed by Niebauer *et al.* [50] and by Meers and Strain [51]. Using their results, the shot noise limited signal to noise ratio for a small signal s, representing a phase difference between two interfering beams, and for a laser power I_0, is given by

$$(S/N)^2 = \frac{I_0\, s^2 F^2}{2\hbar\omega_L\, \Delta f} \quad , \tag{3.45}$$

where ω_L is the angular frequency of the laser light, Δf is the measurement bandwidth and F is determined by the efficiency of the modulation/demodulation scheme and can take a value in the range $0 \rightarrow 1$.

For example, consider an angular misalignment, α, of the two beams. Substituting for the signal s, the expression

$$s = \frac{\sqrt{2\pi}\omega_0 \alpha}{\lambda} \quad , \tag{3.46}$$

gives a limit to the sensitivity of the detection technique of

$$\alpha^2 > \frac{\hbar\omega_L \lambda^2 \Delta f}{I_0 {\omega_0}^2 \pi F^2} \quad . \tag{3.47}$$

For example if $I_0 = 10^{-3}\,\mathrm{W}$, $\omega_0 = 10^{-3}\,\mathrm{m}$, $\lambda = 514\,\mathrm{nm}$, and if $F = \sqrt{\frac{2}{3}}$ corresponding to the case of sinusoidal modulation and demodulation, then the resulting shot noise limit is

$$\alpha > 7 \times 10^{-12}\,\mathrm{rads}/\sqrt{\mathrm{Hz}} \; . \tag{3.48}$$

For a lateral offset, a, between the two beams, the signal s is given by

$$s = \sqrt{\frac{2}{\pi}}\frac{a}{\omega_0} \quad , \tag{3.49}$$

which gives a shot noise limit of

$$a^2 > \frac{{\omega_0}^2 \pi \hbar \omega_L\, \Delta f}{I_0\, F^2} \; . \tag{3.50}$$

Using the parameters given above gives

$$a > 4 \times 10^{-11} \mathrm{m}/\sqrt{\mathrm{Hz}} \, . \tag{3.51}$$

Similar calculations can be performed to estimate the shot noise limit for detecting beam curvature and size mismatches. The calculation may also be extended to include the case of alignment of the mirrors in a resonant optical cavity by suitably modifying the factor F according to the characteristics of the cavity [50].

3.3.9 Alignment signal for a cavity resonating in higher order modes

When using a resonant optical cavity it is often possible to lock the cavity so that higher order spatial modes are resonant and not, as is usually the case, the fundamental. It is interesting to calculate what sort of signal an alignment system based on the differential phase sensing technique would give in such a situation. In the following discussion this will be carried out for a cavity locked in the first order mode, although in principle the calculation could be performed for any of the higher order spatial modes.

In order to see what happens consider the input light which is directed towards the cavity as being tilted by an angle α with respect to the cavity axis. Concentrating on the spatial characteristics of this beam, then in one dimension the amplitude of the electric field of the beam is proportional to

$$e^{-\frac{X^2}{2}} \, e^{j\gamma X} \, , \tag{3.52}$$

where $\gamma = \frac{\sqrt{2}\pi}{\lambda} \omega_0 \, \alpha$. This expression can be written in terms of all the possible normal spatial modes of the beam since from [52]

$$e^{-\frac{X^2}{2}} \, e^{j\gamma X} = e^{-\frac{\gamma^2}{4}} \sum_{k=0}^{\infty} \frac{\left(\frac{j\gamma}{2}\right)^k}{k!} H_k(X) \, e^{-\frac{X^2}{2}} \, , \tag{3.53}$$

and $H_n(X)$, the nth order Hermite polynomial is directly proportional to the nth order spatial mode. The amount of light which can be considered to be in the first

order mode is therefore directly proportional to

$$\frac{j\gamma}{2} e^{-\frac{\gamma^2}{4}} . \tag{3.54}$$

This goes through a maximum when $\gamma = \pm\sqrt{2}$. Therefore, if a resonant cavity is locked in the first order mode, the coupling of the input beam into this mode is maximised for a tilt angle of $\alpha = \pm\frac{\lambda}{\pi\omega_0}$.

The alignment signal can also be calculated as a function of γ, with the cavity locked in the first order mode. The two interfering beams which are viewed in reflection off the cavity consist of the directly reflected input light whose amplitude in terms of γ and X is just proportional to

$$e^{-\frac{X^2}{2}} e^{j\gamma X} , \tag{3.55}$$

and the light leaking out of the cavity on resonance. Now since the cavity is locked in the first order mode the amplitude of the electric field leaking out of the cavity in terms of γ and X, from equation 3.53, is proportional to

$$e^{-\frac{\gamma^2}{4}} \frac{j\gamma}{2} 2X\, e^{-\frac{X^2}{2}} . \tag{3.56}$$

The alignment signal which is sensed using the differential phase sensing method is given by difference of the product of these two expressions integrated over each half of the split photodiode (see section 3.3.3). The alignment signal is therefore proportional to

$$\int_0^\infty e^{j\gamma X} \left(j\gamma X\, e^{-\frac{\gamma^2}{4}}\right) e^{-X^2}\, dx \; - \int_{-\infty}^0 e^{j\gamma X} \left(j\gamma X\, e^{-\frac{\gamma^2}{4}}\right) e^{-X^2}\, dx \; . \tag{3.57}$$

This can be simplified and is proportional to

$$\int_0^\infty X \cos(\gamma X) e^{-X^2} dx \; . \tag{3.58}$$

This is a known integral and its solution is (see *e.g.* [52])

$$\frac{1}{2} - \frac{\gamma}{4} \sum_{k=0}^{\infty} \frac{(-1)^k k!}{(2k+1)!} \gamma^{(2k+1)} . \tag{3.59}$$

This function does not give an error signal which is 0 for $\gamma = 0$ *i.e.* the auto alignment signal would not steer the mirrors of the cavity (or the input laser beam) so that the alignment was optimised for the fundamental. It does however give a bi-polar error signal which will cause the system to align towards a particular value of γ. This value can be determined by solving the following equation

$$\frac{\gamma}{4} \sum_{k=0}^{\infty} \frac{(-1)^k k!}{(2k+1)!} \gamma^{(2k+1)} = \frac{1}{2} . \tag{3.60}$$

This equation was solved numerically giving $\gamma = \pm 1.85$.

Therefore this alignment technique does not optimise for the first order mode or the fundamental when the cavity is resonating in the first order mode.

3.4 Experimental demonstration of an automatic alignment system using a simple benchtop Michelson interferometer

As an initial test of the automatic alignment technique described in the previous sections it was decided to try out the method on a simple benchtop Michelson interferometer.

As explained in section 3.2, in an equal path length Michelson the two beams as viewed at the output of the interferometer can only be misaligned in angle. A single quadrant photodiode sensing angular offsets in two orthogonal directions (tilt and rotation of the beams) is all that is required to fully determine the relative misalignments of the two interfering beams. This helped to simplify the experimental set up so that the basic principles of the differential phase gradient sensing technique could be tested.

3.4.1 Experimental layout

Figure 3.8 shows a schematic layout of the apparatus, showing the alignment control system. The interferometer was mounted on a large aluminium optical table. All of the mirrors, beamsplitter, laser and photodiode sensors were rigidly mounted on the table, except for one of the end mirrors. This was mounted on a cylindrical aluminium mass which was suspended as a pendulum from a support structure mounted on the optical table. Small permanent magnets were attached to the back of the aluminium mass and, by driving a current through three coils mounted on a backplate fixed to the optical bench, the mass could be controlled in three degrees of freedom - tilt, rotation, and longitudinal. (Note: sideways damping of the mass was also required and was done using a separate coil/magnet system mounted on the side of the suspended mass.)

The aluminium mass was damped locally to ground in order to allow crude alignment of the interferometer. Shadow sensors, fitted inside the coil formers, sensed the motion of the suspended mass. In each sensor, a flag attached to the test mass intercepts a beam of light emitted from an LED directed towards

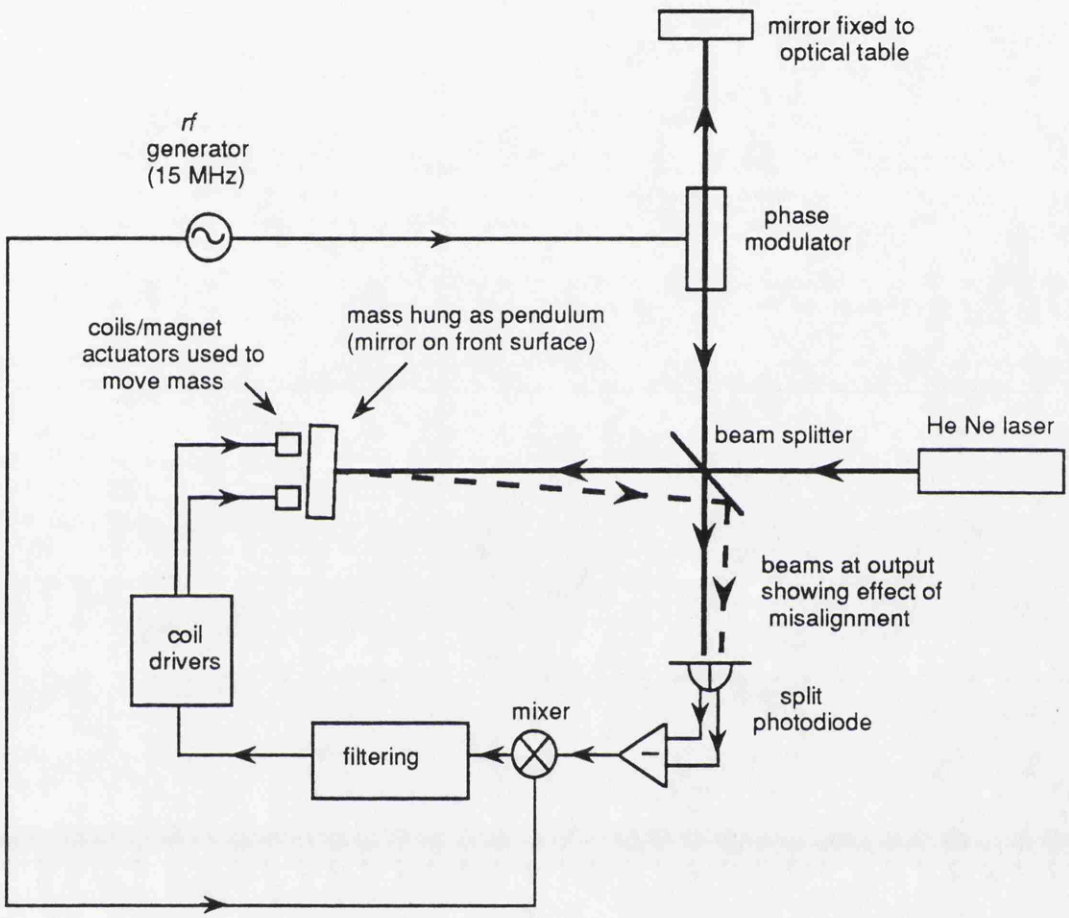

Figure 3.8: *Schematic layout of simple Michelson interferometer and the main elements of the control system used for auto alignment in one degree of freedom.*

a photodiode. Motion of the test mass is sensed as a change in the photocurrent through the photodiode. The shadow sensors were arranged such that tilt, rotation, longitudinal and sideways motion of the mass could be sensed. These signals were then fed back to the coil/magnet actuators allowing the mass to be locally damped in all four degrees of freedom. Adjustable DC currents through the coils allowed manual alignment of the two interfering beams at the output.

3.4.2 Operation of the interferometer

The interferometer, after some initial alignment, was locked onto a dark fringe at its output. This was done using the differential phase modulation technique described in section 3.3.3 which allowed the relative phase of the two beams at the output to be measured. A Pockels cell was placed in one arm of the interferometer and phase modulation applied to the light in this arm at a frequency of 15 MHz. The intensity of the interference pattern was detected using a photodiode and the resulting signal demodulated at the modulation frequency. After some electronic filtering required to give the servo sufficient gain to acquire and maintain lock, this signal was fed back to the coil/magnet actuators which push longitudinally on the suspended mirror, allowing the interferometer to be locked onto a dark fringe.

With the main locking system in operation, the automatic alignment system could then be implemented.

Some of the output light was directed towards a quadrant photodiode, the interference pattern being roughly centered on the photodiode by monitoring the DC signals from each quadrant. By subtracting the signals sensed on opposing sides of the centre of the quadrant photodiode, it was possible to obtain information on the misalignment of the two interfering beams at the output of the interferometer in two orthogonal directions. These signals, after demodulation and some low pass filtering, were then fed back to the tilt and rotation actuators controlling the suspended mirror, so allowing optimum alignment of the interfering beams. The tuned photodiode front end is shown in figure 3.10.

3.4.3 Performance of the system

After crude alignment of the system using the local DC controls acting on the suspended mirror, the interferometer could be locked onto a dark fringe. Switching on both alignment feedback systems (*i.e.* tilt and rotation) resulted in the expected optimisation of fringe visibility confirming that the system was indeed aligning itself. In fact, with the automatic alignment system in operation, controlling the tilt and rotation of the suspended mirror, the local control tilt and rotation systems could be switched off and the interferometer would remain stably locked.

Both the tilt and rotation control systems were designed to have unity gain between 80 and 100 Hz and an open loop gain of > 40 dB below 1 Hz. This was confirmed experimentally by injecting a test signal into the feedback electronics and measuring the response of the closed loop system.

3.5 Experimental demonstration of an automatic alignment system on a 10 m long suspended optical cavity

Following on from the successful demonstration on a simple benchtop Michelson interferometer of an automatic alignment system based on the differential phase sensing method, it was decided to implement the technique on one of the suspended 10 m long optical cavities which forms part of the prototype gravitational wave detector here in Glasgow (a detailed description of which is given in Chapter 4).

The cavity is locked using the standard *rf* reflection locking technique [53]. In such a situation, the two interfering beams of interest are the directly reflected light from the input mirror and the light which leaks out of the cavity on resonance. Differential phase modulation is achieved by phase modulating the light which is directed towards the cavity. The component which is directed reflected retains the modulation whereas the light leaking out of the cavity on resonance has no modulation (since the sidebands are not resonant in the cavity).

As mentioned in section 3.2, misalignment of the suspended cavity mirrors can cause both angular and lateral misalignments of these two interfering beams. The automatic alignment system described here enabled the ideas on sensing of lateral offsets, signal mixing and electronic feedback methods discussed in previous sections to be tested on a fully suspended interferometer.

No attempt was made however to control any mismatches in the beam size or curvature.

3.5.1 Experimental set up

The 10 m cavity used to demonstrate the automatic alignment system consists of two high quality dielectric supermirrors suspended as pendulums (to give some isolation from seismic noise) and situated inside a vacuum system. The mirrors were coated directly onto cylindrical fused silica test masses; 5 inches diameter, 4 inches long and having a mass of about 3 kg. The input mirror had a transmission of 500 ppm in intensity and was plane. The rear mirror, which was of maximum

reflectivity, had a radius of curvature of about 15 m. The waist of the cavity is situated at the surface of the input mirror and is $\sim$ 1 mm. Typically, during the operation of the automatic alignment tests the fringe visibility was quite poor – around about 30%, limited by excess loss in the cavity due to contamination of the mirrors. The finesse of the cavity was around about 3000.

In operation, the laser light (provided by a *cw* argon ion laser – wavelength 514 nm) is phase modulated at 12 MHz using a Pockels cell and directed towards the cavity through a polarising beamsplitter and a quarter wave plate. This ensures that the light impinging on the cavity is circularly polarised. The reflected light is circularly polarised in the opposite direction and is therefore rejected from the polarising beamsplitter after passing back through the quarter wave plate and can be detected using one or more photodiodes. Demodulating the signal detected from a single photodiode at the modulation frequency gives a signal directly proportional to the offset of the cavity from resonance (provided the offset is small). By feeding back suitable signals to control the axial position of the mirrors which form the cavity, or, as is done on this particular cavity, feeding back signals to control the frequency of the laser light, the system can be locked so that the light resonates in the cavity.

3.5.2 Optical arrangement of the automatic alignment system

The optical arrangement of the system and some of the sensing and mixing electronics is shown schematically in figure 3.9. Two quadrant photodiodes were used to provide alignment information in two orthogonal directions. Figure 3.10 shows a schematic diagram of the front end electronics for one dimension of the photodiodes. The two diodes, representing the two halves of the quadrant photodiode, are used as part of a tuned circuit designed to be resonant at the modulation frequency, 12 MHz. Both diodes are connected in series with the primary winding on a transformer. The signal obtained from the secondary winding conveniently represents the difference signal from the two halves of the quadrant photodiode.

By examining the interference pattern in reflection using the first quadrant

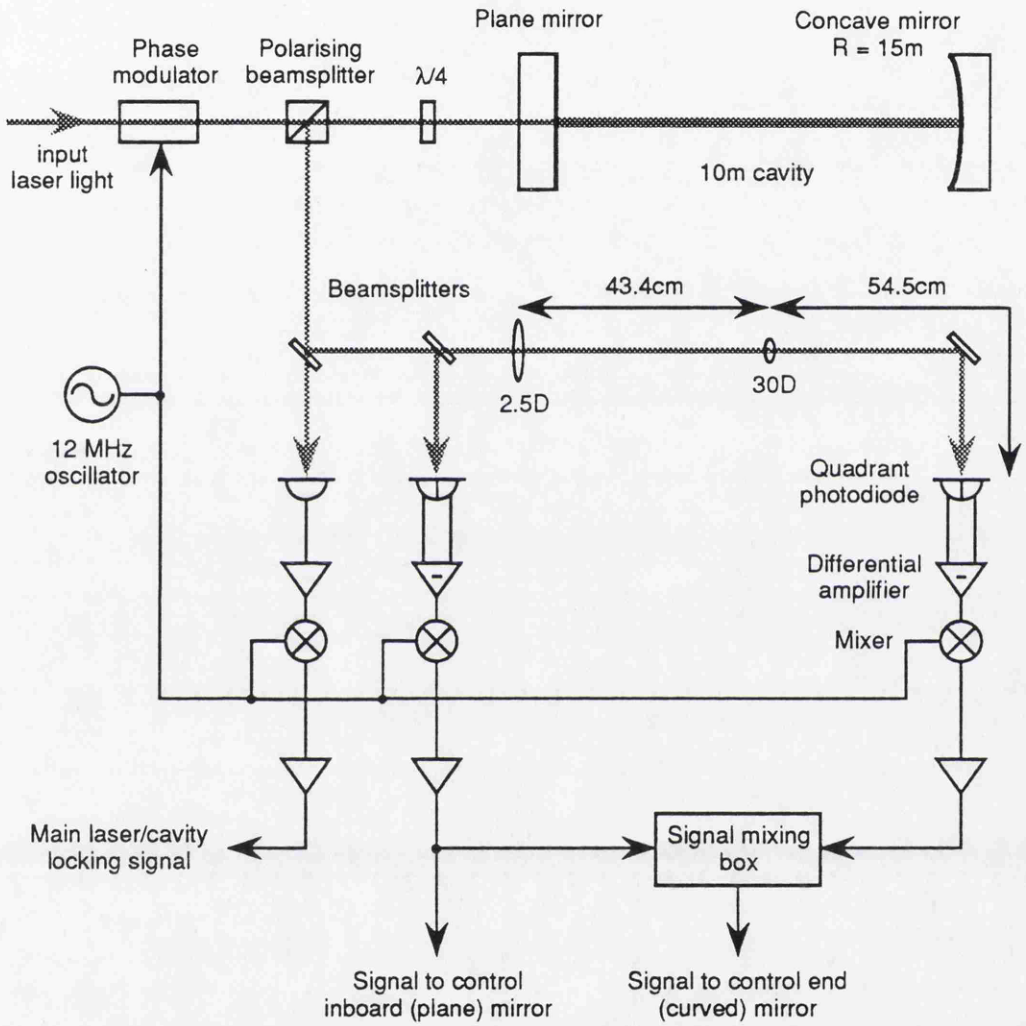

Figure 3.9: *Schematic layout of 10 m suspended optical cavity and the main elements of the control system used for auto alignment in one degree of freedom.*

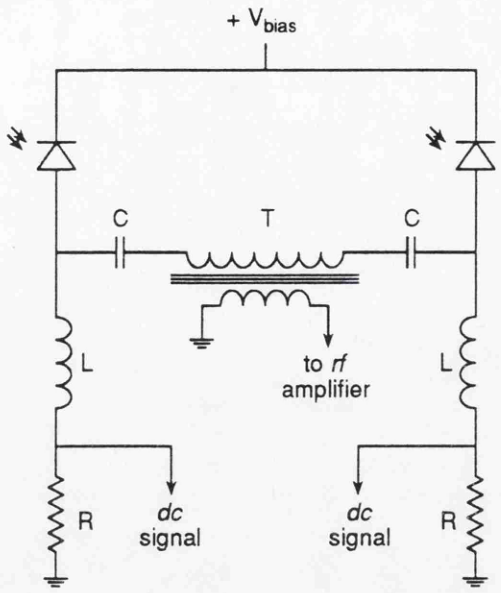

Figure 3.10: *Schematic diagram showing one dimension of a tuned front end.*

photodiode shown in the diagram, the angular misalignment of the two beams can be determined (since this photodiode is reasonably close to the waist). This signal can depend only on the misalignment of the input mirror and so can be directly fed back (after suitable filtering) to control the orientation of the mirror.

In order to sense the lateral misalignments of the two beams, a series of lenses was used. In theory, the second photodiode could simply be placed a sufficiently large distance away from the sensing position of the first photodiode. However in practice this is not really possible since, in order to introduce a sufficient phase shift between the first order and fundamental mode necessary to allow the detection of a lateral offset (see section 3.3.3), the photodiode would have to be placed several meters away from the beam waist. In order to reduce this distance, a single lens could be used, with the photodiode placed at the focal point of the lens. However, reasonably short focal lengths, $< 1\,\mathrm{m}$, need to be used in order to keep the physical size of the optical system manageable. Even for a focal length of 1 m, the spot size at the waist is $\sim 100\,\mu\mathrm{m}$ for an input spot size of 1 mm. With quadrant photodiodes whose segments are separated by $\sim 200\,\mu\mathrm{m}$, this is just too small to be able to sensibly position the interference spot onto the centre of the photodiode without having the additional complication of using an extra servo to do this. In addition to this, most of the light would fall on the split between the photodiode

segments and would not be detected. In practice a multiple lens system was used which was relatively compact in size ($\sim$ 1 m in length) which could give a phase shift of $\sim 20°$ between the first order and fundamental modes and keep the spot size about 1 mm on the quadrant photodiode. The lens system used is shown in figure 3.11. In theory it should be possible to design a lens system which can give

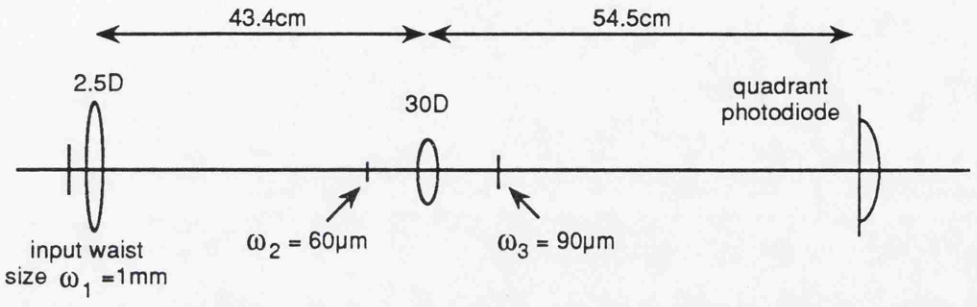

Figure 3.11: *The series of lenses used to allow some sensing of the lateral misalignment of the two interfering beams.*

a full 90° phase shift between the fundamental and first order modes. However the system used here appeared to give a reasonably good sensitivity to misalignments of the rear mirror whilst maintaining a spot size of $\sim$ 1 mm on the photodiode.

Since the second photodiode does not sense purely lateral offsets, but some linear combination of lateral and angular misalignments, it does not produce a suitable signal which can be fed back to control the orientation of the rear mirror. It is necessary therefore to mix the signals sensed using both photodiodes in order to derive a signal which is solely dependent on the misalignment of the rear mirror. In practice this was achieved by dithering the alignment of the input mirror at a few hertz and observing the resulting signal in the output of the mixer after the second quadrant photodiode. This signal could then be tuned out by suitably mixing the signals from both quadrant photodiodes, so that the resulting signal could only be due to the misalignment of the rear mirror.

Coil/magnet actuators were used to control the orientation of the suspended mirrors. By driving current through the coils, forces are applied to magnets attached to a control block used to suspend the cavity mirrors. This allows the tilt and rotation of the mirrors to be adjusted. These actuators are also used along

with shadow sensors and optical levers to locally damp the high Q pendulum resonances to prevent excessive motion of the mirrors at these resonant frequencies. Typically each automatic alignment servo was designed with suitable electronic filtering in order to give each servo a bandwidth of about 10 Hz and an open loop gain of about 20 dB below the pendulum resonances ($\sim$ 1 Hz).

3.5.3 Performance

The performance of the system could be judged by observing the visibility of the fringe seen at the output of the cavity as viewed in reflection. Any misalignment of the mirrors of the cavity with respect to the input light results in a coupling of the light in the system into higher order modes. The amount of light in the fundamental mode of the two interfering beams at the output will subsequently decrease (for an angular misalignment this can be seen by looking at the expression for the fundamental mode in equation 3.53). Therefore misalignment of the interfering beams results in a decrease in the observed visibility.

As a test of the alignment system, each mirror was deliberately misaligned a small amount in each of the four degrees of freedom. The servo systems were then switched on one at a time resulting in the stepwise improvement in the visibility as shown in figure 3.12. The visibility was improved from about 20% to the optimum value of 30%. This last figure represents the optimum value for the visibility of the cavity which could be achieved by manually aligning the mirrors using the DC orientation controls.

It is also interesting to note that the fluctuations in the visibility are reduced when the cavity is optimally aligned. This is due to the fact that static offsets in the alignment of the cavity mirrors increase the coupling of large low frequency motions of the suspended mirrors into the intensity of the light observed at the output.

The error points of the servos were also measured and calibrated in order to give an estimate of the angular fluctuations in the system as viewed by the automatic alignment systems. The error point of the servo used to control the tilt of the

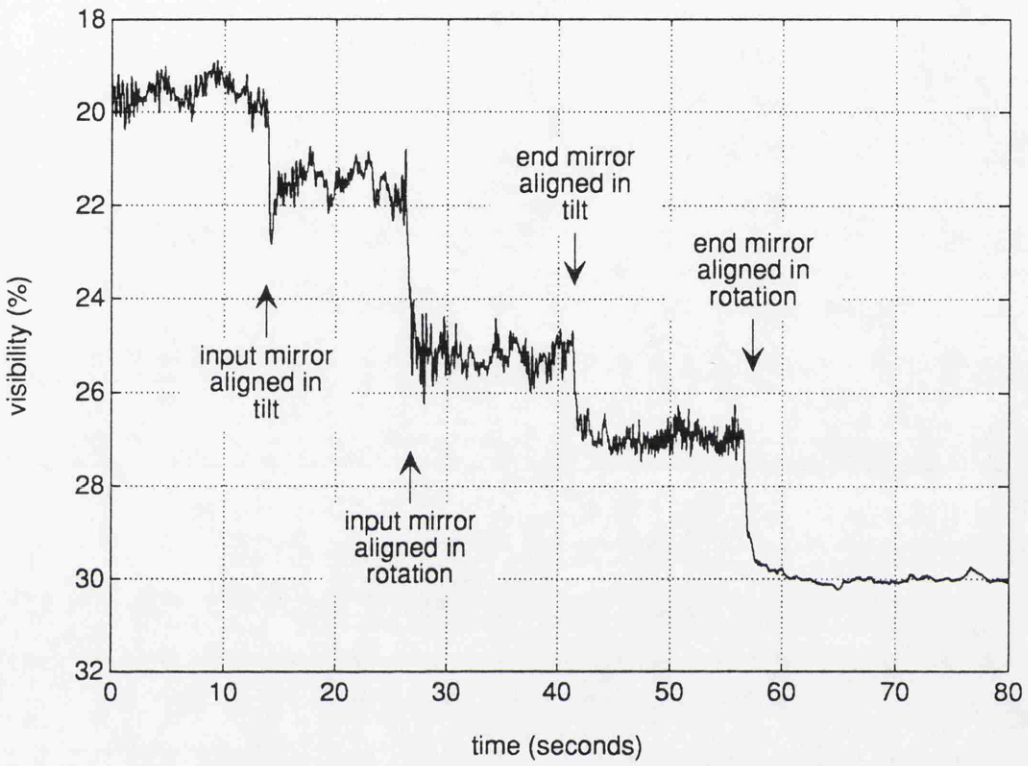

Figure 3.12: *Effect of the automatic alignment system on the fringe visibility of the 10 m cavity.*

curved mirror is shown in figure 3.13. With the servo switched off (upper trace), it can be seen that the low frequency angular fluctuations correspond to a level of a few 10^{-6} rads/$\sqrt{\text{Hz}}$ and fall off into the background measurement noise level at around 10 Hz. This spectrum was similar for all of the servo systems used to control the orientation of the two mirrors in the cavity. The low frequency fluctuations are probably due to seismic noise which propagates through the system with almost no attenuation at these frequencies. The background noise is not shot noise but excess noise on the light at the *rf* modulation frequency caused by a lack of optical isolation in the system.

Switching on the alignment system (lower trace) results in a reduction of the angular fluctuations at low frequencies by at least 20 dB. This was as expected since the bandwidth of the servo was designed to be around 10 Hz.

3.5.4 Problems and limitations

Despite the success of the automatic alignment technique there were a few problems associated with the operation of the system. A high level of DC stability is required in the feedback electronics. Offset voltages can arise at the output of the mixers and also at the inputs to the various amplifiers used to derive the alignment error signal. While these can in principle be nulled out when initially setting up the alignment system, for example by setting the error signal to zero with no light directed towards the photodiodes, any drifting of these voltages will cause a misalignment of the cavity mirrors. For an alignment system which will be relied upon to keep such an interferometer correctly aligned over long timescales, particular care will need to be taken in correcting for or eliminating these offsets.

A similar problem is caused by *rf* pickup in the electronics before the mixer. This also shows up as a DC offset in the alignment error signal. Although this effect can also be dealt with by nulling out the offsets using a suitable correction voltage, the amount of pickup in the front end electronics can be surprisingly variable. Good shielding of the electronics is therefore essential if the amount of pickup is to be minimised and the DC stability of the system maintained.

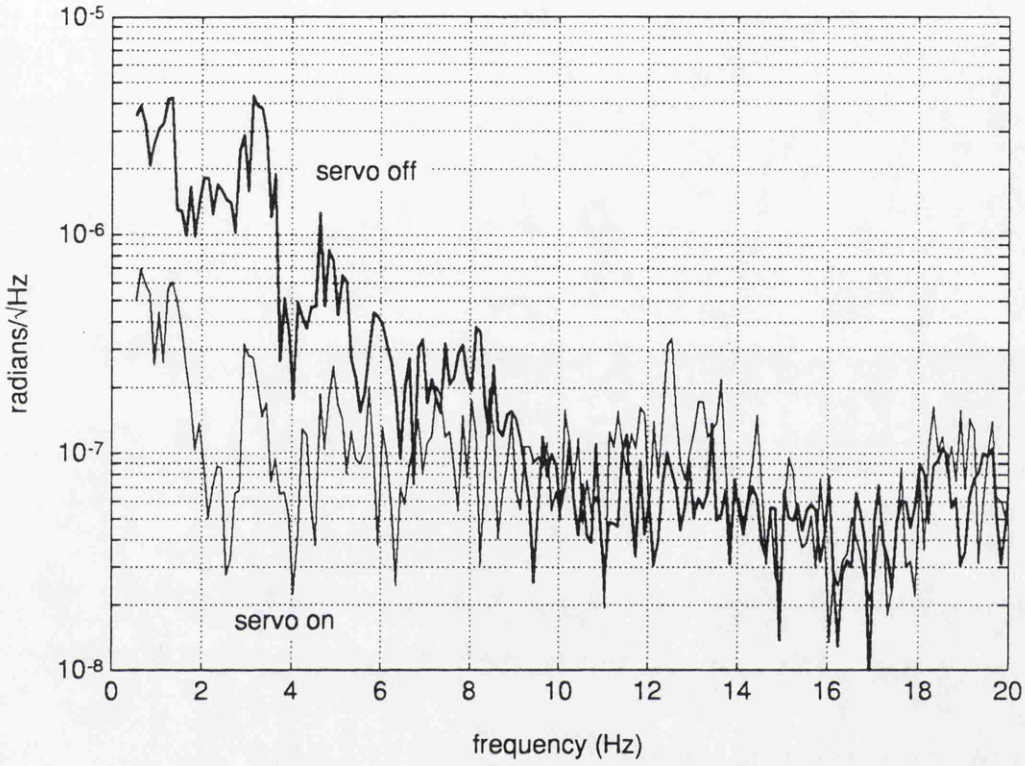

Figure 3.13: *Angular fluctuations as viewed by the sensing system used to control the tilt of the curved mirror.*

The main limit to sensitivity of the technique in this test was set by the the excess noise on the light at the *rf* modulation frequency. This limited the accuracy of alignment of the mirrors to around 10^{-7} rads/$\sqrt{\text{Hz}}$. However it should be possible to significantly reduce this noise level with additional optical isolation.

3.6 Summary and conclusions

It has been shown that it is possible to determine full information regarding the misalignment of two interfering beams using a technique based on differential phase sensing.

A mathematical description of the method has been presented, demonstrating that information on lateral and angular misalignments can be deduced from measurements using a split or quadrant photodiode and that beam waist size and positional offsets can be detected using an annularly split photodiode.

The technique has been experimentally demonstrated on a simple benchtop Michelson interferometer where a single quadrant photodiode was used to monitor and correct for small angular misalignments of the two interfering beams at the output. Following on from this, the system was successfully tested on one of the 10 m long suspended optical cavities in the Glasgow prototype gravitational wave detector where lateral as well as angular offsets have to be controlled. In this particular case, the alignment system was shown to be capable of reducing the angular fluctuations of the cavity mirrors by more than 20 dB at frequencies below 10 Hz.

Chapter 4

The 10 m prototype laser interferometric gravitational wave detector.

4.1 Introduction

The construction of a 10 m prototype laser interferometric gravitational wave detector was started in Glasgow in 1978. The initial configuration consisted of two perpendicular three mirror ring cavities 10 m long and illuminated with a commercial *cw* argon ion laser. The first measurements were performed on this system around 1981, the measured sensitivity of the interferometer being about $3 \times 10^{-15}\,\mathrm{m}/\sqrt{\mathrm{Hz}}$ at 1 kHz. Since then the detector has undergone various stages of development and reconstruction with its performance and sensitivity steadily improving. The present configuration of the interferometer consists of two perpendicular 10 m long high finesse Fabry-Perot cavities (a full description of the interferometer is given in section 4.2).

Prototype laser interferometric gravitational wave detectors have also been developed at Caltech, the Max-Planck-Institut für Quantenoptik in Munich and MIT (see [54], [55] and [56]). The Caltech detector is very similar to the Glasgow prototype, consisting of two 40 m long Fabry-Perot cavities, whereas the Munich and MIT prototypes were based on two multiple bounce delay lines.

These prototype detectors have enabled many of the ideas on interferometry and high precision measurement which will be used on the proposed full scale detectors (see [7], [17] and [18]) to be implemented and tested. In order to suc-

cessfully detect gravitational waves, extremely high demands are placed on the performance and sensitivity which must be achieved using full scale detectors. It is essential therefore that the various noise sources present in the prototype interferometers are understood and possible methods for their suppression successfully demonstrated.

The following chapter describes in detail the work carried out on the prototype laser interferometric gravitational wave detector in Glasgow from early 1991 to the end of 1992.

4.2 The 10 m prototype – general description

4.2.1 General description

A schematic diagram of the interferometer showing the main optical components situated inside the vacuum system is shown in figure 4.1.

The detector basically consists of two high finesse Fabry-Perot cavities, 10 m in length, formed between two ultra low loss dielectric mirrors. The mirrors were coated directly onto fused silica test masses which were superpolished before coating. The input mirror in each cavity is plane, with a transmission of 500 ppm (intensity) while the rear mirrors have a radius of curvature of 15 m and are of maximum reflectivity. The cavities typically have storage times in the range $100 \rightarrow 180\,\mu$s limited by excess loss due to contamination of the mirrors. A description of these mirrors can be found in [31].

The test masses are individually suspended as pendulums in order to attenuate the transmission of seismic noise. In addition to this the test mass suspension point is supported by a five layer lead/rubber seismic isolation stack which itself is supported by the main vacuum system. A description of the design and operation of the pendulum suspension systems used to support the end masses is given in Chapter 5. The high Q pendulum suspensions are electronically damped using local control servo systems based on local optical sensors (shadow sensors and optical levers) and coil/magnet feedback actuators. The coil/magnet actuators are also used to apply DC forces to the test masses allowing their orientation to

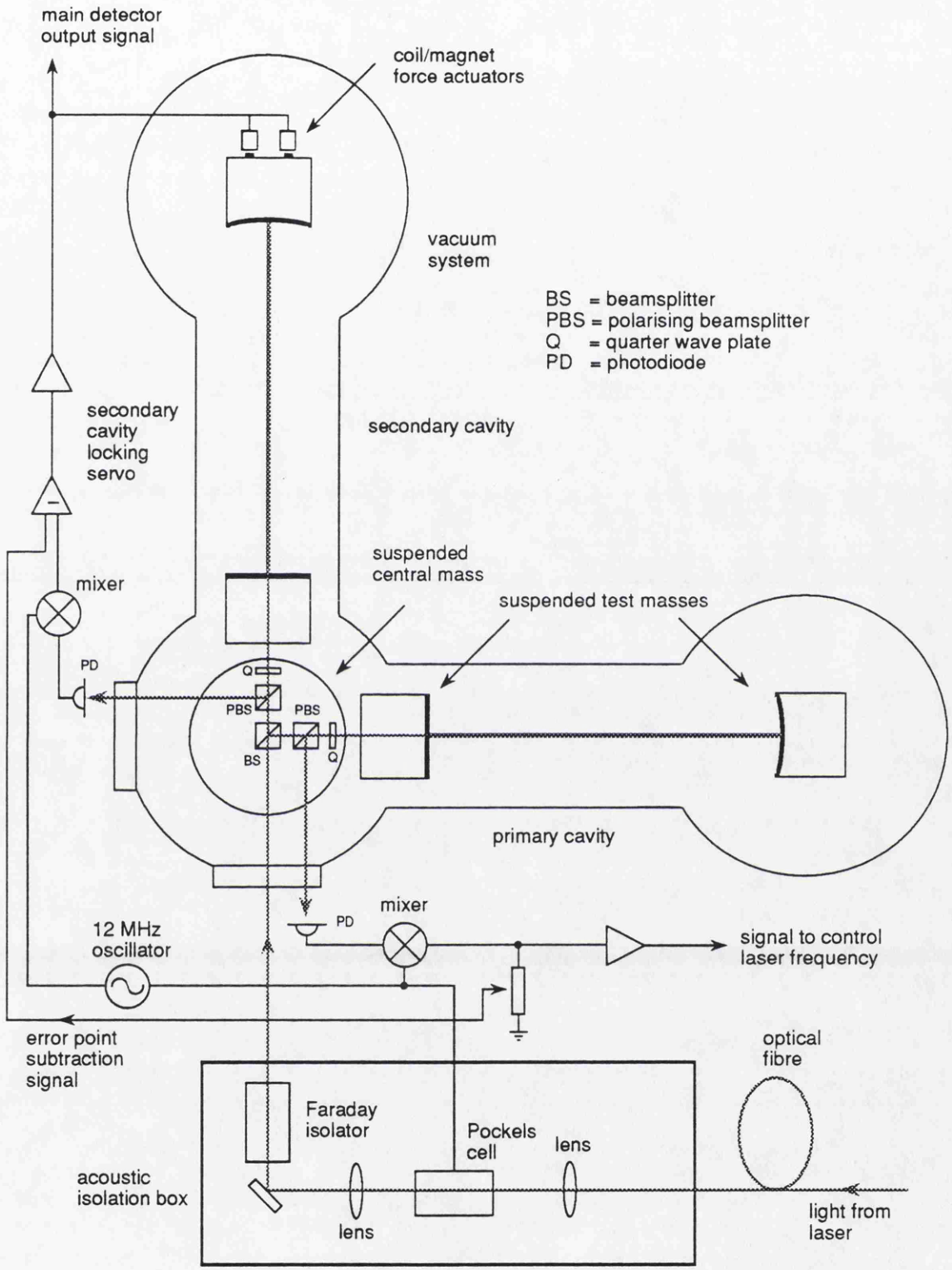

Figure 4.1: *Schematic diagram of the main elements of the 10 m prototype interferometer.*

be controlled. This is necessary in order to correctly align the cavities with the input laser light so that it resonates in the cavity.

The interferometer is illuminated using a commercial *cw* argon ion laser which has been extensively modified (see [57]). The laser is housed in its own custom built resonator made from four Invar rods. The laser cavity mirrors are mounted on the resonator giving good isolation from the vibrational noise of the laser water cooling system. The low coefficient of thermal expansion of the Invar rods also reduces the fluctuations in the laser frequency and intensity due to thermal variations.

The laser light is prestabilised to a small reference cavity after which it is passed through a monomode optical fibre. This acts as a modecleaner and effectively reduces the amount of higher order modes present in the laser beam. The light is then phase modulated using a Pockels cell and mode matched into the 10 m optical cavities of the interferometer using suitable lenses.

The light enters the vacuum system *via* a quartz port hole as indicated in figure 4.1 and directed towards a 50/50 beamsplitter. The beamsplitter directs the light towards the two perpendicular cavities. Each beam is passed through a further polarising beamsplitter and quarter wave plate situated immediately before the input mirror of the cavity. These components and the first beamsplitter are all mounted on a solid suspended aluminium plate, commonly referred to as the central mass. The low frequency motion of the suspended plate is damped using local control systems similar to those used to damp the suspended cavity mirrors.

The polarising beamsplitter/quarter wave plate combination ensures that the light impinging on the input mirrors of the cavities is circularly polarised. On reflection from the cavity, the light is circularly polarised in the opposite sense and so is rejected by the polarising beamsplitter after passing through the quarter waveplate. The reflected light from each cavity can therefore be monitored using a photodiode (these are currently located outside of the vacuum system). The light returning from each arm of the interferometer is not recombined as in a conventional Michelson interferometer, instead each cavity is monitored separately.

4.2.2 Operation of the detector

Figure 4.1 shows the main elements of the control systems used to lock the detector enabling a signal to be obtained which represents the differential arm length change of the interferometer.

The technique of *rf* reflection locking is used on both main cavities [53]. The light directed towards each cavity is *rf* phase modulated (in this case at 12 MHz). Sidebands are therefore imposed on the laser frequency at the modulation frequency. The light directly reflected off the input mirror of the cavity retains the sidebands, whereas the light which leaks out of the cavity on resonance has no sidebands (since the linewidth of the cavity is much less than the modulation frequency). The two beams returning from the cavity are effectively differentially phase modulated with respect to each other. Any change in frequency of the laser light with respect to the cavity, or equivalently, any change in length of the cavity with respect to the laser frequency results in a change in the relative phase of the directly reflected light and the light which leaks out of the cavity and can be measured by coherently detecting the modulated intensity of the interfered beams returning from the cavity. This technique has the advantage that the measurement is made at frequencies (around 12 MHz) where the laser intensity noise is limited by shot noise. The low frequency intensity noise present in the laser light does not interfere with the measurement provided the cavity is accurately locked in the centre of a fringe.

The signal obtained using this technique on the primary cavity is used as part of the laser stabilisation system (as discussed in the next section) to frequency stabilise the laser to the primary cavity. This ensures that the light remains on resonance with the primary cavity. The wavelength of the light which is directed towards the secondary cavity therefore represents the length of the primary cavity. The reflected light from the secondary cavity is also coherently detected and the signal obtained is fed back to coil/magnet force actuators which act on the end mirror of the cavity to hold it on resonance with the laser light. The feedback signal is therefore proportional to any differential arm length change between the primary and secondary cavities. This is the signal which can be analysed for evidence of

gravitational waves.

As can be seen on the diagram, some of the primary error point signal is subtracted from the secondary error point signal. This reduces the effect of any excess frequency fluctuations in the laser which have not been removed by the primary cavity stabilisation system.

4.2.3 The two loop laser stabilisation system

The displacement sensitivity of the 10 m prototype at the beginning of 1991 was at best about $1.7 \times 10^{-18}\,\mathrm{m}/\sqrt{\mathrm{Hz}}$ around $2 \rightarrow 3\,\mathrm{kHz}$. In order to ensure that frequency noise present in the laser light does not compromise the performance of the detector it is necessary to ensure that the frequency fluctuations are reduced to a sufficiently low level. This requires being able to stabilise the frequency of the laser to $\sim 10^{-4}\,\mathrm{Hz}/\sqrt{\mathrm{Hz}}$.

This can be achieved using a suitable servo system, where the frequency of the laser is compared to a stable frequency reference (in this case one of the 10 m long suspended high finesse cavities) and the resulting signal fed back to control the frequency of the laser. Given a sufficiently stable reference, one simply requires enough loop gain in the servo to reduce the frequency fluctuations of the laser to an acceptable level.

Typically the frequency fluctuations of the laser used on the 10 m prototype (after various attempts at passively stabilising the laser) are around $2\,\mathrm{kHz}/\sqrt{\mathrm{Hz}}$ at 1 kHz and rising to as much as $500\,\mathrm{kHz}/\sqrt{\mathrm{Hz}}$ at 100 Hz (see [58]). In order to reduce the frequency fluctuations to $< 10^{-4}\,\mathrm{Hz}/\sqrt{\mathrm{Hz}}$ at 1 kHz therefore requires a servo gain of $> 10^7$. This is achieved in practice using a two loop stabilisation scheme.

The particular stabilisation scheme used is shown in figure 4.2. Initially, the laser is frequency locked (using the *rf* reflection locking technique) to a small reference cavity. The reference cavity consists of two mirrors mounted either end of a Zerodur tube. The cavity is situated inside a small vacuum tank to reduce acoustic noise and the tank is mechanically isolated from the optical table on which

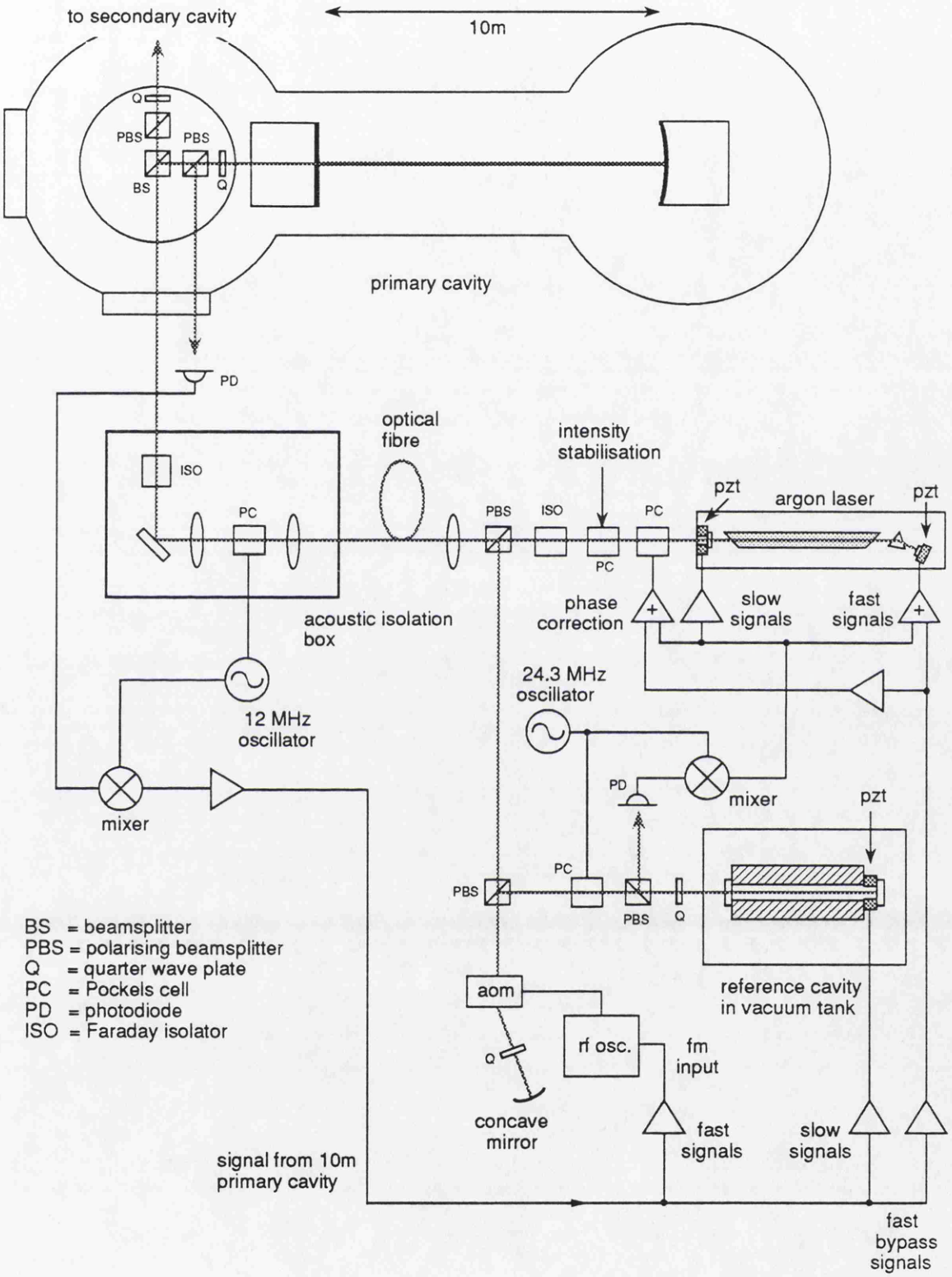

Figure 4.2: *Schematic diagram of the two loop laser stabilisation scheme used on the 10 m prototype.*

it sits using a few layers of rubber.

A small amount of light is split off from the main laser beam and double passed through an acousto-optic modulator (*aom*) before it is directed, *via* a Pockels cell towards the cavity. The *aom* is used as the main feedback element for the second loop and has no real effect on the operation of the first loop other than to produce a DC frequency shift of the light entering the reference cavity. The light reflected from the cavity is then monitored using a photodiode. By phase modulating the light entering the reference cavity and demodulating the signal from the photodiode at the modulation frequency it is possible to determine the fluctuations in the laser frequency with respect to the length of the reference cavity. This signal can therefore be fed back to the laser to stabilise the laser light to the cavity. The slow signals are fed back to a *pzt* controlling the axial position of the front mirror of the laser cavity (this element has a large dynamic range but limited bandwidth), whereas the fast signals are fed back to a specially designed *pzt* controlling the axial position of the rear mirror (this element has a limited dynamic range but wide bandwidth).

Typically, this system is capable of reducing the frequency fluctuations in the laser to $\sim 0.3\,\mathrm{Hz}/\sqrt{\mathrm{Hz}}$ below 3 kHz and is limited by shot noise on the light directed towards the reference cavity.

Once the laser has been stabilised to the reference cavity, the second servo system can be turned on. The light reflected from the primary cavity gives a signal proportional to the frequency fluctuations of the laser light with respect to the primary cavity. This signal is fed back to the *aom* which acts as the main feedback element for the second loop. The *aom* is driven using a voltage controlled oscillator; signals fed to the *aom* driver essentially change the frequency of the oscillator which results in a frequency shift of the light passing through the *aom* crystal. The signal detected using the light which is reflected from the primary cavity is therefore used to change the frequency of the light which is directed towards the reference cavity. With the first loop locked, feeding back signals to the *aom* effectively changes the frequency of the laser light (at frequencies where the first loop has sufficient gain). Thus, the second loop acts to maintain the laser

light on resonance with the primary cavity.

A full description of the development of this system and its performance can be found in [58].

The effectiveness of the frequency stabilisation system can be judged by examining the noise at the primary error point (*i.e.* immediately after the mixer in the second loop) and comparing this with the shot noise level. A typical example of this is shown in figure 4.3. As can be seen, the error point is $\sim$ a factor of 2 above shot noise at 1 kHz, rising to $\sim$ a factor of 5 above shot noise at 3 kHz. It should be noted that it is possible to turn up the gain of the laser stabilisation servo so that the noise at the error point can be further reduced around 1 kHz. This unfortunately makes the stabilisation servo slightly unstable and it tends to lose lock more frequently in this state, so the system is usually run with the gain set slightly lower.

The shot noise limit in this particular case corresponds to a displacement sensitivity of $\sim 4 \times 10^{-19}\,\mathrm{m}/\sqrt{\mathrm{Hz}}$ at 1 kHz. Assuming that the fluctuations in the length of the primary cavity are less than this then the frequency of the light is stable to $\sim 4 \times 10^{-5}\,\mathrm{Hz}/\sqrt{\mathrm{Hz}}$ at 1 kHz.

The fact that the error point of the stabilisation system is above shot noise does not prevent the interferometer from reaching the shot noise displacement sensitivity limit. The residual frequency fluctuations as viewed at the primary error point (provided they are due to excess frequency fluctuations in the laser light and not due to some other effect such as fluctuations in the length of the primary cavity) should be subtractable from the secondary error point using the electronic subtraction system (shown in figure 4.1). This system is typically capable of subtracting $\sim$ 20 dB of common mode signal from the main detector signal.

4.3 Calibration of the detector

The main detector output signal, representing the differential arm length change of the two perpendicular cavities, is obtained from the main feedback signal in the secondary cavity locking servo. The volts at the output of the final amplifier used

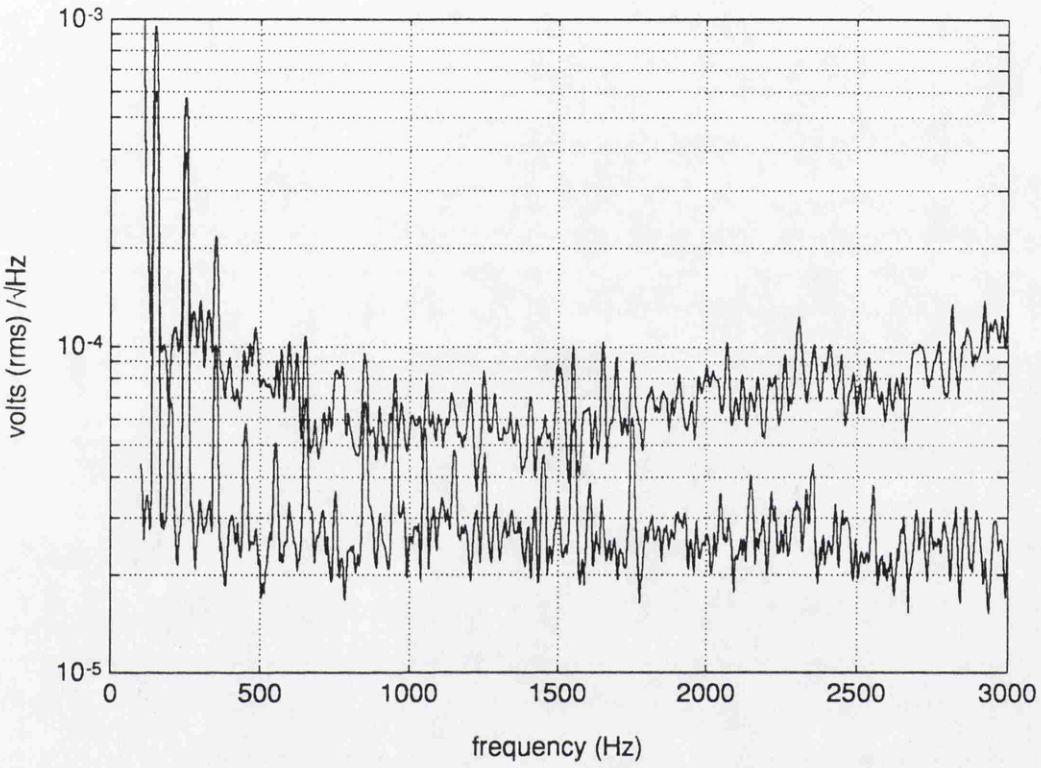

Figure 4.3: *Noise measured at the primary cavity error point with the laser stabilisation system in operation (upper trace) compared to shot noise (lower trace).*

to drive the feedback signal to the coil/magnet actuators acting on the end mirror in the secondary cavity are filtered and monitored using a low noise amplifier. Figure 4.4 shows a typical spectrum measured using an HP3582A spectrum analyser. In order to calibrate this signal in terms of $m/\sqrt{Hz}$ it is necessary to calculate a conversion factor. This factor will be frequency dependent and must therefore be calculated for each frequency of interest.

The method of calibrating the detector had previously been to drive a sinusoidal signal onto the coil/magnet actuators acting on the end mirror of the primary cavity. The level of the drive signal was noted and, knowing the DC response of the end mirror to a voltage applied at this point, the corresponding motion of the end mirror could be calculated (taking into account the $\frac{1}{f^2}$ roll off above the resonant frequency of the pendulum). The DC response of the pendulum to a voltage applied to the coil/magnet actuators was measured using a travelling microscope. The sinusoidal signal driven onto the end mirror shows up in the output signal of the detector. The level of the background noise in the output signal which limits the sensitivity of the detector can therefore be calibrated in terms of $m/\sqrt{Hz}$ by comparison with the calibration peak.

This method of calibration is rather tedious and laborious requiring several measurements to be made in order to allow the entire spectrum (100 Hz $\rightarrow$ 3 kHz) to be calibrated. Also, any change made to the actuators, suspension or control systems used on the suspended end mirror required re-measuring the DC response of the mirror. This measurement was quite tricky and usually only accurate to $\sim \pm 20\%$. It was therefore decided to develop another method of calibration which would be quicker, more reliable and give a measure of the sensitivity over the entire spectrum.

By driving a large enough signal onto the end mirror of the primary cavity, it is possible to detect this signal in the feedback to the *aom*, which acts as the main feedback actuator in the primary cavity locking servo (the second loop of the laser stabilisation system). Since the loop gain of the primary cavity servo is substantially greater than 1 in the frequency range of interest (100 Hz $\rightarrow$ 3 kHz) the signal driven to the *aom* gives a direct measure of the frequency fluctuations of

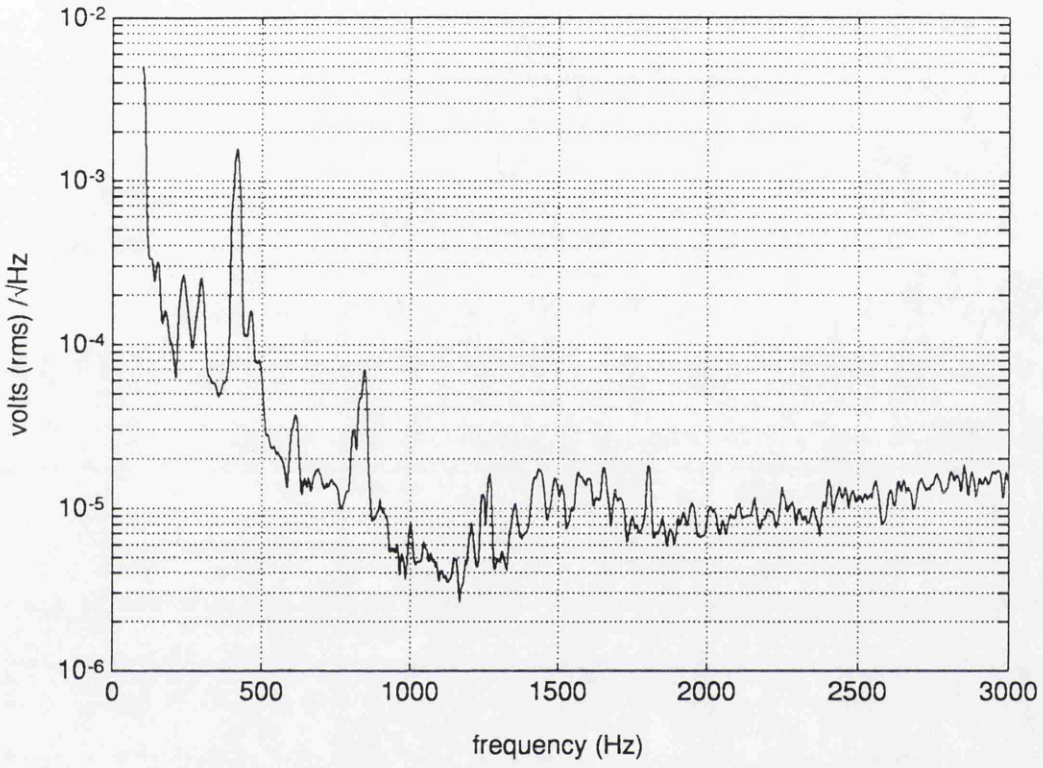

Figure 4.4: *Spectrum showing the uncalibrated main detector output signal.*

the laser light (after having been stabilised to the reference cavity), or equivalently, the length changes of the primary cavity. The response of the voltage controlled oscillator used to drive the *aom* was measured to be 3.385 MHz/V. Since the light is double passed through the *aom* crystal, the resulting frequency shift which is imposed on the main laser light due to a signal applied to the *aom* driver is 6.77 MHz/V. Therefore, by driving a suitable signal onto the end mass of the primary cavity and measuring it in the feedback to the *aom*, the resulting frequency shift imposed on the laser light in order to keep the cavity on resonance can be calculated. The corresponding displacement of the end mass, Δl, can then be calculated from the relationship $\frac{\Delta l}{l} = \frac{\Delta \nu}{\nu}$ (this is derived in Appendix A).

Unfortunately, the size of the signal required to be driven onto the end mass of the primary cavity in order to ensure that a signal can be seen above the noise in the feedback to the *aom* is too large to allow the secondary cavity to remain locked whilst this measurement is carried out. Therefore, the signal must be sufficiently attenuated (by $\sim 10^3$) before it can be detected in the secondary cavity feedback signal (*i.e.* the main detector output signal). Knowing the response of the *aom* and the attenuation used when measuring the response of the secondary cavity, the main output signal can be calibrated in terms of $\mathrm{m}/\sqrt{\mathrm{Hz}}$.

This is of course very similar to the calibration procedure which had previously been used, the difference being that the drive to the *aom* is used to calculate the displacement of the test mass caused by the calibration test signal rather than calculating the displacement from a knowledge of the DC response and $\frac{1}{f^2}$ behaviour of the mirror suspension. Comparing the two techniques provides a good check on the calibration process as discussed later in section 4.3.1.

In order to determine the displacement sensitivity of the detector at all frequencies from 100 Hz→3 kHz, use was made of the swept sinewave generator on the HP3582A spectrum analyser. This feature allows a transfer function to be measured between the drive signal (provided by the signal generator in the spectrum analyser) and the measured response of the system under test. The analyser measures the response of the system over a range of frequencies by injecting signals at specific frequencies and measuring the response at each frequency. The number

of measurements, averages *etc.* can all be set on the analyser.

The procedure devised for calibrating the detector was as follows:

(a) The response of the primary cavity was measured by driving a signal onto the end mirror and measuring the corresponding signal in the drive to the *aom*. This was done over the frequency range of interest (*e.g.* 100 Hz→3 kHz) and the resulting transfer function saved to disk under a suitable name (*e.g.* ACAL). A typical transfer function is shown in figure 4.5.

(b) The drive to the end mirror was suitably attenuated (the attenuator used gave -57.6 dB attenuation) and, with the detector running, the response of the main detector output to the drive signal applied to the end mirror in the primary cavity was measured. Again, this transfer function was saved to disk under a suitable name (*e.g.* DCAL); an example of a measured transfer function is shown in figure 4.5.

(c) The main detector output signal is spectrum analysed and saved to disk (*e.g.* as DSPEC). An example of a typical uncalibrated spectrum was given earlier in figure 4.4.

The spectrum analysed detector output signal can then be calibrated in terms of $\mathrm{m}/\sqrt{\mathrm{Hz}}$ by performing the following calculation:

$$DSPEC \times F \times \frac{ACAL}{DCAL}\,, \tag{4.1}$$

where F is a conversion factor which can be calculated from the known response of the *aom* (6.77 MHz/V), the frequency of the laser light (5.8×10^{14} Hz), the length of the cavity (9.7 m) and the attenuation used when measuring $DCAL$ (-57.6 dB *i.e.* a factor of 1.3×10^{-3}). In addition to this the signal measured from the *aom* drive was amplified by ×10. The conversion factor F is therefore given by

$$\begin{aligned} F &= (6.77 \times 10^{6})(1.3 \times 10^{-3})(5.8 \times 10^{14})^{-1}(0.1)(9.7) \qquad (4.2) \\ &= 1.5 \times 10^{-11}\,\mathrm{m/V}\,. \end{aligned}$$

The resulting sensitivity spectrum is shown in figure 4.6.

It should be noted that the calibration procedure only works in the frequency region where the feedback to the *aom* dominates over any other feedback path.

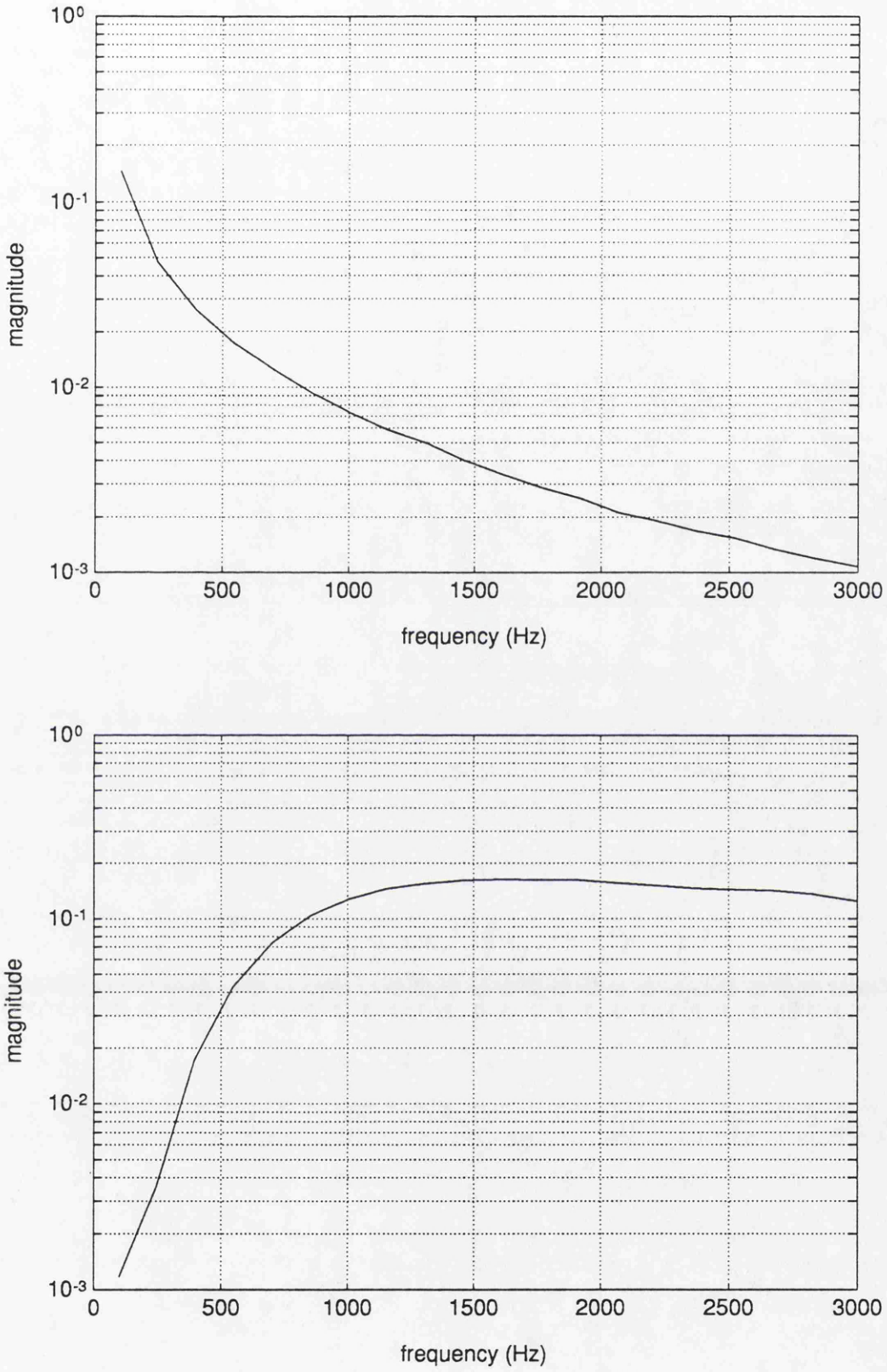

Figure 4.5: *An example of the detector calibration transfer functions. The upper graph shows the response of the feedback to the aom (ACAL) and the lower graph shows the response of the main detector output signal (DCAL).*

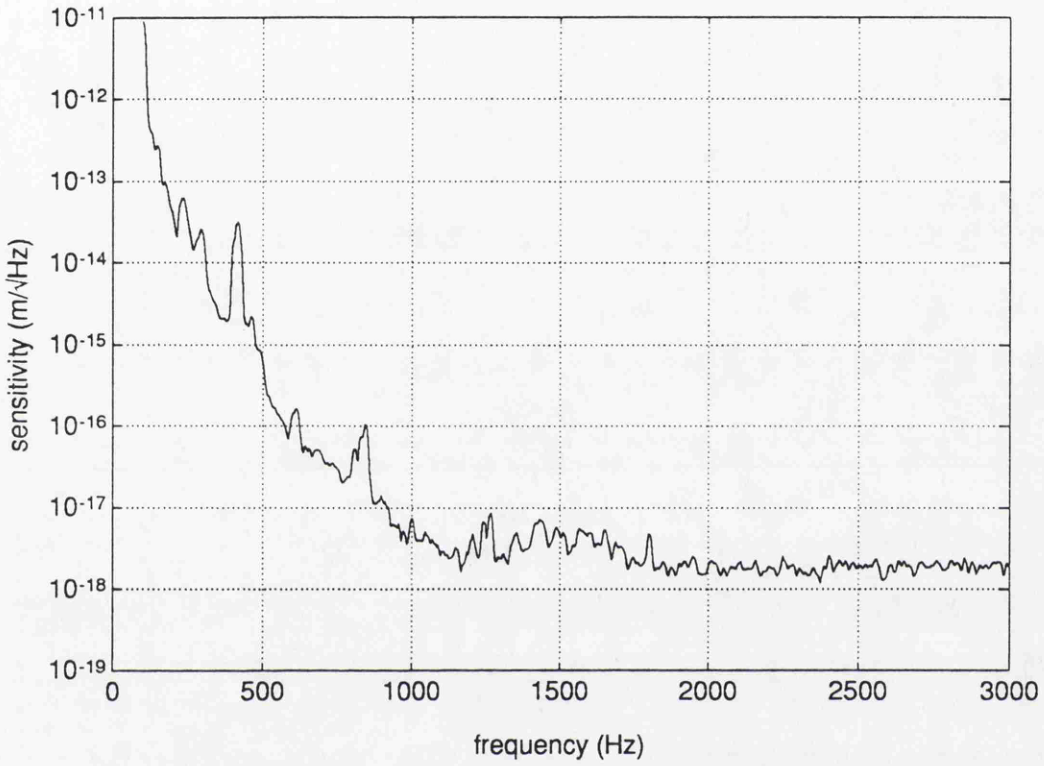

Figure 4.6: *Calibrated detector sensitivity spectrum measured in April 1991.*

This was verified in the frequency region of interest (100 Hz $\rightarrow$ 3 kHz) by injecting test signals into the feedback loop and observing the relative size of the signals in the various different feedback paths.

4.3.1 Verification of the calibration procedure

Having successfully demonstrated the calibration of the interferometer output signal using the response of the *aom* it was essential to check the validity of the calibration.

Comparison of the calibration using the *aom* with the measured response of a suspended mirror

As mentioned in the previous section, the detector output signal had previously been calibrated using the measured response of one of the suspended mirrors. The validity of the new calibration technique could therefore be checked by comparing the calibrated detector output signal obtained using this method.

The DC response of the coil/magnet actuator acting on the end mirror in the secondary cavity was measured. The suspended mirror has 3 magnets attached to its rear surface. The mirror is moved by applying forces to the magnets using 3 coils wired in series. By driving a DC current through the coils (which could be measured by noting the voltage across a resistor connected in series with the coils) and noting the resulting displacement of the mirror, using a travelling microscope, the DC response of the coil/magnet actuators could be measured. The response was measured to be 4 mm/A $\pm$20%. The resonant frequency of the pendulum was also measured to be 0.95 Hz.

The calibration factor used in equation 4.1 (*i.e.* $F \times \frac{ACAL}{DCAL}$) can be calculated independently from the response of the *aom* using these figures. In order to do this it is also necessary to know the relationship between the volts measured at the output of the final driving amplifier in the secondary servo system (where the main detector output signal is measured) and current through the feedback coils. At an arbitrarily chosen frequency of 2.5 kHz this was measured to be 4×10^{-4} A/V. In

addition to this it is also necessary to know the closed loop gain of the secondary cavity locking servo at the chosen frequency. This was measured by injecting a test signal, at 2.5 kHz, into the secondary cavity servo and measuring the size of the signal with the loop open and closed. With the loop closed the signal was reduced by 7.8 dB (a factor of 0.41) at 2.5 kHz. The calibration factor calculated from the characteristics of the suspended mirror and coil/magnet actuator is given by

$$\left(\frac{0.95}{2.5 \times 10^3}\right)^2 (0.41)\left(4 \times 10^{-4}\right)\left(4 \times 10^{-3}\right) = 9.5 \times 10^{-14}\,\mathrm{m/V}\,(\pm 20\%)\,. \quad (4.3)$$

This can be compared to the value obtained from the calibration factor found using the response of the *aom*. At 2.5 kHz $\frac{ACAL}{DCAL}$ was found to be -42.9 dB giving a calibration factor of 1.0×10^{-13} m/V. Clearly the two calibration techniques are in good agreement at 2.5 kHz. The measurements were repeated at different frequencies to confirm the agreement.

The above calculation relies on the fact that the motion of the test mass due to a constant applied force falls as $\left(\frac{f_0}{f}\right)^2$ above the pendulum resonant frequency, f_0. The fact that the calculated calibration factors agree at different frequencies confirms this relationship, but it was decided to try a slightly different method for checking the calibration procedure and the $\frac{1}{f^2}$ response of the pendulum. This is described in the following section.

Verification of the $\frac{1}{f^2}$ mechanical response of a pendulum

The $\frac{1}{f^2}$ mechanical response of the pendulum suspension system used to support the end mirror in the primary cavity was measured, both as a check on the calibration procedure used to calibrate the main detector output signal, and as an interesting check on the mechanical response of a pendulum suspension system. The experiment was carried out using only the primary cavity and so served as an independent check on the calibration procedure which was verified in the previous section.

Signals were applied to the coils used for calibrating the detector. The current driven through the coils (which act on the suspended end mirror of the primary

cavity) was compared with the volts driven to the *aom* with the primary cavity locked. Again, the current driven through the calibration coils was measured by monitoring the volts (through a $\times 10$ low noise amplifier) across a $100\,\Omega$ resistor in series with the coils. The ratio of the two signals can be seen in figure 4.7. The graph shows the clear $\frac{1}{f^2}$ roll off due to the mechanical response of the suspended mirror in the 50 Hz to 5 kHz region. The slope of the graph deviates from this at high frequencies due to the difficulty in driving enough signal onto the end mass in order to see the signal above the noise in the feedback to the *aom*. There is also some deviation from the expected behaviour at low frequencies due to the fact that the *aom* is no longer the dominant feedback element at these frequencies.

In addition to checking the $\frac{1}{f^2}$ behaviour of the pendulum, the calibration can be checked as before by using the measured DC response of the coil/magnet actuators acting on the mirror. This was found to be 13 mm/A ($\pm 20\%$) and the resonant frequency of the pendulum was 0.9 Hz. The response of the mirror to a signal driven onto the coils is given at 1 kHz by

$$\left(10^{-3}\right)\left(\frac{0.9}{1\times 10^{3}}\right)^{2}\left(13\times 10^{-3}\right) = 1.1\times 10^{-11}\,\mathrm{m/V}\,. \tag{4.4}$$

This can be compared to a similar figure derived from the known response of the *aom* (6.77 MHz/V) *i.e.* for a cavity which is 9.7 m in length we have

$$(6.77\times 10^{6})(5.8\times 10^{14})^{-1}(9.7) = 1.13\times 10^{-7}\,\mathrm{m/V}\,. \tag{4.5}$$

The ratio of these two figure is -80.2 dB which agrees very well with the value obtained from figure 4.7 at 1 kHz (-81.5 dB).

Comparison of the theoretical shot noise limited sensitivity with an estimate derived from the calibration

Knowledge of the characteristics of the interferometer (the cavity storage times, visibility, light power *etc.*) allows the theoretical shot noise limited displacement sensitivity of the detector to be calculated (see Appendix A). This can be compared with an estimate of the shot noise limited performance of the detector obtained

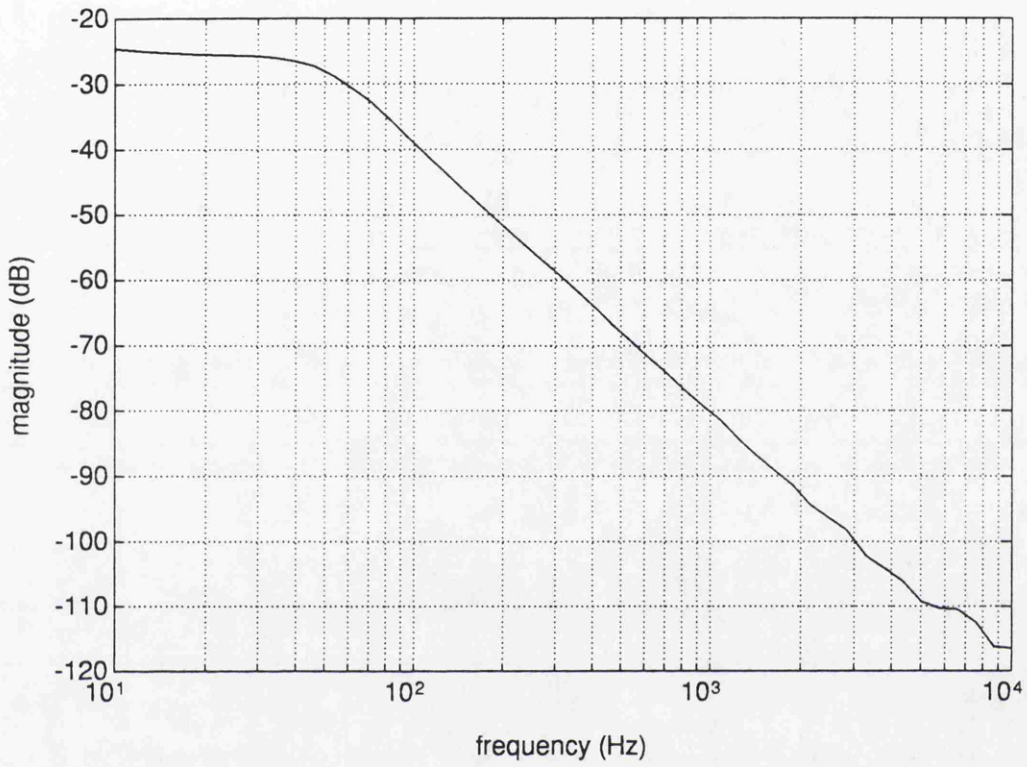

Figure 4.7: *Ratio of the volts driven to the aom and current driven through the calibration coils showing the* $\frac{1}{f^2}$ *behaviour of the pendulum.*

from various measurement on the system. Not only does this verify the calibration procedure, it also checks the validity of the shot noise calculation. It is interesting to note that this technique does not require the performance of the interferometer to be limited by shot noise.

White light (provided by a torch bulb) was used to illuminate the secondary cavity photodiode and its intensity adjusted to correspond to the light level present on the photodiode whilst the cavity was locked. The resulting shot noise could then be observed at the point at which the interferometer output signal was normally measured. Note that this measurement is performed with the secondary cavity servo open loop, but with the gain of the electronics in the servo set at the level which is used when the loop is closed and the cavity resonating. In this particular test, the shot noise level recorded on the detector output signal was measured to be $-121\,\mathrm{dBV}/\sqrt{\mathrm{Hz}}$ (*i.e.* $8.9 \times 10^{-7}\,\mathrm{V}/\sqrt{\mathrm{Hz}}$) at 2.5 kHz. The intensity of light falling on the photodiode gave $\sim 5\,\mathrm{mA}$ of photocurrent, corresponding to a typical locked light level.

The loop gain of the secondary locking servo was measured in this case to be $-11.06\,\mathrm{dB}$ (a factor of 0.280). Note that this is slightly different from the previous measurement due to the the fact that the cavity characteristics had changed. This measurement was carried out by injecting a test signal at 2.5 kHz into the secondary servo error point and observing the difference in the magnitude of the test signal with the secondary cavity locked and unlocked. The calibration factor ($F \times \frac{ACAL}{DCAL}$) was also slightly different, at 2.5 kHz it was measured to be $(1.46 \times 10^{-11}) \times (6 \times 10^{-3})$. The shot noise limited sensitivity of the secondary cavity at 2.5 kHz can be calculated as follows

$$\left(8.9 \times 10^{-7}\right)(0.280)^{-1}\left(1.46 \times 10^{-11}\right)\left(6 \times 10^{-3}\right) = 2.8 \times 10^{-19}\mathrm{m}/\sqrt{\mathrm{Hz}}\,. \quad (4.6)$$

The shot noise limited sensitivity can also be calculated using the formula detailed in Appendix A from a knowledge of the various parameters of the cavity. The figure obtained from the theoretical calculation is $2.9 \times 10^{-19}\,\mathrm{m}/\sqrt{\mathrm{Hz}}$ (the observed visibility of the secondary cavity was measured to be 54% and the storage time 120 μs). The two figures are in excellent agreement.

4.4 Displacement sensitivity of the 10 m prototype

Having succeeded in obtaining agreement between the various calibration techniques, the sensitivity of the interferometer could be measured with confidence in the frequency range of interest, using the technique described in the previous section (section 4.3). The ability to measure the sensitivity over a broad range of frequencies proved to be extremely useful in determining the various noise sources present in the detector output signal. These investigations and the subsequent steps taken in an attempt to reduce the noise present in the detector signal are discussed in the remainder of this chapter.

4.4.1 Detector sensitivity at the end of 1991

The displacement sensitivity of the 10 m prototype gravitational wave detector at the end of 1991 is shown in figure 4.6. The noise present in the detector output signal at that time was almost flat at high frequencies ($2 \rightarrow 3$ kHz), at a level corresponding to $\sim 1.7 \times 10^{-18}\mathrm{m}/\sqrt{\mathrm{Hz}}$. This was well clear of the expected shot noise limit, which at that time was $\sim 6 \times 10^{-19}\mathrm{m}/\sqrt{\mathrm{Hz}}$ in this frequency region. At lower frequencies it can be seen that the noise level rose dramatically, reaching a level of $\sim 10^{-12}\mathrm{m}/\sqrt{\mathrm{Hz}}$ at 100 Hz.

There was some evidence to suggest that the alignment of the laser beam with respect to the input mirrors of the 10 m cavities influenced the level of noise observed in the $2 \rightarrow 3$ kHz region. For example, when the mirrors currently in use were first installed, the laser beam was several millimetres off centre with respect to the cavity input mirrors. This resulted in the high frequency noise rising to $\sim 3 \times 10^{-18}\mathrm{m}/\sqrt{\mathrm{Hz}}$.

In order to reduce any effects arising from the misalignment of the laser beam, the input mirrors of the 10 m cavity were carefully re-aligned. In practice it was possible to position the laser beam to within ~ 1 mm of the centre of the mirrors. The effect on the sensitivity can be seen by looking at figure 4.8. As can be seen, the noise level in the $2 \rightarrow 3$ kHz region was significantly reduced and in fact reached the shot noise limit at 3 kHz.

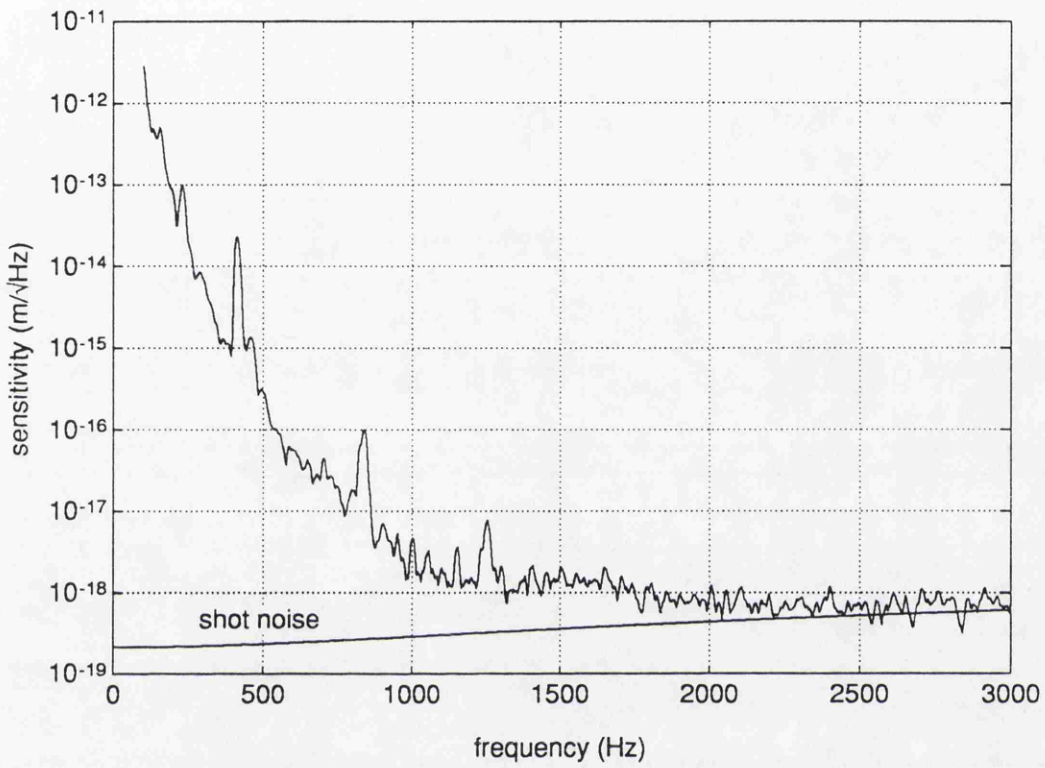

Figure 4.8: *Displacement sensitivity of the 10 m prototype after careful re-alignment of the cavity input mirrors with respect to the laser beam. Also shown on the graph is the calculated shot noise limit.*

There are various possible explanations as to why such misalignments could couple noise into the detector output signal. One rather obvious way is through excess noise present in the orientation control servos (discussed in greater detail in Chapters 2 and 5). As the beam is moved away from the centre of rotation (or tilt) of the mirror, any noise which is imposed onto the orientation of the mirror will couple into the effective length of the cavity. However one would expect the noise which is imposed onto the motion of the mirrors (*via* the coil/magnet actuators) to be attenuated above the resonant frequency of the mirror suspension system. As can be seen from figure 4.6, the noise level is reasonably flat above 1 kHz.

One other, rather popular theory, was that by offsetting the laser beam with respect to the input mirrors, large amounts of low frequency signals coupled into the detected signals from the two cavities (due to the underdamped motion of the mirrors in tilt and rotation). In the primary cavity, some of these low frequency signals (up to 30 Hz) were fed back directly to the end mirror, preventing large low frequency signals appearing in the feedback to the rear *pzt* in the reference cavity and also to the *aom*. There was some concern that these large signals being fed back to the end mirror in the primary cavity (again *via* coil/magnet actuators) could be frequency up-converted by some non-linearity in the actuators causing broadband high frequency noise. The double pendulum suspension system which is described in the first half of Chapter 5 was designed to reduce this noise in the $2 \rightarrow 3$ kHz region. In fact, because of the improved stability of the primary cavity after installing the new suspension system, it was possible to dispense with the low frequency feedback to the end mirror in the primary cavity.

The reason for the apparent variation in noise in the detector output signal due to the relative position in the laser beam with respect to the primary inboard test mass therefore remains unclear. However, having almost reached the shot noise limit at 3 kHz, it was decided to try to reduce the large amount of low frequency noise present in the detector output signal. The experimental investigations carried out to determine the source of the noise in the 100 Hz $\rightarrow$ 1 kHz region and the subsequent steps taken to reduce the noise are discussed in the following section.

4.5 Low frequency (100 Hz → 1 kHz) noise in the 10 m prototype detector

Examination of the spectrum shown in figure 4.8 shows the large amount of low frequency noise present in the detector output signal. The main source of this noise was found to be electronic noise in the local control servos, acoustic noise and also excess light noise due to insufficient optical isolation. Each of these are discussed in the following sections.

4.5.1 Local damping and orientation control systems

The problem of noise in the local control systems used to damp the high Q mirror suspension systems is discussed at length in Chapter 2. In the prototype detector all four mirrors forming the two 10 m long cavities are suspended as pendulums which are locally damped to prevent excessive motion of the mirrors at the pendulum resonant frequencies. The low frequency noise present in the detector output signal as shown in figure 4.8 was, at that time, found to be almost entirely due to these local damping control systems.

The primary and secondary cavity input mirror local control systems

The local control systems used to damp these mirrors were based on optical levers sensing the tilt and rotation motions of the mirrors and feeding back signals to coil/magnet actuators. The optical levers consisted of a beam of light from a HeNe laser, directed towards the suspended mirror, with the reflected beam being diverted onto a position sensitive photodiode. Any tilt or rotation of the mass could be detected by monitoring the position of the reflected beam on the photodiode. Both mirrors were suspended from individual aluminium crosses using two loops of wire. Each aluminium cross had four magnets attached to it allowing the cross, and therefore the mirror to be controlled in tilt and rotation. The cross itself was suspended from the top of the lead/rubber stack, from which the beamsplitter central mass was also suspended. Some longitudinal control of the position of the

mirror was also possible using a *pzt*, mounted on the stack and attached to the cross *via* a short piece of wire. (For a detailed description of this systems see [19].) Note that there was no local sideways or longitudinal damping of the masses.

The orientation control feedback systems were originally designed to give a reasonable amount of gain at DC, whilst damping the pendulum resonances which occur between 1 and 2 Hz. This required a servo with a bandwidth of a few tens of Hz (typically 30 Hz). Because of this the front end noise from the sensing system imposed a significant amount of noise onto the orientation of the cavity mirrors at low frequencies (100 Hz $\rightarrow$ 1 kHz).

The noise present in the orientation control servos used on the input mirrors was measured by monitoring the current being driven through the actuator coils. The level of noise present in these systems when related to actual motion of the interferometer masses was very close to the measured sensitivity shown in figure 4.8. For example, the noise measured in the tilt orientation control of the primary cavity input mirror corresponded to $\sim 3 \times 10^{-5} \mathrm{A}/\sqrt{\mathrm{Hz}}$ at 200 Hz. Taking into account the pendulum resonance in tilt at around 1.5 Hz and the DC response of the coil/magnet actuators (measured to be $\sim$ 5 mm/A), the noise corresponds to a displacement noise level of $\sim 8 \times 10^{-12} \mathrm{m}/\sqrt{\mathrm{Hz}}$ at 200 Hz. Since the actuator controls the tilt of the mirror, this noise is not coupled directly into the apparent longitudinal motion of the cavity. However, if a coupling factor of $\sim$ 10% is assumed then this control would limit the sensitivity of the detector to $\sim 8 \times 10^{-13} \mathrm{m}/\sqrt{\mathrm{Hz}}$, which is reasonably close to the measured noise level observed in the detected output signal at 200 Hz as shown in figure 4.8.

In order to reduce the level of noise being imposed onto the motion of the cavity mirrors, the orientation control servos were re-designed. The feedback strategy discussed in Chapter 2 was employed, *i.e.* the pendulum resonances were only lightly damped and no DC feedback was used, requiring a servo which feeds back signals only around the pendulum resonance. This allows the electronic gain of the system to be steeply filtered above the pendulum resonance (in this case with a 5 pole RC filter starting at 10 Hz) whilst maintaining a reasonable phase margin around the unity gain frequency (which is chosen to be near the pendulum

resonance).

It is worth noting that the old feedback system was intentionally designed to have gain at DC. This effectively locks the orientation of the mirror to the position of the photodiode used in the optical lever sensor. It was believed that such an arrangement would give good long term pointing stability of the mirrors. However, the pointing stability of the new system (and the control systems subsequently employed on the end mirrors) with no DC feedback appeared to be as good, if not better than the old system (probably because the old system was susceptible to drifting in the pointing stability of the reference laser).

An example of the amount of noise present in one of these servos (the primary inboard mass tilt servo) is shown in figure 4.9. The graph shows the current noise flowing through one of the actuator coils used to damp and control the orientation of the mirror. The upper trace shows the noise in the old system and the lower trace the noise in the redesigned servo system. As can be seen, the noise has been dramatically reduced, in this case by $\sim 80\,\mathrm{dB}$ at 200 Hz. Note that the noise in the new system is dominated by the final driving amplifier stage above $\sim 100\,\mathrm{Hz}$. This would probably limit the sensitivity of the detector at 200 Hz to $\sim 10^{-17}\,\mathrm{m}/\sqrt{\mathrm{Hz}}$

The sensitivity of the 10 m prototype detector after improving the noise performance of these local control servos can be seen in figure 4.10. As can be seen in comparison to the previously measured sensitivity (the upper trace), the noise present in the detector output signal has been reduced by $\sim 20\,\mathrm{dB}$ from 100 Hz $\rightarrow$ 700 Hz. It is also interesting to note the reduction in the wire resonance peaks, seen at around 450 and 900 Hz. Previously, these peaks (which were identified as being due to the suspension wires supporting the input mirrors) were being excited by the noise in the orientation control servos. The wire resonances present in the lower trace however were identified as being due mainly to the wires supporting the end mirror in the primary cavity.

It should be pointed out that the spectra shown in figures 4.10 and 4.11 were originally taken from 100 Hz $\rightarrow$ 3 kHz and so some of the resolution is lost when concentrating on the 100 Hz $\rightarrow$ 1 kHz region. This accounts for the difference in appearance of these spectra when compared to the other spectra shown in this

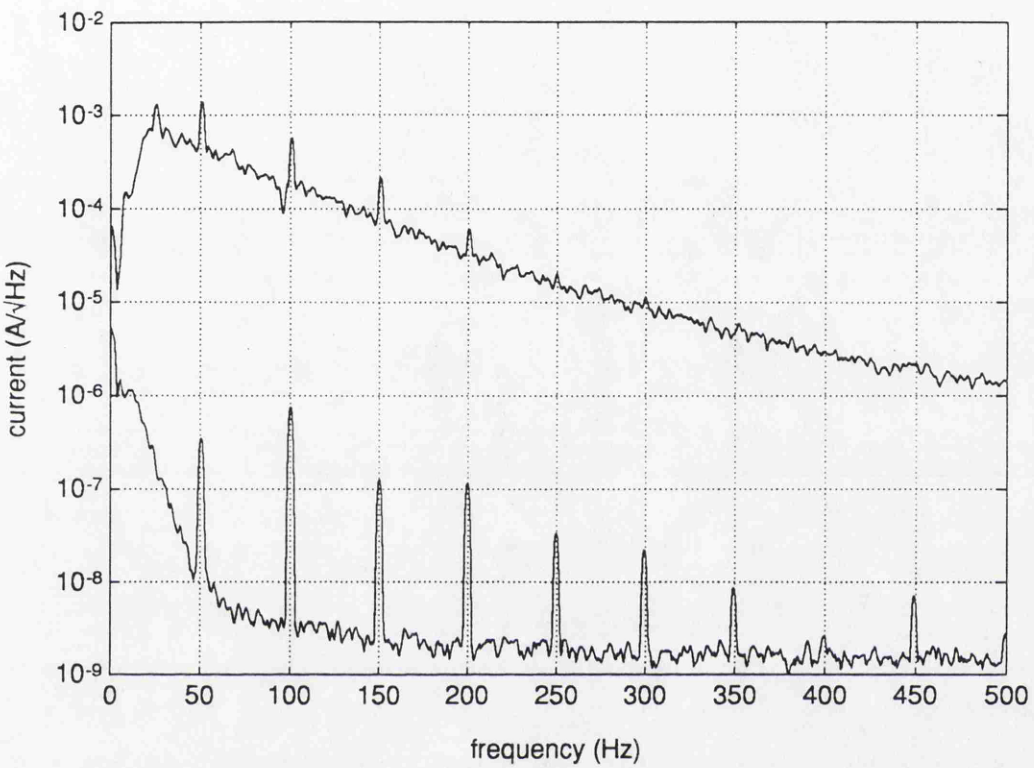

Figure 4.9: *Noise measured in the current through one of the feedback actuator coils controlling the tilt of the primary input mirror. The upper trace shows the noise in the old feedback system, the lower trace showing the noise in the re-designed system.*

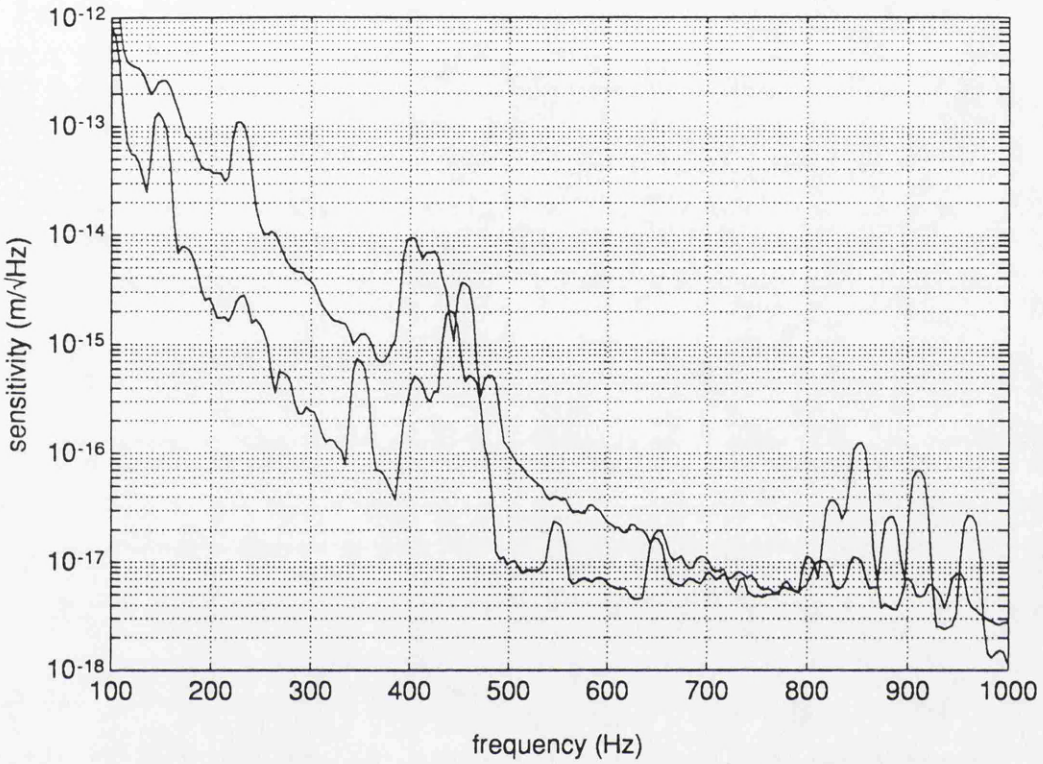

Figure 4.10: *Displacement sensitivity of the 10 m prototype before and after reducing the level of noise present in the input mirror orientation control servos. The upper trace is the same as in figure 4.8.*

chapter.

The primary and secondary cavity end mirrors

As discussed in Chapter 5, the suspension systems used to support the end mirrors in the primary cavity were replaced with low noise double pendulum suspension systems. The original systems installed in the end tank of the primary cavity (discussed in the first half of Chapter 5) had no effect on the detector noise at the time of installation. Having then improved the noise performance of the input mirror suspension control systems, the most likely candidates for limiting the low frequency sensitivity of the detector were the secondary end mirror local control systems.

This suspicion was confirmed experimentally by reducing the low pass filtering on the drive signal to the control actuators in this system. The result was an increase in the low frequency noise in the detector output signal.

The suspension system and the local controls were replaced by a two stage pendulum with local control (sensing and feedback) applied only to the intermediate mass (discussed in detail in the second half of Chapter 5). The predicted limit to the detector sensitivity using such a system is $\sim 8 \times 10^{-19}\,\mathrm{m}/\sqrt{\mathrm{Hz}}$ at 100 Hz and falls off very steeply after this (see figure 5.21 in Chapter 5).

The effect of replacing the suspension system and local control of the end mirror in the secondary cavity with the double pendulum system can be seen in figure 4.11. Again the noise level present in the detector output signal decreased by $\sim 20\,\mathrm{dB}$ at low frequencies. The peaks in the spectra due to the wire resonances remained at the same level, confirming that these were due to the wires supporting the end mirror in the primary cavity. Indeed most of the background noise appeared now to be due to the local control system used on the primary cavity end mass. Studying the predicted noise in this control system (which is shown in figure 5.14 in Chapter 5) one can see that it is very close to the detector sensitivity in the low frequency region. This was confirmed experimentally by adjusting the gain of the primary end mirror local control systems and observing the corresponding increase

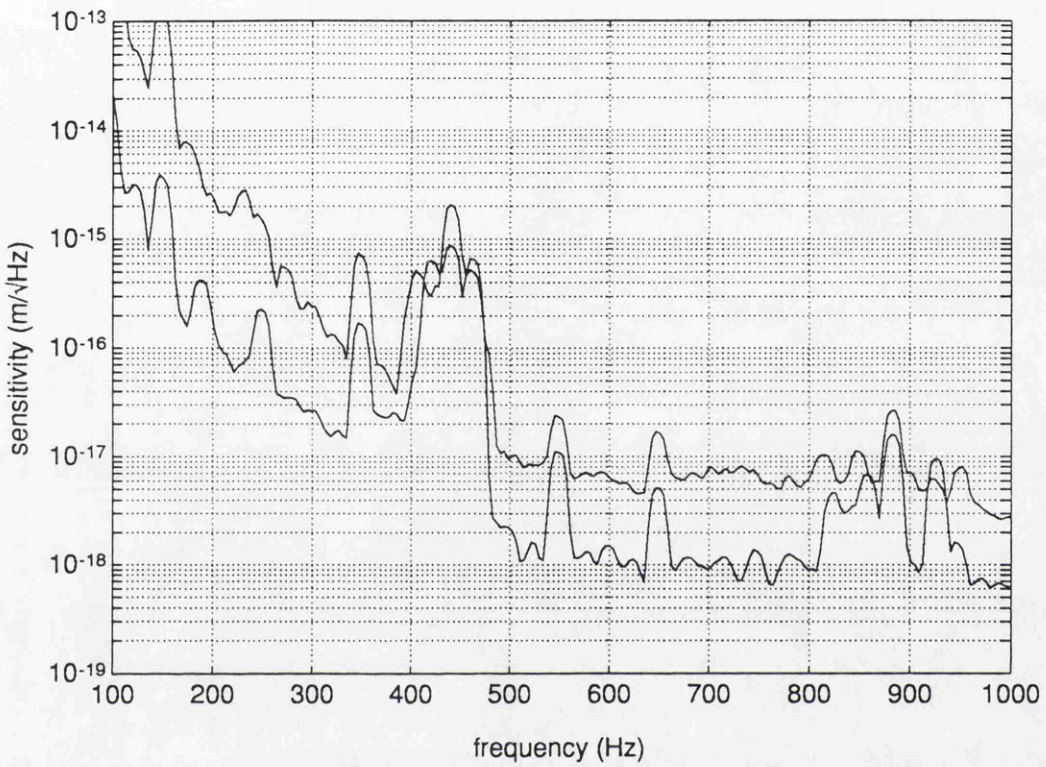

Figure 4.11: *Displacement sensitivity of the 10 m prototype before and after replacing the secondary cavity end mirror suspension and local control system.*

or decrease in the low frequency noise in the detector signal.

Because of the relatively poor low frequency noise performance of this particular control system (compared to the system installed to support the secondary end mirror) it was decided to replace the double pendulum system controlling the primary end mirror with one similar to the control system installed to support the secondary end mirror. This once again resulted in an improvement in the low frequency performance of the interferometer, as can be seen in figure 4.12. It is interesting to note that not only has the background noise been reduced by up to 15 dB at some frequencies, but the wire resonances have also been significantly reduced. The remaining peaks are probably due to wire resonances in the cavity input mirror suspension systems.

4.5.2 Acoustic noise

It was often noted when examining the detector sensitivity, that parts of the spectrum could be excited by acoustic noise. One of the most significant sources of acoustic noise in the lab appeared to originate from the fan built into the rear of the spectrum analyser used to measure the detector sensitivity. The top graph in figure 4.13 shows the effect on the detector sensitivity of simply switching on and off the fan. The upper trace here is the same as was shown in figure 4.6, *i.e.* the detector sensitivity as recorded immediately after the new calibration procedure had been tested. A broad band of noise can be clearly seen between 1.2 and 1.7 kHz. Although this particular problem could temporarily be solved by switching off the analyser fan whilst taking measurements, as can be seen in the upper plot in figure 4.13, even with the fan switched off, there is some indication that a small amount of noise is still present in the detector output.

A similar effect was noticed at lower frequencies during investigations into the orientation control servos mentioned in the previous section. The lower graph in figure 4.13 shows the increase in noise present in the 800 Hz region on the raw detector output signal due to acoustic excitation of the detector input optics (the excitation being provided by a loudspeaker driven by a white noise source). In

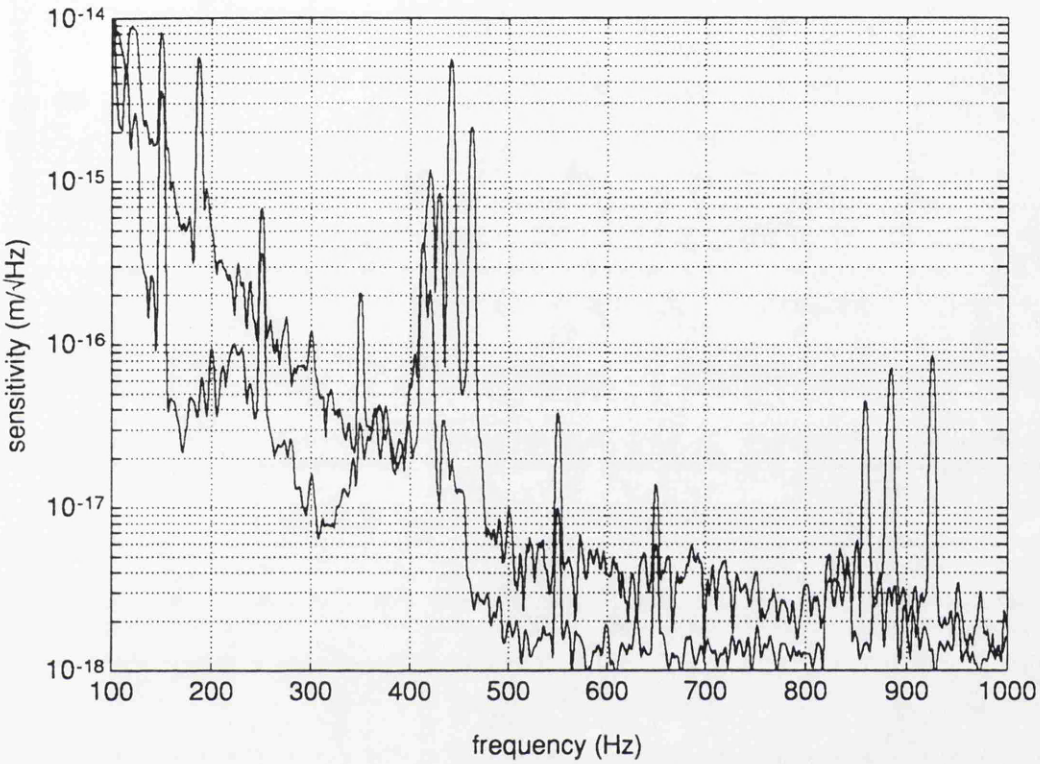

Figure 4.12: *Displacement sensitivity of the 10 m prototype before and after replacing the double pendulum suspension control system used on the primary cavity end mirror to a system similar to the one used in the secondary cavity end mirror.*

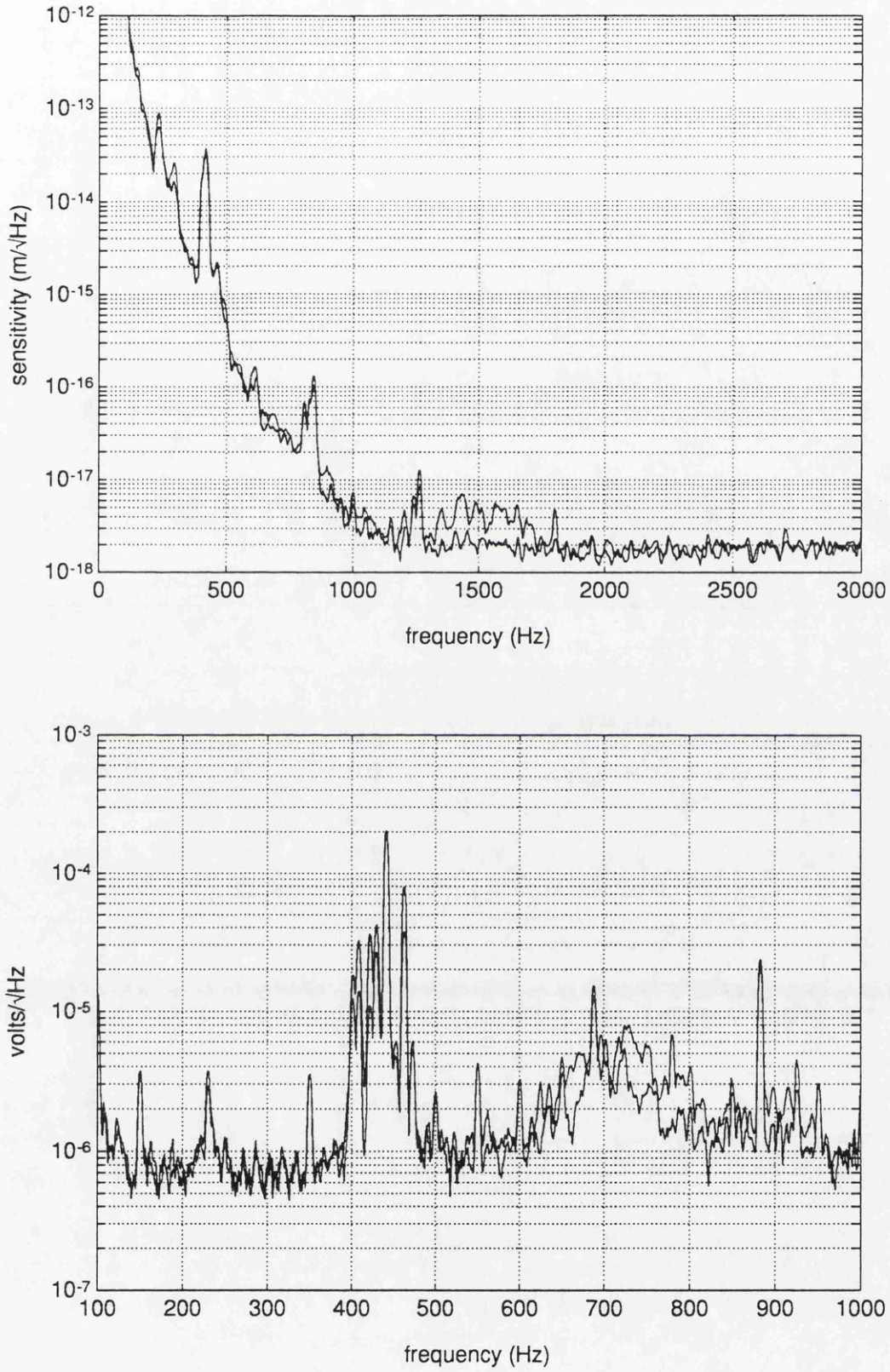

Figure 4.13: *Acoustic noise affecting the noise levels present in the 10 m prototype detector output signal. The upper graph shows the calibrated detector output signal, whereas the lower graph shows the raw uncalibrated detector output.*

particular it was noted that the mount which was used to hold the end of the optical fibre was particularly sensitive to acoustic noise.

One of the most likely ways in which acoustic or vibrational noise in the lab can couple into the detector signal is through inducing fluctuations in the position of the input laser beam with respect to the suspended cavities. The problem of positional and geometrical fluctuations in a laser beam and its effect on interferometric measurement has been discussed by Meers [19] and by Rüdiger *et al.* [28]. One possible mechanism through which positional fluctuations can couple into the signal detected from two interfering beams occurs when there is a static spatial phase difference between the beams. For example, consider the electric fields of two interfering beams at the output of an interferometer, E_1 and E_2, where E_2 has been tilted by an angle α with respect to E_1. The combined electric field can be written as

$$E_1 + E_2 e^{j(\phi + k\,\alpha\,x)}\ , \tag{4.7}$$

where ϕ represents the phase difference between the two beams (which is normally what is detected) and the time dependence of the electric fields is implicitly assumed in E_1 and E_2. A fluctuation in the lateral position of the second beam can be represented by $x \rightarrow x + \delta x$. This introduces a spurious phase difference, $k\,\alpha\,\delta x$ between the two beams. Any system which may be used to detect the phase difference between the two beams will therefore also detect a signal proportional to the fluctuations in the lateral position of the two beams.

Relating this effect to the two cavities in the 10 m prototype, one can see that if the two beams viewed in reflection from the cavities are slightly misaligned (due to a misalignment of the cavity mirrors with respect to the input laser beam) then positional fluctuations of the input beam can couple into the detected signal. In order to reduce these effects, steps were taken to suppress the positional fluctuations induced due to acoustic and vibrational disturbances in the lab. Further improvements could be obtained by implementing an automatic alignment system, such as the one discussed in Chapter 3, to minimise the misalignment of the two interfering beams viewed in reflection from each cavity.

Experimental investigations revealed that most sensitive component appeared

to be the output end of the optical fibre. Although the fibre end and all of the following optics situated outside of the main detector vacuum system were housed inside an acoustic shield (consisting of a perspex box covered in lead backed foam), the effectiveness of the shield in reducing the acoustic noise from the lab was found to be minimal. The acoustic shielding around the input optics was substantially improved by replacing the perspex box with one made from wood (the wooden box was also clad in lead backed foam). Also, the aluminium plate on which the optics were mounted was supported by two 3 layer lead/rubber stacks to give some isolation from the vibrations present in the optical table on which it sat.

In addition, the mount which held the fibre and the matching lens was not particularly rigid and was therefore replaced with a solid mount machined from a block of aluminium. The new mount, which can be seen in figure 4.14, has the matching lens bolted firmly to the front of the fibre holder. The fibre itself is glued into a short length of glass capillary tube and can be finely positioned using the adjustment mechanism. Once correctly in position the fibre can be glued into the mount.

These measures have proved to be extremely successful in reducing the coupling of acoustic noise into the detector output signal. No effects due to acoustic noise in the lab, such as the ones shown in figure 4.13, have since been observed, despite significant improvements in the detector's low frequency performance. However as the sensitivity continues to improve, the problem of acoustic noise coupling into the detector output signal will undoubtedly return and the only real solution to the problem will be to suspend the fibre end inside the main detector vacuum system, or alternatively, implement a suspended mode-cleaner (which should reduce the effect of acoustically induced positional fluctuations of the beam).

4.5.3 Excess noise on the laser light at *rf*

As the overall low frequency performance of the detector improved due to the reduction in the orientation and local control noise as discussed in earlier sections, more structure became apparent in the low frequency output noise. To illustrate

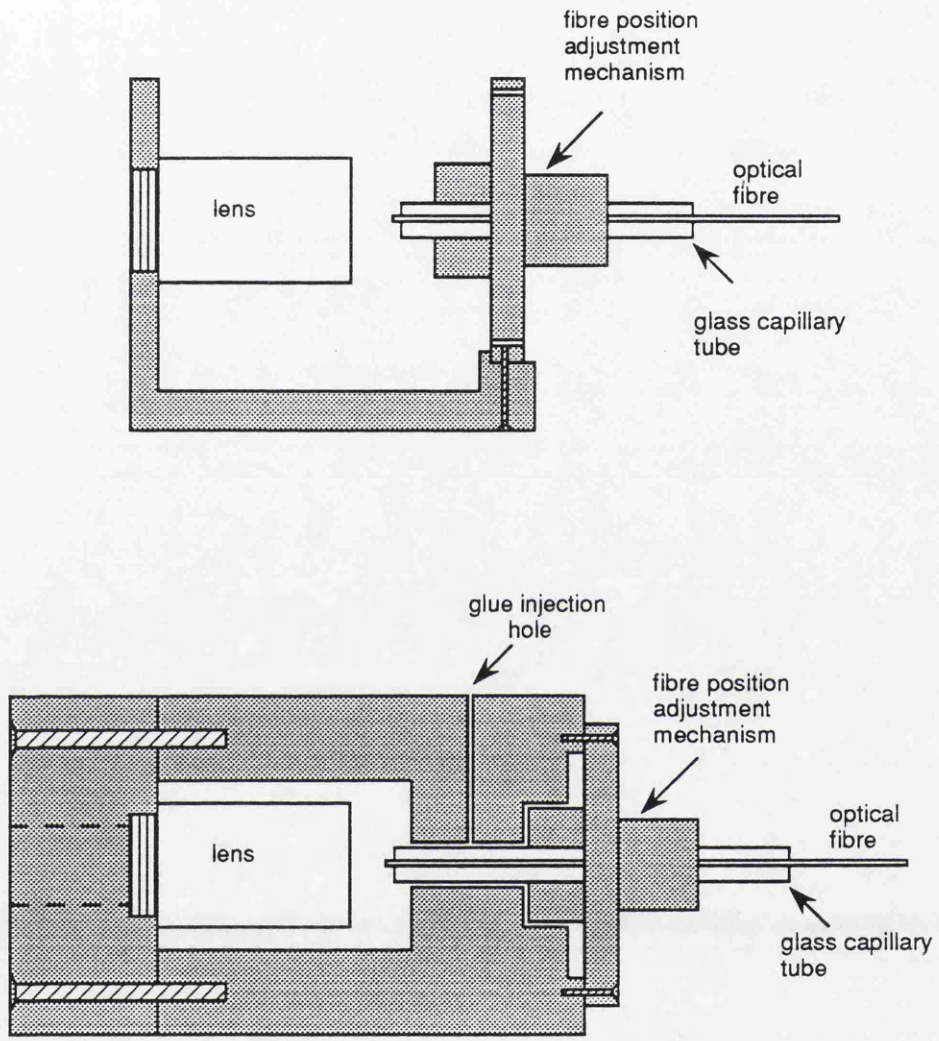

Figure 4.14: *Schematic diagram showing a side view of the old (above) and new (below) optical fibre mounts.*

this, examine the noise shown in figure 4.12. The upper trace, showing the detector output signal is dominated by noise in the local damping control system used to control the end mirror in the primary cavity. The smooth background of noise which can be seen here is fairly typical of electronic noise or sensor noise originating from the local damping controls. After significantly reducing this noise however, the background takes on a more structured appearance. In fact the structure apparent in the noise shown on this graph was very similar to the structure which could be observed on the intensity of light at frequencies close to the modulation frequency (12 MHz).

To illustrate how this noise arises, consider light reflected from one of the cavities in the 10 m prototype when the cavity is off resonance. The reflected light, which is *rf* phase modulated, is rejected from the polarising beamsplitter and detected using a photodiode. Some of the reflected light does however return back towards the main beamsplitter and the input optics. If some of this light is then reflected back towards the cavity (*e.g.* by reflection off the Pockels cell or the fibre end) it will interfere with the main reflected beam. A signal will therefore be detected, at the modulation frequency, proportional to the phase difference between these two beams which will vary if the back reflecting components (including the main cavity input mirror) move or vibrate (*e.g.* due to seismic excitation). This shows up as 'excess light noise' above the shot noise level on the signal appearing at the output of the mixer which follows the detection photodiode. The excess light noise measured on the signal detected after the mixer on the primary cavity photodiode is shown in figure 4.15, along with the measured shot noise from a white light source of equal intensity (3 mA DC photocurrent through the photodiodes, representing the minimum light intensity on the photodiodes with the cavities locked). As can be seen, there is a significant amount of excess light noise present on the demodulated signal at low frequencies and there appears also to be an effect at higher frequencies. The actual level of light noise varied depending on how well the motion of the input mirrors and central mass were damped. Clearly, with the improvements in the low frequency performance of the interferometer, these large levels of excess light noise could not be tolerated since they

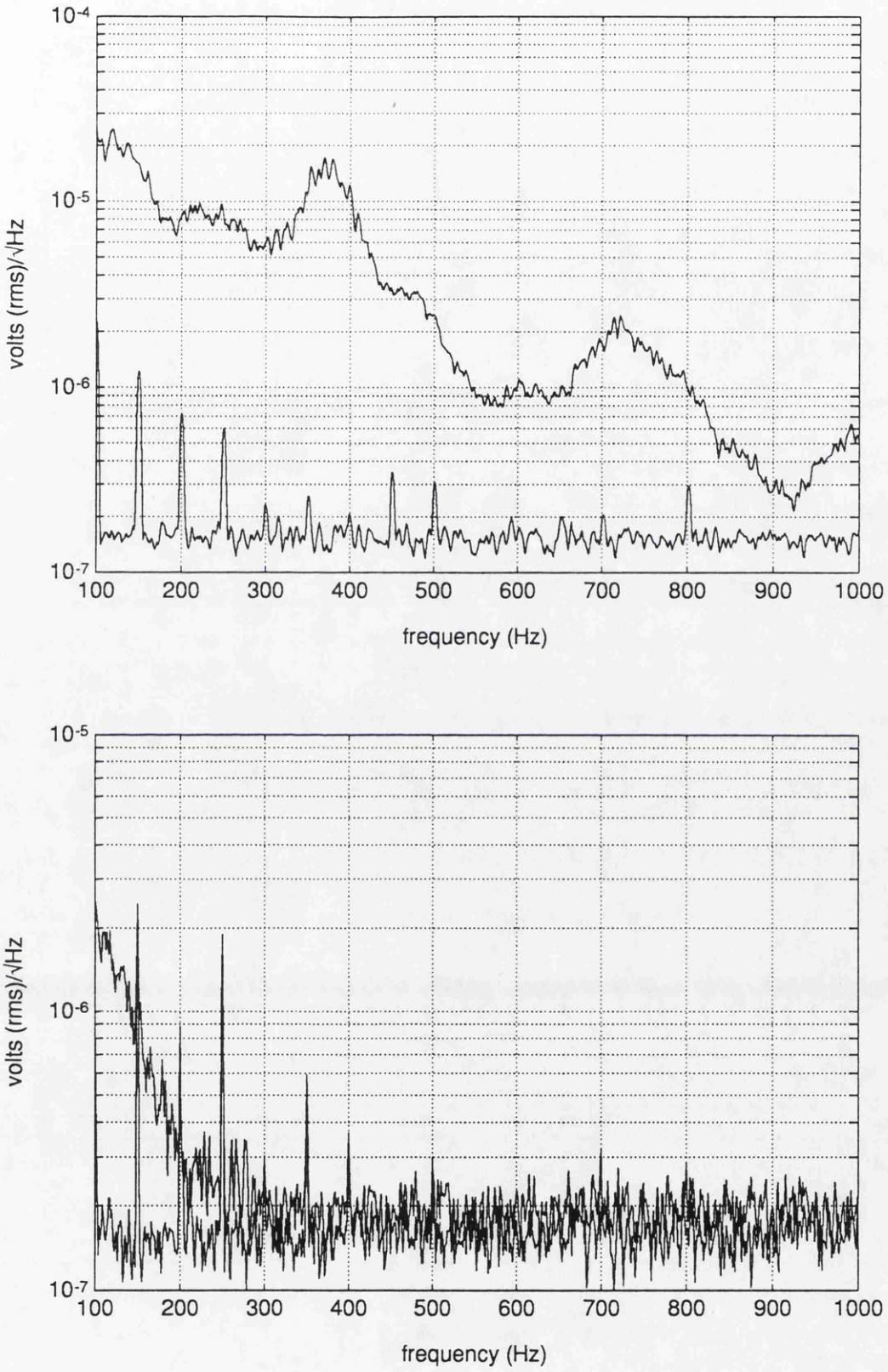

Figure 4.15: *Excess light noise and shot noise as viewed at the error point of the primary cavity servo before (upper trace) and after (lower trace) improving the optical isolation.*

were already high enough to potentially limit the sensitivity. For example, the excess noise is $\sim 20\,\mathrm{dB}$ above shot noise at 500 Hz. This would limit the detector sensitivity to $\sim 2 \times 10^{-18}\mathrm{m}/\sqrt{\mathrm{Hz}}$. This was very close to the actual noise level measured in the detector output signal (see figure 4.12).

The single Faraday isolator (which can be seen in figure 4.1) was replaced by two new isolators, which together could give up to 80 dB of isolation (compared to the 30 dB of isolation which could be achieved using the old isolator). In addition an extra isolator was inserted between the output of the optical fibre and the Pockels cell and also between the laser and the input to the optical fibre. The resulting reduction in the light noise can be seen in the lower graph on figure 4.15. The light noise has been reduced to the shot noise limit at $\sim 300\,\mathrm{Hz}$.

With the excess light noise significantly reduced, the noise present in the detector output signal was also reduced, as can be seen in figure 4.16. From the graph it can be seen that there has been a significant reduction of the noise around 400 Hz, suggesting that the peak of excess light noise around this frequency was indeed limiting the detector sensitivity.

The introduction of the extra optical isolation, whilst significantly reducing the levels of excess light noise, unfortunately reduced the throughput of the input optics. This seriously limited the amount of light power which could be used in the interferometer, in this case to $\sim 40\,\mathrm{mW}$ of light after the final isolator. In order to achieve good high power performance with such an interferometer, high quality, low loss optical components will be required in addition to simply increasing the power of the laser.

4.6 Summary and future prospects

Figure 4.17 shows the significant improvements which have been made to the sensitivity of the 10 m prototype detector here in Glasgow over the past 2 years. From 100 Hz up to about 400 Hz the level of noise present in the detector output signal has been reduced by almost 4 orders of magnitude, whereas the noise at higher frequencies has been reduced by almost a factor of 3.

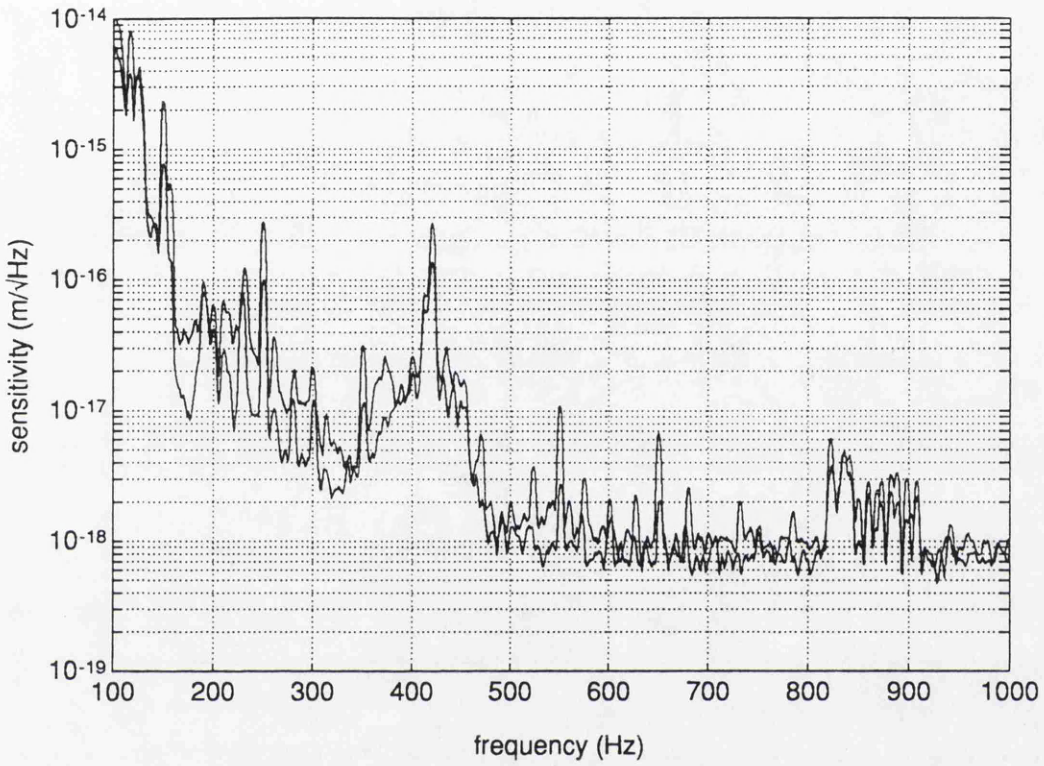

Figure 4.16: *Displacement sensitivity of the 10 m prototype before and after inserting additional optical isolators into the system.*

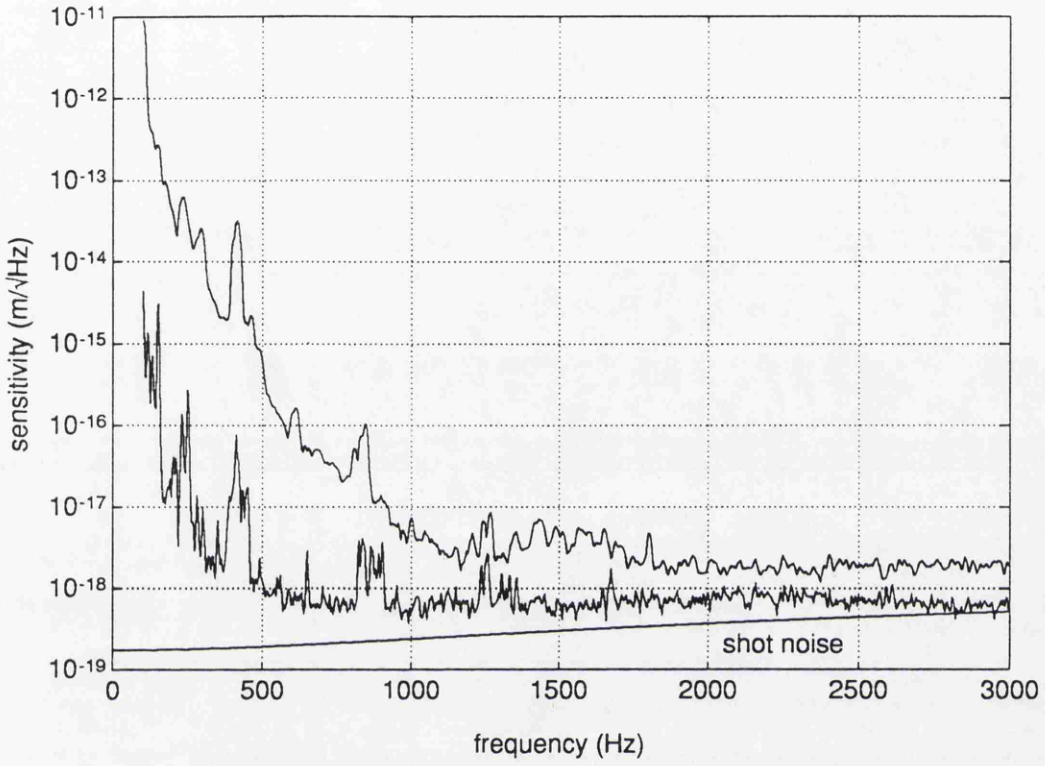

Figure 4.17: *Comparison of the displacement sensitivity of the 10 m prototype detector. The upper trace shows the sensitivity as measured in April 1991, the lower trace as measured in October 1992.*

Most of the reduction in noise, particularly at the lower end of the spectrum, has been due to the replacement and re-design of the local damping controls used on the suspended cavity mirrors, although effects such as excess light noise and beam positional fluctuations began to limit the detector performance as the sensitivity was improved.

The sensitivity around the 3 kHz region now appears to have reached the shot noise limit. However in the $1 \rightarrow 2$ kHz, the noise level was always $1 \rightarrow 2$ dB above shot noise. The most probable explanation for this was the level of electronic noise present in the primary and secondary cavity servo systems, particularly the secondary servo system. In order for the detector to reach the shot noise limited sensitivity, it is essential that shot noise actually dominates over electronic noise at the point where the detector output signal is actually measured (this is discussed in section 2.3.1). In practice, shot noise was only clear of electronic noise in the main detector output signal by at most 6 dB at 1 kHz, due mainly to a lack of gain in the front end. This problem can be solved either by increasing the light power used in the interferometer, or by suitably altering the disposition of gain within the servo system.

The remaining noise at lower frequencies is still significantly above shot noise (by almost 4 orders of magnitude at 100 Hz). The performance of the detector is probably still limited at these frequencies by the orientation control noise in the systems controlling the suspended input mirrors. There is probably also a contribution from seismic noise and possibly from low frequency positional fluctuations in the input laser beam. In order to reduce this noise it will be necessary to install similar low noise double pendulum suspension and control systems for the cavity input mirrors of the type that are now used on the cavity end mirrors. This, along with the suspension in vacuum of the input optics (as suggested in the previous section) should hopefully reduce the low frequency noise to levels close to the shot noise limit.

Once the shot noise limit has been reached over a reasonable range of frequencies it would seem sensible to try to increase significantly the light power in the interferometer in order to try to reach sub 10^{-19} m/$\sqrt{\text{Hz}}$ displacement sensitivities.

At these sensitivities it is likely that other noise sources will begin to influence the sensitivity of the detector. For example, current estimates for the limit to the sensitivity of the detector set by thermal noise in the mirrors themselves (see section 1.6.3), which have been measured to have an internal Q of around 10^4 at the fundamental longitudinal resonance, is around $10^{-19}\,\mathrm{m}/\sqrt{\mathrm{Hz}}$ at 500 Hz.

Overall, the recent improvements in the sensitivity and performance of the 10 m prototype are extremely encouraging. At the time of writing, the displacement sensitivity of the prototype is the best which has been achieved by any laser interferometric detector. Hopefully, future developments should allow further progress to be made. It is hoped that the experience and knowledge gained from the operation of this and other prototypes will ensure that when the proposed large scale detectors are built, they will be able to reach the required sensitivities to enable detection of gravitational waves.

Chapter 5

Double pendulum suspension systems for the 10 m prototype gravitational wave detector.

5.1 Introduction

From the discussions on noise in control systems used in laser interferometric gravitational wave detectors in Chapter 2, and the desire to have good seismic isolation of the interferometer test masses [22], it is clear that the most sensitive components in such an interferometer will almost certainly have to be suspended using a two (or more) stage pendulum if displacement sensitivities of the order of $10^{-22}\,\mathrm{m}/\sqrt{\mathrm{Hz}}$ are to be reached down to 100 Hz. It was therefore decided to build a two stage pendulum suspension system for one of the test masses in the 10 m prototype detector here in Glasgow.

Originally, a system was required to replace the single stage suspension system used for the test mass which acts as the end mirror in the primary cavity of the detector. (For a description of the operation of the 10 m prototype, see Chapter 4.) Here, forces were applied directly to the main test mass to locally damp the mass to ground, using a feedback system based on shadow sensors and coil/magnet feedback actuators (the small permanent magnets being glued directly onto the rear of the test mass). In addition to this, some of the low frequency signals from the laser stabilisation system were also fed back to the test mass, preventing large excursions of the laser frequency (which is stabilised to the primary cavity) at low frequencies (<10 Hz).

There was great concern that these large low frequency signals, fed back directly to the end mass in the primary cavity, could be up-converted *via* some non-linear process (*e.g.* squeezing of the glue joints between the magnets and the test mass, or Barkhausen noise in the magnets), providing broadband noise at detection frequencies which could potentially set a limit to the sensitivity of the interferometer. By careful design of a suitable two stage pendulum suspension, all control forces applied *via* the coil/magnet actuators to the main test mass could be transferred to similar actuators acting on an intermediate mass. Provided the control systems acting on the intermediate stage are reasonably narrowband, any high frequency noise ($1 \rightarrow 3\,\mathrm{kHz}$) caused by the up-conversion of large low frequency signals should be passively attenuated by the action of the extra pendulum stage between the actuator and the main test mass.

Such a two stage pendulum was subsequently designed and implemented on the 10 m prototype. The original shadow sensors (which sensed the motion of the main test mass) were retained, whilst all the feedback forces were applied to an intermediate mass. A full discussion of this is given in section 5.2.

Following the successful operation of this system on the 10 m prototype it was decided to build a similar system based on the same mechanical design but with all of the local control sensing and feedback performed at the intermediate mass. This system was installed as a replacement for the suspension system supporting the end mirror in the secondary cavity of the 10 m prototype. As a result of this particular sensing and feedback arrangement, the noise performance of this system at low frequencies ($100\,\mathrm{Hz} \rightarrow 500\,\mathrm{Hz}$) is much better than that of the original system. The design, testing and evaluation of this system is described in section 5.3.

The study of these systems and the effects of noise in local control damping systems led to a great deal of work being carried out on the prototype resulting in a substantial reduction in the low frequency noise present in the detector output signal (as discussed in greater detail in Chapter 4).

5.2 A two stage pendulum suspension system for the end mirror in the primary cavity of the 10 m prototype.

5.2.1 Mechanical design of the double pendulum.

The original suspension system used to support the end mass in the primary cavity consisted of a single loop of steel wire (0.006″ diameter). The length of the pendulum suspension was $\sim$ 33 cm. Small silica 'lugs' were attached to the side of the test mass, with suitable grooves cut along the sides, providing well defined break off points for the wire on either side of the test mass. The suspension wires were held using two clamps which sat on an aluminium support structure (commonly referred to as the 'top hat' support structure) which itself was supported by a 5 layer lead/rubber seismic isolation system. This construction was situated inside the end tanks of the interferometer vacuum system.

Local damping of this high Q pendulum suspension system (to prevent excessive motion of the pendulum at its resonant frequency due to seismic noise) was performed using standard shadow sensors, feeding back signals to coil/magnet actuators.

To simplify the design of the new double pendulum suspension system it was decided to retain the 5 layer stack and the 'top hat' support structure, and simply replace the single stage suspension with a two stage system. The 'top hat' provided a convenient structure from which the various coils, which were to apply the feedback forces to the intermediate mass, could be attached. Unfortunately, due mainly to the limited amount of space inside the top hat structure, and to ensure ease of access to the intermediate mass and actuators, this meant that the intermediate mass had to be physically smaller than the main test mass. The upper pendulum was chosen to be about 10 cm and consisted of two single steel wires (0.012″ diameter) clamped either side of the intermediate mass and attached to two clamps on top of the 'top hat' support structure; the lower suspension consisted of two loops of steel wire (0.006″ diameter) slung around the main test mass and clamped to the sides of the intermediate mass. This particular suspension

arrangement allowed the tilt, rotation, longitudinal and sideways motion of the main test mass to be fully controlled by applying forces only to the intermediate mass.

The suspension system is shown schematically in figure 5.1.

As discussed in Chapter 2 (section 2.4.4), a system in which both suspended masses are approximately equal and both suspensions are of the order of 0.5 m long would have probably been more desirable. Such a system is, as far as local control noise is concerned, capable of much better performance since both pendulum resonances are reasonably low in frequency and quite close together. This allows a very narrowband servo to be used to damp the pendulum resonances, and, since the resonances occur at around 1 Hz, any noise resulting from the local control system at the detection frequencies (100 Hz up to a few kHz) is greatly attenuated by the $\frac{1}{f^4}$ behaviour of the double pendulum. However, with the particular pendulum lengths and masses which were chosen (allowing the new double pendulum to be accommodated into the existing pendulum support structure), the principles of the control of a two stage pendulum and the resulting noise performance of such a system could nevertheless be tested.

5.2.2 Actuators and sensors

The signals used to locally damp the double pendulum system were derived from the existing shadow sensors, situated behind the main test mass. These are shown in figure 5.2, which shows a side view of the two stage pendulum and the 'top hat' support structure. Also shown are some of the coil/magnet actuators used to apply forces to the intermediate mass.

Three shadow sensors, positioned equilaterally around the rear of the test mass produce signals which can be suitably combined to derive signals corresponding to the tilt, rotation and longitudinal motion of the mass. Sideways motion was detected using an additional sensor situated near the side of the main test mass. These signals, after suitable filtering (which is discussed later in section 5.2.4) were then fed back to the coil/magnet actuators which can be seen in figure 5.3. Each

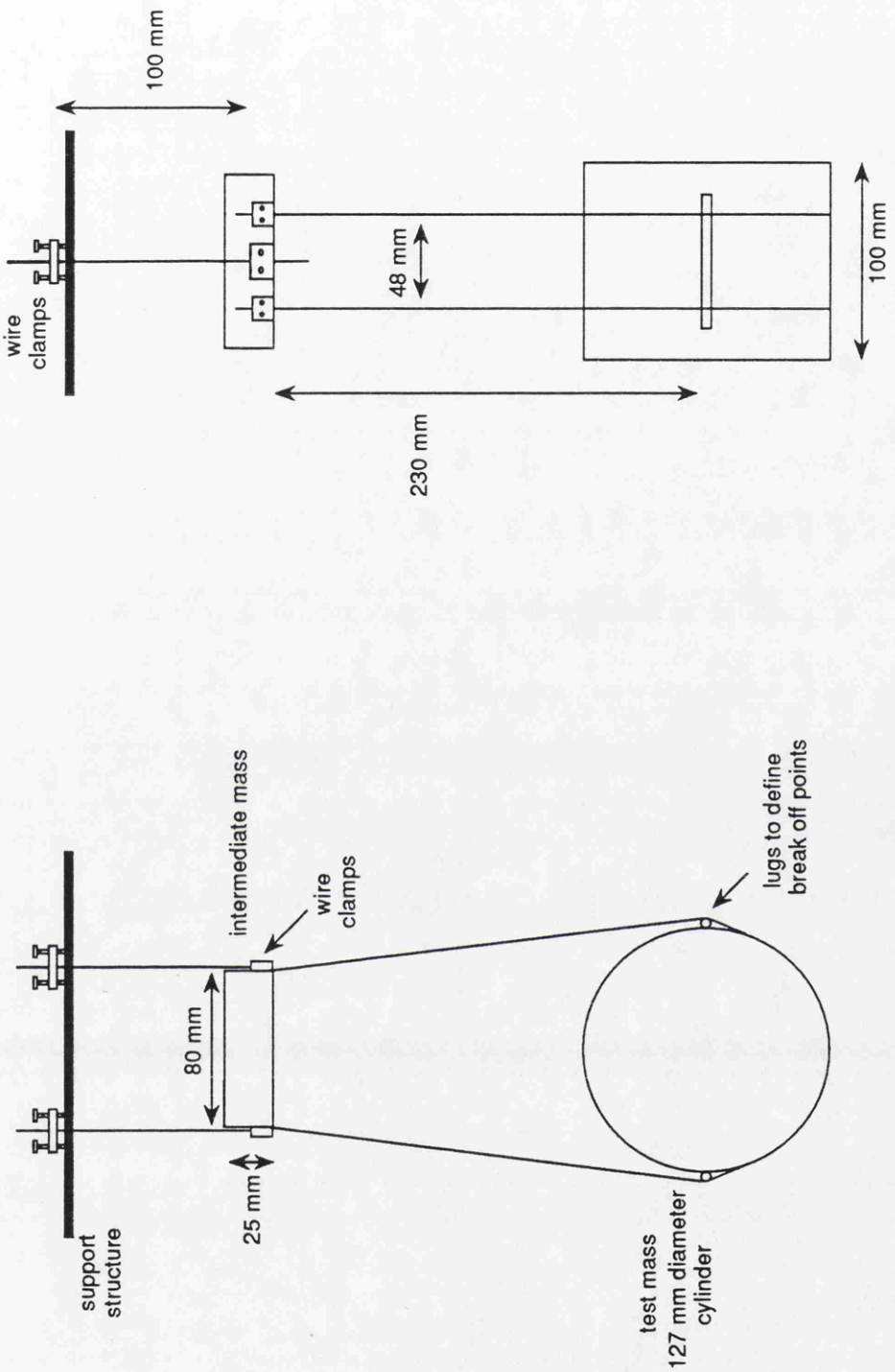

Figure 5.1: *Schematic diagram of the two stage pendulum suspension designed for use in the 10 m prototype interferometric gravitational wave detector.*

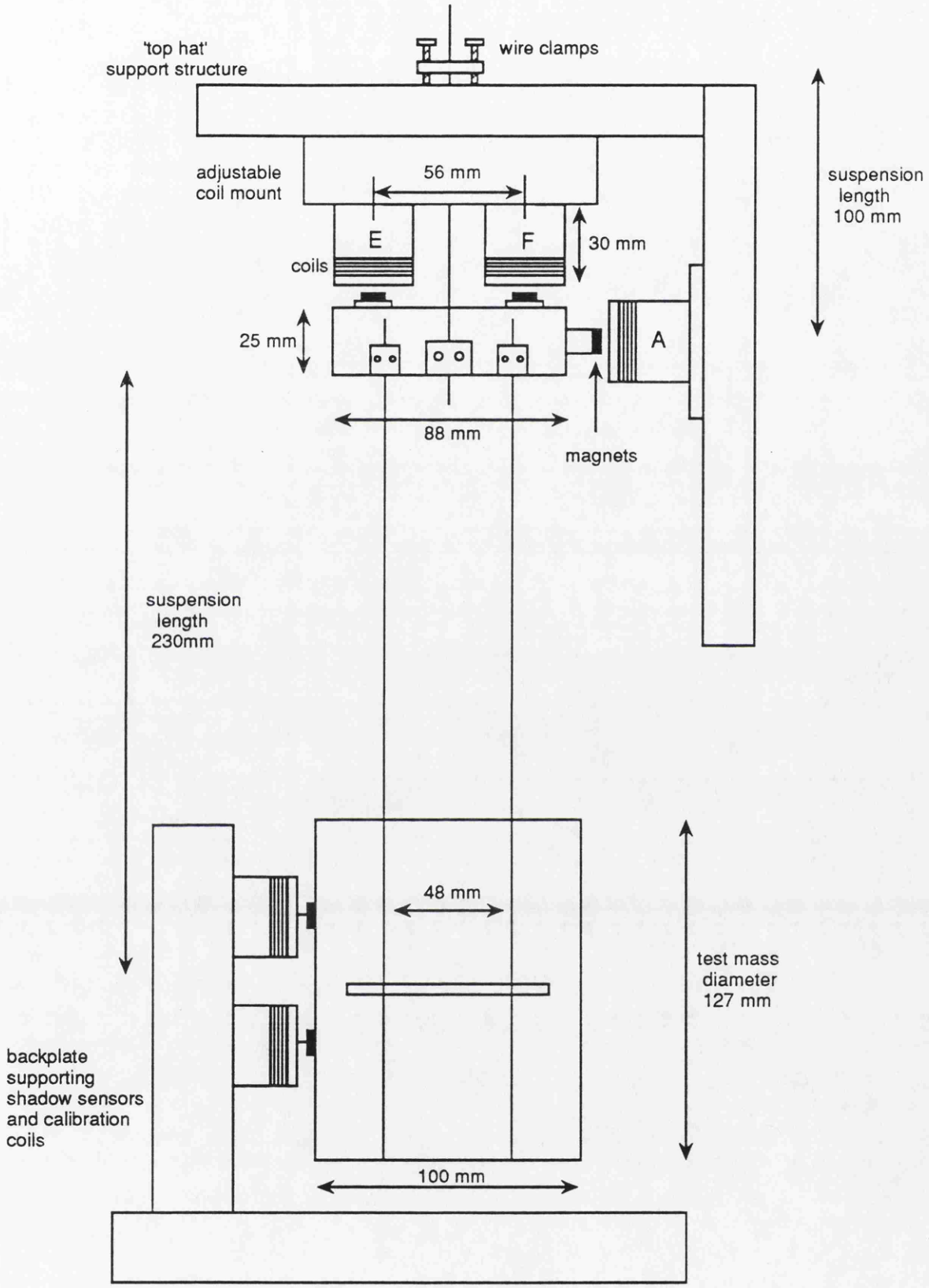

Figure 5.2: *Schematic diagram of the two stage pendulum suspension designed for use in the 10 m prototype interferometric gravitational wave detector (as viewed from the side).*

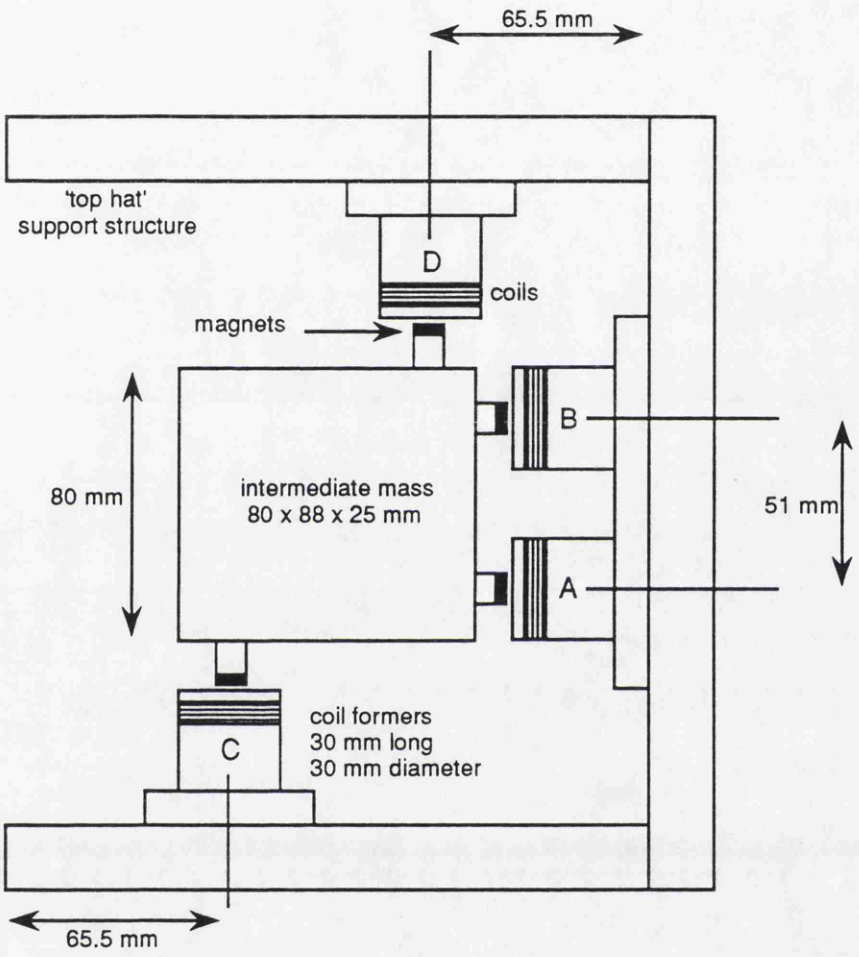

Figure 5.3: *Plan view of the intermediate mass of the two stage pendulum showing the coil/magnet actuators used to control the longitudinal, rotation and sideways motion of the pendulum.*

coil consisted of approximately 500 turns of enameled copper wire wound round plastic coil formers (indicated on both figure 5.2 and figure 5.3). The plastic coil formers were obtained from the gravitational wave group at the Max-Planck-Institut für Quantenoptik in Munich, where they are used extensively in the local damping controls of the 30 m prototype gravitational wave detector [54]. The magnets used were small disc NdFeB magnets (9mm diameter, 3 mm thick).

As can be seen from the diagrams, two actuators are used to control each of the four degrees of freedom. By driving common signals to actuators A and B, the mass can be moved longitudinally; similarly, by driving common signals to actuators C and D the mass can be rotated. Differential signals applied to actuators C and D allow the mass to be moved sideways and differential signals applied to actuators E and F tilt the mass.

The actuators were carefully set up so as to ensure minimum cross-coupling between different degrees of freedom. Their positions could be crudely adjusted using the screws and slotted holes in the coil backing plates which attached the coils to the 'top hat' structure. In addition to this, the coils used to adjust the tilt of the mass had a sprung adjustment mechanism allowing these coils to be positioned reasonably accurately with respect to the magnets on the intermediate mass.

5.2.3 Pendulum transfer functions

In order to characterise the mechanical response of the two stage pendulum, some measurements were made to determine the transfer functions of the degrees of freedom of the system which were to be controlled.

Sinusoidal forces were applied to the intermediate mass by driving the actuators from a signal generator. The response of the main test mass was measured using the shadow sensors which were to provide the signals for local damping of the pendulum system. Once the transfer functions between applying a force to the intermediate mass and the motion of the main test mass were determined, the electronics necessary to complete the local damping feedback loop could be

designed to suit this particular system.

Figures 5.4 and 5.5 show the response of the main test mass to signals applied *via* the coil/magnet actuators at the intermediate mass. As can be seen from the first three graphs, two resonances are present in the longitudinal, rotational and sideways degrees of freedom, whereas for tilt only one resonance appears below 10 Hz. In fact, there is an upper resonance in tilt (caused by the 'stretching' of the lower suspension wires) and was measured to be at ~ 45 Hz. Above the upper resonances in all cases the transfer functions fall with the expected $\frac{1}{f^4}$ response (implying a phase lag of 360°).

The resonant frequencies in each degree of freedom are as follows: longitudinal and sideways, 0.9 and 4.6 Hz; rotation, 1.3 and 8.5 Hz; and tilt, 1.5 and ~ 45 Hz.

The two resonant frequencies measured for the longitudinal degree of freedom can also be calculated from the simple mathematical model of a two stage pendulum described in section 2.4.2. The parameters of the pendulum are: $l_1 = 0.1$ m, $l_2 = 0.23$ m, $m_1 = 0.45$ kg and $m_2 = 3$ kg. From equation 2.17 then, the two resonant frequencies of the system are given by

$$\omega^2 = 540 \pm 509 \,\mathrm{rads^2 s^{-2}} \,, \tag{5.1}$$

which gives 0.9 Hz and 5 Hz. These figures agree very well with the measured values.

It is worth noting that in some of the graphs shown, small amounts of cross-coupling can be seen *e.g.* in the tilt response there is a small 'bump' at ~ 0.9 Hz, caused presumably by cross-coupling with the longitudinal (or sideways) degrees of freedom.

5.2.4 Design of the feedback electronics

General design philosophy

Given the experimentally measured mechanical transfer functions of the two stage pendulum (shown in figures 5.4 and 5.5), it is reasonably straightforward to design the required feedback electronics necessary to perform the local damping.

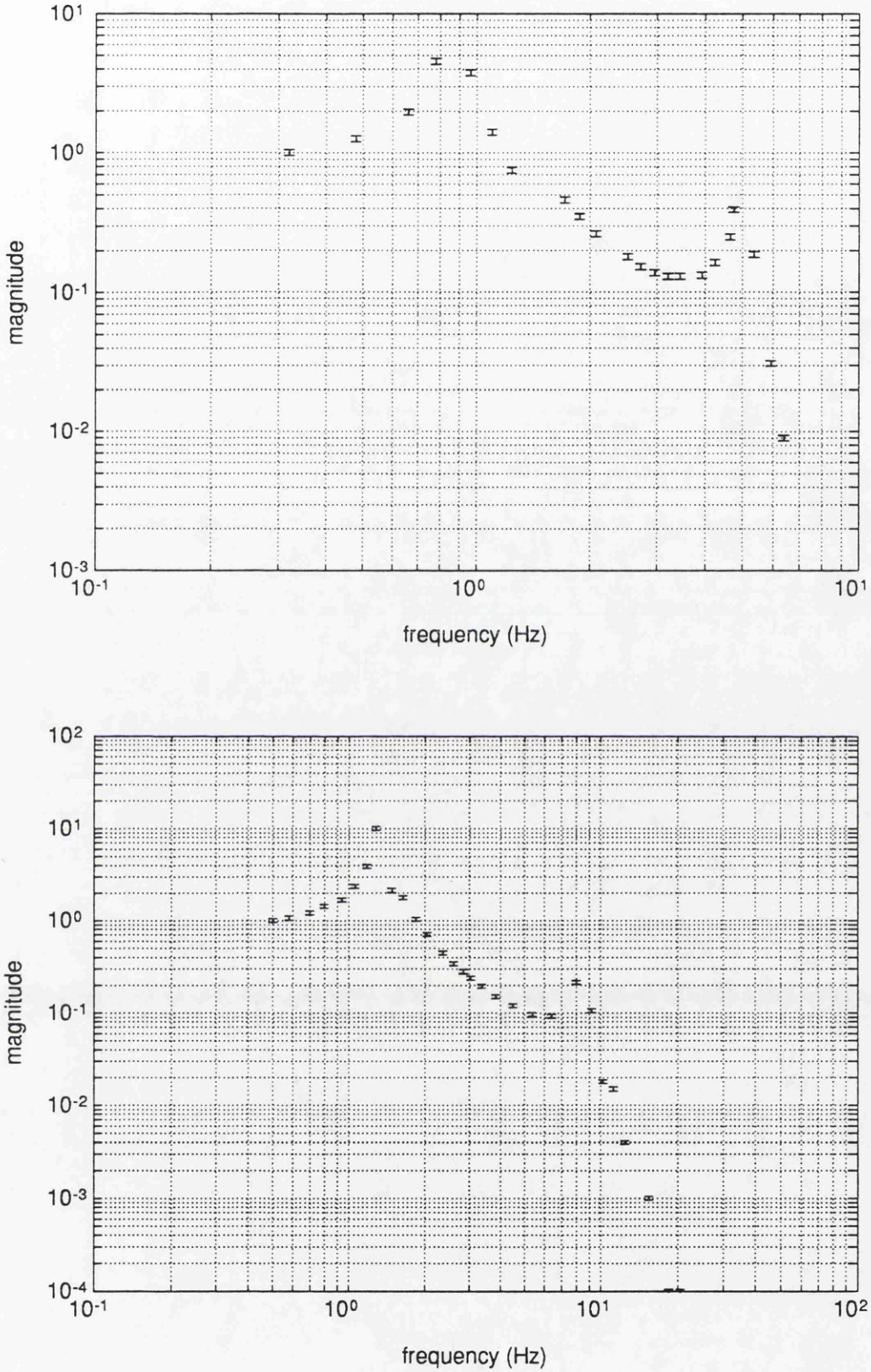

Figure 5.4: *Longitudinal (upper) and rotational (lower) transfer functions of the two stage pendulum.*

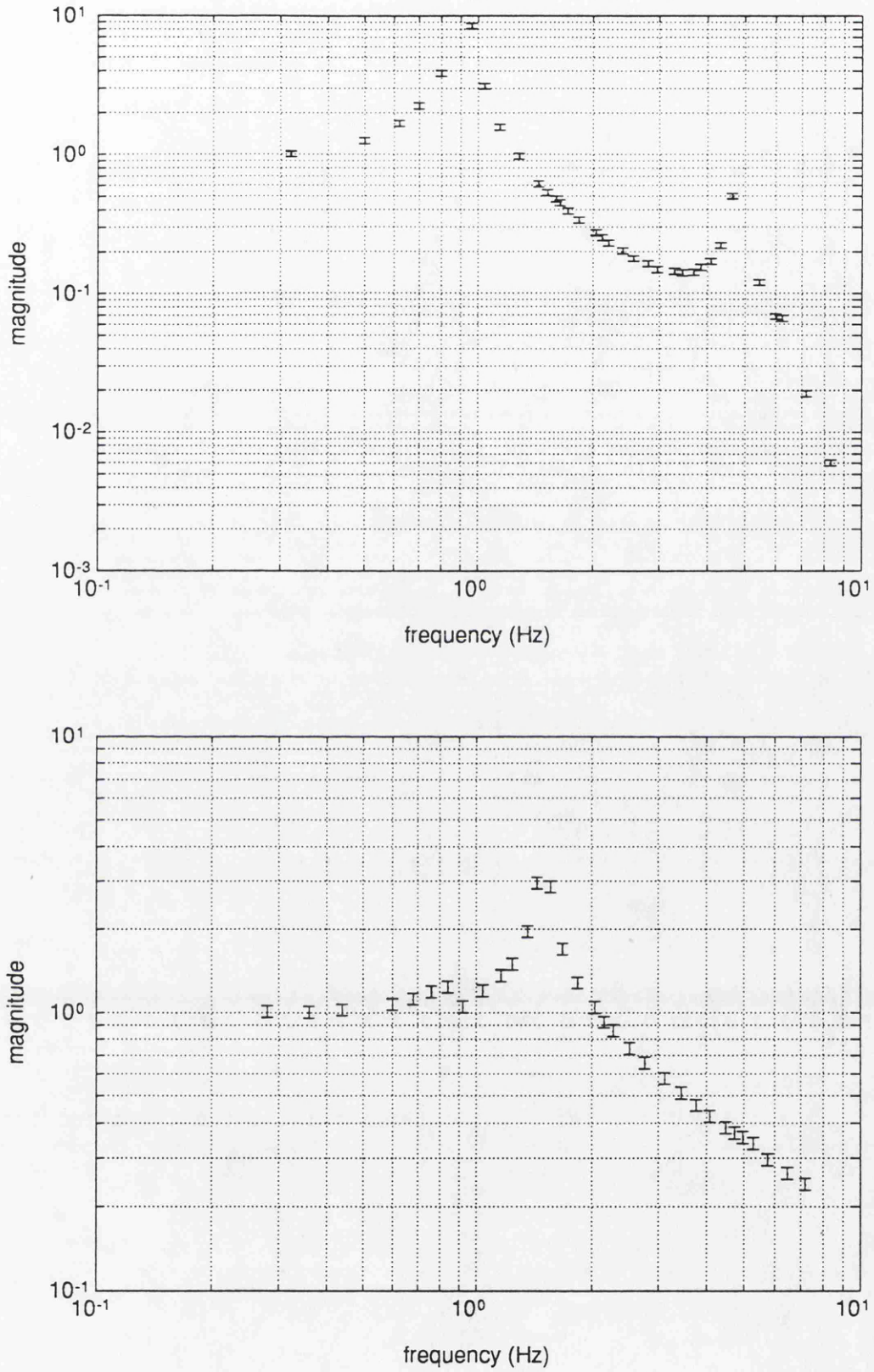

Figure 5.5: *Sideways (upper) and tilt (lower) transfer functions of the two stage pendulum.*

In all degrees of freedom considered (except tilt) two resonances occur, reasonably close together, below 10 Hz. In such a situation it is necessary to control (damp) both resonances. In tilt, since the upper resonance is at $\sim$ 45 Hz, it was possible to damp the lower resonance without exciting the upper resonance which could be left undamped.

In order to control both resonances, it is necessary for the feedback system to have sufficient gain around the resonant frequencies whilst maintaining stability. This is achieved by suitably amplifying and filtering the signals derived from the shadow sensors before feeding back to the pendulum *via* the actuators.

From the plotted transfer functions it can see that above the first resonance, the response of the mechanical system falls off as $\frac{1}{f^2}$, implying a phase lag of 180°. To ensure stability of the damping system at the lower resonance it is necessary to introduce some phase lead in the electronic filtering stage. This can be achieved using a single differentiator. However, above the upper resonance, the response of the mechanical system falls off as $\frac{1}{f^4}$ implying a phase lag of 360°. In order to control the upper resonance and keep the feedback system stable, it is also necessary to ensure that a phase advance of $> 180°$ is introduced *via* the electronic filtering stage.

In general, 3 differentiation stages were used to achieve this, one starting from zero frequency and the other two starting at a frequency roughly between the two resonances. These differentiators were continued up to a sufficiently high frequency to ensure a reasonable phase margin at the upper resonance. Although each degree of freedom had slightly different parameters, the strategy used was similar for each.

A simplified Bode diagram of the electronic filtering used in the longitudinal degree of freedom is shown in figure 5.6. As can be seen, there are three differentiator stages, two of which begin at 1.9 Hz (which is roughly between the two pendulum resonances at 0.9 and 4.6 Hz). These are continued up to $\sim$ 34 Hz. In practice some low pass filtering was also added to the system in order to attenuate as much as possible the amount of noise from the front end which reaches the test mass at 100 Hz. However, since only 20° of phase margin was achieved in the first place at the upper resonance it was not possible to include a great deal of filtering

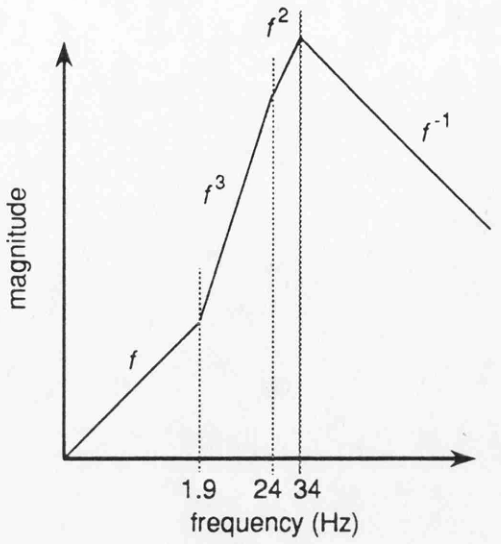

Figure 5.6: *A simplified Bode diagram showing the form of the electronic filtering in the longitudinal feedback control system.*

without compromising the stability of the closed loop system. In the end a single cut at around 24 Hz was introduced which reduced the phase margin at 4.6 Hz to about 10°. Such a filtering arrangement allows the feedback system to be used to lightly damp both the upper and lower pendulum resonances of the two stage pendulum.

The open loop phase and magnitude Bode plots of the complete feedback system (*i.e.* including the electronic filtering and mechanical transfer function of the double pendulum) are shown in figure 5.7. As can be seen from the figure the system has a similar amount of open loop gain at the two resonances. Also, the phase of the system in the regions where the gain is ≥ 1 is $< +180°$ and $> -180°$, implying that the system is stable when the loop is closed.

The modelled step response of the closed loop system is shown in figure 5.8. As can be seen, with the gain set to unity around the upper pendulum resonance, the system is stable and damps down both pendulum resonances in a few seconds.

A block diagram of the circuitry used to perform the local damping of the pendulum is shown in figure 5.9. The electronics can be split up into three main

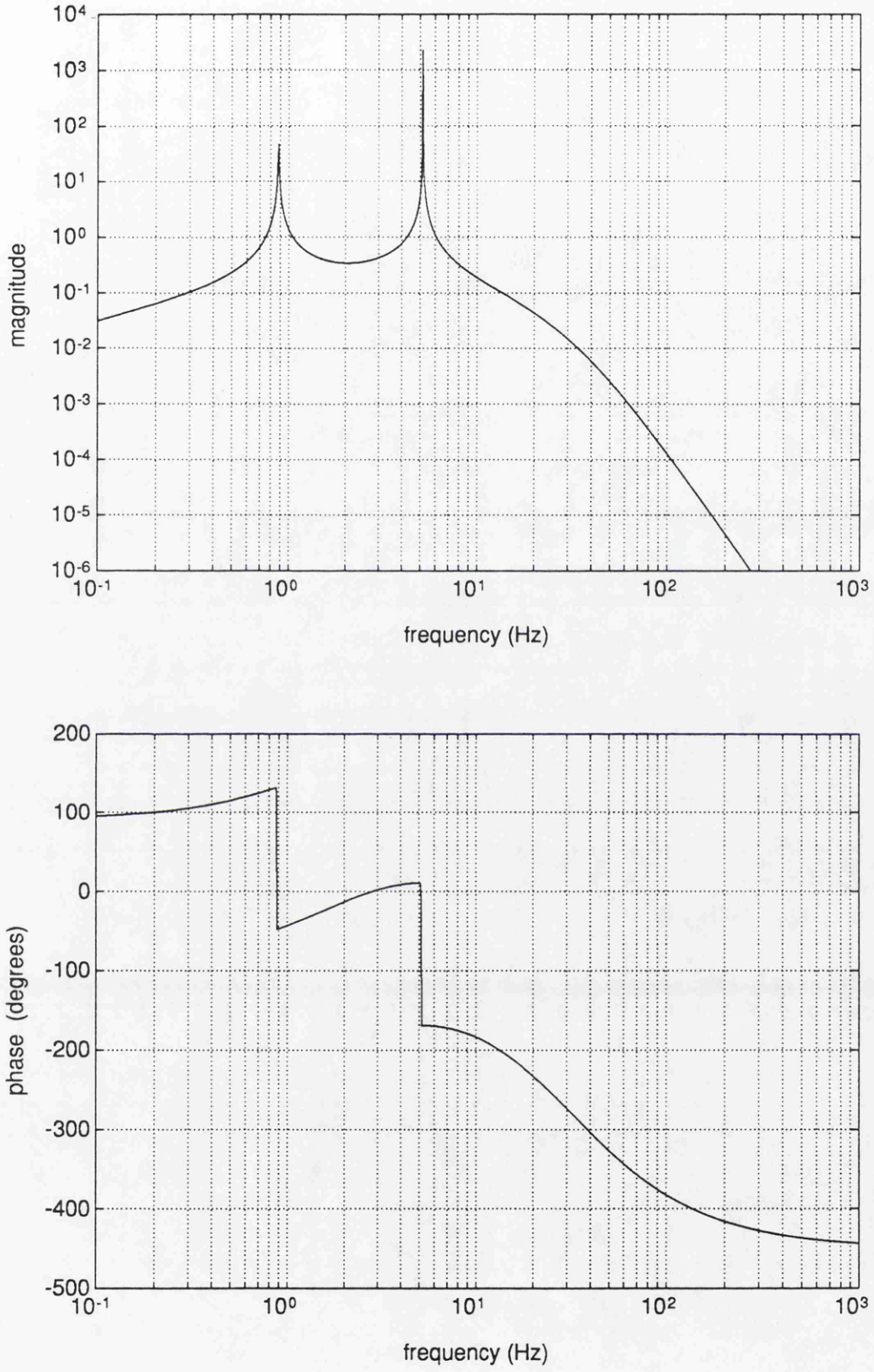

Figure 5.7: *Open loop gain and phase Bode plots for the complete damping system.*

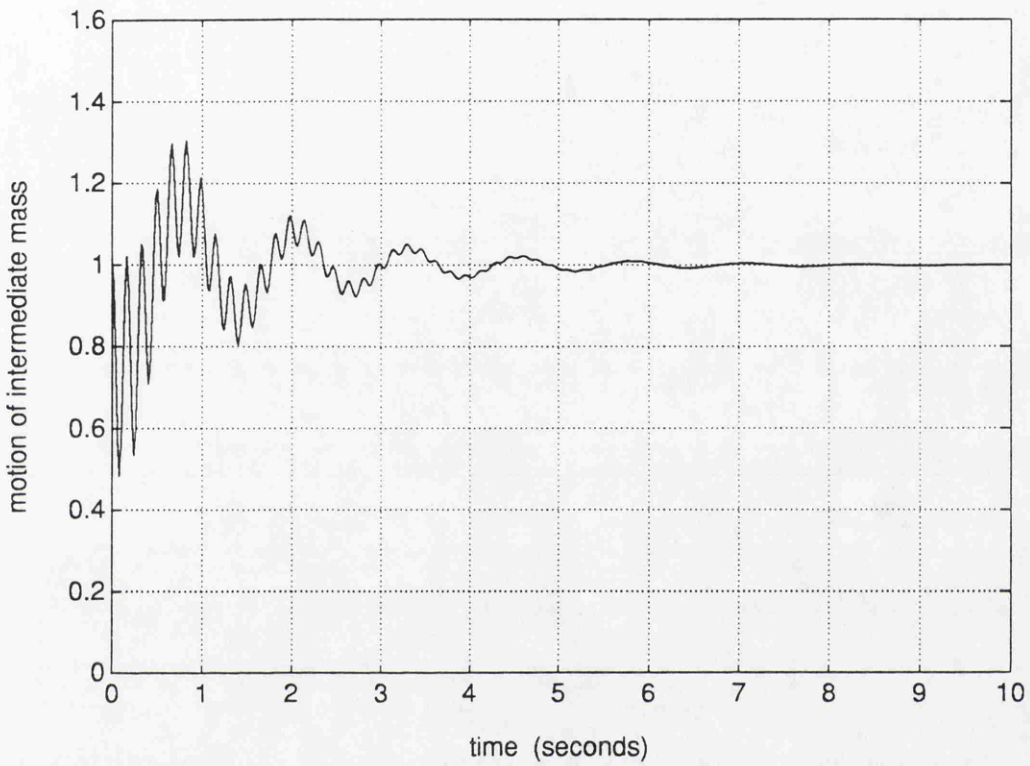

Figure 5.8: *Computed step response of the electronic damping system.*

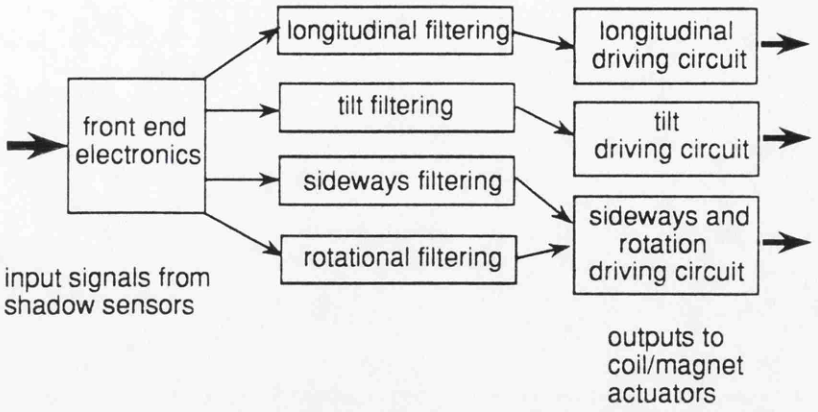

Figure 5.9: *A block diagram showing the main elements of the pendulum damping control system.*

section as follows:

The front end electronics

Here, signals derived from the shadow sensors, which sense the motion of the main test mass, are suitably combined to produce signals corresponding to the longitudinal, tilt, rotation and sideways motion of the pendulum. The particular circuit used is shown in figure 5.10.

The filtering stage

The signals from the front end electronics are suitably amplified and filtered at this stage, the exact form of the filtering depending on which degree of freedom is being dealt with. Sufficient gain and phase margin must be achieved in order to ensure that the closed loop system is stable and that the resonances of the system are sufficiently well damped (as discussed earlier in this section). The filtering circuits for the longitudinal and rotational degrees of freedom are shown in figure 5.11 whilst the circuits used for the sideways and tilt degrees of freedom are shown in

figure 5.12.

The coil drivers

The final stage of the electronics is used to drive current through the coils which are used as part of the actuators in the feedback system. The drivers must be capable of producing sufficient current to apply forces which can damp the mass and control its orientation (*via* the DC alignment controls). It is also important to ensure that this stage is sufficiently quiet in the detection frequency range (100 Hz $\rightarrow$ a few kHz) so that the performance of the detector is not compromised (see discussion on 'back end' noise in section 2.3.2).

The circuit diagrams in figure 5.13 show the particular arrangement of the electronics used for the final drive stage. Each driver consists of an LM759CP power op-amp with a low noise LT1028 op-amp connected to the input of the 759; the feedback on the LT1028 being derived from the output of the 759. Such an arrangement gives a system which has the current driving capabilities of the 759 (which can supply up to 325 mA) whilst retaining the low noise characteristics of the LT1028 (the typical input noise voltage of this device being $\sim 1\mathrm{nV}/\sqrt{\mathrm{Hz}}$).

In operation, 1 V input to the driver stage produces a force *via* the coil/magnet actuators (described in section 5.2.2) which could typically move the intermediate mass by $\sim$ 1 mm.

5.2.5 Performance of the system

The two stage pendulum was initially constructed outside of the main detector vacuum system in order to fully test out the control and operation of the damping system. Following this, the complete system was installed in the 10 m prototype to suspend the end mirror in the primary cavity.

The initial performance of the system was judged to be satisfactory. The damping system prevented large motions of the suspended test mass in the vacuum system, allowing the laser frequency to be stabilised to the primary cavity (for more details on this see section 4.2.3 on frequency stabilisation). The orientation

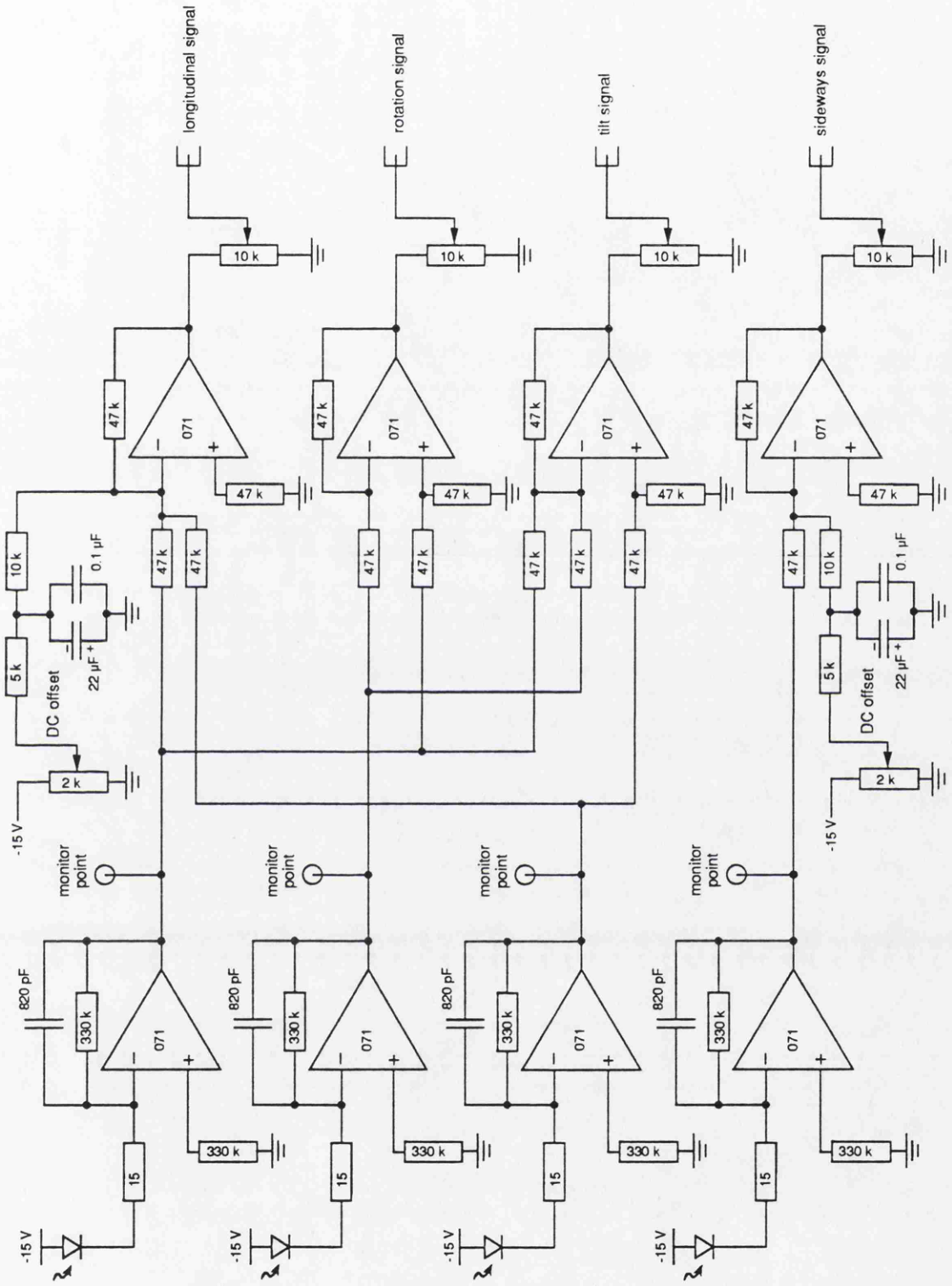

Figure 5.10: *The front end electronics used in the local damping system.*

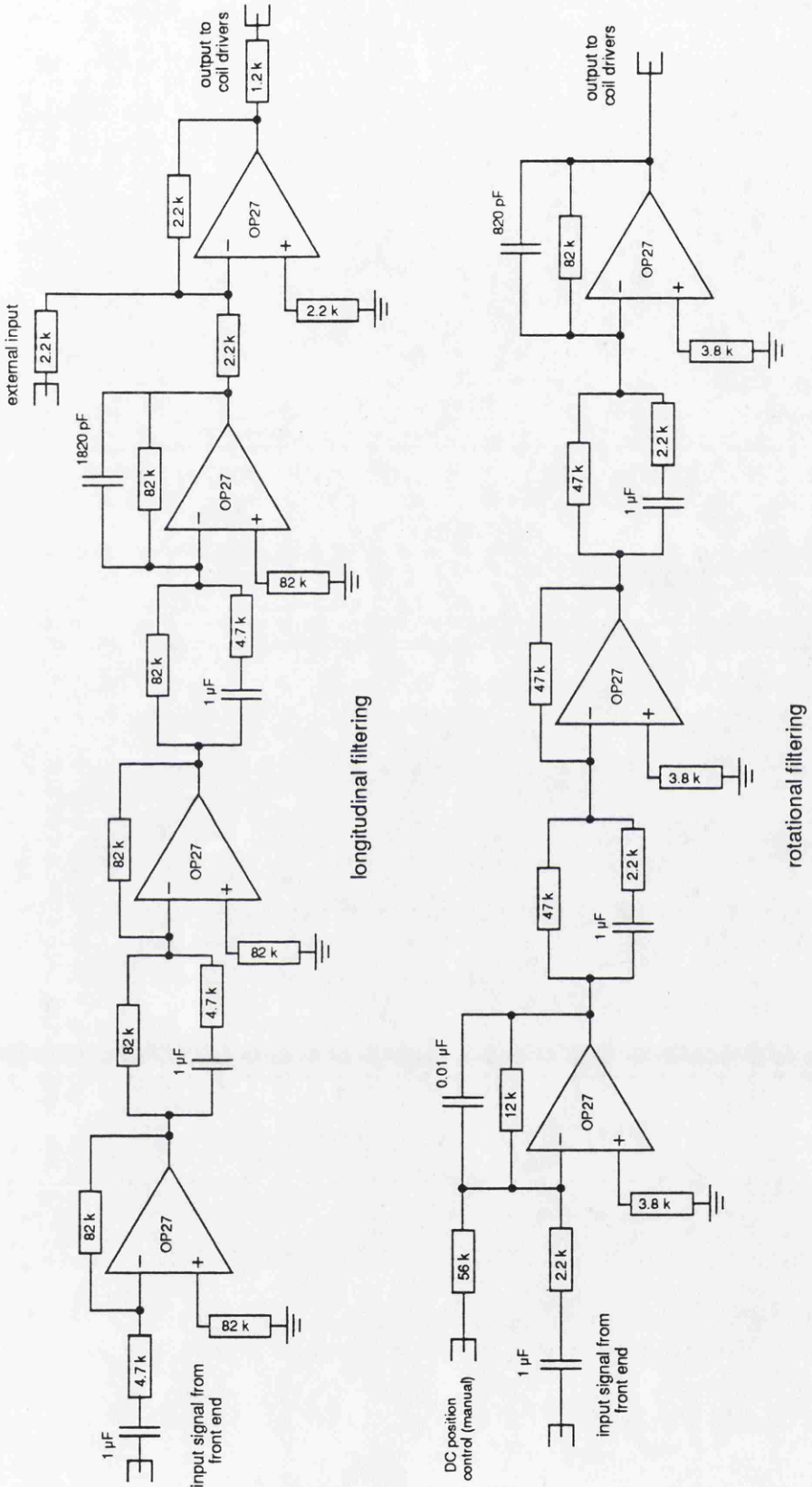

Figure 5.11: *The longitudinal and rotation filtering stages of the local damping system.*

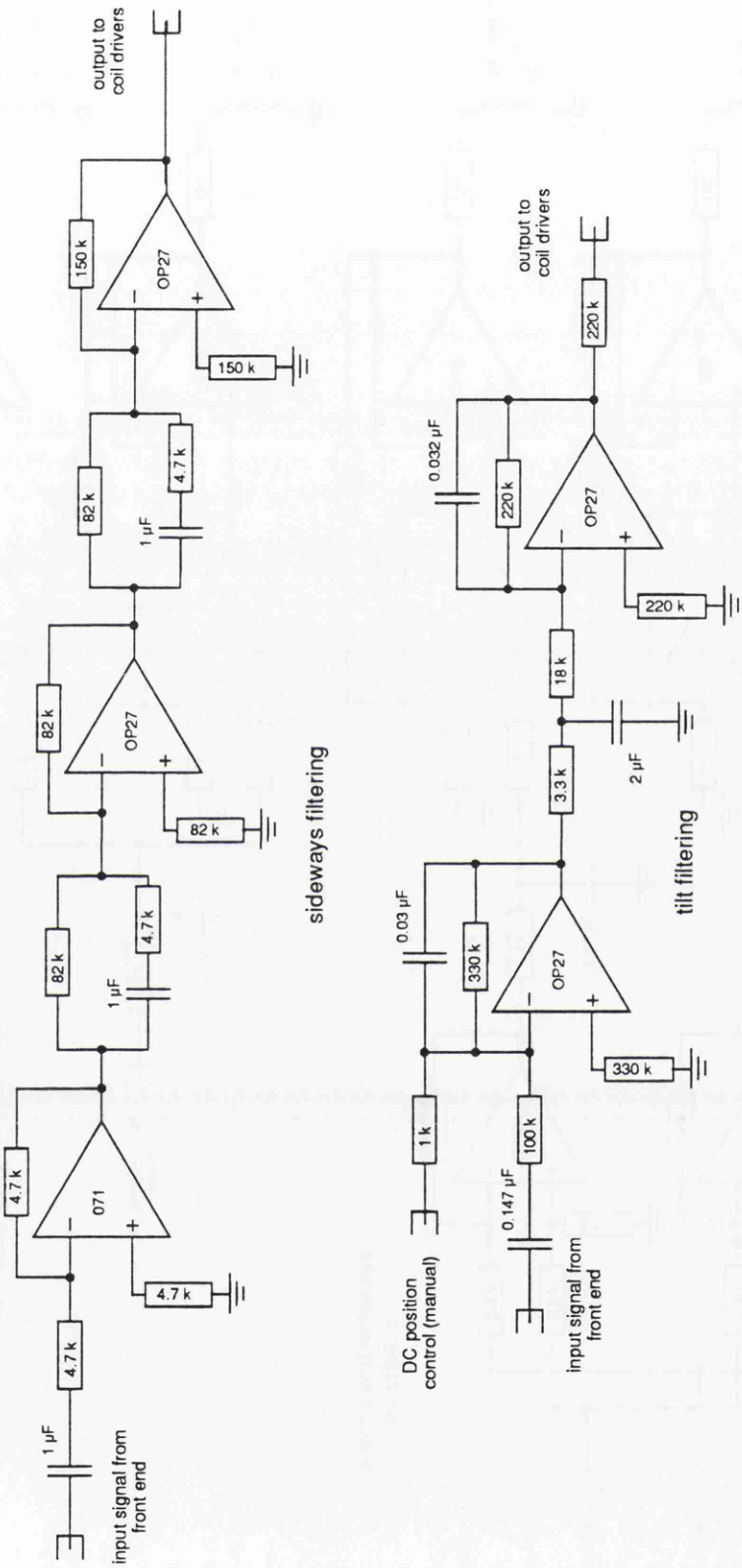

Figure 5.12: *The sideways and tilt filtering stages of the local damping system.*

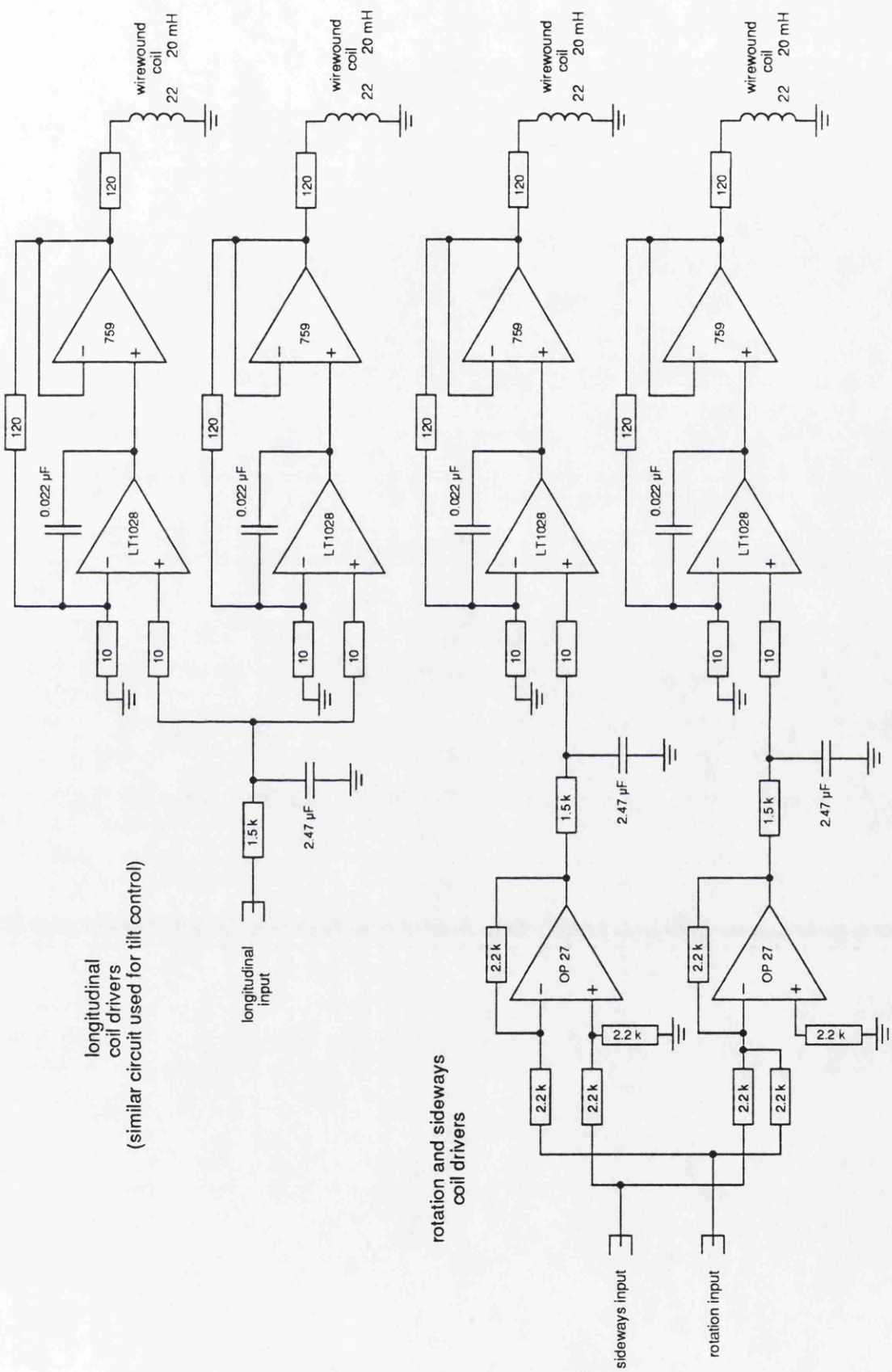

Figure 5.13: *The coil-driving circuitry used in the local damping system.*

controls had sufficient dynamic range to allow both coarse and fine adjustments of the alignment of the cavity mirror.

Indeed the low frequency stability of the primary cavity appeared to have been improved by the installation of the new suspension system. Previously, some of the low frequency signal in the laser stabilisation system (up to $\sim 10\,\mathrm{Hz}$) was fed back to the end mass in the primary cavity. This helped to prevent large low frequency fluctuations in the laser frequency due to the motion of the suspended mirrors and so eased the acquisition of lock of the secondary cavity (since the secondary servo system effectively locks the length of the secondary cavity to the laser frequency – for a more detailed description see Chapter 4). This low frequency feedback signal to the end mass in the primary cavity was no longer required after the installation of the new suspension system.

Installation of the new suspension had no immediate effect on the sensitivity of the prototype detector. However, after some substantial improvements had been made to the low frequency performance of the interferometer (due mainly to improvements made to other orientation control systems as discussed in Chapter 4), this system was to provide the dominant noise source in the low frequency region (1 kHz and below). This is discussed in greater detail in section 4.5.1.

The noise imposed on the motion of the test mass can be estimated for the longitudinal degree of freedom. Since there is very little attenuation of the front end signal in the electronic filtering stage, the noise due to the shot noise in the front end is the dominant noise source in the system from 100 Hz upwards. Assuming a unity gain frequency at around 4.6 Hz (*i.e.* near the upper resonance), the effect of the front end noise on the motion of the test mass can be estimated (from knowing the form of the open loop transfer function).

Figure 5.14 shows the estimated level of noise imposed on the test mass due to the front end noise in the feedback system. The shadow sensors were estimated as having a noise floor of $\sim 10^{-10}\,\mathrm{m}/\sqrt{\mathrm{Hz}}$.

As can be seen, from about 700 Hz upwards, the noise imposed on the test mass is $< 10^{-18}\,\mathrm{m}/\sqrt{\mathrm{Hz}}$ and falls off very rapidly. This was well below the detector sensitivity at the time of installation. However, the low frequency performance of

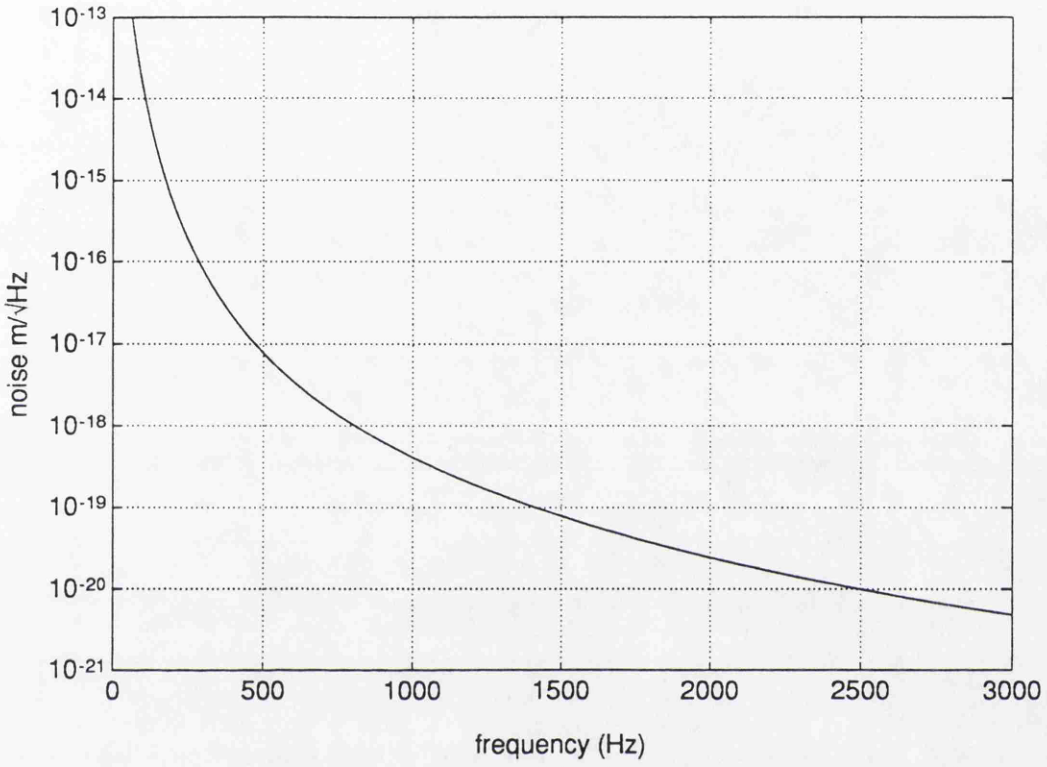

Figure 5.14: *Displacement noise imposed onto the detector sensitivity due to front end noise in the local damping system. It has been assumed that the wire resonances occur at* $\sim 400\,Hz$*, resulting in a decrease in the attenuation of the noise due to the pendulum above the frequency of the wire resonances. The high Q peak in the displacement noise due to the wire resonances is not shown.*

this particular system is quite poor. For example, the noise which is imposed on the motion of the main test mass at 100 Hz is estimated as being around $10^{-14}\,\mathrm{m}/\sqrt{\mathrm{Hz}}$. Not only is the low frequency noise quite poor but the high level of noise around the wire resonances of the suspension system caused large peaks to appear in the detector sensitivity (at frequencies corresponding to the wire resonances and their harmonics; 400 Hz, 800 Hz *etc.*).

In order to reduce the unacceptably high level of noise imposed on the test mass in the low frequency region it is necessary to use a local control system which senses and feeds back signals only to the intermediate mass. The problem with feeding back forces to the intermediate mass, derived from signals sensed at the main test mass, is that in order to control the upper resonance a phase lag in the response of the mechanical system of 360° must be overcome in order to ensure stability. The three differentiator stages used to reduce this large amount of phase lag to less than 180° resulted in a large amount of electronic gain in the feedback system at frequencies above the pendulum resonances. Although this gain is sufficiently reduced by the passive attenuation of pendulum at frequencies above 1 kHz, resulting in good noise performance at these frequencies, there is little attenuation of the front end noise at lower frequencies (especially around 100 Hz) and so the noise performance of the system is not so good.

The mechanical transfer function corresponding to driving signals to the intermediate mass and sensing at the intermediate mass on the other hand falls only as $\frac{1}{f^2}$ above the upper resonance. The phase lag in the response of the mechanical system is therefore only 180°. It is therefore possible to use a very narrowband servo to perform the local damping which need only advance the phase by a few degrees at the upper resonance to ensure stability. This can be achieved using a single differentiator (compared to the previous case where 3 differentiators were required) and hence the level of front end noise which is imposed on the motion of the test mass at low frequencies is dramatically reduced.

The next section deals with the construction, design and subsequent testing of such a system which was installed to suspend the test mass which acts as the end mirror in the secondary cavity of the 10 m prototype detector.

5.3 A two stage pendulum suspension system for the end mirror in the secondary cavity of the 10 m prototype.

In an attempt to improve upon the low frequency noise performance of the local damping control system described in the previous section, a similar two stage suspension was constructed where the local damping of the pendulum was achieved by sensing and feeding back signals only to the intermediate mass. This system was installed in the 10 m prototype detector, replacing the suspension system which was used to support the end mirror in the secondary cavity.

5.3.1 Design of the suspension system

It was decided to retain most of the features of the two stage pendulum originally designed for the end mass in the primary cavity, changing only the sensing and feedback electronics used to locally damp the system.

The coil/magnet actuators described in section 5.2.2 were slightly modified to incorporate the new sensing system. Small shadow sensors were inserted inside each of the 6 coil formers and flags were attached to each magnet on the intermediate mass. This allowed the 4 degrees of freedom of the intermediate mass which required damping to be sensed.

In order to correctly align the shadow sensors with the flags on the intermediate mass, the mounts used to fix the coil formers (and hence the shadow sensors) to the 'top hat' support structure had to be suitably modified. Holes were machined into the coil former mounts to accommodate the coil formers, allowing the shadow sensors to be accurately positioned with respect to the intermediate mass by simply moving the coil formers in or out of the holes. Once correctly positioned, the coil formers could be secured by tightening small grub screws on the side of the mounts.

5.3.2 Design of the electronics

The signals sensed using the 6 shadow sensors positioned around the intermediate mass were combined to give signals corresponding to the longitudinal, sideways, tilt and rotation degrees of freedom of the mass. These signals then require suitable amplification and filtering before being fed back to the coil/magnet actuators in order to ensure the closed loop system is stable.

In this case, the feedback strategy used is based on the same system described in section 2.4.3. A single differentiator starting from zero frequency is used to advance the phase at the pendulum resonances, after which the gain of the system is rolled off using low pass filters. As many low pass filters as possible are used in order to maximise the attenuation of the front end noise (from the shadow sensors) at detection frequencies (100 Hz and above) whilst maintaining a sufficient phase margin at the upper resonance.

Concentrating again on the longitudinal damping system, the particular form of the electronic filtering used is shown in the simplified Bode plot in figure 5.15. Comparing this with figure 5.6 which shows the equivalent circuit used for the

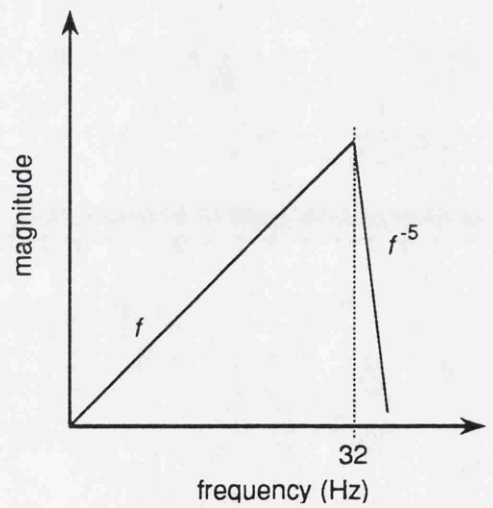

Figure 5.15: *A simplified Bode diagram showing the form of the electronic filtering in the longitudinal feedback control system.*

local damping control system described earlier, one can clearly see the difference in the relative gains of the two systems.

Figure 5.16 shows the computed magnitude and phase bode plots for the complete open loop system, including the pendulum response. As can be seen, in the regions where the gain is ≥ 1, the phase of the system is always $< +180°$ and $> -180°$ implying that the system is stable when the loop is closed. This is confirmed by examining the step response of the closed loop system shown in figure 5.17. As can be seen the system is indeed stable and damps down to a steady state in a few seconds. The difference in the gain of the open loop system between the unity gain point (around 5 Hz) and the lowest frequency of interest for detecting gravitational waves (100 Hz) is around 10^4. Any noise originating from the front end is not only attenuated by this factor of 10^4, but also by the mechanical response of the pendulum ($\sim 10^4$ at 100 Hz), before it is imposed on the motion of the main test mass. Compare this with the earlier control system (by examining the bode plots in figure 5.7) where the difference in gain between the unity gain point and 100 Hz was also about 10^4. In this case, since the motion of the actual test mass itself is sensed, any noise originating from the front end is only attenuated by this factor of 10^4 before being imposed directly onto the motion of the test mass. This comparison clearly illustrates the improvement in the noise performance of the second system.

One point worth mentioning is the difference between this system and the one mentioned in section 2.4.4. Here, the two resonances are at 0.9 Hz and 4.6 Hz and so are reasonably well separated in frequency (due to the differences in pendulum masses and suspension lengths). This makes it harder to design a control system which is capable of damping both resonances whilst maximising the attenuation of the front end noise. However, adopting the feedback strategy outlined in Chapter 2 still gave a reasonably satisfactory system when applied to this particular pendulum system. Because of the differences in the pendulum resonant frequencies, the actual noise performance achieved ($\sim 8 \times 10^{-19}$ m/$\sqrt{\text{Hz}}$ at 100 Hz – discussed later in section 5.3.3) is significantly worse than the example given in Chapter 2 (where both resonances were reasonably close together and < 2 Hz), but is nevertheless well below the best sensitivity which could be achieved with the 10 m prototype.

The electronic circuitry used to perform the local damping is shown in fig-

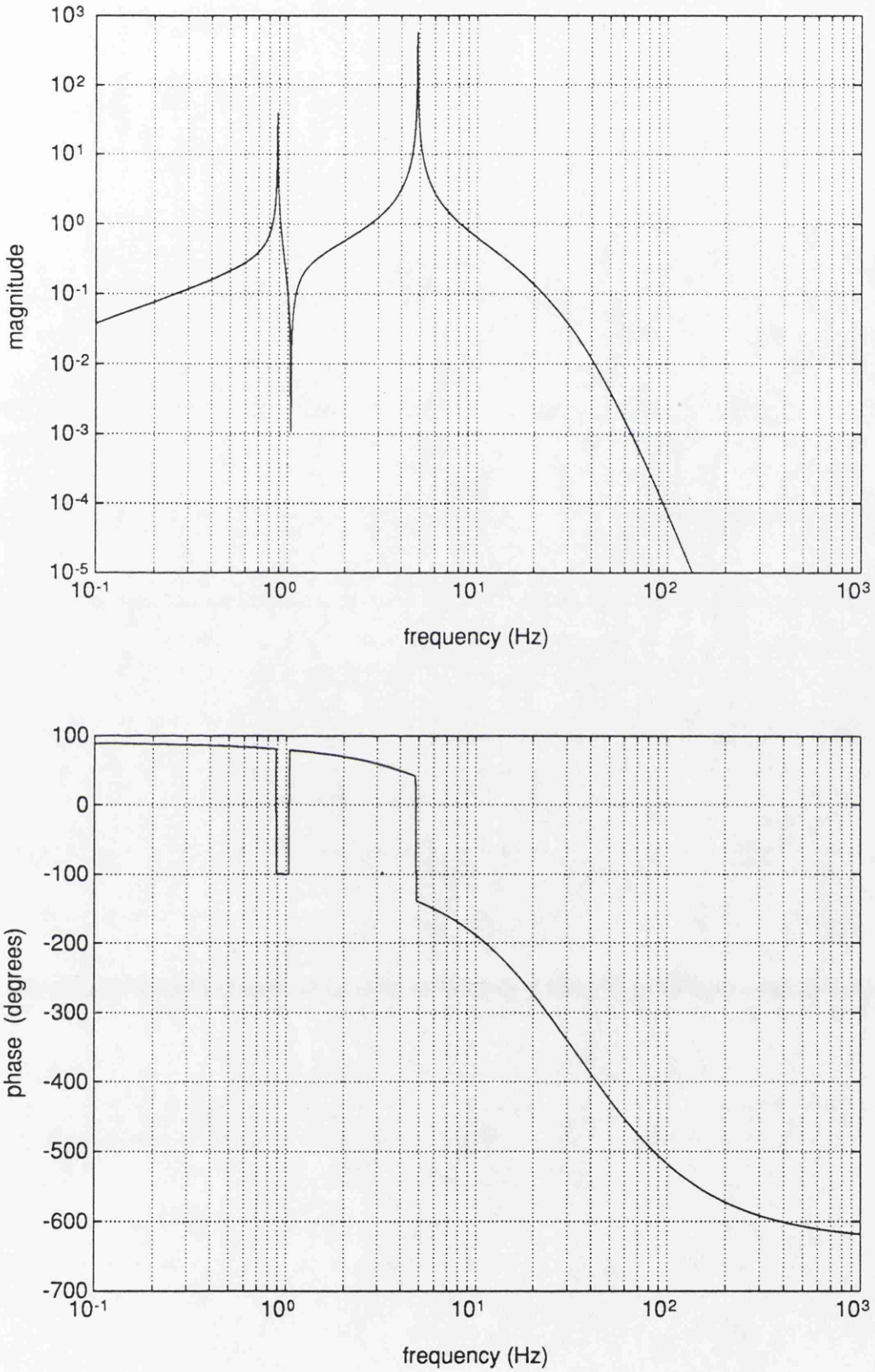

Figure 5.16: *Open loop gain and phase Bode plots for the complete damping system.*

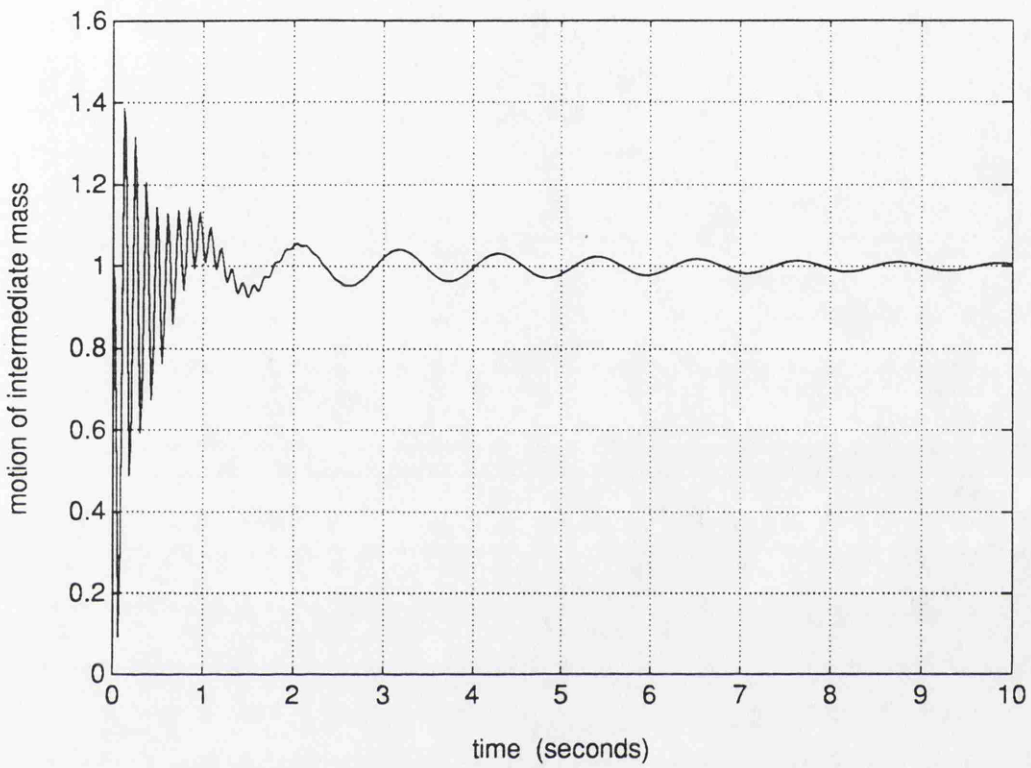

Figure 5.17: *Computed step response of the electronic damping system.*

ures 5.18, 5.19 and 5.20. The final coil-driving electronics is basically the same as that used in the damping system described earlier, with some slight changes to the filtering on the input stages. The front end electronics and the filtering stages for the longitudinal and rotation degrees of freedom can be seen in figure 5.18 and for the sideways and tilt degrees of freedom in figure 5.19. In each case, two shadow sensor signals are combined to produce a signal corresponding to the particular degree of freedom to be controlled. These signals are then amplified and filtered (as described earlier in this section) before being transferred to the coil drivers.

5.3.3 Performance of the system

After the initial construction and testing of the pendulum system and the damping electronics, the suspension system was installed to support the end mass in the secondary cavity. This resulted in an immediate reduction in the low frequency noise in the 10 m prototype's output signal (described in greater detail in section 4.5.1).

As for the previous system it is possible to estimate the noise performance from knowing the open loop gain of the system and the magnitude of the various noise sources in the servo. Plotted in figure 5.21 is the estimated noise imposed onto the motion of the main test mass by the local control servo. The sensing noise was assumed to be at the $10^{-10}\,\mathrm{m}/\sqrt{\mathrm{Hz}}$ level and the input noise of the current drivers around $2\,\mathrm{nV}/\sqrt{\mathrm{Hz}}$ (these were representative of the typical values measured on the actual system). As can be seen, the front end noise is very steeply filtered (both by the electronics and the response of the two stage pendulum). This results in the servo only being front end limited up to $\sim 400\,\mathrm{Hz}$. Above this, the back end noise, due to the final coil driver stage, is the dominant noise source (the back end noise in this case is only attenuated by the action of the two stage pendulum).

Comparison with the equivalent noise graph plotted for the control system studied earlier (see figure 5.14) clearly shows the improvement in noise performance achieved by sensing and feeding back only to the intermediate mass. This system is almost a factor of 10^4 quieter at 100 Hz and a factor of 10^6 quieter at 400 Hz (near the wire resonances).

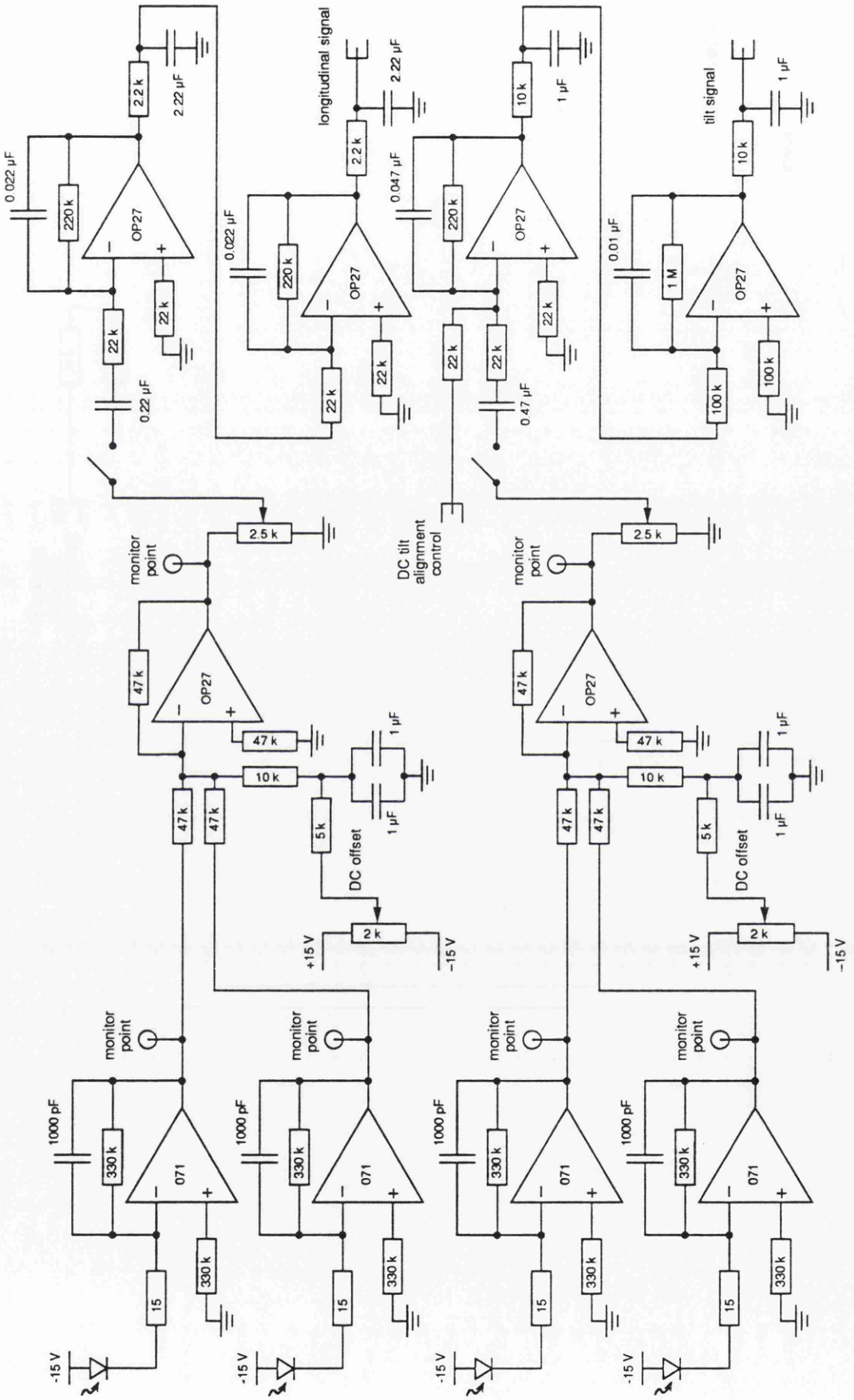

Figure 5.18: *The front end electronics and filtering stages used in the longitudinal and tilt local damping systems.*

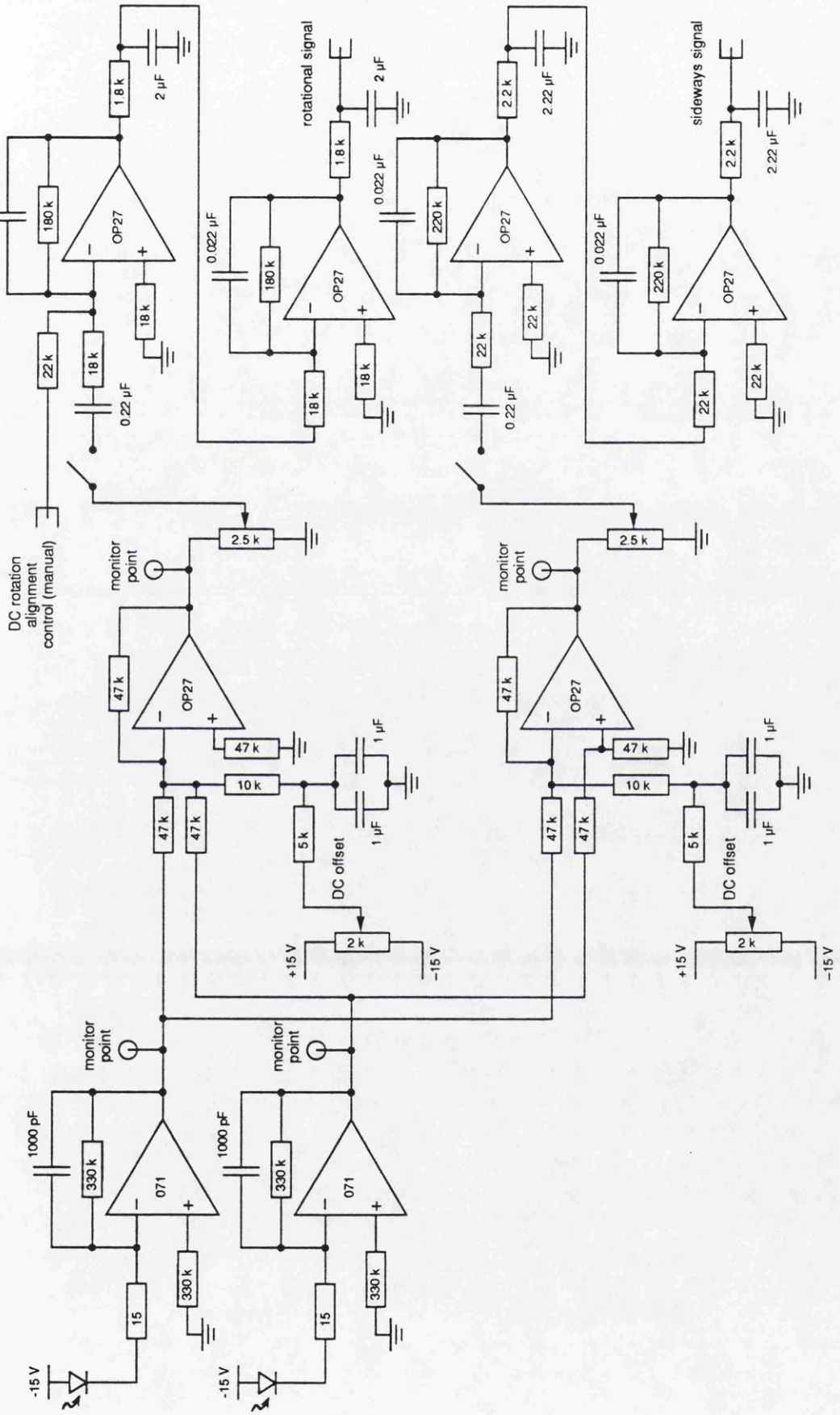

Figure 5.19: *The front end electronics and filtering stages used in the rotational and sideways local damping systems.* 185

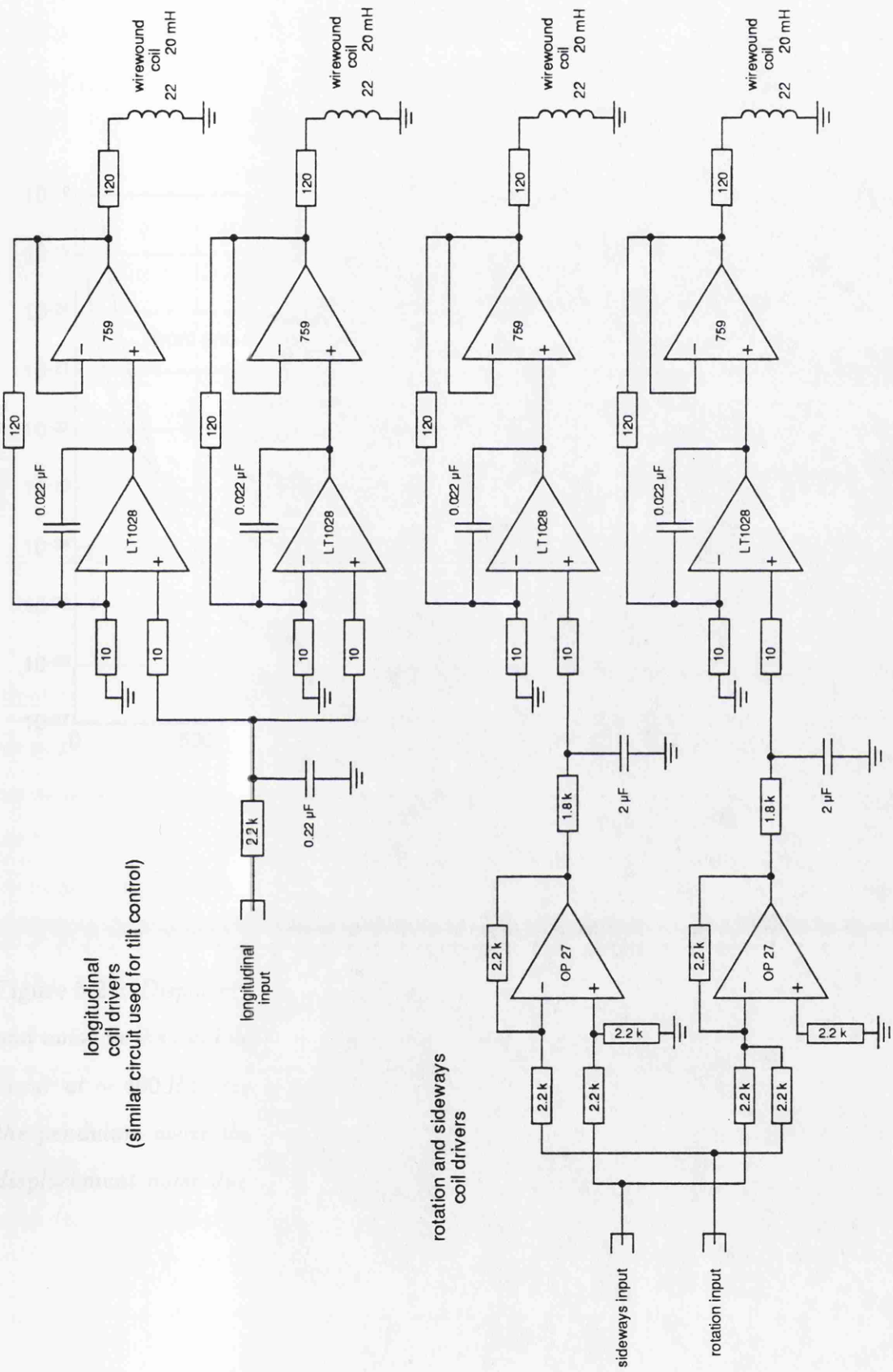

Figure 5.20: *The coil-driving circuitry used in the local damping system.*

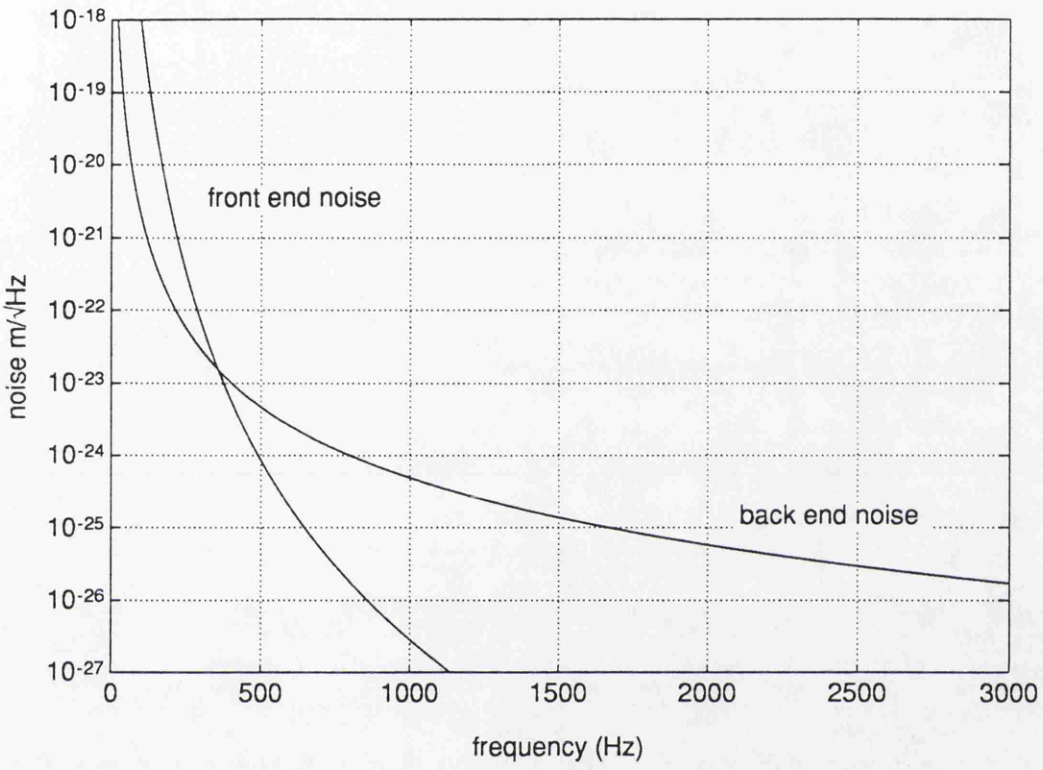

Figure 5.21: *Displacement noise imposed onto the detector sensitivity due to front end noise in the local damping system. It has been assumed that the wire resonances occur at* $\sim 400\,Hz$*, resulting in a decrease in the attenuation of the noise due to the pendulum above the frequency of the wire resonances. The high Q peak in the displacement noise due to the wire resonances is not shown.*

The step response of the system was measured by injecting a DC voltage into the feedback loop and observing the response of the servo system. This is plotted in figure 5.22 and can be compared with the computed step response shown earlier in figure 5.17. As can be seen, the model predicts very well the actual response of the damping system. Since the volts shown in figure 5.22 were measured at the output of the sensing system, it is possible to calculate the motion of the intermediate mass from the measured response of the shadow sensors (the two shadow sensors used gave $\sim 14\,\mathrm{V/mm}$). On the graph, then, 1 V corresponds to $\sim 70\,\mu\mathrm{m}$ and the residual motion of the damped pendulum is therefore less than $2\,\mu\mathrm{m}$ rms.

The actual noise being driven onto the intermediate mass *via* the coil/magnet force actuators was also measured. This is shown in figure 5.23. This graph shows the voltage measured across one of the $47\,\Omega$ resistors in series with the coils which form part of the actuator which applies longitudinal forces to the intermediate mass (see the circuit diagram shown in figure 5.20). As can be seen, with the servo switched on, the noise, which is due to the shot noise in the shadow sensor, dominates over the electronic noise in the system which can be measured with the servo switched off (since the servo switch is positioned immediately after the signal derived from the shadow sensors in the electronics, as indicated in figure 5.18). The shot noise, which is the dominant signal in the servo from $\sim 30\,\mathrm{Hz}$ up, corresponds to a sensing limit of $1 \times 10^{-10}\,\mathrm{m}/\sqrt{\mathrm{Hz}}$

The open loop gain of the electronic filtering stage was also measured to be $\sim 28\,\mathrm{dB}$ between 100 Hz and the unity gain frequency (which was around 4.6 Hz). Combining these figures with the mechanical response of the pendulum it is possible to calculate the limit which such a damping system would set to the sensitivity of an interferometer containing one of these suspension systems. The limit set is calculated as being $\sim 8 \times 10^{-19}\,\mathrm{m}/\sqrt{\mathrm{Hz}}$ at 100 Hz. This is in excellent agreement with the predicted noise performance shown in figure 5.21.

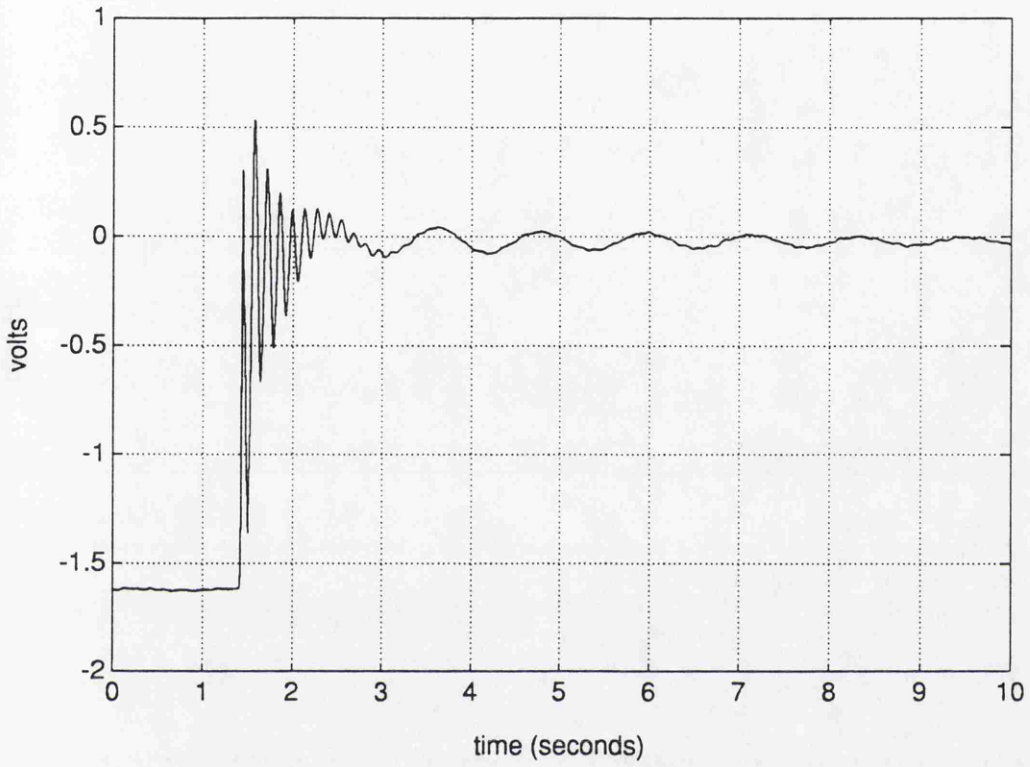

Figure 5.22: *Measured step response of the local damping system used to control the two stage pendulum which senses and feeds back signals only to the intermediate mass. The volts plotted correspond to the output of the shadow sensor system used to monitor the longitudinal motion of the intermediate mass.*

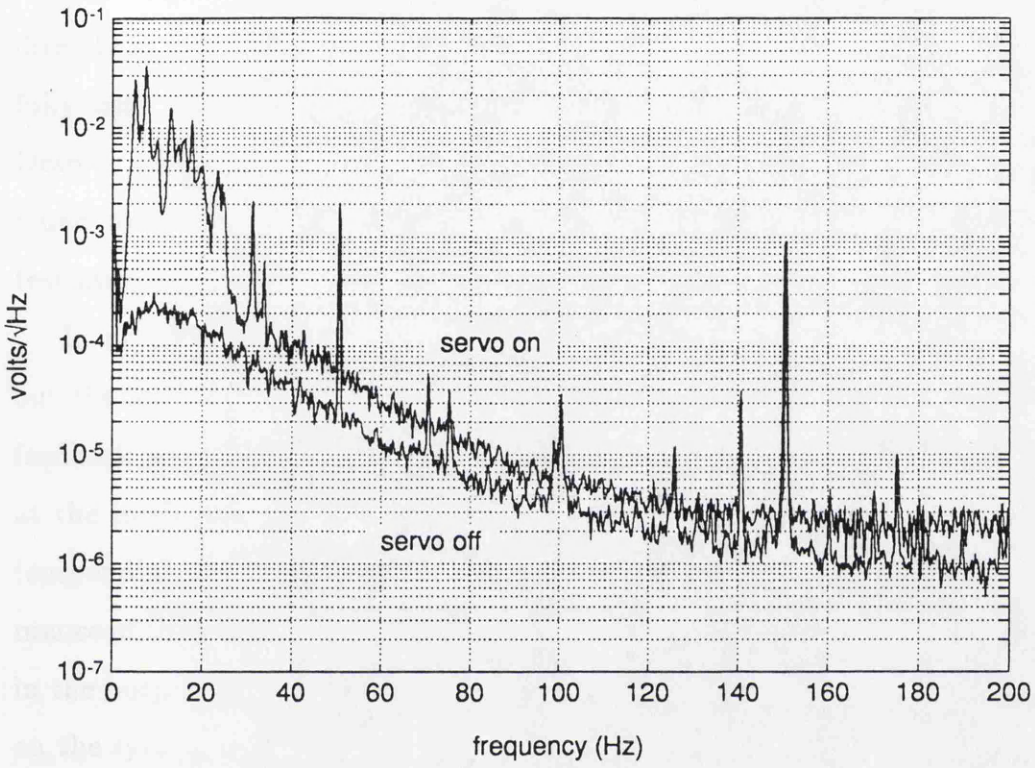

Figure 5.23: *Noise measured in the current being driven through one of the coils in the longitudinal actuator with the servo switched on and off. The voltage plotted is that developed by the current flowing through a 47Ω resistor.*

5.4 Summary

Two types of local control systems for use in damping the high Q resonances of a two stage pendulum have been investigated.

The first type, based on a system which senses the motion of the pendulum directly at the main test mass and feeds back to the intermediate mass, was successfully installed to suspend the end mass in the primary cavity of the 10 m prototype. Despite its good low noise performance in the $2 \rightarrow 3$ kHz region this system was found to impose reasonably large amounts of noise onto the motion of the main test mass at lower frequencies.

In an effort to reduce the low frequency noise in such a system, and to test out the ideas discussed in Chapter 2 on noise and control systems, the electronic feedback was redesigned so that the signals for the local control were also sensed at the intermediate mass. This system was also installed in the 10 m prototype (suspending the end mass in the secondary cavity). The excellent low noise performance of this system resulted in an immediate reduction in the low frequency noise in the output signal of the 10 m prototype. Subsequent measurements performed on the system confirmed its low noise performance.

Due to the success of this system, a duplicate has since replaced the local control damping system originally designed for the end mass in the primary cavity. Again, this resulted in a further reduction in the low frequency noise present in the output signal of the prototype detector as discussed in section 4.5.1.

Chapter 6

Summary

The analysis of the effects of noise in the control feedback systems used in laser interferometric gravitational wave detectors given in Chapter 2 has proved extremely useful, both in the recent developments on the 10 m prototype detector, and in evaluating possible systems for use in longer baseline detectors.

In particular it has been shown that extreme care must be taken when designing even the simple local control systems used to damp the high Q pendulum resonances of the suspended interferometer components. These considerations will, to a large extent, dictate the detailed design of the suspension systems used. One particular system based on sensing the position of a test mass, which is suspended using a double pendulum, with simple LED/photodiode shadow sensors has been analysed and its performance estimated from typical laboratory measurements – the results indicating that such a system should be able to meet the requirements of an advanced long-baseline detector.

The main interferometer locking system has also been studied and the possible problems associated with split and single feedback strategies have been outlined. This area clearly requires some detailed experimental investigation and testing – possibly on the prototype detector.

A novel system for providing the local damping control based on an inertial sensor was also investigated experimentally and its operation successfully demonstrated. Some of the main drawbacks of this technique, particularly the poor low frequency stability associated with the use of the inertial sensor, were analysed.

The technique for automatic alignment of the suspended components in an in-

terferometer, discussed in Chapter 3, could prove to be of great importance in the successful operation of proposed long-baseline interferometers. Any interferometer which is locked by differentially phase modulating two interfering beams can be aligned using the technique described. In addition to accurately aligning the two interfering beams both laterally and angularly, it is also possible to use the technique to correct for any mismatch in the beam size or radius of curvature of the phase fronts of the two beams. A full mathematical treatment of the technique based on the normal spatial modes of the beams has been presented.

The technique has been successfully demonstrated both on a simple benchtop Michelson interferometer and on one of the 10 m long suspended optical cavities in the prototype gravitational wave detector. These tests allowed the theoretical ideas which were developed to be tested and also highlighted some problems associated with the technique, most critically the need for good DC stability in the electronics associated with the feedback control.

Much progress has been made in the development of the 10 m prototype detector over the past few years, particularly in understanding the source of much of the low frequency noise present in the detector output. The study of these noise sources and their subsequent suppression has led to some dramatic improvements in the sensitivity of the detector – almost a factor of 10^3 between 100 Hz and 500 Hz. Future work will probably continue the investigation of noise sources in the detector and efforts will be made to try to increase significantly the light power entering the interferometer in order to reach displacement sensitivities below $10^{-19}\,\mathrm{m}/\sqrt{\mathrm{Hz}}$.

Due to these recent improvements, the displacement sensitivity of the prototype detector at Glasgow is better than any other prototype in the 200 Hz $\rightarrow$ 3 kHz frequency region. The detailed examination and subsequent suppression of the various noise sources present in the 10 m prototype have proved to be extremely useful in improving the sensitivity of the detector. Indeed, the ability to achieve high sensitivities with the prototype lends confidence to the hope that future large scale detectors will ultimately reach the required sensitivities necessary for the detection and study of gravitational waves.

Appendix A

Shot noise limited sensitivity of an optical cavity used as a frequency discriminator.

The Fabry-Perot cavities used in the arms of the 10 m prototype gravitational wave detector in Glasgow are locked on resonance using the *rf* reflection locking technique [53], as discussed in Chapter 4, allowing the frequency fluctuations of the input laser light to be determined with respect to the length of the cavity.

A fundamental limit to the sensitivity of such a system is set by photon shot noise. This has been discussed by several authors and recently reviewed (see papers by Niebauer *et al.* [50] and Meers and Strain [51]) to take into account the effects of the various modulation schemes used on the shot noise limit. The shot noise limit to the detectable frequency fluctuations, $\delta\nu$, observed using a cavity locked using the *rf* reflection locking scheme is given by Hough *et al.* [26] (and correctly modified according to [50] for the case of sinewave *rf* modulation of the input light and sinewave demodulation of the detected signal) as

$$\frac{\delta\nu}{\nu} = \frac{\lambda}{4\pi\tau_s c}\sqrt{\frac{h\nu}{\epsilon I_0}}\,\frac{\sqrt{1 - {J_0}^2 M V_{opt} + 2MA_cJ_0J_2}}{M_0J_0J_1A_c}\,\sqrt{1+(2\pi f\tau_s)^2}\,/\sqrt{\mathrm{Hz}}\,, \qquad \text{(A.1)}$$

where A_c represents the relative amplitude of the light leaking out of the cavity on resonance (for perfect modematching and no modulation), M is the modematching factor, representing the fraction of the incident light power I_0 which is correctly matched to the fundamental mode of the cavity (again with no modulation present), ϵ is the quantum efficiency of the photodetector, V_{opt} is the optimum

fringe visibility which would be observed with no modulation and perfect mode-matching, f the detection frequency, J_0, J_1 and J_2 are first order Bessel functions and τ_s is the storage time of the cavity (the $\frac{1}{e}$ decay time of the cavity mode amplitude, which is also the reflected $\frac{1}{e}$ decay time of the reflected intensity when the cavity shifts off resonance).

In a laser interferometric gravitational wave detector it is the differential displacement between the two orthogonally oriented arms which is of interest. In the 10 m prototype, each arm consists of an optical cavity in which the input laser light resonates. For a cavity on resonance the length of the cavity corresponds to an integral number of half wavelengths of the laser light, *i.e.*

$$l = \frac{n\lambda}{2} . \tag{A.2}$$

Differentiating this equation gives the relation

$$\frac{\delta l}{l} = -\frac{\delta \nu}{\nu} . \tag{A.3}$$

By using this relationship it is possible to calculate from equation A.1 the shot noise limited sensitivity of an optical cavity to a relative displacement of its two mirrors.

It should be noted that in order to reach the shot noise limited displacement sensitivity using a single cavity, the frequency of the light which is used to determine the differential displacement of the two cavity mirrors must itself be stabilised to a level below the level set by equation A.3. In practice two cavities can be used, as in the 10 m prototype, where the frequency of the light is initially stabilised to the primary cavity to a level which is near the shot noise limit. The stabilised light is then directed towards the second cavity (the secondary cavity). The signal which is detected when the secondary cavity is locked so that the light is resonant in the cavity represents the differential arm length change of the two cavities.

Any excess frequency fluctuations in the laser light which are not reduced to the shot noise limit in the primary cavity stabilisation system can be subtracted electronically (as described in section 4.2.2) ensuring that the detector can indeed

reach the shot noise limited displacement sensitivity. Alternatively, the two beams returning from each cavity can be optically recombined at a beamsplitter and the main detector signal obtained by monitoring the interference at the beamsplitter output. Again this eliminates the effect of any excess frequency fluctuations which would otherwise prevent the detector from reaching the shot noise limited displacement sensitivity.

The shot noise limited sensitivity of the detector can be calculated from knowing the theoretical shot noise limited displacement sensitivity of the primary cavity, δx_{pc}, and the secondary cavity, δx_{sc}, by adding the (independent) noise signals in quadrature using the following expression:

$$\delta x = \sqrt{{\delta x_{pc}}^2 + {\delta x_{sc}}^2} \, . \tag{A.4}$$

As an example, consider the shot noise limited sensitivity of the 10 m prototype gravitational wave detector, described in Chapter 4. Typical values for the cavity parameters are as follows: the storage times of the cavities are around 150 μs (although this figure could vary depending on the level of contamination of the cavity mirrors); the observed visibility, V_{obs}, around 54%; and the unlocked photocurrent detected from the photodiodes $(\frac{q\epsilon J_0}{h\nu}) \sim 6\,\mathrm{mA}$. The phase modulation of the input light is arranged so that the power in each of the first order modulation sidebands is $\frac{1}{6}$ of the power at the fundamental laser frequency, giving $J_0 = 0.862$, $J_1 = 0.352$ and $J_2 = 0.069$ (this choice of modulation depth gives the optimum sensitivity for cavities with the visibilities which were typically observed during the operation of the detector). The transmission of each cavity input mirror, T, is 500 ppm (in intensity). The relative amplitude of the light leaking out of the cavity on resonance can be calculated from

$$A = \frac{T c \tau_s}{2l} \, , \tag{A.5}$$

where l is the length of the cavities (in this case $l = 9.7\,\mathrm{m}$), giving a value for A of 1.16. The optimum visibility is given by

$$V_{opt} = 2A - A^2 \, , \tag{A.6}$$

giving a value of $V_{opt} = 0.974$. The modematching factor can be calculated from

$$M = \frac{V_{obs}}{J_0^2 V_{opt}} , \tag{A.7}$$

giving $M = 0.74$. If these values are then substituted into equations A.1 and A.3, then the shot noise limited displacement sensitivity of the detector is given by

$$\delta x = 1.8 \times 10^{-19} \sqrt{1 + \left(\frac{f}{1.1\,\mathrm{kHz}}\right)^2}\ \mathrm{m}/\sqrt{\mathrm{Hz}} . \tag{A.8}$$

This is shown on figure 4.17 in Chapter 4.

Bibliography

[1] A. Einstein, Sitzungsber Preuss. Akad. Wiss., 688 (1916)

[2] B.F. Schutz, *A First Course in General Relativity,* (Cambridge University Press, Cambridge, 1985)

[3] I.R. Kenyon, *General Relativity*, (Oxford University Press, Oxford, 1990)

[4] R.L. Forward, *General Relativity for the Experimentalist*, Proc. IRE (May 1961)

[5] J.H. Taylor, L.A. Fowler and P.M. McCulloch, Nature, **277**, 437 (1979)

[6] K.S. Thorne, in *300 Years of Gravitation* edited by S. W. Hawking and W. Israel, (Cambridge University Press, Cambridge, 1987)

[7] J. Hough *et al.*, *Proposal for a Joint German-British Interferometric Gravitational Wave Detector.* Report **MPQ 147**, (Max-Planck-Institut für Quantenoptik, Garching, 1989)

[8] B.F. Schutz, Nature, **323**, 310 (1986)

[9] J. Hough, B.J. Meers, G.P. Newton, N.A. Robertson, H. Ward, B.F. Schutz and R.W.P. Drever, *A British Long Baseline Gravitational Wave Observatory*, Design Study Report GWD/RAL/86-001 (1986)

[10] J. Weber, Physical Review, **117**, 306 (1960)

[11] J. Weber, Physical Review Letters, **22**, 1302 (1969)

[12] P.J. Veitch, in *The Detection of Gravitational Waves* edited by D. G. Blair, (Cambridge University Press, Cambridge, 1991)

[13] J.P. Richard and W.M. Folkner, in *The Detection of Gravitational Waves* edited by D. G. Blair, (Cambridge University Press, Cambridge, 1991)

[14] F. Ricci and Hu En Ke, in *Proceedings of the Fifth Marcell Grossman Meeting on General Relativity*, edited by D. G. Blair and M. J. Buckingham, (World Scientific, Singapore, 1989)

[15] E. Amaldi *et al.*, in *Proceedings of the Fifth Marcell Grossman Meeting on General Relativity*, edited by D. G. Blair and M. J. Buckingham, (World Scientific, Singapore, 1989)

[16] R.L. Forward, Physical Review D, **17**, 379 (1978)

[17] R.E. Vogt, R.W.P. Drever, K.S. Thorne, F.J. Raab and R. Weiss, *LIGO proposal*, (Caltech, 1989)

[18] A. Giazotto, A. Brillet *et al.*, *The VIRGO project report*, (1989)

[19] B.J. Meers, Ph.D thesis, Glasgow University (1983)

[20] B.J. Meers, Physical Review D, **38**, 2317 (1988)

[21] F.R. Connor, *Noise*, (Edward Arnold, London, 1982)

[22] N.A. Robertson, in *The Detection of Gravitational Waves* edited by D. G. Blair, (Cambridge University Press, Cambridge, 1991)

[23] C.A. Cantley, Ph.D thesis, Glasgow University (1991)

[24] R. Del Fabbro, A. Di Virgilio, A. Giazotto, H. Kautsky, V. Montelatici and D. Passuello, Review of Scientific Instruments, **59**, 292 (1988)

[25] P.R. Saulson, Physical Review D, **42**, 2437 (1990)

[26] J. Hough *et al.*, in *The Detection of Gravitational Waves* edited by D. G. Blair, (Cambridge University Press, Cambridge, 1991)

[27] N.A. Robertson, S. Hoggan, J.B. Mangan and J. Hough, Applied Physics B, **39**, 149 (1986)

[28] A. Rüdiger, R. Schilling, L. Schnupp, W. Winkler, H. Billing and K. Maischberger, Optica Acta, **28**, 641 (1981)

[29] B.J. Meers, G.P. Newton and R.W.P. Drever, unpublished report, Glasgow University

[30] K.S. Thorne, LIGO technical report, (Caltech, 1989)

[31] N.A. Robertson, K.A. Strain and J. Hough, Optics Communications, **69**, 345 (1989)

[32] W. Winkler, K. Danzmann, A. Rüdiger and R. Schilling, Physical Review A, **44**, 7022 (1991)

[33] R.W.P. Drever, in *Quantum Optics, Experimental Gravitation, amd Measurement Theory*, edited by P. Meystre and M. O. Scully, (Plenum Press, New York, 1983)

[34] K.A. Strain, Ph.D thesis, Glasgow University (1990)

[35] P. Fritschel, D. Shoemaker and R. Weiss, Applied Optics, **31**, 1412 (1992)

[36] K.A. Strain and B.J. Meers, Physical Review Letters, **66**, 1391 (1991)

[37] J. Mizuno, K.A. Strain, P.G. Nelson, J.M. Chen, R. Schilling, A. Rüdiger, W. Winkler and K. Danzmann, submitted to Physics Letters A, (1992)

[38] S. Thomson, *Control Systems Engineering and Design*, (Longman Scientific and Technical, 1989)

[39] R.C. Dorf, *Modern Control Systems*, (Addison Wesley, 1976)

[40] Burr-Brown IC Data Book, Volume 33, 2-55

[41] P.G. Nelson, presentation given at the WE-Heraeus Seminar on *The Detection of Gravitational Waves*, Bad Honnef, Germany (June 1992)

[42] L.E. Holloway *et al.*, *A Coil System for VIRGO Providing a Uniform Magnetic Field Gradient*, unpublished VIRGO report, (1991)

[43] A. Rüdiger, presentation given at the WE-Heraeus Seminar on *The Detection of Gravitational Waves*, Bad Honnef, Germany (June 1992)

[44] B.J. Meers, *An Automatically Aligning Optical Cavity*, unpublished report, University of Glasgow

[45] D.Z. Anderson, Applied Optics, **23**, 2944 (1984)

[46] N.M. Sampas and D.Z. Anderson, Applied Optics, **29**, 394 (1990)

[47] H. Kogelnik and T. Li, *Laser Beams and Resonators*, Applied Optics, **5**, 1550 (1966)

[48] G.D. Boyd and J.P. Gordon, Bell Syst. Tech. J., **40**, 489 (1961)

[49] E. Morrison, B.J. Meers, D.I. Robertson and H. Ward, to be submitted to Applied Optics

[50] T.M. Niebauer, R. Schilling, K. Danzmann, A. Rüdiger and W. Winkler, Physical Review A, **43**, 5022 (1991)

[51] B.J. Meers and K.A. Strain, Physical Review A, **44**, 4693 (1991)

[52] I.S. Gradshteyn and I.M. Ryzhik, *Table of Integrals, Series and Products*, (Academic Press, inc., London, 1980)

[53] R.W.P. Drever, J.L. Hall, F.W. Kowalski, J. Hough, G.M. Ford, A.J. Munley and H. Ward, Applied Physics B, **31**, 97 (1983)

[54] D. Shoemaker, R. Schilling, L. Schnupp, W. Winkler, K. Maischberger and A. Rüdiger, Physical Review D, **38**, 423 (1988)

[55] R.E. Vogt *et al.*, in *Proceedings of the Sixth Marcell Grossman Meeting on General Relativity*, Kyoto, Japan, (World Scientific, Singapore, 1991)

[56] M.E. Zucker *et al.*, in *Proceedings of the Sixth Marcell Grossman Meeting on General Relativity*, Kyoto, Japan, (World Scientific, Singapore, 1991)

[57] G.A. Kerr, Ph.D thesis, Glasgow University (1986)

[58] D.I. Robertson, Ph.D thesis, Glasgow University (1989)